Cyclic Dipeptide and Silk Fibroin-based (Bio)materials and Their Applications

A Thesis Submitted for the Degree of

Doctor of Philosophy

By

Shivaprasad Manchineella

Bioorganic Chemistry Laboratory, New Chemistry Unit

Jawaharlal Nehru Centre for Advanced Scientific Research

(*A Deemed University*)

Jakkur, Bengaluru-560064

India

July-2016

Dedicated to My Parents

CERTIFICATE

I hereby certify that the work embodied in the thesis entitled "***Cyclic Dipeptide and Silk Fibroin-based (Bio)materials and Their Applications***" has been carried out by **Mr. Shivaprasad Manchineella** under my supervision at Bioorganic Chemistry Laboratory, New Chemistry Unit, Jawaharlal Nehru Centre for Advanced Scientific Research (JNCASR), Bengaluru, India and that it has not been submitted elsewhere either in part or full for the award of any degree or diploma.

Prof. T. Govindaraju

(Research Supervisor)

DECLARATION

I hereby declare that the work embodied in the thesis entitled "***Cyclic Dipeptide and Silk Fibroin-based (Bio)materials and Their Applications***" is the resultant of investigations carried out by me at Bioorganic Chemistry Laboratory, New Chemistry Unit, Jawaharlal Nehru Centre for Advanced Scientific Research (JNCASR), Bengaluru, India under the supervision of **Prof. T. Govindaraju** and that it has not been submitted elsewhere either in part or full for the award of any degree or diploma.

In keeping with the general practice in reporting the scientific observations, due acknowledgement has been made whenever the work described is based on the findings of other investigators. Any omission that might have occurred due to oversight or error in judgement is regretted.

Shivaprasad Manchineella

(Ph.D. Student)

ACKNOWLEDGEMENTS

Firstly, I express sincere gratitude to my research supervisor Prof. T. Govindaraju, Bioorganic Chemistry Laboratory, New Chemistry Unit, JNCASR for his extended support and supervision all through the course of my Ph.D. journey. I am thankful to him for giving me an opportunity to work with him for my Ph.D. thesis.

I owe everything to my mother (Jayamma) and father (Sathyanarayana). I thank them for their unconditional love and extended support during difficult times of my life. I also thank my brother (Sairam), sisters (Radhika and Kalyani), brother-in-law (Ramprasad) and nephew (Rithwik) for their love and support.

I thank Prof. C. N. R. Rao, FRS, Chairman, New Chemistry Unit for being the constant source of inspiration, generous support and encouragement throughout my stay at JNCASR. I also thank him for providing the infrastructure and facilities to carry out my research work.

I am thankful to Prof. Subi J. George, Prof. Jayanta Haldar and Prof. Sridhar Rajaram from JNCASR, Prof. Sidhartha P. Sharma and Prof. P. Balaram from IISc for their invaluable course work teaching.

I sincerely thank Prof. U. Deva Priyakumar and Dr. V. Prathyusha from IIIT-Hyderabad, Prof. Praveen C. Ramamurthy, Dr. Khadija K. Khanum, Prof. Bikramjit Basu and Dr. Greeshma Thrivikraman from IISc, Bengaluru for their valuable collaborations.

I express sincere gratitude to my teachers Mr. Veerabadram (ZPSS), Mrs. Laxmi (ZPSS), Dr. Venkateswarlu (VDC), Mrs. Bhargavi (VDC), Mr. Prasad (VDC), Mr. Rambabu (VDC), Prof. David (OU), Prof. Ram Reddy (OU) for their encouragement and support.

I shall never forget the contributions of my labmates and the lessons I learned from them during my Ph.D. I extend my gratitude to Dr. Avinash, Dr. Debabrata Maity, Dr. Nagarjun, Dr. Pandeeswar, Mr. Rajasekhar, Ms. Suseela, Mr. Anand Raj, Mr. Sandeepa, Mr. Manjunath, Mrs. Manju, Dr. Atul, Ms. Shilpa, Ms. Malabika, Dr. Madhu, Dr. Chandrashekar, Dr. Sangita, Mr. Sulendar, Mr. Vardhaman, Dr. Abhaya, Mr. Sourav, Mr. Debasis, and Mr. Satyajit. I would like to thank the short-term students Avinash, Komal, Shreya, and Akshay. Special thanks to Dr. M. B. Avinash, co-guide for my summer project (SRFP) for all his teachings and support throughout the project work.

I thank Prof. S. N. Bhat for giving me an opportunity to teach undergraduate chemistry laboratory course (POCE), Prof. Sridhar Rajaram, Prof. Ranga Udaykumar, Prof. Rajesh Ganapathy and Ms. Lakshmi Kumari (JNC-EH&S) for helping me in learning the laboratory safety, chemical waste management and first aid measurements.

I sincerely acknowledge the timely help of technical staff Mr. Vasu (UV/PL/IR/TG/DSC), Mr. Mahesh (NMR), Mrs. Selvi (FESEM), Mrs. Usha (TEM), Mrs. Bhavya (SEM), Ms. Sonia (MALDI), Mr. Shiva Kumar (HRMS/CHNS), Mr. Basavaraj (AFM), Mr. Anil (PXRD), Mr. Peer, Mr. Mune Gowda and Mr. Dileep (Audio/Visual). I am also thankful to Mrs. Rajani, Mr. Naveen and Mrs. Shweta from NCU office for all their timely help and support.

I would like to express my sincere thanks to all the Academic, Administrative, Security, Library, Complab, JNC Health Centre (Dhanvantri), Hostel Office and Housekeeping staff for making JNC campus life hurdle free and memorable.

I thank all my friends from school, college, B.Sc, M.Sc, and Ph.D. for their company and support. Especially, Sathish, Balveer, Navya, Subbu, Swapna, Manohar,

Dayakar, Vijay, Yugandar, Anand Acharya, Saraiah, Saidulu, Vijaya, Praveen, Vasudev, Anand Raj, Prathyusha, Sandeep, Bhadram, Mohit, Ankit, Venkateswarlu, Diwakar, Chandradhish, Suresh, Murthy, Lingampalli, Subba Reddy, Ramana, Arjun, Pavan, Chidambar, Sharma, Karteek, Satya, Shafeekh, Sunita Dey, Pramoda, Sreedhara, Gopal, Krishnendu, Bhavani, Kiruthika, Jiaul, Khadija, Prathyusha, Bhavya, Rajani, Raghavi, Loukya, Manjusha, Prasoona, Santosh, Sneh, Neethu, Rasmi, Yugandhara, Nisha, and Manasa.

I would like to thank Murali Mohan Charitable Trust, Hyderabad (M.Sc), JNCASR (SRFP and Monetary Support) for their financial aid at various stages of my education. I am profoundly thankful to Council of Scientific and Industrial Research (CSIR), India for awarding research fellowship (JRF and SRF) to pursue Ph.D.

Shivaprasad Manchineella

PREFACE

The thesis entitled "***Cyclic Dipeptide and Silk Fibroin-based (Bio)materials and Their Applications***" is divided into six chapters.

Chapter 1 introduces the general structure and functions of natural peptides and proteins. An overview of the recent developments and potential applications of peptide and protein-based systems for material, biomedical applications is presented. The major emphasis is given to the design strategies utilized for the development of cyclic dipeptide, silk fibroin-based systems for material, biomedical and tissue engineering applications.

Chapter 2 presents the molecular design strategy, synthesis and hydrogelation properties of cyclic dipeptides (CDPs). **Chapter 2.1** deals with the synthesis and hydrogen bond directed self-assembly of *cyclo*(Gly-*L*-Lys) with ε-amino group functionalized using aliphatic (tert-butyloxycarbonyl) and aromatic (fluorenylmethoxy carbonyl) moieties into low molecular weight organo- and hydrogels. The detailed study emphasized the significance of secondary interactions in driving the molecular gelation and crucial role of aromatic π-π interactions in facilitating the hydrogelation of designed CDPs. The potential application of CDP gels for drug and dye loading is presented. **Chapter 2.2** presents a rational design strategy for the development of ambidextrous CDP supergelators and *in situ* hydrogelation under physiological conditions. Detailed CDP structure-gelation studies revealed the significance of tert-butyloxycarbonyl group in driving the gelation through attractive van der Waals interaction. *Cyclo*(*L*-Phe-*L*-Glu(OtBu)) forms hydrogels *in situ*, in phosphate buffered saline (PBS), when injected from its

N-methyl-2-pyrrolidone (NMP) solutions. The potential of non-cytotoxic *cyclo*(Phe-Glu(OtBu) for possible parenteral drug delivery applications is demonstrated through *in situ* hydrogelation in presence of incorporated anticancer molecule curcumin.

Chapter 3 presents molecular design strategy employed to understand and mimic the observed homochirality in nature. *L*-Lysine containing CDPs with varying chiral and achiral amino acids are employed as chiral auxiliaries for orchestrating the homochiral self-assembly of CDP functionalized napthalenediimides (NCDPs). NCDPs form a novel molecular platform to engineer chiral assembly of the synthetic small molecule through aromatic, hydrogen bonding interactions and influence of external stimuli. The detailed self-assembly study using NCDPs emphasized the significance of nature of chirality in CDP auxiliaries and decisive role played by solvent composition in modulating the helical self-assembly of chromophores, and in mastering the handedness of chiral assemblies.

Chapter 4 deals with the synthesis and applications designed CDPs containing proteinogenic and non-proteinogenic phenolic amino acids with strong radical scavenging properties. CDPs showed amino acid-dependent antioxidant properties along with good cytocompatibility in murine brain PC12 cells. Preliminary studies with amyloid beta (Aβ) indicated the potential of antioxidant CDPs to modulate the toxic aggregates. The strong antioxidant properties and ability to modulate the protein aggregates emphasizes their potential for biomedical applications.

Chapter 5 presents the design strategies for the development of electroactive and free radical scavenging biomaterial scaffold films and electrospun mats for skeletal muscle tissue engineering (SMTE) using silk fibroin (SF) protein. The

electroactive and free radical scavenging properties were imparted to the silk using naturally occurring biodegradable pigment melanin. The detailed studies using murine myoblasts (C2C12) highlighted the improved myoblast assembly and formation of aligned high aspect ratio myotubes on silk fibroin/melanin composite nanofibrous scaffolds. Thus, the potential application of silk fibroinmelanin composite electrospun mats as a bio-derived electroactive platform for proliferation and differentiation of myoblasts into myotubes for tissue engineering applications is demonstrated.

Chapter 6 deals with the development of surface functionalized silk fibroin films (SFFs) for adult stem cell differentiation applications. Surface functionalization of SFFs with laminin-β1 derived peptide (GYIGSR) sequence modulated the transdifferentiation of human mesenchymal stem cells (hMSC) into neuronal cells. The detailed studies including gene expression analysis for neuronal markers highlighted the potential application of surface functionalized SFFs as bio-derived, biomaterial scaffolds for stem cell differentiation. These silk-biomaterials will have implications in stem cell differentiation and regenerative therapy applications.

In summary, low molecular weight CDP derivatives were designed in a minimalistic rational design and employed for the preparation of molecular gels for drug delivery (**Chapter 2**), as chiral auxiliaries for homochiral helical assembly of naphthalenediimides (**Chapter 3**) and as antioxidant molecules for biomedical applications (**Chapter 4**). SF-based electroactive and antioxidant scaffolds were employed for skeletal muscle tissue engineering (**Chapter 5**) and surface functionalized SF films for directed transdifferentiation of hMSCs into neuron-like cells (**Chapter 6**).

TABLE OF CONTENTS

Certificate	I
Declaration	III
Acknowledgements	V
Preface	IX
Chapter 1: Introduction	1
1.1 Peptides and Proteins	3
1.2 Self-assembly	7
1.3 Molecular Gels	8
1.4 Cyclic Dipeptides	9
1.5 Silk Fibroin	17
1.6 Melanins	21
1.7 Helical Chirality	21
1.8 Antioxidants	22
1.9 Tissue Engineering	23
1.10 Objective	24
1.11 References	25
Chapter 2: Orchestrated Self-assembly of Designer Cyclic Dipeptides into Molecular Gels	37
2.1 Hydrogen Bond Directed Self-Assembly of Designer Cyclic Dipeptide Derivatives: Gelation and Ordered Hierarchical Architectures	39
2.1.1 Introduction	39
2.1.2.1 Synthesis of CDPs	41
2.1.2.2 Gelation studies	42
2.1.2.3 Dye and drug entrapment	44
2.1.2.4 CDP 2 aggregation studies	44
2.1.2.5 FESEM analysis	45
2.1.2.5 NMR studies	46
2.1.3 Conclusion	51

2.2 Cyclic Dipeptide-based Ambidextrous Supergelators: Minimalistic Rational Design and In Situ Hydrogelation 52
2.2.1 Introduction 52
2.2.2.1 Synthesis of CDPs 54
2.2.2.2 Gelation studies 57
2.2.2.3 FESEM analysis 60
2.2.2.4 Thermal stability of CDP gels 61
2.2.2.5 Visco-elastic properties of CDP gels 62
2.2.2.6 NMR studies 63
2.2.2.7 Host-guest interactions 65
2.2.2.8 In situ gelation studies 66
2.2.2.9 Cytotoxicity study 68
2.2.3 Conclusion 69
2.2.4 Experimental Section 70
2.2.5 Appendix 83
2.2.5 References 90

Chapter 3: Solvent-induced Helical Assembly and Reversible Chiroptical Switching of Chiral Cyclic Dipeptide Functionalized Naphthalenediimides 97
3.1 Introduction 99
3.2.1 Synthesis of NCDPs 101
3.2.2 NCDP helical assembly and chiroptical switching 107
3.2.3 Dynamic light scattering studies 111
3.2.4 Effect of CDP substituent and chiral centre on chiral helical assembly 116
3.2.5 NMR studies 123
3.2.6 Reversible chiroptical switching studies 124
3.2.7 Isostructural solvent effects 127
3.3 Conclusion 130
3.4 Experimental Section 130
3.5 Appendix 145
3.6 References 152

Chapter 4: Antioxidant Phenolic Cyclic Dipeptides 159
4.1 Introduction 161
4.2.1 Synthesis of CDPs 165
4.2.2 Antioxidant activity 165
4.2.3 Cytotoxicity analysis 167
4.2.4 $A\beta_{1-42}$ disaggregation study 169
4.3 Conclusion 170
4.4 Experimental Section 171
4.5 Appendix 179
4.6 References 186

Chapter 5: Pigmented Silk Nanofibrous Composite for Skeletal Muscle Tissue Engineering 189
5. 1 Introduction 191
5.2.1 Fabrication of silk and silk/melanin composite scaffolds 193
5.2.2 Characterization of scaffolds 197
5.2.3 Cytocompatibility of scaffolds 203
5.2.4 Oxidative stress control in myoblasts 205
5.2.5 Myogenic differentiation of myoblasts on scaffolds 206
5.3 Conclusion 210
5.4 Experimental Section 210
5.5 References 218

Chapter 6: Surface Functionalized Silk Fibroin Films for Transdifferentiation of hMSCs into Neuron-like Cells 225
6.1 Introduction 227
6.2.1 Synthesis of surface-functionalized SFFs 231
6.2.2 Characterization of SFFs 233
6.2.3 Cell culture 237
6.2.4 Differentiation of hMSCs into neuron-like cells 241
6.2.5 Gene expression analysis 243
6.3 Conclusion 245
6.4 Experimental Section 246

6.5 Appendix 254
6.6 References 257

List of Publications 263

Miscellaneous Highlights of Ph.D Work 265

Brief Curriculum Vitae 267

Chapter 1

Introduction

1.1 Peptides and Proteins

Polypeptides (peptides and proteins) are polymers of amino acids connected through amide bonds also referred as peptide bonds. Peptides and proteins are essential biomolecules with a wide range of biological functions necessary to maintain the normal physiology and growth of an organism. The essential functions carried out by peptides and proteins include but not limited to enzymatic catalysis, molecular recognition, ion or biomolecule transportation, hormonal activity, immunomodulation, radical scavenging, cytoskeleton and structural maintenance of the organism.[1-4] The polypeptides are synthesized in living organisms through a multi-step process. Peptide biosynthesis begins with the transcription of genetic information coded in DNA to messenger RNA (mRNA), which is followed by the translation of information coded in mRNA into polypeptides with the help of ribosomal machinery.[2,4] Ribosomal synthesis is the most common biosynthesis of peptides in nature and the majority of the peptides and proteins are produced through this translational process. There also exists non-ribosomal peptide synthesis (NRPS) which is facilitated by class of enzymes known as peptide synthetases (PSs) in an alternative pathway allowing the production of peptides without going through the translational process. NRPS mostly results in the production of indispensable secondary metabolites with few amino acid residues (2-50).[5-7]

The structure and functions of peptides and proteins solely depend on their amino acid composition. Amino acids are chemically *aminoalkanoic acids* with an amine ($-NH_2$) and acid (-COOH) functionalities along with chemically diverse side chain at α-carbon (R) (Figure 1.1). There are twenty proteinogenic *L*-amino acids with varying physicochemical properties. Depending on the nature of side chain (R), proteinogenic amino acids are categorized as nonpolar (aliphatic and aromatic), polar (uncharged,

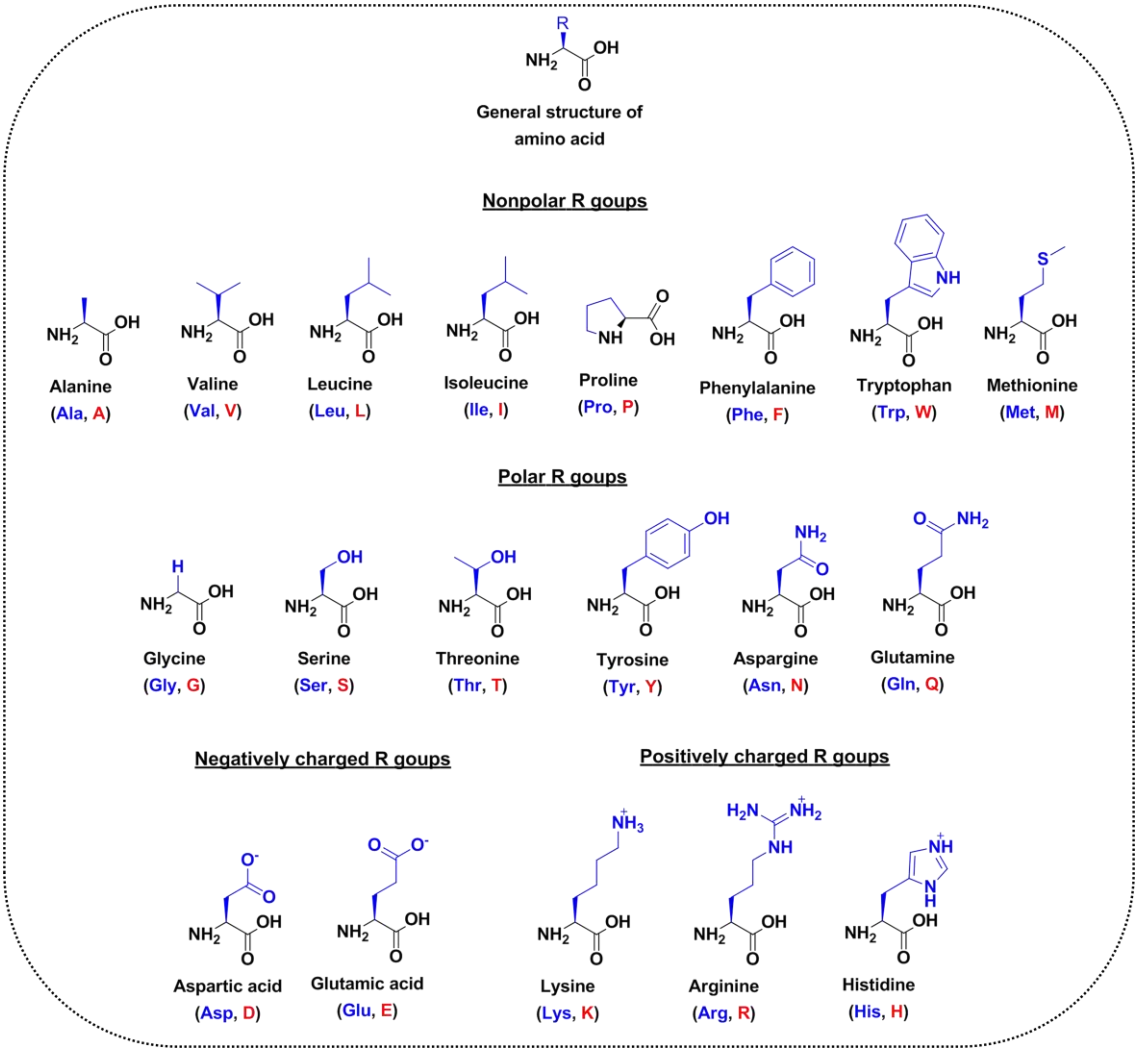

Figure 1.1 Classification and chemical structures of 20 proteinogenic amino acids. Amino acid three letter (blue) and single letter (red) codes are indicated in parenthesis.

positively and negatively charged) R-group containing amino acids and the molecular structures are shown in Figure 1.1, along with their three letter and single letter codes.[1-4]

Proteins exhibit different levels of organization namely primary, secondary, tertiary and quaternary structures. The primary structure of a polypeptide is the sequence and composition of amino acids, which at large determines the next level of peptide chain organization. The secondary structure constitutes noncovalent interaction, especially hydrogen bond driven specifically ordered structures. The major secondary structures

observed are either α-helical structures that are stabilized by intramolecular hydrogen bonding or β-sheet structures that are stabilized by intra- and intermolecular hydrogen bonding along with other noncovalent interactions defined by the amino acid composition.[1-4] The other less commonly observed secondary structures of peptides and proteins include turns and coils.[1-4,8] The tertiary structure of polypeptides in functional proteins refers to the three-dimensional organization of polypeptide units driven by hydrophobic and hydrophilic interactions facilitating the packing of hydrophobic units of peptide chain inside the structure and exposing only hydrophilic groups on the surface. The quaternary structure of a protein represents the three-dimensional orientation of multi-subunit proteins or the multimeric association of individual proteins into a functional structure. The quaternary structure is stabilized by secondary interactions such as hydrophobic, electrostatic interactions, disulfide, and salt bridges.[1-4,8]

The subtle difference in the nature of noncovalent interactions defined by their amino acid composition directs the organization of proteins into globular and fibrous forms with varying biophysical properties. Globular proteins are polypeptides formed by about 1000 amino acids and are mainly involved in the cellular biochemical functions. Whereas the fibrous proteins are very high molecular weight (up to ~300000 kDa) polypeptides formed by few thousand of amino acids and are mostly associated with the structural maintenance.[2,9,10] The intrinsic aggregation propensity of polypeptides is reflected in the formation of exceptionally marvel structures and materials such as silks under physiological conditions.[11-14] On the other hand, misfolding and aggregation of polypeptides is responsible for pathological outcomes as seen in neurodegenerative disorders such as Alzheimer's, Prion and Parkinson diseases.[15-19]

Inspired by the diverse structure and functions of peptides and proteins, there is an increased interest in developing either natural or synthetic peptide-based materials for a wide range of material and biological applications. Peptide-based materials have been used for the development of therapeutics, templated synthesis of nanomaterials, drug delivery agents, biomaterials for tissue engineering and many other biomedical applications.[20-29] The potential advantages of peptide-based materials over other biomolecules include,

i. The large scale availability from renewable sources such as biomass and ease of large-scale production by genetic engineering or recombinant DNA nanotechnology and chemical synthesis.
ii. Versatility to modify the structure and function through chemical synthesis.
iii. Relative stability under ambient conditions as compared to other biomolecules, facilitating the ease of handling.
iv. Inherent biocompatibility, biodegradability, and bioresorbability.
v. Molecular recognition through noncovalent interactions.
vi. Inherent aggregation propensity with the availability of diverse chemical functionalities with respect to amino acid composition, to modulate physicochemical and biological properties.
vii. The possibility of processing peptides in aqueous and organic solvents into various physical formats including gels, films, nanofibres foams, porous systems and non-woven mats for various applications.

Peptidomimetics are the class of organic molecules that mimic a natural peptides structure and function and retains the ability to interact with a biological target and to produces the similar or sometimes better biological effect.[30-33] Peptidomimetics

circumvents some of the limitations of peptides such as physiological enzymatic degradation and poor bioavailability. Peptidomimetics have been used as synthetic tools for drug discovery applications among other biomaterials applications. Apart from the superior biological activity, peptidomimetics such as foldamers help in understanding the fundamental phenomenon of peptide and protein folding into 3D compact structures orchestrated by noncovalent interactions. These foldamers have shown potential applications in understanding the natural peptide assembly and in designing the materials for biomedical applications.[34,35.]

1.2 Self-assembly

Self-assembly is the process of spontaneous organization of individual components into ordered structural and functional entities using attractive noncovalent interactions.[23] Nature employs self-assembly to orchestrate the elegant biological machinery which includes functional systems such as DNA double helical structure, quaternary structure of enzymes, ribosomes (the protein synthesizing complex) and biological structural entities such as cell membranes, cytoskeleton and triple helical structure of collagen and their biomineralized forms.[4,36,37] The process of molecular self-assembly is driven by weak yet powerful and attractive secondary or noncovalent interactions such as hydrogen bonding, aromatic π-π interactions, van der Waals forces, electrostatic and ionic interactions.[37-40] The nature and outcome of the self-assembly process exclusively depend on the information encoded in the individual molecular building blocks *i.e.* molecular synthons or scaffolds. The self-assembly process and applications of the resulting structural or functional systems can be modulated by the judicious design of molecular synthons.[37]

Nature judiciously engages biomolecules such as peptides, proteins, RNA, DNA, phospholipids and carbohydrates for the self-assembly to construct its functional systems and materials. On the other hand, synthetic organic and inorganic molecular building blocks have been utilized for the preparation of self-assembled systems having material and biological applications.[38-40] Apart from organic molecular building blocks, peptides, and their derivatives are promising molecular synthons because of their inherent biological relevance to functional and pathological conditions.[22,23,41-46]

1.3 Molecular Gels

Low molecular weight gels (LMWGs) formed by the entrapment of liquids through self-assembled three-dimensional (3D) networks of small organic molecules are an important class of soft materials.[47] Unlike the polymeric gelators wherein high molecular weight macromolecules drives the gelation, the LMWGs are formed by noncovalent interaction-driven self-assembly of designed small molecules. Ease of synthesis, wide range availability of chemical modification procedures and functionalities to tune the physical and chemical properties, makes small molecules promising gelators for both material and biomedical applications. Similarly, small peptide-based gelators are indispensable subgroup of organic molecular gelators for various material, biological and biomedical applications owing to their biological relevance, biocompatibility, tunable properties by the virtue of employing desired amino acids in the sequence.[48-57]

Aromatic protecting groups such as fluorene (Fmoc) and naphthalene (Nap) in the *N*-terminus of peptides are used routinely to assist the intermolecular interactions in the form aromatic π-π attractions in addition to other noncovalent interactions to facilitate the organo- and hydrogelation. *N*-Terminal modified peptides and their derivatives have met

with reasonably good success, for applications such as synthesis of inorganic nanomaterials, drug delivery and as scaffolds for cell culture and tissue engineering. Ulijn *et.al* have pioneered the self-assembly of *N*-terminal Fmoc-(fluorenemethyloxy carbonyl) functionalized short peptide into stimuli-responsive molecular gels for material and biomedical applications.[20,58-60] Supergelators are a class of LMWGs that comprises more than 99% of the liquid yet behaves as solids and are promising candidates for biomedical and tissue engineering applications because of their resemblance to *in vivo* extracellular matrix (ECM).[61]

In situ forming, LMWGs are a special class of soft materials that are promising candidates for the parenteral administration of biologically important molecules and drug delivery with minimal invasion.[53] The *in situ* formed gels acts as a local depot for the incorporated cargo and facilitates its controlled release because of the inherently dynamic nature of the molecular gels. Further, the delivery pattern can be tuned by modulating stimuli-responsive nature of the gelator. Leroux *et.al* have employed *in situ* gelation approach and successfully demonstrated the loading and delivery of drugs such as rivastigmine using amino acid derived organogels.[41,62-64]

1.4 Cyclic Dipeptides

Cyclic dipeptides (CDPs) are the smallest cyclic form of peptides containing a 6-membered core heterocyclic lactam ring and are also known as 2,5-diketopiperazines (DKPs) (Figure 1.2). CDPs are secondary metabolites that are ubiquitously seen in nature ranging from bacteria to humans and they are conserved through the course of evolution.[65] Cyclodipeptide synthases (CDPSs) and non-ribosomal peptide synthetases (NRPSs) carry out the biosynthesis of a number of unmodified and modified CDPs.[66,67] The commonly employed methods for the chemical synthesis of desired CDPs include the

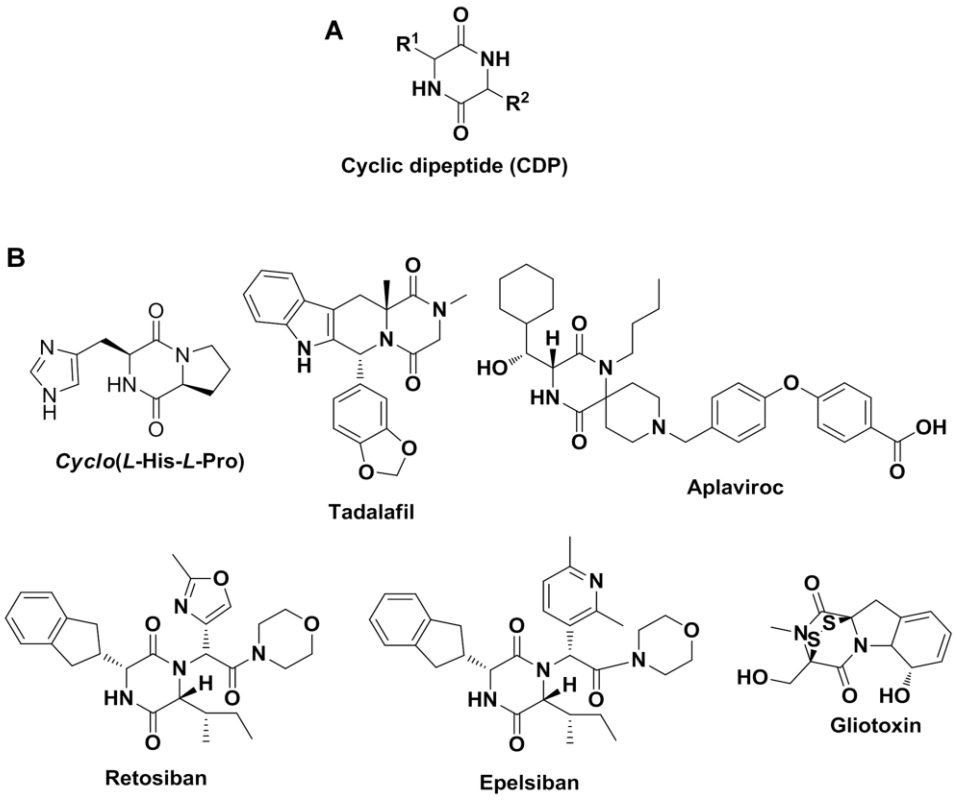

Figure 1.2 General chemical structure of CDP (A) and molecular structures of bioactive CDPs (B). R^1, R^2 in (A) represents the side chain R-group of proteinogenic or non-proteinogenic amino acids.

condensation of individual amino acids either at high temperature in solid-state or under reflux conditions in solution for preparation of symmetric CDPs and intramolecular head-to-tail cyclization of linear dipeptides for the preparation of both symmetric and asymmetric CDPs.[68-70] CDPs and their derivatives obtained either from natural sources or chemical synthesis are an important class of active molecules with biological functions such as bacterial quorum sensing, antibacterial, antimicrobial, anticancer properties, neuroprotective functions and even developed as carriers of biologically active molecules across the blood-brain barrier (BBB).[71-74] CDPs, unlike their linear counterparts, resist fast enzymatic degradation because of their rigid cyclic structure, which further augments the development of CDP-based systems for biomedical applications.[70,71]

CDPs exhibit amino acid-dependent biological activity, which provides the opportunity to modulate their activity by judicious incorporation of desired amino acids into the structure. The most commonly observed amino acids in natural CDPs in both lower microorganisms such as bacteria with quorum sensing properties for communication and in human brain with anti-inflammatory and neuroprotective functions is *L*-proline.[70-74] CDPs are considered as promising scaffolds for designing a variety of active compounds because of their unique biological properties and versatility of chemical modification. The general chemical structures of CDP, the bioactive *cyclo*(*L*-Pro-*L*-His) along with their derivatives such as tadalafil, restobisan, epelsiban, aplaviroc and gliotoxin that are either commercialized or in different phases of clinical trials are shown in Figure 1.2.

Apart from the biological activity, CDPs are ideal candidates for engineering functional architectures through molecular self-assembly, because of their unique properties. CDPs are bestowed with molecular rigidity owing to the cyclic structure and superior hydrogen bonding ability i.e. presence of four hydrogen bonding sites (two donor and two acceptor) from two amide bonds, unlike only two hydrogen bonding sites (an acceptor and a donor) in corresponding linear dipeptide with one amide bond (Figure 1.3A).[75,76] Along with hydrogen bonding interactions, other noncovalent interactions that are useful for driving molecular self-assembly such as aromatic π-interactions, van der Waals forces, electrostatic and ionic interactions can be incorporated with ease by the choice of amino acid composition in the CDP. The versatile CDP molecular platform facilitates the self-assembly either by the formation of 1D molecular chains or 2D layers depending on the type of amino acids and the stereochemistry at α-carbons (Figure 1.3B,C).[68,69,77-79]

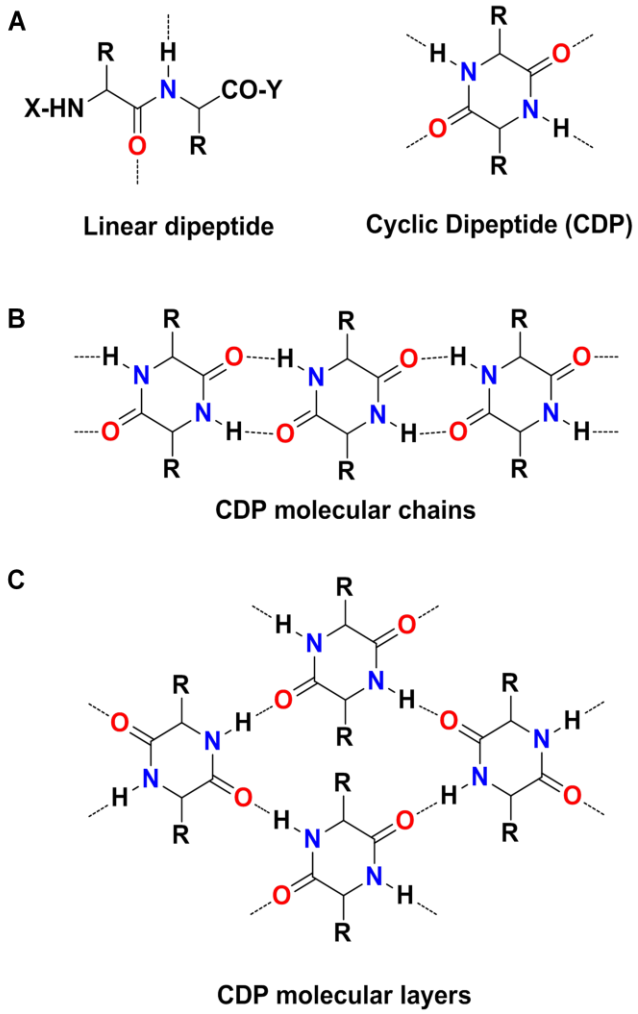

Figure 1.3 Molecular self-assembling patterns of CDPs. Hydrogen bonding propensity of linear dipeptide and CDP (A), a schematic representation of hydrogen bonded CDP molecular chains (B) and molecular layers (C). X and Y in (A) represent the protecting groups or extended structures.

The versatile molecular platform to harness requisite secondary interactions and a tendency to self-assemble, because of rigid cyclic structure and propensity to form hydrogen bond mediated self-assembled molecular chains and layers inspired the development of CDP-based systems for several applications. In one of the earliest reports on CDP-based molecular gels Hanabusa *et.al* have systematically studied the effect of alkyl side chain substitution to harden organic fluids.[80-82] Further, they have developed ionogels from CDPs containing cationic side chains with promising applications in

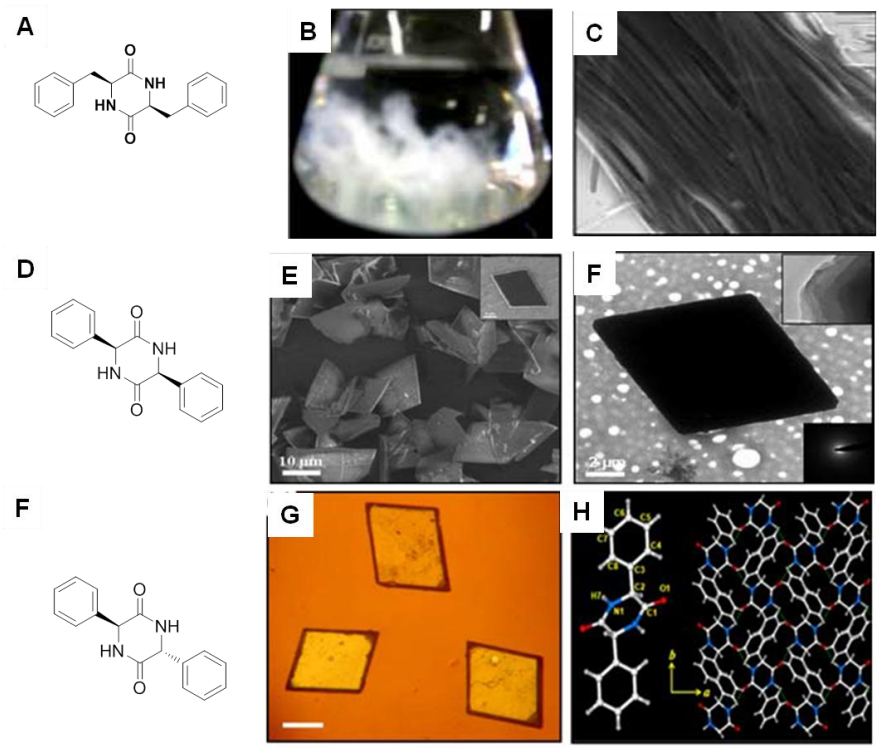

Figure 1.4 Molecular structures and self-assembled nano- and mesostructures of CDPs. Molecular structure of *cyclo*(*L*-Phe-*L*-Phe) (A), photograph (B) and SEM image (C) of its self-assembled hierarchical fiber bundles. Reproduced with permission from reference 68. Molecular structure *cyclo*(*L*-Phg-*L*-Phg) (D), FESEM (E) and HRTEM (F) images of 2D nanosheets. Inset in (F) shows the shows layered hierarchy (upper) and amorphous nature (lower) of mesosheets. Molecular structure *cyclo*(*L*-Phg-*D*-Phg) (F), crystalline rhomboidal sheets (G) and Ortep diagram and molecular layers (H). Reproduced with permission from reference 69.

energy storage.[83] Feng *et.al* have developed a series of symmetric and asymmetric CDP-based derivatives with a strong propensity to form ambidextrous supergelators for various biomedical applications.[84,85] Further, CDP derivatives have been used for the development of soft materials, nanoarchitectures for biomedical and material applications, respectively.[86-88]

Our group reported the self-assembly of designed CDPs *cyclo*(*L*-Phe-*L*-Phe) and *cyclo*(*D*-Phe-*D*-Phe) into hierarchical fiber bundles and molecular gels in organic solvents (Figure 1.4A-C).[68] The concept of fine tuning the formation of technologically important

hierarchical nanostructures i.e. biomimetic fiber bundles and molecular gels of CDPs containing phenylalanine would be useful in understanding the natural hierarchical architectures and developing self-assembled materials with a nanoscale order for material and biomedical applications. Further, diastereomeric CDPs of unnatural and simplest aromatic amino acid phenylglycine *cyclo*(*L*-Phg-*L*-Phg) and *cyclo(D*-Phg-*D*-Phg) were designed and studied their stereochemical effects on the solution-phase self-assembly into two-dimensional (2D) nano- and mesosheets (Figure 1.4D-E).[69] Further, the exfoliation of hierarchical meshosheets into nanosheets and star-like hierarchical structure under acidic conditions was demonstrated. The self-assembly is governed by solvent nature and formation of star-like hierarchical structures were observed in HFIP from *cyclo*(*L*-Phg-*L*-Phg).[89] The formation of large hierarchical rhomboidal amorphous mesosheets and single crystals from the simplest *cyclo(D*-Phg-*L*-Phg), highlights the crucial role of the stereochemistry of constituting amino acids, along with orthogonal aromatic and hydrogen bonding interactions in engineering the molecular architectures for various biomaterial and bionanotechnology applications (Figure 1.4F-H).[89,90]

Our group engineered the self-assembly of *cyclo*(*L*-Phg-*L*-Phg), *cyclo*(*L*-Phg-*D*-Phg), *cyclo*(*L*-Ala-*L*-Ala) and *cyclo*(*L*-Ala-*D*-Ala) into solid-state structures with exceptional mechanical properties.[88] The crystallization of low molecular weight CDPs into structures with mechanical properties comparable and even better than those observed in nature with very high molecular weight such as silks and other man-made materials was achieved by simple evaporation of the corresponding CDP solutions from dichloromethane and methanol (v/v: 1:1). The homochiral stereochemistry in CDPs *cyclo*(*L*-Phg-*L*-Phg) and *cyclo*(*L*-Ala-*L*-Ala) favored the formation of 1D molecular chains and heterochiral stereochemistry in *cyclo*(*L*-Phg-*D*-Phg) and *cyclo*(*L*-Ala-*D*-Ala) facilitated the formation of 2D molecular layered arrangement (Figure 1.5), highlighting

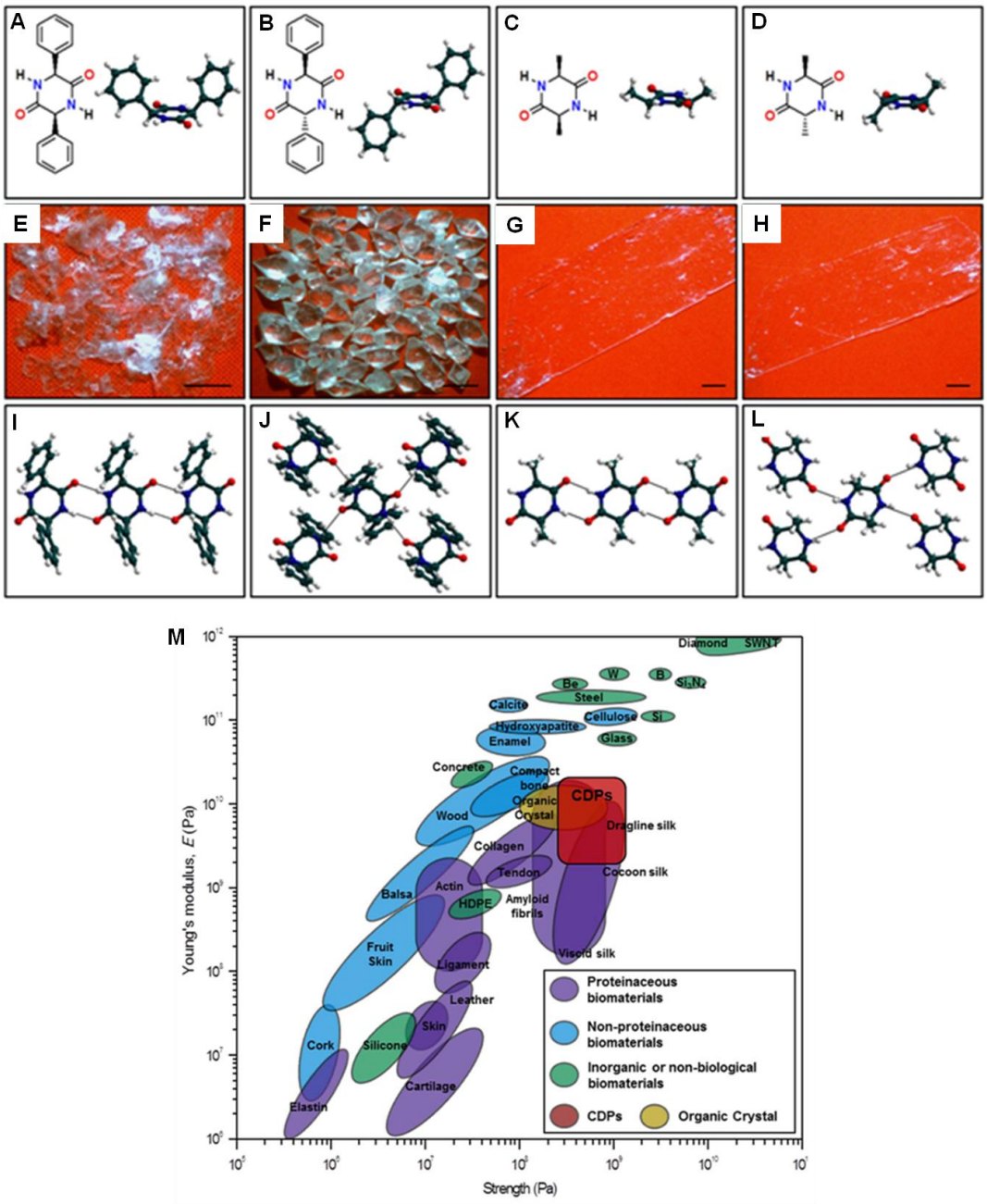

Figure 1.5 Chemical structures, single crystalline self-assembled architectures and mechanical properties of CDPs. (A)-(D) molecular structures (E)-(H) optical microscope images of *cyclo*(*L*-Phg-*L*-Phg), *cyclo*(*L*-Phg-*D*-Phg), *cyclo*(*L*-Ala-*L*-Ala) and *cyclo*(*L*-Ala-*D*-Ala). Crystal packing structures of hydrogen bonded 1D chains of *cyclo*(*L*-Phg-*L*-Phg) (I), 2D layers of *cyclo*(*L*-Phg-*D*-Phg) (J), 1D chains of *cyclo*(*L*-Ala-*L*-Ala) (K), 2D layers of *cyclo*(*L*-Ala-*D*-Ala) (L). Mechanical property comparison plot showing elastic modulus versus strength for CDPs with known strong materials (M). Reproduced with permission from reference 88.

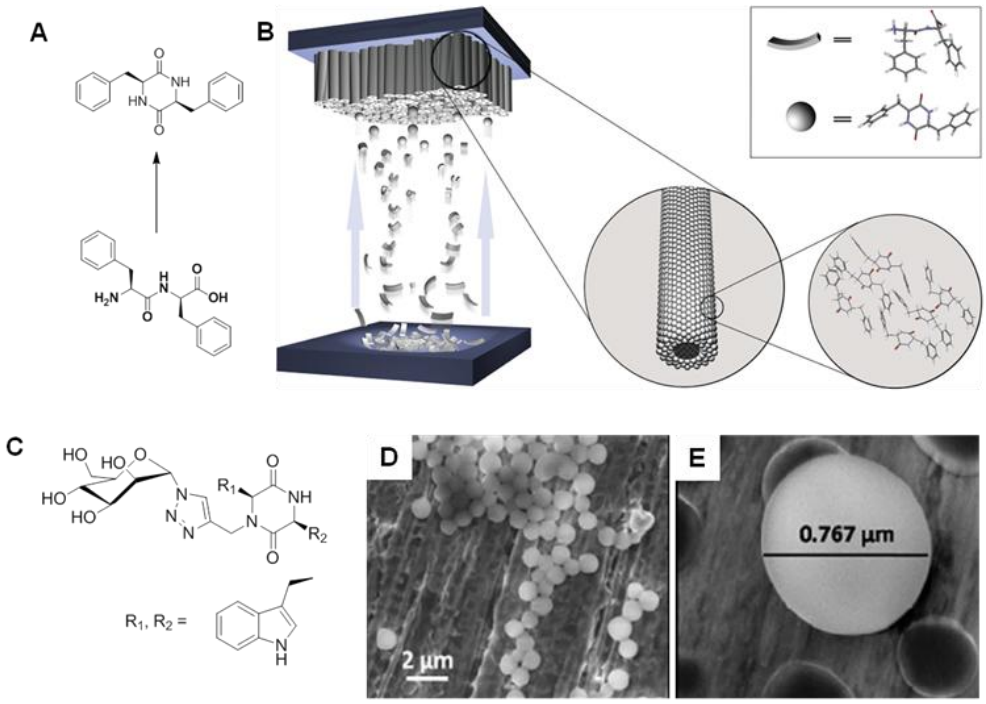

Figure 1.6 Self-assembled CDP architectures. Evaporation-induced cyclization of diphenylalanine into *cyclo*(Phe-Phe) (A) and schematic representation of its self-assembly nanotubes. Tapes and spheres in (B) represent the linear and cyclic diphenylalanine respectively. Reproduced with permission from reference 93. Amide *N*-substituted tryptophan CDP (C) self-assembly into spherical architectures. SEM images of spherical structures (D), (E). Reproduced with permission from reference 94.

the crucial role of stereochemistry in controlling the molecular self-assembly. *Cyclo*(*L*-Phg-*D*-Phg) with heterochiral Phg exhibited surpassing mechanical properties among the other CDPs owing to strong C-H--O, C-H--π and N-H--O interactions along with stereochemically controlled molecular packing with strong aromatic interactions. The simple solution processed CDPs showing exceptional mechanical properties demonstrate the potential of bioinspired design strategies in engineering the molecular self-assembled material for bionanotechnology and biomaterial applications.

Gazit *et.al* pioneered the self-assembly of short peptides into functional architectures.[91,92] Evaporation of linear dipeptide H-*L*-Phe-*L*-Phe-OH at 220 ºC under

vacuum facilitated its intramolecular cyclization to CDP and *in situ* formation of micrometer long aligned and oriented nanotubes on the collector placed vertically above the heater (Figure 1.6A-C).[93] Further, the aromatic phenyl groups and nanotextured surface resembling that of lotus leaf imparted the surfaces modified with nanotubes coating the hydrophobic property. These hydrophobic coatings of *cyclo*(*L*-Phe-*L*-Phe) nanotubes have used in the preparation of self-cleaning surfaces, and for tailoring the properties of microfluidic devices for diagnostic applications.[94] Verma *et.al* have systematically studied the effect of substitution on CDP self-assembly both in solution and solid-state into 1D and 2D nanostructures. Interestingly, the CDP amide substitution facilitated the self-assembly of CDPs into spherical aggregates (Figure 1.6C-E).[94] These results highlighted the crucial role of nature and position of substitution on CDP self-assembly.[79]

1.5 Silk Fibroin

Silk fibroin (SF) is a high molecular weight (~400 kDa) fibrous protein produced by silkworms.[95,96] Other than silkworms, silk proteins are secreted by members of Arthropoda include bees and spiders. Silks are produced inside the specialized glands in arthropods and each type of silk is characterized by specific amino acid sequence and composition. Territorial and cannibalistic nature of spiders limits the large-scale arability of spider silks for biomaterial applications.[97,98] On the other hand, domesticated silkworm *Bombyx mori* (*B. mori*) silks are readily available in large scale from sericulture farms. Silk fibroin is natural biopolymers characterized by unique physicochemical properties including water stability, modular mechanical properties, and resistance to fast enzymatic degradation owing to the presence of high β-sheet content in the structure.[99,100] Silkworm silk fibers have been used for centuries as textile fiber and suture material.

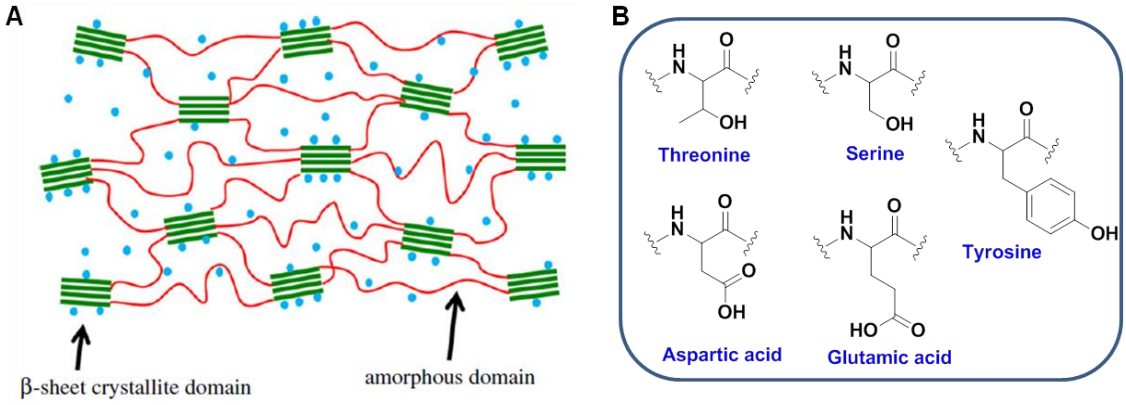

Figure 1.7 Structure and composition of silk fibroin (SF). (A) Segregated hydrophobic crystalline β-sheet and amorphous regions of SF. Blue dots in the structure indicate water molecules. Reproduced with permission from reference 100. (B) Chemically modifiable amino acids in the SF, threonine, serine, aspartic acid, glutamic acid and tyrosine.

The natural silk fibers produced by silkworms (*B. mori*) consist of two triangular crystalline silk fibroin (SF) strands glued together by an amorphous sericin protein. Sericin acts as an adhesive for SF strands and helps in maintaining the structure of cocoon, hence protects the silk moth inside from adverse environmental conditions. SF is extracted from silkworm cocoons and sericin which is believed to cause immunogenic response is removed during the process of SF extraction. Regenerated SF solutions from *B. mori* cocoons have been used for the fabrication of a variety of biomaterials with potential applications in tissue engineering and regenerative medicine.[101] SF is bestowed with unique properties, which include biocompatibility, controlled proteolytic biodegradability, bioresorbability, modular mechanical properties and malleability into various physical formats. SF fibers are composed of β-sheet content arising from the anti-parallel chains of the protein through hydrogen bonding. SF is a block-co-polymer consisting large hydrophobic crystalline domains interspaced with short hydrophilic

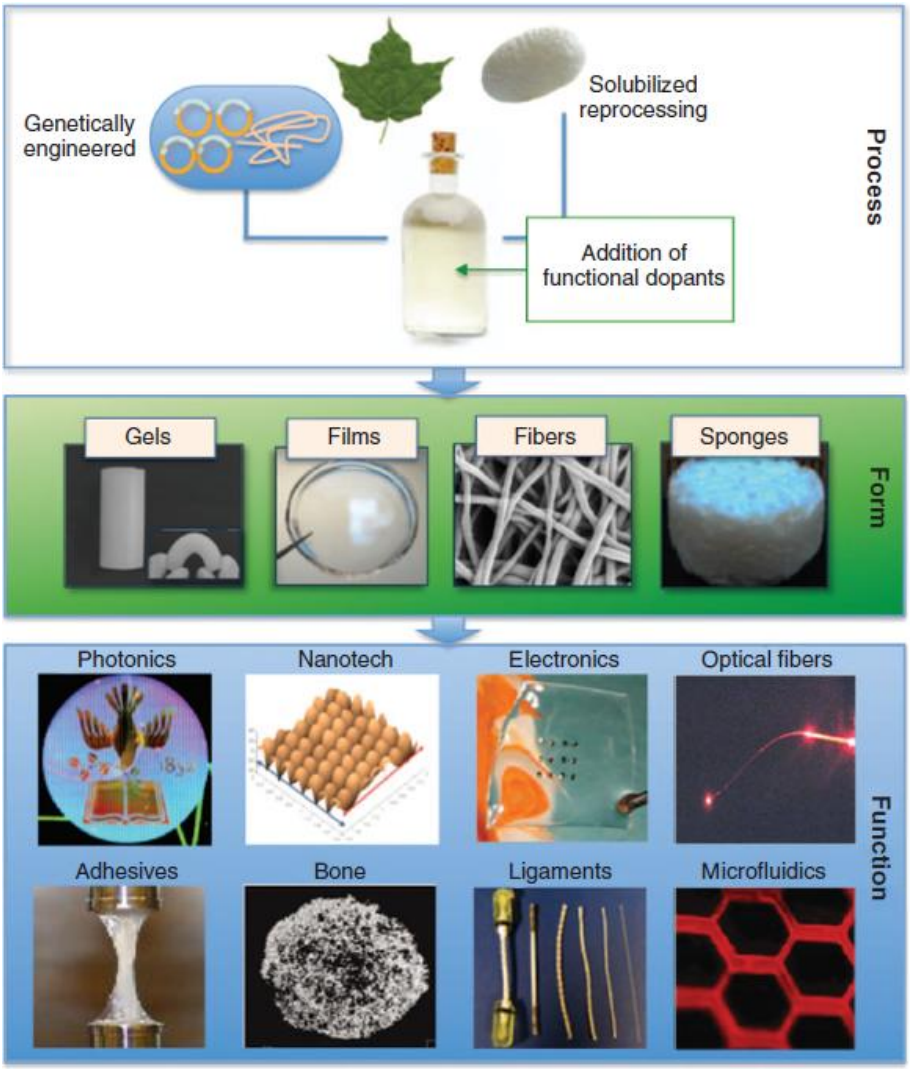

Figure 1.8 Preparation of regenerated silk fibroin solution, fabrication of biomaterial scaffolds and their functional applications. Reproduced with permission from reference 101.

amorphous domains that facilitate the assembly of silk and confers the strength and resiliency to the natural silk fibers (Figure 1.7A).[99,100] Apart from, providing structural hierarchy to the silk fibers, the hydrophilic domains are bestowed with functionalizable amino acids such as threonine, serine, aspartic acid, glutamic acid and tyrosine through diverse chemical modifications for requisite biomedical applications (Figure 1.7B).[102] Besides, the chemical modification the physicochemical and biological properties of SF can be modulated by simple physical mixing with desired materials.

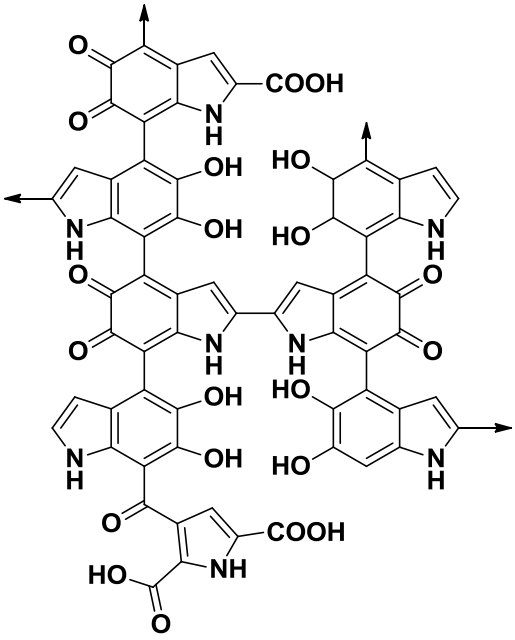

Figure 1.9 General chemical structure of melanin showing conjugated aromatic structure along with catechol moieties.

The promising properties of SF have inspired the design of scaffolds for many materials and biological applications. Kaplan *et.al* have developed SF scaffolds for tissue engineering, regenerative medicine, storage and stabilization of sensitive biomolecules at room temperature and for biophotonic and bioelectronic applications.[102.103] More recently, SF has been used as an edible coating for the storage of perishable fruits.[104] Han *et.al* have developed a simple way of producing the intrinsically colored and luminescent silk fibroin by feeding silkworms with dyes such as rhodamines, acridine orange, and fluorescein sodium along with mulberry leaves. These intrinsically colored and luminescent silks are promising candidates for textile and biological applications.[105,106] Regenerated SF either from natural silk fibers or genetically engineered silks have been used for the preparation of biomaterial scaffolds such as gels, films, non-woven fibers, porous sponges, 3D printed microfluidics (Figure 1.8).[101]

1.6 Melanins

Melanins are naturally occurring polymeric pigments having functionalities responsible for structural coloration to protection from sunlight and radicals.[107] Melanins are naturally synthesized by the organisms in a two-step enzyme catalyzed reactions. The first step involves the enzymatically-controlled oxidation of phenyl moieties from amino acids and in a second step, the oxidized intermediate undergoes uncontrolled oxidative polymerization resulting in the formation of melanins. Chemically, synthetic melanins are prepared by the oxidation of tyrosine followed by oxidative polymerization.[108] Melanins are heterocyclic in nature and contain repeating units of 5,6-dihydroxyindole and 5,6-dihydroxyindole-2-carboxylic acid, a general structure of melanin is shown in Figure 1.9. Melanins owing to their polyphenolic nature and presence of catechol groups are redox active and shows excellent free radical scavenging properties.[107] Melanins are bestowed with electrical conducting property because of the oligomeric aromatic backbone and hydration dependent ionic conduction.[108-111] Therefore, melanin is a promising material for the preparation of biomaterial scaffolds for tissues that respond to electrical stimuli and in bioelectronic applications, owing to its biocompatibility, biodegradability, and electroactive nature.[111]

1.7 Helical Chirality

Helical chirality is widely found in biological systems such as in DNA and proteins.[112-114] The helical conformations adopted by synthetic oligomers and polymers are pertinent to various applications, such as chiral recognition, asymmetric catalysis, chiral separation, and chiroptical switching.[115-117] In recent times, helical chirality in self-assembled systems has attracted considerable interest due to the intrinsic dynamic nature of such materials and the ease with which their structural and functional properties may be tuned

compared to covalent polymers.[118-121] Induction of helical chirality in self-assembled molecular polymers through structural variations at the molecular self-assembly level is challenging due to the interplay of multiple noncovalent interactions. In general, the noncovalent synthesis of self-assembled polymers can be modulated through external stimuli capable of influencing the mode of molecular self-assembly. In this context, literature reports suggest that helical handedness in a self-assembly system can be achieved by employing similar external stimuli and chiral auxiliaries.[122-123] External stimuli such as temperature, light, solvent, and additives have been successfully used to control the chiral handedness of synthetic oligomers and polymers. Some of the successful reports on chiral modulation in noncovalent systems have dealt with solvent-modulated chirality of merocyanines, squarine dyes, and benzenetricarboxylic acid assemblies.[124-126] Faul *et. al* employed sugars as chiral auxiliaries for the self-assembly of perylenediimides into homochiral helical assemblies.[127] Developing such systems using short peptides as chiral auxiliaries would aid in understanding the homochiral assemblies that exist in nature and for material applications as well.

1.8 Antioxidants

A critical amount of free radicals is essential to maintain certain biochemical functions under normal physiological conditions. However, the presence of excessive reactive radical species beyond the critical concentration that cannot be controlled by natural antioxidant mechanisms adversely affect almost every organ function and pose severe health problems.[128-133] Oxidative stress due to excessive free radicals causes cellular and tissue damage leading to cancer, inflammatory bowel disease and responsible for various neurodegenerative disorders including Alzheimer's disease (AD), Parkinson disease (PD), multiple sclerosis, amyotrophic lateral sclerosis (ALS).[134,135] Among all the

neurodegenerative disorders, AD is the most common form of dementia epitomized by the progressive impairment of cognitive ability leading to death.[135] AD is associated with the production of excessive reactive species by metal associated Aβ aggregates. The toxicity in AD is multifactorial and many *in vitro* studies on the disease models and clinical studies have demonstrated that Aβ aggregate-induced oxidative stress plays a key role in the loss of cognitive function and disease progression.[136] Natural polyphenolic compounds such as non-flavonoid curcumin, resveratrol, tannic acid, melanins and flavonoid quercetin, epigallocatechin gallate (EGCG), silibinin and few synthetic polyphenolic compounds have been studied for modulating the oxidative stress associated toxicity in AD.[136] The major problem associated with the existing natural or synthetic molecules for controlling oxidative stress in disease conditions such as AD is their limited bioavailability, blood-brain barrier (BBB) crossing ability along with other unwanted health effects.

1.9 Tissue Engineering

Tissue engineering (TE) is an interdisciplinary field that applies the principles of engineering and life sciences toward the development of biological substitutes that can restore, maintain, or improve tissue function.[137] The rapidly developing field of (TE) aims to regenerate damaged tissues by combining cells from the body with appropriate scaffolds known as biomaterials that function as templates for tissue growth or regeneration in the presence of suitable biochemical cues or signaling molecules. Cells, scaffolds, and signaling molecules together are considered as the TE triad.[137,138]

Biomaterial scaffold characteristics such as stiffness, wettability, topography, magnetic, and conducting properties along with soluble growth factors play a pivotal role in cellular adhesion, proliferation, and differentiation for tissue engineering (TE)

applications.[138] Further, biomaterials with specific scaffold properties are required for the TE of specific tissues. Developing scaffolds for soft tissue regeneration is more challenging because of the unique properties of corresponding extracellular matrix (ECM) in the organism. Electroactive biomaterial scaffolds have drawn enormous attention in tissue engineering and regenerative medicine applications for tissues, whose functions are highly coordinated by endogenously generated electric fields (bioelectricity).[139,140] Cardiac myocytes, skeletal myoblasts, neurons, and osteoblasts are the examples of cells that respond to electric stimuli.[141] Developing biomaterial scaffolds with preferred physical and chemical cues from peptides and proteins are very much in demand for tissue engineering and regenerative medicine owing to their unique biocompatibility and biodegradability.

1.10 Objective

Motivated by the unparalleled biological functions of natural peptides and proteins and potential applications of naturally derived and synthetically prepared peptide-based materials for various (bio)material applications, we have studied the (bio)material applications of designed small cyclic dipeptides (CDPs) and silk fibroin (SF) protein. Specifically, low molecular weight cyclic dipeptides and large molecular weight biopolymer silk were chosen to harness the differential potential of small peptides in biomimetic reductionistic approach and high molecular weight protein, in material fabrication for biomedical applications

In this thesis, CDP and SF based materials were prepared and explored their potential for various material and biomedical applications. CDP-based molecular gelators were designed for organic and aqueous solvents that are capable of entrapping biologically active molecules are presented in **Chapter 2.1**. Further, CDP ambidextrous

supergelators were developed through structure-gelation studies and *in situ* hydrogelation ability of CDPs with loaded drug molecules with potential applications for parenteral drug delivery are presented in **Chapter 2.2**. In **chapter 3**, CDPs were employed as chiral auxiliaries for the first time to orchestrate the homochiral helical assembly of functional aromatic molecules with relevance to the existence of homochiral biomolecules and their assemblies in nature. CDPs with antioxidant properties were developed from proteinogenic and non-proteinogenic phenolic amino acids, their applications for scavenging free radicals and the preliminary studies indicating the modulation of toxic protein aggregates are presented in **Chapter 4**. In **Chapter 5**, antioxidant and electroactive composite electrospun scaffolds were fabricated from the silk fibroin/melanin composite and successfully utilized for the *in vitro* skeletal muscle tissue engineering using murine myoblasts. In **Chapter 6**, surface functionalized smart SF films with laminin-derived short peptides were fabricated and successfully utilized as biomaterial platform for the directed transdifferentiation of human mesenchymal stem cells (hMSC) into neuron-like cells with potential applications in regenerative therapy.

1.11 References

1. Langel, U.; Cravatt, B. F.; Graslund, A.; Heijne, N. G. H.; Zorko, M.; Land, T.; Niessen, S. *Introduction to Peptides and Proteins.* CRC Press, London, NY **2009**.

2. Nehete, J. Y.; Bhambar, R. S.; Narkhede, M. R.; Gawali, S. R. Natural proteins: Sources, isolation, characterization and applications. *Pharmacogn. Rev.* **2013**, *7*, 107-116.

3. Kastin, A. J. *Handbook of biologically active peptides*, 2nd *Ed.* Academic Press, San Diego, CA, USA, **2013**.

4. Voet, D.; Voet, J. G.; Pratt, C. W. *Fundamentals of biochemistry: life at the molecular level*. *4th Ed*. Wiley, Hoboken, NJ, USA **2013**.

5. Zuber, P. Non-ribosomal peptide synthesis. *Curr. Opin. Cell Biol*. **1991**, *3*, 1046-1050.

6. Strieker, M., Tanović, A.; Marahiel, M. A. Nonribosomal peptide synthetases: structures and dynamics. *Curr. Opin. Struct. Biol.* **2010**, *20*, 234-240.

7. Evans, B. S. *Nonribosomal peptide and polyketide biosynthesis*, Springer, Saint Louis, MO, USA, **2016**.

8. Marth, J. D. A unified vision of the building blocks of life. *Nat. Cell Biol.* **2008,** *10*, 1015-1016.

9. Scheraga, H. A. Proteins and synthetic polypeptides. *Annu. Rev. Phys. Chem.* **1959**, *10*, 191-218.

10. Berg, J. M.; Tymoczko, J. L.; Stryer, L. *Biochemistry, 5th Ed.* W H Freeman, NY, USA **2002**.

11. Shakhnovich, E. Protein folding thermodynamics and dynamics: where physics, chemistry,

and biology meet. *Chem. Rev.* **2006**, *106*, 1559-1588.

12. Marsh, R. E.; Corey, R. B.; Pauling, L. An investigation of the structure of silk fibroin. *Biochim. Biophys. Acta* **1955**, *16*, 1-33.

13. Knight, D.; Vollrath, F. Liquid crystalline spinning of spider silk. *Nature* **2001**, *410*, 541-548.

14. Li, G.; Zhou, P.; Shao, Z.; Xie, X.; Chen, X.; Wang, H.; Chunyu, L.; Yu, T. The natural silk spinning process. *Eur. J. Biochem.***2001**, *268*, 6600-6606.

15. Soto, C. Protein misfolding and disease; protein refolding and therapy. *FEBS Lett.* **2001**, *498*, 204-207.

16. Soto, C. Unfolding the role of protein misfolding in neurodegenerative diseases. *Nat. Rev. Neurosci*. **2003**, *4*, 49-60.

17. Selkoe, D. J. Cell biology of protein misfolding: the examples of Alzheimer's and Parkinson's diseases. *Nat. Cell Biol.* **2004**, *6*, 1054-1061.

18. Chiti, F.; Dobson, C. M. Protein Misfolding, functional amyloid, and human disease. *Annu. Rev. Biochem.* **2006**, *75*, 333-366.

19. Hamley, I. W. Peptide fibrillization. *Angew. Chem. Int. Ed.* **2007**, *46*, 8128-8147.

20. Reches, M.; Gazit, E. Casting metal nanowires within discrete self-assembled peptide nanotubes. *Science* **2003**, *300*, 625-627.

21. Löwik, D. W. P. M.; Leunissen, E. H. P.; Heuvel, M.; Hansen, M. B.; Hest, J. C. M. Stimulus responsive peptide based materials. *Chem. Soc. Rev.* **2010**, *39*, 3394-3412.

22. Reches, M.; Gazit, E. Formation of closed-cage nanostructures by self-assembly of aromatic dipeptides. *Nano Lett.* **2004**, *4*, 581-585.

23. Gazit, E. Self-assembled peptide nanostructures: the design of molecular building blocks and their technological utilization. *Chem. Soc. Rev.* **2007**, *36*, 1263-1269.

24. Rica, R.; Matsui, H. Applications of peptide and protein-based materials in bionanotechnology. *Chem. Soc. Rev.* **2010**, *39*, 3499-3509.

25. Webber, M. J.; Kessler, J. A.; Stupp, S. I. Emerging peptide nanomedicine to regenerate tissues and organs. *J. Intern. Med.* **2010**, *267*, 71-88.

26. Webber, M. J.; Tongers, J.; Renault, M-A.; Roncalli, J. G.; Losordo, D. W.; Stupp, S. I. Development of bioactive peptide amphiphiles for therapeutic cell delivery. *Acta Biomater.* **2010**, *6*, 3-11.

27. Liu, L.; Yang, J.; Xie, J. Luo, Z.; Jiang, J.; Yang, Y. Y.; Liu, S. The potent antimicrobial properties of cell penetrating peptide-conjugated silver nanoparticles with excellent selectivity for Gram-positive bacteria over erythrocytes. *Nanoscale* **2013**, *5*, 3834-3840.

28. Rodriguez, A. L.; Parish, C. L.; Nisbet, D. R.; Williams, R. J. Tuning the amino acid sequence of minimalist peptides to present biological signals via charge neutralised self assembly. *Soft Matter* **2013**, *9*, 3915-3919.

29. Giano, M. C.; Ibrahim, Z.; Medina, S. H.; Sarhane, K. A.; Christensen, J. M.; Yamada, Y.; Brandacher, G.; Schneider, J. P. Injectable bioadhesive hydrogels with innate antibacterial properties. *Nat. Commun.* **2014**, *5*, 4095.

30. Ripka, A. S.; Rich, D. H. Peptidomimetic design. *Curr. Opin. Chem. Biol.* **1998**, *2*, 441-452.

31. Vagner, J.; Qu, H.; Hruby, V. J. Peptidomimetics, a synthetic tool of drug discovery. *Curr. Opin. Chem. Biol.* **2008**, *12*, 292-296.

32. Rajasekhar, K.; Narayanaswamy, N.; Mishra, P.; Suresh, S. N.; Manjithaya, R.; Govindaraju, T. Synthesis of hybrid cyclic peptoids and identification of autophagy enhancer. *ChemPlusChem* **2014**, *79*, 25-30.

33. Jain, D. R.; Ganesh, K. N. Clickable Cγ-azido(methylene/butylene) peptide nucleic acids and their clicked fluorescent derivatives: synthesis, DNA hybridization properties, and cell penetration studies. *J. Org. Chem.* **2014**, *79*, 6708–6714.

34. Roy, A.; Prabhakaran, P.; Baruah, P. K.; Sanjayan, G. J. Diversifying the structural architecture of synthetic oligomers: the hetero foldamer approach. *Chem. Commun.* **2011**, *47*, 11593-11611.

35. Jedhe, G. S.; Kotmale, A. S.; Rajamohanan, P. R.; Pasha, S.; Sanjayan, G. J. Angiotensin II analogs comprised of Pro-Amb (γ-turn scaffold) as angiotensin II type 2 (AT2) receptor agonists. *Chem. Commun.* **2016**, *52*, 1645-1648.

36. Pelesko, J. A. *Self assembly: the science of things that put themselves together*. CRC Press, NW, FL **2009**.

37. Philp, D.; Stoddart, J. F. Self-assembly in natural and unnatural systems. *Angew. Chem. Int. Ed*. **1996**, *35*, 1154-1196.

38. Greef, T. F. A. D.; Smulders, M. M. J.; Wolffs, M.; Schenning, A. P. H. J.; Sijbesma, R. P.; Meijer, E. W. Supramolecular polymerization. *Chem. Rev.* **2009**, *109*, 5687-5754.

39. Yang, L.; Tan, X.; Wang, Z.; Zhang, X. Supramolecular polymers: historical development, preparation, characterization, and functions. *Chem. Rev.* **2015**, *115*, 7196-7239.

40. Krieg, E.; Bastings, M. M. C.; Besenius, P.; Rybtchinski, B. Supramolecular polymers in aqueous media. *Chem. Rev.* **2016**, *116*, 2414-2477.

41. Vintiloiu, A.; Leroux, J. C. Organogels and their use in drug delivery-a review. *J. Control. Release* **2008**, *125*, 179-192.

42. Park, K.H.; Na, K.; Chung, H. M. Enhancement of the adhesion of fibroblasts by peptide containing an Arg-Gly-Asp sequence with poly(ethylene glycol) into a thermo-reversible hydrogel as a synthetic extracellular matrix. *Biotechnol. Lett.* **2005**, *27*, 227-231.

43. Avinash, M. B.; Govindaraju, T. Engineering molecular organization of naphthalenediimides: large nanosheets with metallic conductivity and attoliter containers. *Adv. Funct. Mater*. **2011**, *20*, 3875-3882.

44. Schneider, J. P.; Pochan, D. J.; Ozbas, B.; Rajagopal, K.; Pakstis, L.; Kretsinger, J. Responsive hydrogels from the intramolecular folding and self-assembly of a designed peptide. *J. Am. Chem. Soc.* **2002**, *124*, 15030-15037.

45. Bong, D. T.; Clark, T. D.; Granja, J. R.; Ghadiri, M. R. Self-assembling organic nanotubes. *Angew. Chem., Int. Ed.* **2001**, *40*, 988-1011.

46. Brea, R. J.; Reiriz, C.; Granja, J. R. Towards functional bionanomaterials based on self-assembling cyclic peptide nanotubes. *Chem. Soc. Rev.* **2010**, *39*, 1448-1456.

47. Steed, J. W. Supramolecular gel chemistry: developments over the last decade. *Chem. Commun.* **2011**, *47*, 1379-1383.

48. Toledano, S.; Williams, R. J.; Jayawarna, V.; Uljin, R. V. Enzyme-triggered self-assembly of peptide hydrogels via reversed hydrolysis. *J. Am. Chem. Soc.* **2006**, *128*, 1070-1071.

49. Uljin, R. V.; Smith, A. M. Designing peptide based nanomaterials. *Chem. Soc. Rev.* **2008**, *37*, 664-675.

50. Johnson, E. L.; Adams, D. J.; Cameron, P. J. Peptide based low molecular weight gelators. *J. Mater. Chem.* **2011**, *21*, 2024-2027.

51. Huang, Y.; Qiu, Z.; Xu, Y.; Shi, J.; Lin, H.; Zhang, Y. Supramolecular hydrogels based on short peptides linked with conformational switch. *Org. Biomol. Chem.* **2011**, *9*, 2149-2155.

52. Zhang, S.; Greenfield, M. A.; Mata, A.; Palmer, L. C.; Bitton, R.; Mantei, J. R.; Aparicio, C.; Cruz, M. O.; Stupp, S. I. A self-assembly pathway to aligned monodomain gels. *Nat. Mater.* **2010**, *9*, 594-601.

53. Ray, S.; Das, A. K.; Banerjee, A. Smart oligopeptide gels: in situ formation and stabilization of gold and silver nanoparticles within supramolecular organogel networks. *Chem. Commun.* **2006**, 2816-2818.

54. Sangeetha, N. M.; Maitra, U. Supramolecular gels: functions and uses. *Chem. Soc. Rev.* **2005**, *34*, 821-836.

55. Tomasini, C.; Castellucci, N. Peptides and peptidomimetics that behave as low molecular weight gelators. *Chem. Soc. Rev.* **2013**, *42*, 156-172.

56. Ryan, D. M.; Nilsson, B. L. Self-assembled amino acids and dipeptides as noncovalent hydrogels for tissue engineering. *Polym. Chem.* **2012**, *3*, 18-33.

57. Pandeeswar, M.; Khare, H.; Ramakumar, S.; Govindaraju, T. Biomimetic molecular organization of naphthalene diimide in the solid state: tunable (chiro-) optical, viscoelastic and nanoscale properties. *RSC Adv.* **2014**, *4*, 20154-20163.

58. Escuder, B.; Miravet, J. F. *Functional molecular gels*. RSC, USA **2013**.

59. Hughes, M.; Birchall, L. S.; Zuberi, K.; Aitkin, L. A.; Debnath, S.; Javid, N.; Ulijn, R. V. Differential supramolecular organisation of Fmoc-dipeptides with hydrophilic terminal amino acid residues by biocatalytic self-assembly. *Soft Matter* **2012**, *8*, 11565-11574.

60. Tang, C.; Ulijn, R.V.; Saiani, A. Self-assembly and gelation properties of Glycine/Leucine Fmoc-dipeptides. *Eur. Phys. J. E* **2013**, *36*, 111.

61. Martin, A. D.; Robinson, A. B.; Thordarson, P. Biocompatible small peptide super-hydrogelators bearing carbazole functionalities. *J. Mater. Chem. B* **2015**, *3*, 2277-2280.

62. Couffin-Hoarau, A. C.; Motulsky, A.; Delmas, P.; Leroux, J. C. In situ-forming pharmaceutical organogels based on the self-assembly of L-alanine derivatives. *Pharm. Res.* **2004**, *21*, 454-457.

63. Bastiat, G.; Leroux, J. C. Pharmaceutical organogels prepared from aromatic amino acid derivatives. *J. Mater. Chem.* **2009**, *19*, 3867-3877.

64. Bastiat, G.; Plourde, F.; Motulsky, A.; Furtos, A.; Dumont, Y.; Quirion, R.; Fuhrmann, G.; Leroux, J. C. Tyrosine-based rivastigmine-loaded organogels in the treatment of Alzheimer's disease. *Biomaterials* **2010**, *31*, 6031-6038.

65. Bellezza, I.; Peirce, M. J.; Minelli, A. Cyclic dipeptides: from bugs to brain. *Trends Mol. Med.* **2014**, *20*, 551-558.

66. Belin, P.; Moutiez, M.; Lautru, S.; Seguin, J.; Pernodet, J-L.; Gondry, M. The nonribosomal synthesis of diketopiperazines in tRNA-dependent cyclodipeptide synthase pathways. *Nat. Prod. Rep.* **2012**, *29*, 961-979.

67. Giessen, T. W. Marahiel, M. A. The tRNA-dependent biosynthesis of modified cyclic dipeptides. *Int. J. Mol. Sci.* **2014**, *15*, 14610-14631.

68. Govindaraju, T. Spontaneous self-assembly of aromatic cyclic dipeptide into fibre bundles with high thermal stability and propensity for gelation. *Supramol. Chem.* **2011**, *23*, 759-767.

69. Govindaraju, T.; Pandeeswar, M.; Jayaramulu, K.; Jaipuria, G.; Atreya, H. S. Spontaneous self-assembly of designed cyclic dipeptide (Phg-Phg) into two-dimensional nano- and mesosheets. *Supramol. Chem.* **2011**, *23*, 487-492.

70. Cook, B.; Hill, R. R.; Jeffs, G. E. Efficient one-step synthesis of diastereoisomeric cyclic dipeptides from amino acids: three diastereoisomers of cyclo-*L*-isoleucyl-*L*-isoleucine. *J. Chem. Soc. Perkin. Trans.* **1992**, 1199-1201.

71. Prasad, C. Bioactive cyclic dipeptides. *Peptides* **1995**, *16*, 151-164.

72. Martins, M. B.; Carvalho, I. Diketopiperazines: biological activity and synthesis. *Tetrahedron*, **2007**, *63*, 9923-9932.

73. Mollica, A.; Costante, R.; Fioritoa, S.; Genovese, S.; Stefanucci, A.; Mathieu, V.; Kiss, R.; Epifano, F. Synthesis and anti-cancer activity of naturally occurring 2,5-diketopiperazines. *Fitoterapia* **2014**, *98*, 91-97.

74 Borthwick, A. D. 2,5-Diketopiperazines: synthesis, reactions, medicinal chemistry, and bioactive natural products. *Chem. Rev.* **2012**, *112*, 3641-3716.

75. Benedetti, E.; Corradini, P.; Pedone , C. Crystal and molecular structure of trans-3,6-dimethyl-2,5-piperazinedione (L-alanyl-D-alanine 2,5-diketopiperazine). *J. Phys. Chem.* **1969**, *73*, 2891-2895.

76. Corey, R. B. The crystal structure of diketopiperazine. *J. Am. Chem. Soc.* **1938**, *60*, 1598-1604.

77. Bergeron, R. J.; PhanstielIV, O.; Yao, G. W.; Milstein, S.; Weimar, W. R. Macromolecular self-assembly of diketopiperazine tetrapeptides. *J. Am. Chem. Soc.* **1994**, *116*, 8479-8484.

78. Desiraju, G. D. Supramolecular synthons in crystal engineering-a new organic synthesis. *Angew. Chem. Int. Ed.* **1995**, *34*, 2311-2327.

79. Palmore, G.T.R.; Luo, T.-J.M.; McBride-Wieser, M.T.; Picciotto, E.A.; Reynoso-Paz, C.M. Engineering crystalline architecture with diketopiperazines: an investigation of the strength of hydrogen-bonded tapes based on the cyclic dipeptide of (S)-aspartic acid. *Chem. Mater*. **1999**, *11*, 3315-3328.

80. Joshi, K. B.; Verma, S. Participation of aromatic side chains in diketopiperazine ensembles. *Tetrahedron Lett.* **2008**, *49*, 4231-4234.

81. Kimura, M.; Kobayashi, S.; Kuroda, T.; Hanabusa, K.; Shirai, H. Assembly of gold nanoparticles into fibrous aggregates using thiol-terminated gelators. *Adv. Mater.* **2004**, *16*, 335-338.

82. Hanabusa, K.; Fukui, H.; Suzuki, M.; Shirai, H. Specialist gelator for ionic liquids. *Langmuir* **2005**, *21*, 10383-10390

83. Hoshizawa, H.; Suzuki, M.; Hanabusa, K. Cyclo(L-aspartyl-L-phenylalanyl)-containing poly(dimethylsiloxane)-based thixotropic organogels. *Chem. Lett.* **2011**, *40*, 1143-1145.

84. Xie, Z.; Zhang, A.; Ye, L.; Feng, Z. Organo- and hydrogels derived from cyclo(L-tyr-L-tyr) and its ε-amino derivatives. *Soft Matter* **2009**, *5*, 1474-1482.

85. Xie, Z.; Zhang, A.; Ye, L.; Wang, X.; Feng, Z. Shear-assisted hydrogels based on self-assembly of cyclic dipeptide derivatives. *J. Mater. Chem.* **2009**, *19*, 6100-6102.

86. Kleinsmann, A. J.; Nachtsheim, B. J. Phenylalanine-containing cyclic dipeptides - the lowest molecular weight hydrogelators based on unmodified proteinogenic amino acids. *Chem. Commun.* **2013**, *49*, 7818-7820.

87. Pianowski, Z. L.; Karcher, J.; Schneider, K. Photoresponsive self-healing supramolecular hydrogels for light-induced release of DNA and doxorubicin. *Chem. Commun,* **2016**, *52*, 3143-3146.

88. Avinash, M. B.; Raut, D.; Mishra, M. K.; Ramamurty, U.; Govindaraju, T. Bioinspired reductionistic peptide engineering for exceptional mechanical properties. *Sci. Rep.* **2015**, *5*, 16070.

89. Govindaraju, T.; Avinash, M. B. Two-dimensional nanoarchitectonics: organic and hybrid materials. *Nanoscale* **2012**, *4*, 6102-6117.

90. Avinash, M. B.; Govindaraju, T. Amino acid derivatized arylenediimides: a versatile modular approach for functional molecular materials. *Adv. Mater.* **2012**, *24*, 3905-3922.

91. Mahler, A.; Reches, M.; Rechter, M.; Cohen, S.; Gazit, E. Rigid, Self-assembled hydrogel composed of a modified aromatic dipeptide. *Adv. Mater.* **2006**, *18*, 1365-1370.

92. Fichman, G.; Gazit, E. Self-assembly of short peptides to form hydrogels: Design of building blocks, physical properties and technological applications. *Acta Biomater.* **2014**, *10*, 1671-1682.

93. Adler-Abramovich, L.; Aronov, D.; Beker, P. Yevnin, M.; Stempler, S.; Buzhansky1, L.; Rosenman, G.; Gazit, E. Self-assembled arrays of peptide nanotubes by vapour deposition. *Nat. Nanotechnol.* **2009**, *4*, 849-854.

94. Barman, A. K.; Verma, S. Solid state structures and solution phase self-assembly of clicked mannosylated diketopiperazines. *RSC Adv.* **2013**, *3*, 14691-14700.

95. Zhou, C. Z.; Confalonieri, F.; Medina, N.; Zivanovic, Y.; Esnault, C.; Yang, T.; Jacquet, M.; Janin, J.; Duguet, M.; Perasso, R.; Li, Z. G. Fine organization of *Bombyx mori* fibroin heavy chain gene. *Nucleic Acids Res.* **2000**, *28*, 2413-2419.

96. Matsumoto, A.; Lindsay, A.; Abedian, B.; Kaplan, D. L. Silk fibroin solution properties related to assembly and structure. *Macromol. Biosci.* **2008**, *8*, 1006-1018.

97. Kundu, S. C. *Silk Biomaterials for Tissue Engineering and Regenerative Medicine*, Woodhead Publishing, Cambridge, UK **2014**.

98. Doblhofer, E.; Heidebrecht, A.; Scheibel, T. To spin or not to spin: spider silk fibers and more. *Appl. Microbiol. Biotechnol.* **2015,** *99*, 9361-9380.

99. Chen, F.; Porter, D.; Vollrath, F. Structure and physical properties of silkworm cocoons. *J. R. Soc. Interface* **2012**, *9*, 2299-2308.

100. Cheng, Y.; Koh, L.D.; Li, D.; Ji, B.; Han, M. Y.; Zhang, Y. W. On the strength of β-sheet crystallites of Bombyx mori silk fibroin. *J. R. Soc. Interface* **2014**, *11*, 2299-2308.

101. Omenetto, F. G.; Kaplan, D. L. New opportunities for an ancient material. *Science* **2010**, *329*, 528-531.

102. Benfenati, V.; Stahl, K.; Gomis-Perez, C.; Toffanin, S.; Sagnella, A.; Torp, R.; Kaplan, D. L.; Ruani, G.; Omenetto, F. G.; Zamboni, R.; Muccini, M. Biofunctional silk/neuron interfaces. *Adv. Funct. Mater.* **2012**, *22*, 1871-1884.

103. Tien, L. W.; Wu, F.; Tang-Schomer, M. D.; Yoon, E.; Omenetto, F. G.; Kaplan, D. L. Silk as a multifunctional biomaterial substrate for reduced glial scarring around brain-penetrating electrodes. *Adv. Funct. Mater.* **2013**, *23*, 3185-3193.

104. Marelli, B.; Brenckle, M. A.; Kaplan, D. L.; Omenetto, F. G. Silk fibroin as edible coating for perishable food preservation. *Sci. Rep.* **2015**, *6*, 25263.

105. Tansil, N.C.; Li, Y.; Teng, C. P.; Zhang, S.; Win, K. Y.; Chen, X.; Liu, X. Y.; Han, M. Y. Intrinsically colored and luminescent silk. *Adv. Mater.* **2011**, *23*, 1463-1466.

106. Tansil, N.C.; Koh, L. D.; Han, M. Y. Functional silk: colored and luminescent. *Adv. Mater.* **2012**, *24*, 1388-1397,

107. d'Ischia, M.; Wakamatsu, K.; Cicoira, F.; Mauro, E. D.; Garcia-Borron, J. C.; Commo, S.; Galván, I.; Ghanem, G.; Kenzo, K.; Meredith, P.; Pezzella, A.; Santato, C.; Sarna, T.; Simon, J. D.; Zecca, L.; Zucca, F. A.; Napolitano, A.; Ito, S. Melanins and melanogenesis: from pigment cells to human health and technological applications. *Pigm. Cell Melanoma Res.* **2015**, *28*, 520-544.

108. Ju, K. Y.; Lee, Y.; Lee, S.; Park, S. B.; Lee, J. K. Bioinspired polymerization of dopamine to generate melanin-like nanoparticles having an excellent free-radical-scavenging property. *Biomacromolecules* **2011**, *12*, 625-632.

109. McGinnes, J.; Corry, P.; Proctor, P. Amorphous semiconductor switching in melanins. *Science* **1974**, *183*, 853-855.

110. Bothma, J. P.; Boor, J. –de.; Divakar, U.; Schwenn, P. E.; Meredith, P. Device-quality electrically conducting melanin thin films. *Adv. Mater.* **2008**, *20*, 3539-3542.

111. Bettinger, C. J.; Bruggeman, J. P.; Misra, A.; Borenstein, J. T.; Langer, R. Biocompatibility of biodegradable semiconducting melanin films for nerve tissue engineering. *Biomaterials* **2009**, *30*, 3050-3057.

112. Watson, J. D.; Crick, F. H. C. Molecular structure of nucleic acids: a structure for deoxyribose nucleic acid. *Nature* **1953**, *171*, 737-738.

113. Pauling, L.; Corey, R. B.; Branson, H. R. The structure of proteins: two hydrogen-bonded helical configuration of the polypeptide chain. *Proc. Natl. Acad. Sci. USA* **1951**, *37*, 205-211.

114. Hein, J. E.; Blackmond, D. G. On the origin of single chirality of amino acids and sugars in biogenesis. *Acc. Chem. Res.* **2012**, *45*, 2045-2054.

115. Yashima, E.; Maeda, K.; Iida, H.; Furusho, Y.; Nagai, K. Helical polymers: synthesis, structures, and functions. *Chem. Rev.* **2009**, *109*, 6102-6211.

116. Feringa, B. L.; Delden, R. A. V.; Koumura, N.; Geertsema, E. M. Chiroptical molecular switches. *Chem. Rev.* **2000**, *100*, 1789-1816.

117. Canary, J. W. Redox-triggered chiroptical molecular switches. *Chem. Soc. Rev.* **2009**, *38*, 747-756.

118. Rowan, A. E.; Nolte, R. J. M. Helical molecular programming. *Angew. Chem. Int. Ed.* **1998**, *37*, 63-68.

119. Serrano, J. L.; Sierra, T. Helical supramolecular organizations from metal-organic liquid crystals. *Coord. Chem. Rev.* **2003**, *242*, 73-85.

120. Mateos-Timoneda, M. A.; Crego-Calama, M.; Reinhoudt, D. N. Supramolecular chirality of self-assembled systems in solution. *Chem. Soc. Rev.* **2004**, *33*, 363-372.

121. Wang, Y.; J. Xu, Wang, Y.; Chen, H. Emerging chirality in nanoscience. *Chem. Soc. Rev.* **2013**, *42*, 2930-2962.

122. J. Cui, A. Liu, Y. Guan, J. Zhang, Z. Shen, X. Wan, Tuning the helicity of self-assembled structure of a sugar-based organogelator by the proper choice of cooling rate. *Langmuir* **2010**, *26*, 3615-3622.

123. Huang, Y. W.; Hu, J. C.; Kuang, W. F.; Wei, Z. X.; Faul, C. F. J. Modulating helicity through amphiphilicity-tuning supramolecular interactions for the controlled assembly of perylenes. *Chem. Commun.* **2011**, *47*, 5554-5556.

124. Lohr, A.; Lysetska, M.; Würthner, F. Thermodynamic self-assembly of helical merocyanine dye nanorods. *Angew. Chem. Int. Ed.* **2005**, *44*, 5071-5074.

125. Jyothish, K.; Hariharan, M.; Ramaiah, D. Chiral supramolecular assemblies of a squaraine dye in solution and thin films: concentration-, temperature-, and solvent-induced chirality inversion *Chem. Eur. J.* **2007**, *13*, 5944-5951.

126. Cantekin, S.; Nakano, Y.; Everts, J. C.; van der Schoot, P.; Meijer, E.W.; Palmans, A. R. A. A stereoselectively deuterated supramolecular motif to probe the role of solvent during self-assembly processes. *Chem. Commun.* **2012**, *48*, 3803-3805.

127. Hu, J. C.; Kuang, W. F.; Deng, K.; Zou, W. J.; Huang, Y. W.; Wei, Z. X.; Faul, C. F. J. Self-assembled sugar-substituted perylene diimide nanostructures with homochirality and high gas sensitivity. *Adv. Funct. Mater.* **2012**, *22*, 4149-4158.

128. Wattamwar, P. P.; Mo, Y.; Wan, R.; Palli, R.; Zhang, Q.; Dziubla, T. D. Antioxidant activity of degradable polymer poly(troloxester) to suppress oxidative stress injury in the cells. *Adv. Funct. Mater.* **2010**, *20*, 147-154.

129.. Liu, W. F.; Ma, M.; Bratlie, K. M.; Dang, T. T.; Langer, R.; Anderson, D. G. Real-time in vivo detection of biomaterial-induced reactive oxygen species. *Biomaterials* **2011**, *32*, 1796-1801.

130. Potter-Baker, K. A.; Capadona, J. R. Reducing the "stress": antioxidative therapeutic and material approaches may prevent intracortical microelectrode failure. *ACS Macro Lett.* **2015**, *4*, 275-279.

131. Pham-Huy, L. A.; He, H.; Pham-Huy, C. Free radicals, antioxidants in disease and health. *Int. J. Biomed. Sci.* **2008**, *4*, 89-96.

132. Essick, E. E.; Sam, F. Oxidative stress and autophagy in cardiac disease, neurological disorders, aging and cancer. *Oxid. Med. Cell. Longev.* **2010**, *3*, 168-177.

133. Reuter, S.; Gupta, S. C.; Chaturvedi, M. M.; Aggarwal, B. B. Oxidative stress, inflammation, and cancer: How are they linked? *Free Radical Biol. Med.* **2010**, *49*, 1603-1616.

134. Zhao, Y.; Zhao, B. Oxidative stress and the pathogenesis of Alzheimer's disease. *Oxid. Med. Cell Longev.* **2013**, *2013*, 10.

135. Sutherland, G. T.; Chami, B.; Youssef, P.; Witting, P. K. Oxidative stress in Alzheimer's disease:primary villain or physiological by-product? *Redox Report* **2013**, *18*, 134-141.

136. Rajasekhar, K.; Chakrabarti, M.; Govindaraju, T. Function and toxicity of amyloid beta and recent therapeutic interventions targeting amyloid beta in Alzheimer's disease. *Chem. Commun.* **2015**, *51*, 13434-13450.

137. O'Brien, F. J. Biomaterials & scaffolds for tissue engineering. *Mater. Today* **2006**, *14*, 88-95.

138. Higuchi, A.; Ling, Q. D.; Ko, Y. A.; Chang, Y.; Umezawa, A. Physical cues of biomaterials guide stem cell differentiation fate. *Chem. Rev.* **2013**, *113*, 3297-3328.

139. McCaig, C. D.; Rajnicek, A. M.; Song, B.; Zhao, M. Controlling cell behaviour electrically: current views and future potential. *Physiol. Rev.* **2005**, *85*, 943-978.

140. Poltawski, L.; Watson, T. Bioelectricity and microcurrent therapy for tissue healing-a narrative review. *Phys. Ther. Rev.* **2009**, *14*, 104-114.

141. Qazi, T. H.; Rai, R.; Boccaccini, A. R. Tissue engineering of electrically responsive tissues using polyaniline based polymers: A review. *Biomaterials* **2014**, *35*, 9068-9086.

Chapter 2

Orchestrated Self-assembly of Designer Cyclic Dipeptides into Molecular Gels

Chapter 2.1 Hydrogen Bond Directed Self-Assembly of Designer Cyclic Dipeptide Derivatives: Gelation and Ordered Hierarchical Architectures

2.1.1 Introduction

In recent years, the scientific community has shown strong interest in the development of low molecular weight (LMW) organo- and hydrogelators as a class of soft materials.[1-4] The LMW gelators can be prepared with ease starting from easily accessible starting materials. Unlike in the case of high molecular weight polymeric gelators, wherein covalent bonding and large association constants are required for gelation, the LMW gels are formed by noncovalent interaction-driven self-assembly of designed small molecules. Noncovalent interactions such as hydrogen bonding, aromatic π–π interactions and van der Waals forces are mainly responsible for the self-assembly of small molecules.[5] The self-assembled fibrillar structures then entangle the solvent molecules owing to high surface tension and capillary action and forms molecular gels.[6] Temperature, light, enzymes, pH and shear force can be used as external stimuli for triggering the process of gelation.[7-14] The LMW gels formed through supramolecular self-assembly are reversible, the property which makes them most interesting soft materials. The applications of LMWgels are vast and includes drug delivery, cell culture, templates for the synthesis and stabilization of inorganic nanomaterials.[15-22] Among LMW gelators, small peptide-based gels are promising owing to their structural similarity with various beneficial biological materials as well as those implicated in disease states such as Alzheimer's, Parkinson, type II diabetes and Prion diseases.[23-27]

The well-ordered hierarchical architectures are of great importance in the field of nanoscience owing to their numerous applications. The top-down approach, classic way

of preparing such architectures, limits the synthesis of ordered architectures in the case of organic molecules owing to their instability. A self-assembly based bottom-up approach for the synthesis of ordered microporous hierarchical architectures is increasingly attracting the interest of researchers owing to its ease of preparation and solution phase processing in comparison to the expensive and tedious procedures involved in top-down approaches. These ordered microporous structures will find potential applications as catalysts, microreactors, and scaffolds for tissue engineering.[28-30] Despite the advantage of bottom-up approaches over top-down approaches, there are only a few reports available for the synthesis of regular hierarchical structures using small molecules and peptides in the literature.[31,32]

Amongst the peptide-based LMW gelators, dipeptide and cyclic dipeptide (CDP) derived molecules presents a class of efficient gelators for organic solvents, organic fluids, and ionic liquids.[6,33,34] In particular, CDPs also familiar as diketopiperazines (DKP) are the smallest possible cyclic form of peptides and are known to form intermolecular hydrogen bonded molecular ladders and layers.[35-39] CDPs are quite often observed in nature with a specific biological activity and *in vitro* CDPs are being exploited as antibiotics and asymmetric catalysts.[40-45] The outstanding structural stability and resistance towards the proteolytic enzymes make them attractive materials for the preparation of soft materials. The molecular self-assembly CDPs was tuned into robust two-dimensional nano- and meso-sheets and one-dimensional fibre bundles with structural hierarchies similar to that of graphene and natural fibres respectively by the judicious choice of amino acid composition.[38,39] Similar to any LMW gelators, noncovalent interactions are the main driving force behind the gelation using CDPs, which are further strengthened by their unique structural features. The rigid structure and

strong intermolecular interactions through hydrogen bonding among other noncovalent interactions enable CDPs to form ordered morphologies.

Herein, we have synthesized and studied the gelation of CDP **1** (*cyclo*(*L*-Lys(tBoc)-Gly)) and CDP **2** (*cyclo*(*L*-Lys(Fmoc)-Gly)). The effect of side chain protection group (*t*Boc or Fmoc) in driving the organo- hydrogelation is studied.

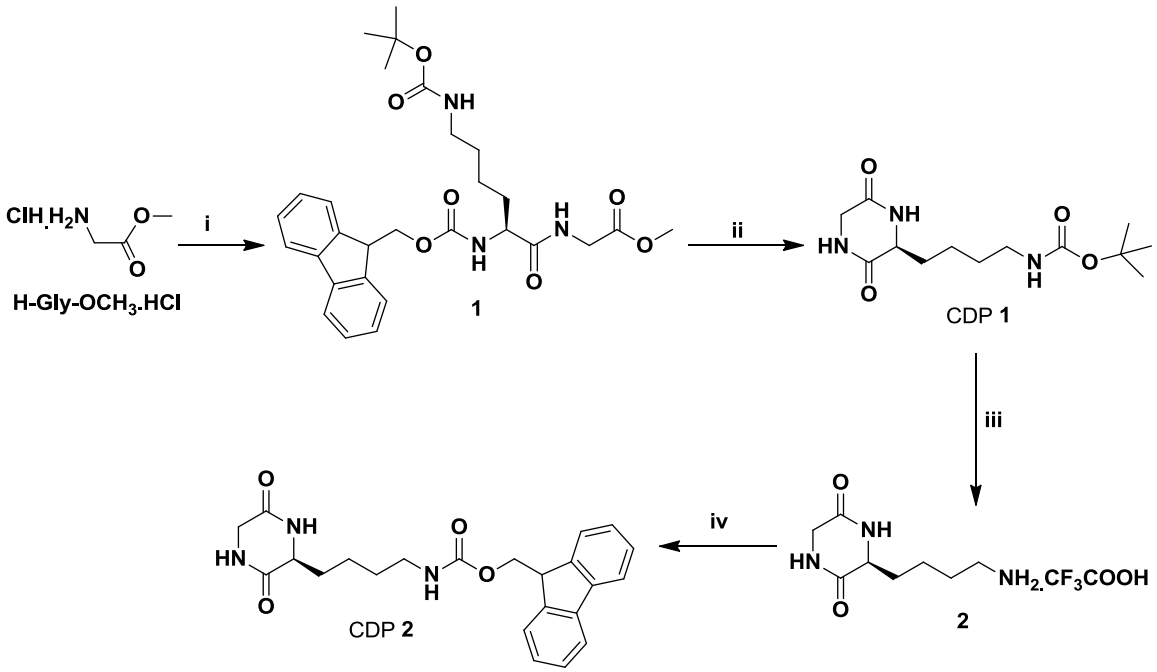

Scheme 2.1.1 Synthesis of CDPs **1** and **2**. Reagents and conditions. (i) Fmoc-*L*-Lys(*t*Boc)-OH, EDC.HCl, HOBt, DIPEA, DCM, 0 ºC- RT, 5 h. (ii) 20% piperidine in DCM, RT, 24 h. (iii) TFA-H_2O (v/v, 1:1), TIPS, RT, 4 h. (iv) Fmoc-OSu, $NaHCO_3$, 1,4-dioxane, H_2O, 0 ºC-RT, 4 h. EDC.HCl = 1-Ethyl-3-(3-dimethylaminopropyl)carbodiimide hydrochloride; HOBt = 1-hydroxybenzotriazole; DIPEA = *N*,*N*-diisopropylethylamine; DCM = dichloromethane. TFA = trifluoroacetic acid, Fmoc-OSu = *N*-(9-fluorenylmethoxycarbonyloxy) succinimide; TIPS = triisopropylsialne, RT = room temperature.

2.1.2 Results and Discussion

2.1.2.1 Synthesis of CDPs

CDP **1** is prepared by the robust method of solution phase linear dipeptide synthesis followed by cyclization using piperidine in dichloromethane. CDP **2** is prepared by

coupling *N*-(9-Fluorenylmethoxycarbonyloxy) succinimide (Fmoc-OSu) with CDP **1** after ε-amine deprotection. (Scheme 2.2.1). Chemical purity and integrity of the prepared peptides was evaluated using NMR, mass spectrometry, and elemental analysis.

2.1.2.2 Gelation studies

CDPs **1** and **2** form molecular gels through non-covalent secondary interaction driven self-assembly process. The gelation ability of CDPs in various organic- and aqueous solvents was studied by heating and cooling cycle through inversion tube method. Specifically, organo gelation was achieved by heating a specified amount of CDP dispersed in the solvent of interest in a closed vial at around 45-50 ºC and cooling the obtained clear solution to room temperature under ambient conditions. The ability of

Table 2.1.1 Gelation test results of CDP **1** and **2**.[a]

Solvent	**Minimal Gelation Concentration (wt%)**	
	CDP 1	**CDP 2**
Hexane	G (5.5)	I
CCl_4	G (4.4)	I
Toluene	G (2.6)	G (3.2)
$CHCl_3$	G (3.2)	VL
DMF	CS	CS
H_2O	CS	G (2.5)

[a]G: gel; CS: clear solution; I: insoluble; VL: viscous liquid

CDPs **1** and **2** to form organogels was eventually determined qualitatively by inverting the vial upside down (inversion tube method). The absence of any solvent flow in the vial confirmed the formation of the organogel. Table 2.1.1 shows the minimum gelation

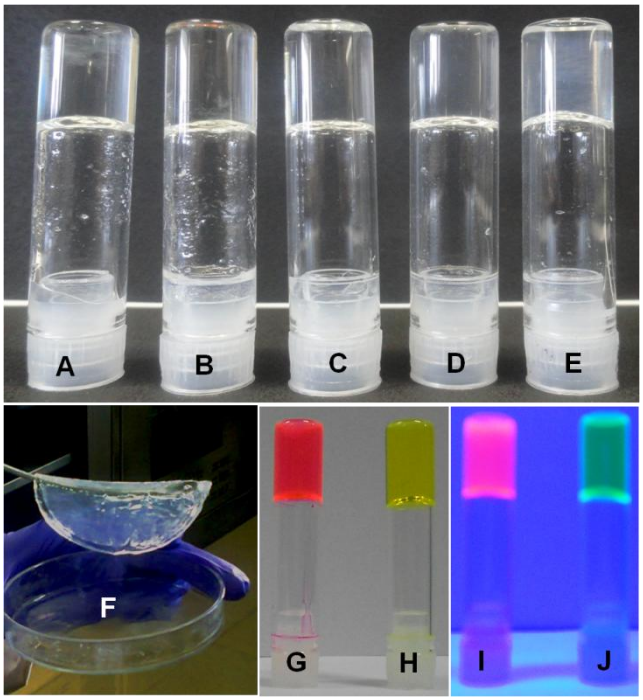

Figure 2.1.1 Photographs of CDP molecular gels and drug loading. CDP **1** in (A) carbon tetrachloride (4.4 wt%), (B) toluene (2.6 wt%), (C) chloroform (3.2 wt%), CDP **2** in (D) toluene (3.2 wt%), (E) water (2.5 wt%); (F) CDP **1** organogel in hexane (5.5 wt%), formed over a large area petri dish, lifted using a spatula. (G), (H) Rhodamine B and curcumin entrapped organogels of CDP **1** in chloroform under visible light and (I), (J) under UV light (λ = 365 nm).

concentrations (MGCs) of CDPs in different solvents which were obtained through the inversion tube method and the corresponding gel images are shown in Figure 2.1.1 The organogels of CDP **1** in chloroform and other solvents were found to be stable for several weeks while that of CDP **2** only for few weeks. CDP **1** organogel in hexane was facilitated over a large area petri dish. The formed gel is mechanically stable and could be lifted using a spatula without any deformation or loss of structural integrity of the soft material (Figure 2.1.1F). CDP **1** failed to form hydrogels under the studied experimental conditions, which is attributed to the absence of additional secondary interactions other than H-bonding. Interestingly, CDP **2** the structural analog of CDP **1** containing Fmoc-group in place of Boc-group facilitated the formation of hydrogels at 2.5 wt% MGC. The formation of hydrogels selectively by CDP **2** is attributed to the presence of additional

aromatic interactions and highlights the significance of chemical structure of gelator for designing molecular gels.

2.1.2.3 Dye and drug entrapment

The potential of CDP gels for biomedical applications is demonstrated by the physical entrapment of biologically important dye, drug molecules rhodamine B and curcumin, respectively. The loading concentrations were optimized and CDP **1** containing 0.1 wt% of rhodamine B and curcumin was found to undergo gelation in chloroform, physically entrapping the dye and drug molecules as indicated by their visible and fluorescent colors (Figure 2.1.1G-J).

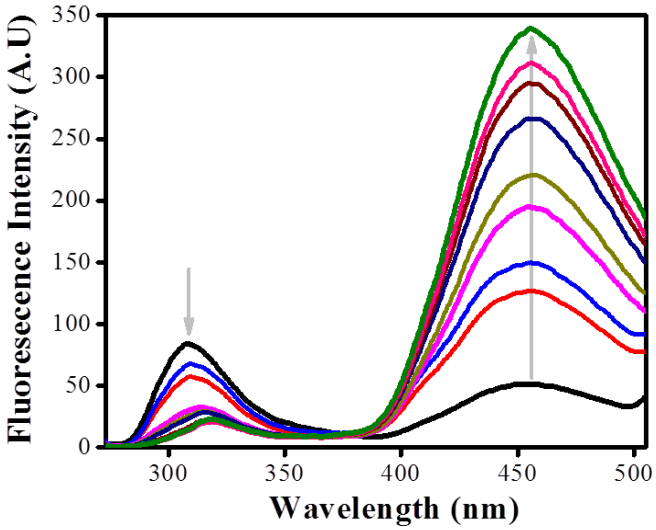

Figure 2.1.2 Emission spectrum of CDP **2** in chloroform with increasing concentration (10 μM-100 μM). Excitation wavelength (λ_{ex}) is 310 nm.

2.1.2.4 CDP 2 aggregation studies

CDP **2** in its molecularly dissolved state (10 μM) in chloroform showed emission band (λ_{max}) at 310 nm and a weak emission band at 460 nm when excited at 260 nm (Figure 2.1.2). The fluorescence emission band at 310 nm red-shifted (15 nm) and the intensity

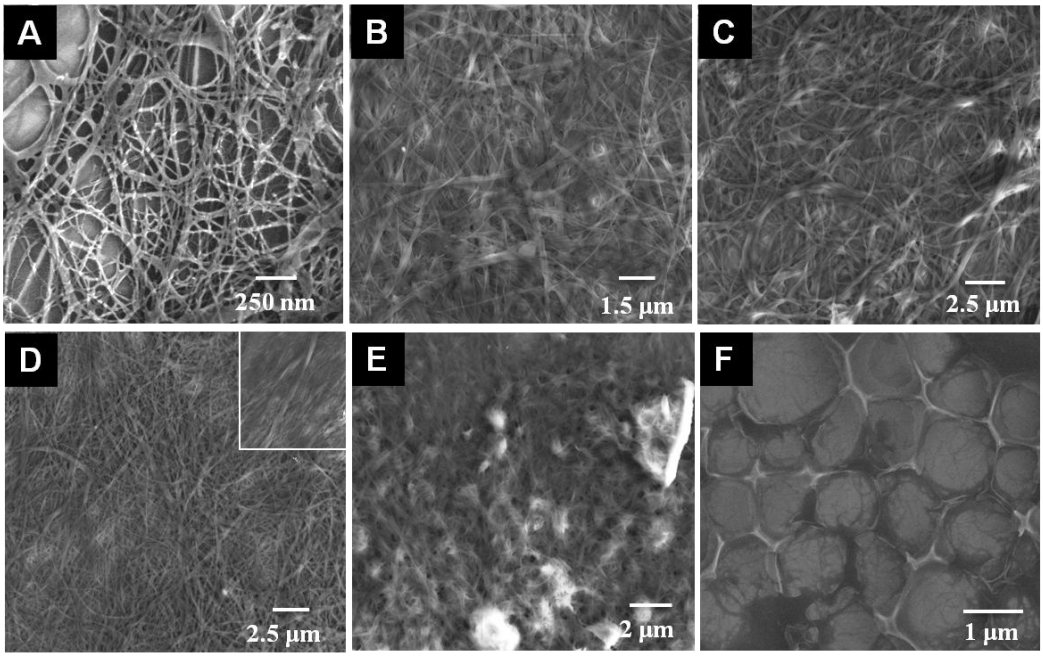

Figure 2.1.3 Microscopy analysis of CDP self-assembly. FESEM images of xerogels of CDP **1** in (A) chloroform, (B) carbon tetrachloride, (C) hexane, (D) toluene, CDP **2** (E) toluene and (F) ordered microporous hierarchical arrays of CDP **2** in chloroform. Inset in (D) shows bundled nanoribbon structures of CDP **1** in toluene.

decreased gradually with a large enhancement at 460 nm as a function of concentration (10-100 µm). The emission peak at 460 nm is the characteristic excimer emission of the Fmoc-group along with the J-type aggregation which is an indication of strong intermolecular interaction.[46]

2.1.2.5 FESEM analysis

LMW gelators enable their molecular self-assembly into gels by the formation of nanofibres, nanoribbons or nanosheets. Insight into the morphology of self-assembled CDP organogelators in different solvents was obtained by field emission scanning electron microscopy (FESEM) analysis. The xerogel of CDP **1** in chloroform revealed the presence of an entangled network of nanofibers having a diameter of a few nanometers and extending to >100 µm in length (Figure 2.1.3A). The xerogel morphology of CDP **1**

in carbon tetrachloride, hexane and toluene were found to be nanoribbons extending to >100 μm length scale (Figure 2.1.3B-D). The nanoribbons were very closely entangled and formation of bundled structures was observed in the case of CDP **1** toluene xerogel (inset, Figure 2.1.3D) The xerogel morphology of CDP **2** in toluene showed the presence of tightly packed nanofibers (Figure 2.1.3E). FESEM analysis of self-assembled structures of CDP **2** from chloroform (100 μM) showed a uniform distribution of microporous hierarchical architectures (Figure 2.1.3F). The ordered microporous hierarchical structures observed in FESEM analysis were of 1-2 μm in size. The presence of nanostructural 3D networks in CDP xerogels elucidates the molecular self-assembly of CDPs at micro scale resulting in the formation of macroscopic organogels. The formation of hierarchical architectures by CDP **2** in chloroform further corroborates the strong intermolecular aromatic interaction leading to the excimer-like emission (Figure 2.1.2).

2.1.2.5 NMR studies

The crucial role of hydrogen bonding and aromatic π-π interactions in the formation of network of self-assembled nanostructures leading to the formation of organogels was validated by concentration and temperature dependent ^{1}H NMR studies of CDPs.[6,47] ^{1}H NMR spectra of CDP **1** recorded at 298 K with varying concentrations (3.5 to 56.0 mM) in deuterated dimethyl sulfoxide (DMSO-d_6) showed linear downfield shift of amide and carbamate protons (Figure 2.1.4A). Such downfield shift of protons with an increase in concentration is a clear evidence of intermolecular hydrogen bonding between CDP units. CDP **1** forms a molecular ladder through amide-protons (-NH^{1} and -NH^{2}) and amide-carbonyls via a pair of intermolecular hydrogen bonding to two of its neighbors. (Figure 2.1.5) Similarly, carbamate-proton (-NH^{3}) and carbamate-carbonyl were involved in the formation of another linear chain of single intermolecular hydrogen bonding. ^{1}H NMR

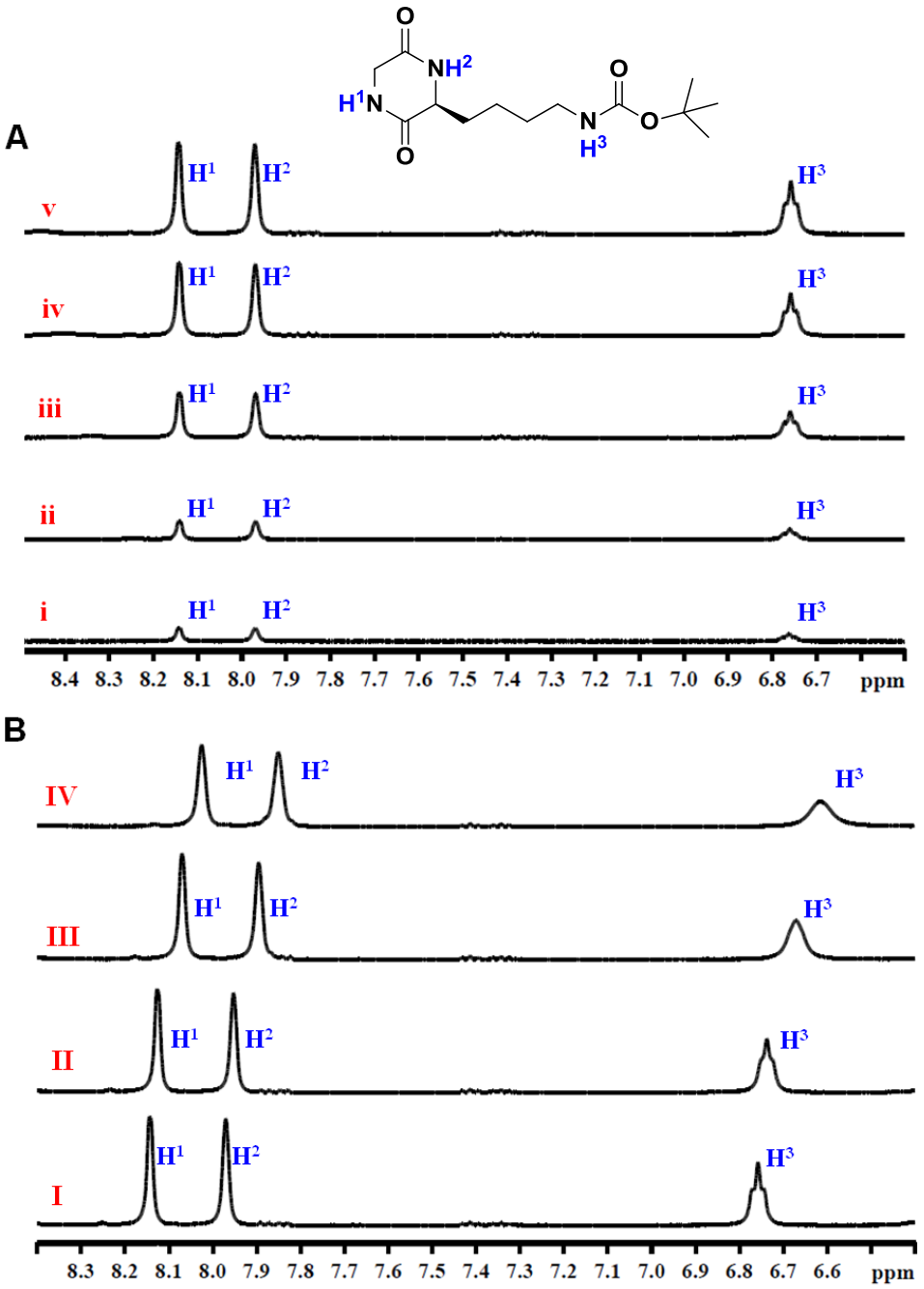

Figure 2.1.4 NMR studies of CDP **1**. (A) Concentration dependant ^{1}H NMR spectra of CDP **1** in DMSO-d_6 at 298 K and (B) Temperature dependent ^{1}H NMR spectra of CDP **1** in DMSO-d_6. i: 3.5 mM, ii: 9.8 mM, iii: 21.7 mM, iv: 33.6 mM , v: 56.0 mM; I: 298 K, II: 303 K, III: 313 K, IV: 323 K.

spectra of CDP **1** (56.0 mM) recorded as a function of temperature (298 K to 323 K) showed an overall upfield shift of 0.12 ppm for amide protons (Figure 2.1.4B). Such an

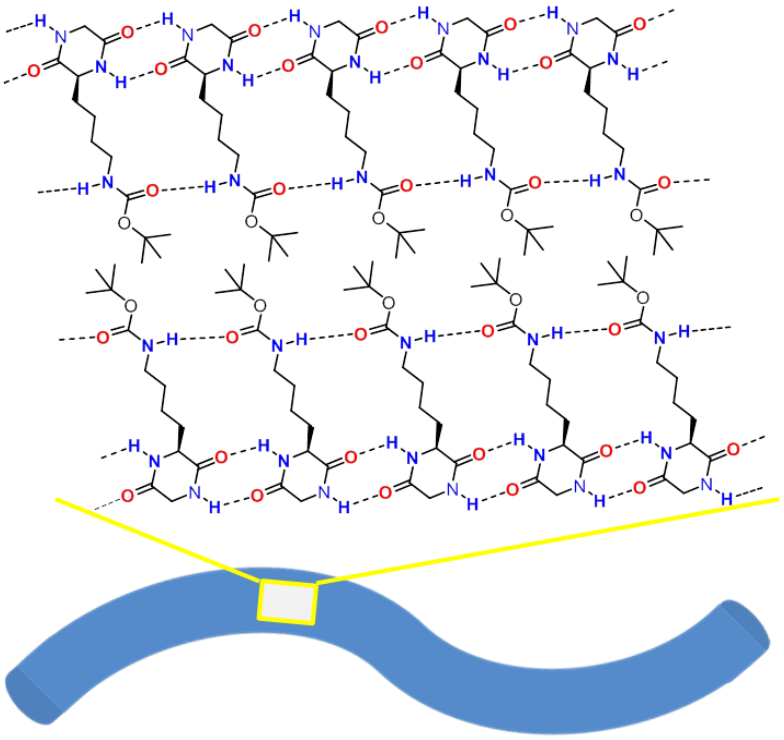

Figure 2.1.5 Pictorial representation of hydrogen bond directed self-assembly of CDP **1** into nanofibres which subsequently form organogels.

upfield shift of amide protons was attributed to the weakening of intermolecular hydrogen bonding at high temperatures. Thus, the observed downfield and upfield shift of amide- and carbamate-protons with an increase in concentration and temperature respectively, strongly support the presence of intermolecular hydrogen bonding and its role in the self-assembly of CDP **1** to form supramolecular nanostructures (Figure 2.1.3A-D).

Similarly, concentration-dependent ^{1}H NMR spectra of CDP **2** (2.9-24.5 mM) were recorded at 298 K. Splitting and downfield shifts of amide- and aromatic protons (Fmoc-) of CDP **2** with increasing concentration was observed (Figure 2.1.6A). The downfield shift of amide protons (0.03 ppm and 0.01 ppm) as a function of concentration was attributed to the presence of strong intermolecular hydrogen bonding. The splitting of Fmoc-protons, as indicated in Figure 2.1.6A, was attributed to the presence of strong

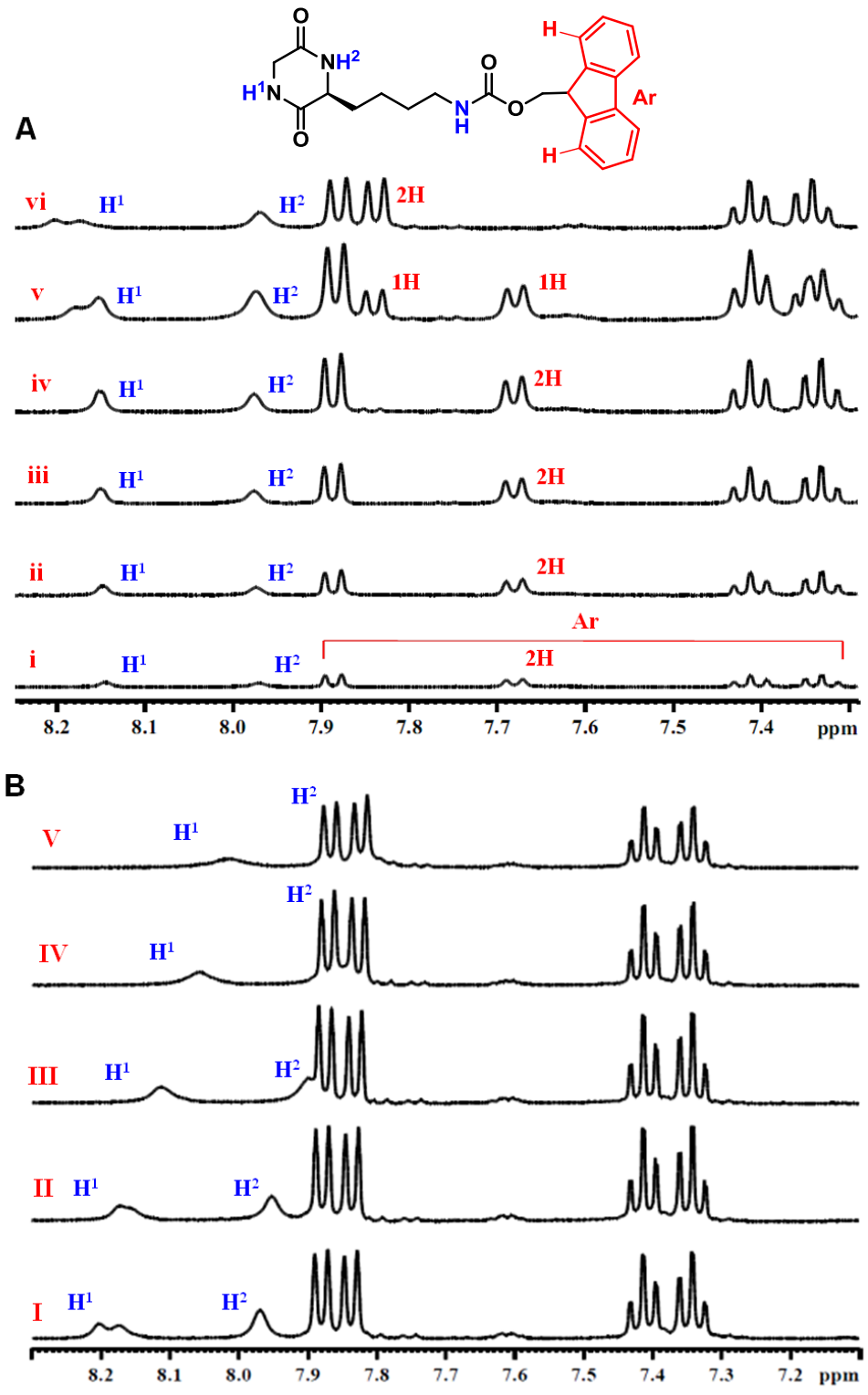

Figure 2.1.6 NMR studies of CDP **2**. (A) Concentration dependent ^{1}H NMR spectra of CDP **2** in DMSO-d_6 at 298 K and (B) temperature dependent ^{1}H NMR spectra of CDP **2** in DMSO-d_6. i: 2.9 mM, ii: 4.9 mM, iii: 7.6 mM, iv: 12.0 mM, v: 24.5 mM vi: 24.5 mM of CDP **2** after one day aging. I: 298K, II: 303 K, III: 313 K, IV: 323 K, V: 333 K.

aromatic π-π interactions. Interestingly, a doublet (2H, 7.66-7.69 ppm) appeared for two aromatic protons of Fmoc-functionality as depicted in Figure 2.1.6A split into two separate doublets for each proton along with the doublet corresponding to one of the protons being downfield shifted from 7.67-7.69 to 7.83-7.85 ppm (H) at a 24.5 mM concentration of CDP **2** (Figure 2.1.6A(v)). Further, we observed the downfield shift and merging of the previously unaffected doublet with that of the already downfield shifted aromatic proton doublet after aging the NMR sample for one day (Figure 2.1.6A(vi)). This is an indication of time-dependent strengthening and stabilization of aromatic interactions. Furthermore, merging of the unaffected proton with an already downfield shifted proton after aging the sample clearly indicates the initial J-type aggregation followed by transformation towards excimer-like arrangement as indicated by the excimer emission of CDP **2** (Figure 2.1.2). The temperature dependent ^{1}H NMR spectra recorded for CDP **2** (24.5 mM) from 298 K to 333 K showed an upfield shift of CDP core amide-protons, and two of them merge with other upfield aromatic proton signals at temperatures 313 K (Figure 2.1.6B). Overall, the concentration and temperature dependent ^{1}H NMR studies confirm the presence of strong intermolecular hydrogen bonding and aromatic π-π interactions and play a major role in the molecular self-assembly of CDP **1** and **2**. As shown in Figure 2.1.5, we propose a model for the self-assembly of CDP **1** and subsequent formation of nanofibers. The hydrophobic Boc-group of CDP **1** is presumed to be the driving force for the organization of [-N-H--O] hydrogen bonded molecular chains into fibrillar structures. These self-assembled nano-fibrillar structures then entangle the solvent molecules owing to high surface tension and capillary action to form a nanofibrous network as found in the organogels.[6]

2.1.3 Conclusion

In summary, we have demonstrated intermolecular hydrogen bond directed self-assembly of cyclic dipeptide derivatives CDP **1** and **2** into nanofibres, nanoribbons, and their subsequent gelation. Concentration and temperature dependent NMR studies clearly demonstrate the involvement of strong intermolecular hydrogen bonding and aromatic π-π interactions in the molecular self-assembly of CDP **1** and **2**. Aromatic and hydrogen bond interactions render the self-assembly of CDP **2** into an ordered microporous hierarchical architecture, which corresponds to excimer emission in chloroform. We have also demonstrated that organogels can be used to physically entrap dye and drug molecules such as rhodamine B and curcumin. The gels reported herein might have potential applications as entrapping agents, drug delivery systems and thermoresponsive soft materials for various (bio)material applications.

Chapter 2.2 Cyclic Dipeptide-based Ambidextrous Supergelators: Minimalistic Rational Design and *In Situ* Hydrogelation

2.2.1 Introduction

Low molecular weight gels (LMWGs) formed by the entrapment of liquids through self-assembled three-dimensional (3D) networks of small organic molecules are important class of soft materials.[1] Self-assembly of small molecules is driven by the weak, yet powerful noncovalent interactions such as hydrogen bonding, aromatic, electrostatic, attractive van der Waals and host-guest interactions.[48,49] Ease of synthesis, wide range availability of chemical modification procedures and functionalities to tune the physical and chemical properties, makes small molecules promising gelators for both material and biomedical applications. Similarly, small peptide-based gelators are indispensable subgroup of organic molecular gelators for various material, biological and biomedical applications owing to their biological relevance, biocompatibility, tunable properties by the virtue of employing desired amino acids in the sequence.[50-54] Aromatic protecting groups such as fluorene (Fmoc) and naphthalene (Nap) in the *N*-terminal of peptides are used routinely to assist the intermolecular interactions in the form aromatic π-π attractions in addition to other noncovalent interactions to facilitate the organo- and hydrogelation. *N*-Terminal modified peptides and their derivatives have met with reasonably good success, for applications such as synthesis of inorganic nanomaterials, drug delivery and as scaffolds for cell culture and tissue engineering.[55-59] The dynamic and noncovalent nature of LMWGs offers flexibility to employ various physical and chemical stimuli to modulate the sol-gel transformation in a solvent of interest.[60-62] Supergelators are a class of LMWGs that comprises more than 99% of the liquid yet behaves as solids and are

promising candidates for biomedical and tissue engineering applications because of their resemblance to *in vivo* extracellular matrix (ECM).[63,64]

Small molecule or peptide supergelators that facilitate loading of biologically important molecules such as drugs and capable of forming *in situ* gels upon injection into the site of the requirement have attracted the attention of researchers on the account of their diverse applications.[16,65,66] *In situ* forming LMWGs are special class of soft materials that are promising candidates for the parenteral administration of biologically important molecules and drug delivery with minimal invasion.[67-70] The *in situ* formed gels acts as a local depot for the incorporated cargo and facilitates its controlled release because of the inherently dynamic nature of the molecular gels. Further, the delivery pattern can be tuned by modulating stimuli-responsive nature of gelator. Jean-Christophe Leroux and coworkers have used similar *in situ* gelation approach and successfully demonstrated the loading and delivery of drugs such as rivastigmine using amino acid derived organogels. *In situ* gelation was achieved by injecting the gelators from their organic solutions containing *N*-methyl-2-pyrrolidone (NMP), an FDA approved biocompatible solvent used for administration of leuprolide acetate through subcutaneous injection for the treatment of prostate and breast cancer.[71-73]

Cyclic dipeptides (CDPs) are heterocyclic 2,5-diketopiperazines (DKPs), the smallest form of cyclic peptides formed mostly through head-to-tail intramolecular cyclization of the corresponding linear dipeptides.[74] CDPs are ubiquitously found in nature ranging from bacteria to humans with diverse biological functions.[41,75,76] CDPs are structurally rigid owing to their cyclic conformation and demonstrate resistance towards the enzymatic hydrolysis compared to their linear counterparts. The propensity to self-assemble both in solution and solid-state through strong intermolecular hydrogen bonding

and other secondary interactions associated with the nature of amino acids incorporated makes the CDP molecules potential candidates in designing soft materials for numerous applications.[37,77,78] CDP derivatives have successfully been used for the gelation of many organic and aqueous solvents by employing physical stimuli such as temperature, shear force and pH.[33,38,39,43,79-82] We anticipated that CDPs owing to their unique physical and chemical properties can be used for the development of *in situ* gelation for parenteral administration of biologically important molecules. Herein, we have designed and synthesized four CDPs with variable chemical modifications and studied their gelation propensity in a range of solvents that include organic, aqueous and phosphate buffer saline (PBS) solutions at physiological conditions. Parameters such as minimum structural requirements for the gelation in both organic and aqueous media, ability to form *in situ* gelation when injected from the biocompatible solvent, entrapment of drug molecules were studied. CDP gels were thoroughly characterized to understand the molecular mechanism inducing gelation, thermal stability, gel strength and biocompatibility using nuclear magnetic resonance (NMR) spectroscopy, gel melting temperature (T_g), rheology analysis and cytotoxicity with murine PC12. To the best of our knowledge, this is the first report showcasing the ambidextrous supergelation propensity of CDPs with *in situ* gelation property at physiological pH and temperature.

2.2.2 Results and Discussion

2.2.2.1 Synthesis of CDPs

CDPs **3** [*cyclo*(*L*-Tyr-*L*-Glu(OtBu))], **4** [*cyclo*(*L*-Phe-*L*-Glu(OtBu))], **5** [*cyclo*(*L*-Phe-*L*-Asp(OtBu))] and **6** [*cyclo*(*L*-Leu-*L*-Glu(OtBu))] were prepared through the robust syntheses routes which invovled synthesis of Fmoc- protected linear dipeptide followed

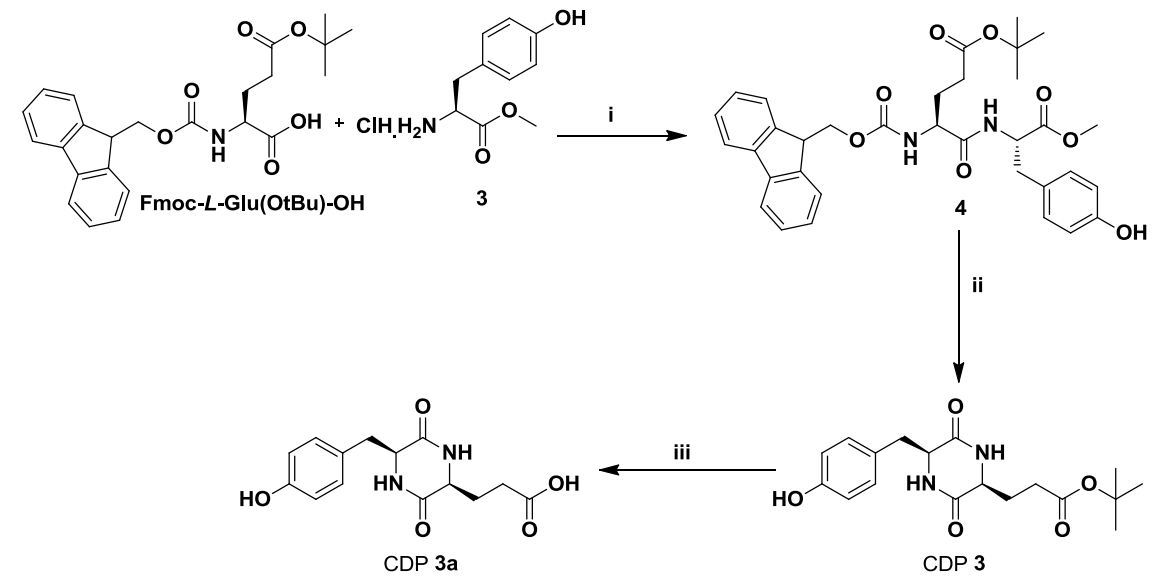

Scheme 2.2.1 Synthesis of CDP **3**. Reagents and conditions: (i) EDC.HCl, HOBt, DIPEA, DCM, 0 ºC- RT, 5 h. (ii) 20% piperidine in DCM, RT, 12 h. (iii) TFA-H_2O (v/v, 1:1), TIPS, RT, 4 h. EDC.HCl = 1-Ethyl-3-(3-dimethylaminopropyl)carbodiimide hydrochloride, HOBt = 1-hydroxybenzotriazole, DIPEA = Diisopropylethylamine, DCM = dichloromethane, TFA = trifluoroacetic acid, RT = room temperature.

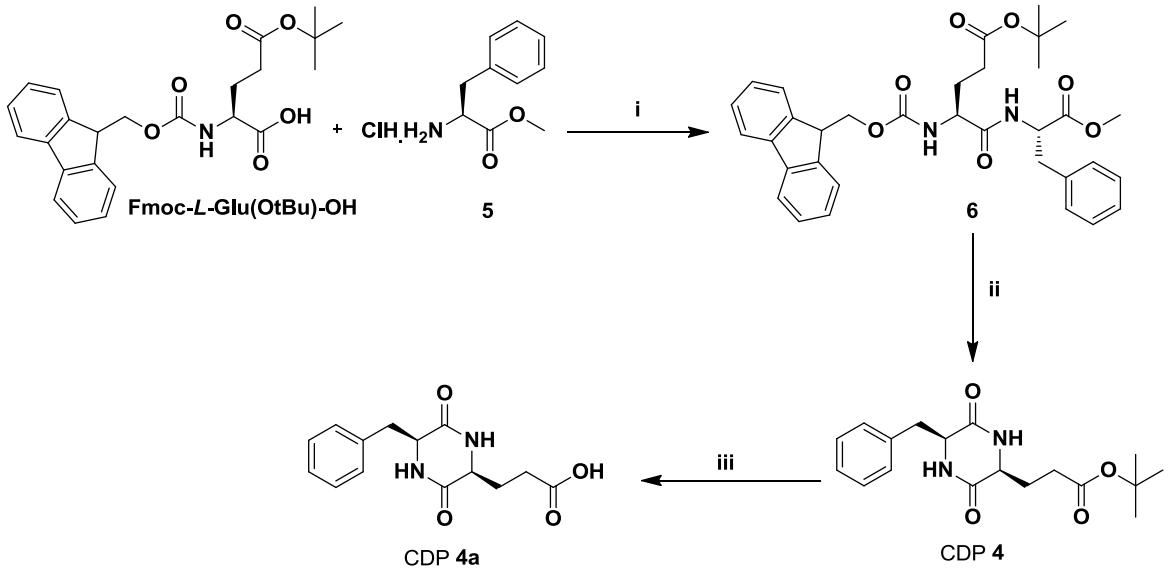

Scheme 2.2.2 Synthesis of CDP **4**. Reagents and conditions: (i) EDC.HCl, HOBt, DIPEA, DCM, 0 ºC- RT, 5 h. (ii) 20% piperidine in DCM, RT, 12 h. (iii) TFA-H_2O (v/v; 1:1), TIPS, RT, 4 h.

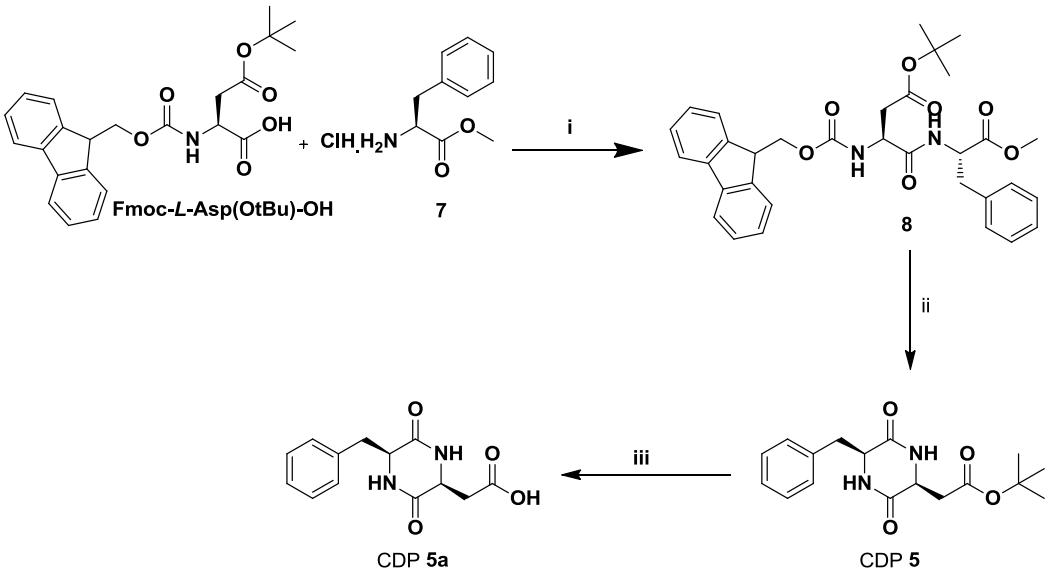

Scheme 2.2.3 Synthesis of CDP **5**. Reagents and conditions: (i) EDC.HCl, HOBt, DIPEA, DCM, 0 ºC- RT, 5 h. (ii) 20% piperidine in DCM, RT, 12 h. (iii) TFA-H_2O (v/v; 1:1), TIPS, RT, 4 h.

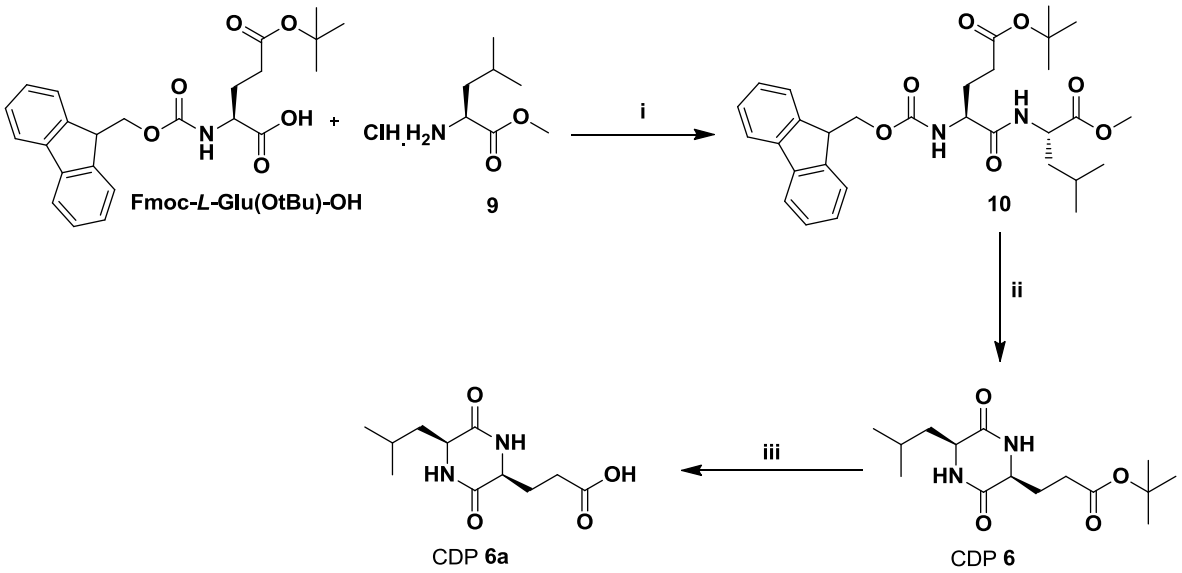

Scheme 2.2.4 Synthesis of CDP **6**. Reagents and conditions: i) EDC.HCl, HOBt, DIPEA, DCM, 0 ºC- RT, 5 h. ii) 20% piperidine in DCM, RT, 12 h. iii) TFA-H_2O (v/v; 1:1), TIPS, RT, 4 h.

by the cyclization of linear dipeptide into corresponding CDP using piperidine in dichloromethane (Scheme 2.2.4-2.2.6).[80,81] The chemical purity and integrity of the prepared peptides and CDPs was evaluated using NMR, mass spectrometry, and

elemental analysis. CDPs **3** and **4** were designed based on the fact that aromatic amino acid derivatives facilitate the self-assembly to form injectable organogels.[71-73,80,81] The other two CDPs **5** [*cyclo*(*L*-Phe-*L*-Asp(OtBu))] and **6** [*cyclo*(*L*-Leu-*L*-Glu(OtBu))] with varying amino acid composition were chosen to understand the significance of amino acid composition on the gelation propensity of CDPs in organic and aqueous solvents as well as *in situ* gelation ability under physiological conditions. Tertiary butyloxycarbonyl (tBoc) moiety was chosen for side chain protection of *L*-glutamic acid (**3**, **4** and **6**) and *L*-aspartic acid (CDP **5**) owing to the ability of tertiary butyl group in driving molecular gelation of peptide derivatives.[80]

2.2.2.2 Gelation studies

The gelation ability of CDPs in various organic- and aqueous solvents was studied by heating and cooling cycle through inversion tube method also known as table top rheology as explained in detail, in the experimental section. CDP **3** showed ambidextrous gelation behavior and formed gels in both organic- and aqueous solvents at less than 1 wt% gelator concentration (Table 2.2.1). The corresponding photographs of gels (inverted vials) are shown in Figure 2.2.1 (upper panel). Thus, CDP **3** behaves as supergelator (MGC <1 wt%), which infers that one molecule of CDP **3** entraps approximately 6500 water molecules and results in the formation of hydrogels.

The gelation ability of CDPs **4**, **5** and **6** was studied to probe the significance of each structural unit in driving the gelation. CDP **4** with *L*-phenylalanine and keeping all other functionalities same as CDP **3** is expected to provide insight into the significance of tyrosine (phenolic-OH group) for gelation. CDP **4** showed excellent gelation property similar to CDP **3** and formed gels in both organic- and aqueous solvents at gelator

Table 2.2.1 Gelation properties of CDPs **3-6**.[a]

Solvent	Minimal Gelation Concentration (wt%)			
	CDP 3	**CDP 4**	**CDP 5**	**CDP 6**
Toluene	TG (0.4)	TG (0.3)	I	TG (0.3)
Chloroform	TG (0.2)	TG (0.3)	CS	CS
Ethylacetate	TG (0.2)	TG (0.2)	I	VL
Dichlomethane	TG (0.2)	TG (0.3)	I	CS
1,2-Dichloro benzene	TG (0.1)	TG (0.1)	LG (4.6)	TG (0.6)
tert-BuOH	TG (0.5)	TG (0.4)	I	VL
sec-BuOH	TG (1.0)	TG (0.3)	I	CS
Acetonitrile	TG (0.4)	TG (0.4)	I	tG
Glycerol (50%)	tG (0.7)	tG (0.4)	I	OG (1.3)
H_2O	tG (0.3)	OG (0.3)	I	OG (2.0)
PBS (pH 7.4)	OG (0.4)	OG (0.5)	VL	OG (2.0)

[a] TG - transparent gel; OG - opaque gel; tG - translucent gel; LG - loose gel; VL - viscous liquid; CS - clear solution; I - insoluble mass. Numbers in parentheses indicate the minimal gelation concentration (MGC, wt%).

concentrations less than 1 wt%, qualifying it as a supergelator (Table 2.2.1). The photographs of inverted vials containing organo- and hydrogels of CDP **4** are shown in Figure 2.2.1 (lower panel). Similar gelation properties of CDP **3** and **4** revealed that phenolic –OH has a minimal role in driving the gelation. The significance of ethylene linker on the side chain of CDPs (CDP **3** and **4**) was evaluated by carrying out the gelation studies of CDP **5** containing *L*-aspartic acid (methylene side chain) in place of *L*-glutamic acid (ethylene side chain). CDP **5** was found to be poor gelator as it formed a

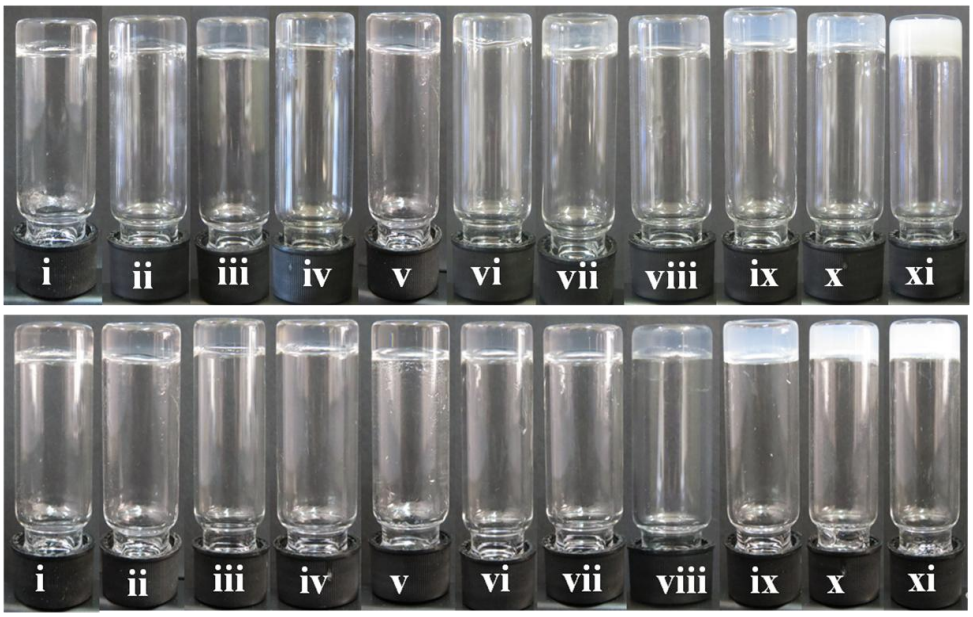

Figure 2.2.1 Photographs of organo- and hydrogels of CDP **3** (upper panel) and CDP **4** (lower panel) at their minimal gelation concentration under ambient conditions. i: toluene, ii: chloroform, iii: ethylacetate, iv: dichloromethane, v: 1,2-dichlorobenzene, vi: *tert*-butanol, vii: *sec*-butanol, viii: acetonitrile, ix: 50% glycerol, x: water and xi: 1X phosphate-buffered saline (PBS, pH 7.4).

loose gel only with aromatic solvent 1,2-dichlorobenzene at a very high concentration (45 mg/mL) (Table 2.2.1). Subsequently, we studied gelation propensity of CDP **6** with *L*-leucine to probe the role of aromatic interactions (as in the case of CDP **3** and **4**) in driving gelation. However, we kept the second amino acid (*L*-glutamic acid with Boc-protection) intact as in CDP **3** and **4**. The studies revealed poor gelation properties of CDP **6** compared to CDP **3** and **4**. However, CDP **6** showed relatively good gelation property compared to CDP **5** in terms of a number of solvents that can be gelled. CDP **6** gelates selectively aromatic solvents at lower concentrations and aqueous solvents at relatively higher concentrations (Table 2.2.1). Nevertheless, the gels formed from CDP **6** were found to be relatively less stable at ambient conditions.

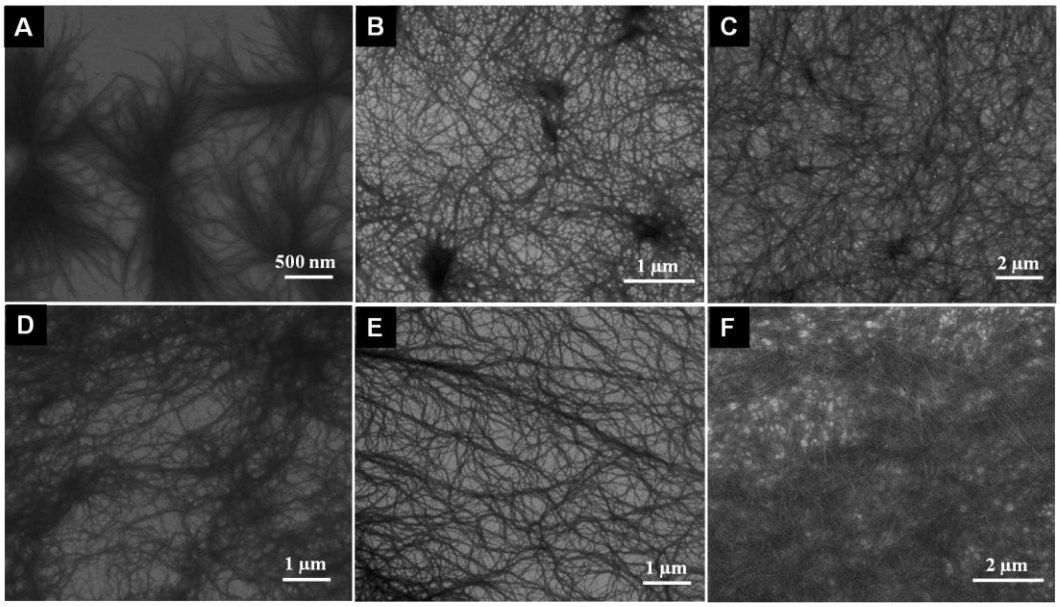

Figure 2.2.2 Self-assembled nanostructures of CDPs. FESEM images of CDP **3** xerogels in toluene (A), chloroform (B), water (C), CDP **4** xerogels in toluene (D), chloroform (E) and water (F).

The gelation study described above exemplified the significance of ethylene linker as in *L*-glutamic acid in facilitating the formation of LMWGs from the CDPs (**3**, **4**, **6**). The gelation ability of CDPs was further improved by the presence of aromatic moiety in the second amino acid, as evident from the excellent gelation properties of CDP **3** and **4** (Table 2.2.1) compared to CDP **6** which has aliphatic *L*-leucine. The Boc-deprotected CDPs with free carboxylic acid functionality (**3a**, **4a**, **5a,** and **6a**; Scheme 2.2.1-2.2.4) were found to be non-gelators in both organic and aqueous solvents under the similar gelation conditions studied at physiological pH and temperature in agreement with the earlier reports from literature.[83,84] Thus, we chose CDP **3** and **4** for further gel characterization, *in situ* gelation and cytocompatibility studies because of their ambidextrous supergelation properties.

2.2.2.3 FESEM analysis

The self-assembled nanostructures of CDPs encapsulate solvent molecules to form molecular gels were visualized by field emission scanning electron microscopy (FESEM). Figure 2.2.2 show the FESEM images of CDP **3** and **4** xerogels from toluene, chloroform, and water. CDP **3** toluene xerogel showed the presence of bundled fiber assemblies with nanometer fiber diameter and length of several microns (Figure 2.2.2A). The morphological analysis of CDP **3** xerogels in chloroform and water revealed the presence of interpenetrated 3D network of nanofibers (Figure 2.2.2B,C). Similarly, CDP **4** xerogels from toluene, chloroform and water showcased the presence of entangled 3D nanofiber networks (Figure 2.2.2D-F). The presence of extended nanostructure network in xerogel samples confirmed the noncovalent interaction driven self-assembly of CDPs in organic and aqueous solvents.

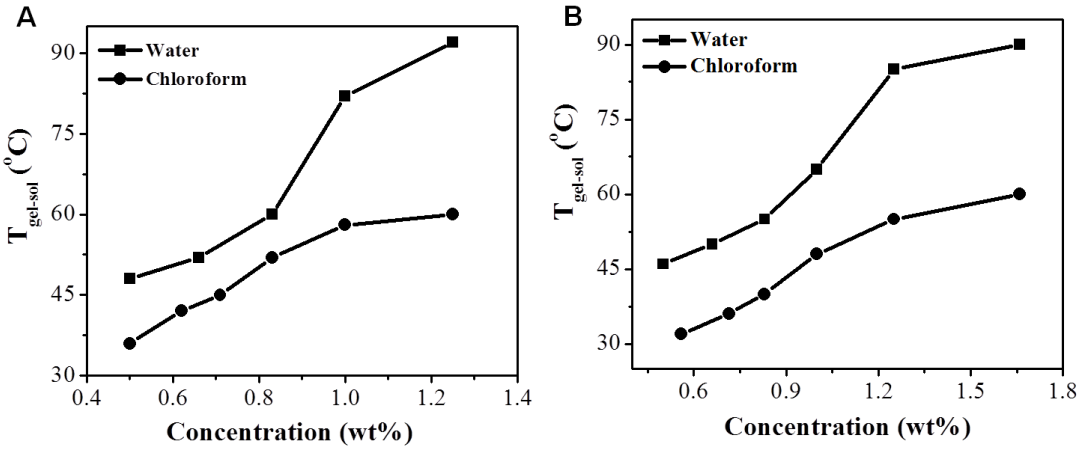

Figure 2.2.3 Thermal stability of CDP gels. Gel melting curves of CDP **3** (A), CDP **4** (B) organogels from chloroform and hydrogels at different concentrations.

2.2.2.4 Thermal stability of CDP gels

Thermal stability of CDP organogels (chloroform) and hydrogels (water) was evaluated by measuring the corresponding melting temperature (T_g) of gels prepared at various

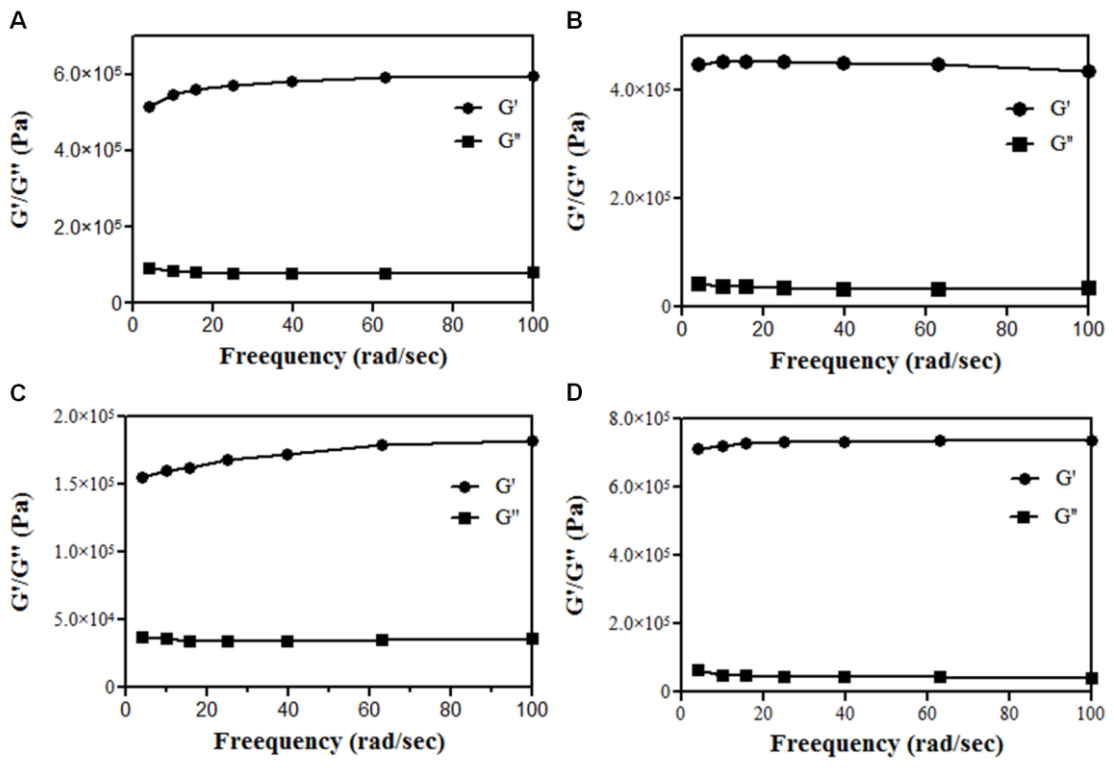

Figure 2.2.4 Visco-elastic properties of CDP gels. Storage (G') and loss modulus (G") of CDP **3** organogel (A) and hydrogel (B); CDP **4** organogel (C) and hydrogel (D). The frequency sweep measurements were carried at 1 wt% gel concentration and 0.1% strain under ambient conditions.

gelation concentrations (Figure 2.2.3**)**. A steady increase in T_g value with increase in CDP concentration was observed for both organo- and hydrogels of CDP **3** and **4**, indicating the presence of strong intermolecular interactions. High T_g values for CDP gels ascertained the presence of strong attractive interactions of gelators with solvent molecules.

2.2.2.5 Visco-elastic properties of CDP gels

The visco-elastic properties and physical strength of organo- and hydrogels of CDP **3** and **4** were evaluated by measuring the storage (G') and loss modulus (G") using oscillatory rheology measurements under ambient conditions. Frequency sweep experiments at 0.1%

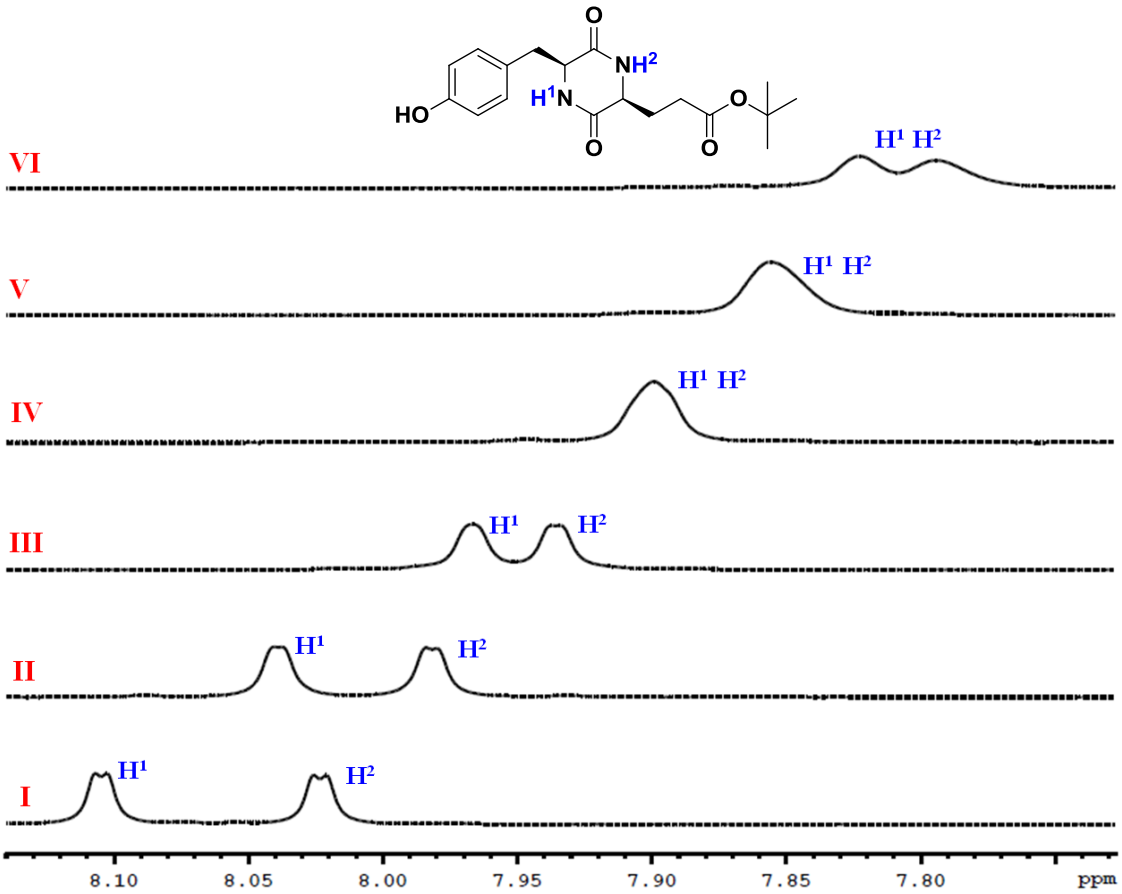

Figure 2.2.5 NMR studies of CDP **3**. Temperature dependent ^{1}H NMR spectra of CDP **3** in DMSO-d_6 at 57.4 mM concentration. I: 300 K, II: 310 K, III: 320 K, IV: 330 K, V: 340 K and VI: 350 K.

strain was conducted for 1 wt% CDP gels at room temperature. The storage modulus of CDP **3** organo- and hydrogels were found to be in the range of 10^4-10^5 Pa and were nearly one order greater than the corresponding loss modulus (Figure 2.2.4A, B). Similarly, organo- and hydrogels of CDP **4** exhibited one order higher G' than G'' (Figure 2.2.4C, D). Overall, the viscoelastic measurements showed that G' is greater than G" which confirmed the formation of strong CDP organo- and hydrogels.

2.2.2.6 NMR studies

The presence of strong intermolecular hydrogen bonding interactions, the major driving

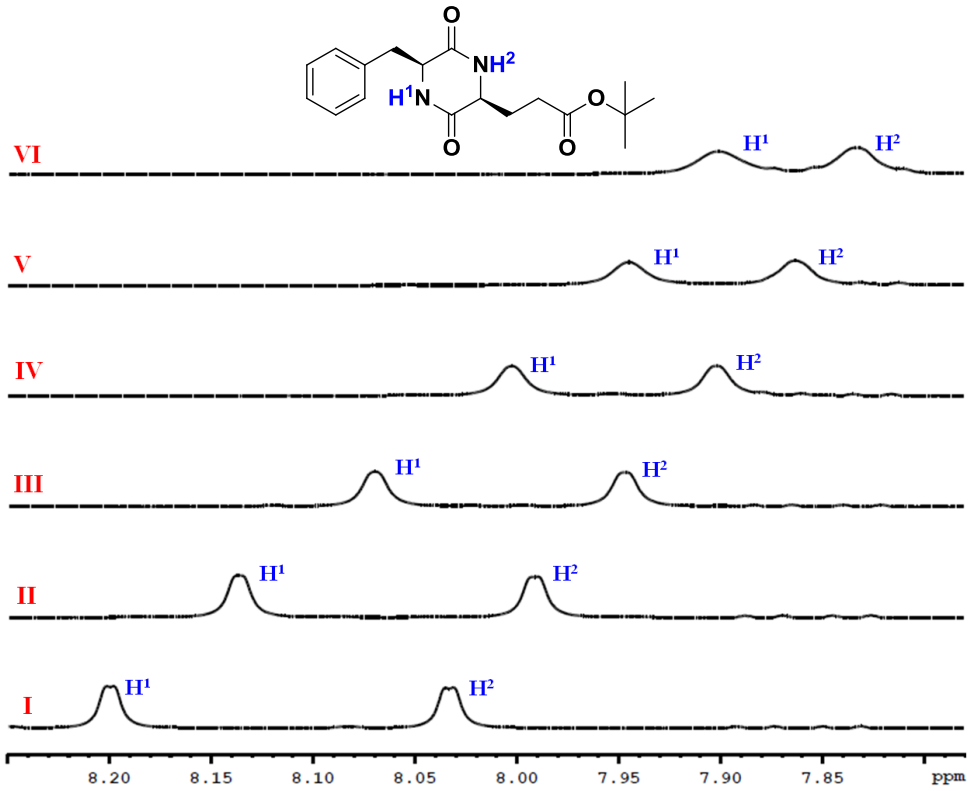

Figure 2.2.6 NMR studies of CDP **4**. Temperature dependent ^{1}H NMR spectra of CDP **4** in DMSO-d_6 at 31.9 mM concentration. I: 300 K, II: 310 K, III: 320 K, IV: 330 K, V: 340 K and VI: 350 K.

force for the self-assembly of CDPs was evaluated by the concentration and temperature-dependent ^{1}H NMR studies. ^{1}H NMR spectra of CDP **3** recorded in DMSO-d_6 at 300 K showed a marginal downfield shift of amide protons as a function of increased concentration from 3.18 to 28.7 mM (data not shown). The temperature-dependent ^{1}H NMR spectra of CDP **3** (57.4 mM) recorded at 300, 310, 320, 330, 340, 350 K showed an upfield shift of amide protons from 8.10 ppm to 7.78 ppm ($\Delta\delta$ = 0.31 ppm), 8.02 to 7.82 ppm ($\Delta\delta$ = 0.20 ppm) with an increase in temperature confirming the presence of strong intermolecular hydrogen bonding interactions (Figure 2.2.5). Similarly, amide protons of CDP **4** (31.8 mM) at 8.20 and 8.03 ppm upfield shifted to 7.90 ($\Delta\delta$ = 0.30 ppm) and 7.83 ppm ($\Delta\delta$ = 0.20 ppm) respectively as a function of increased temperature from 300 K to 350 K (Figure 2.2.6). Therefore, concentration and temperature dependent ^{1}H NMR

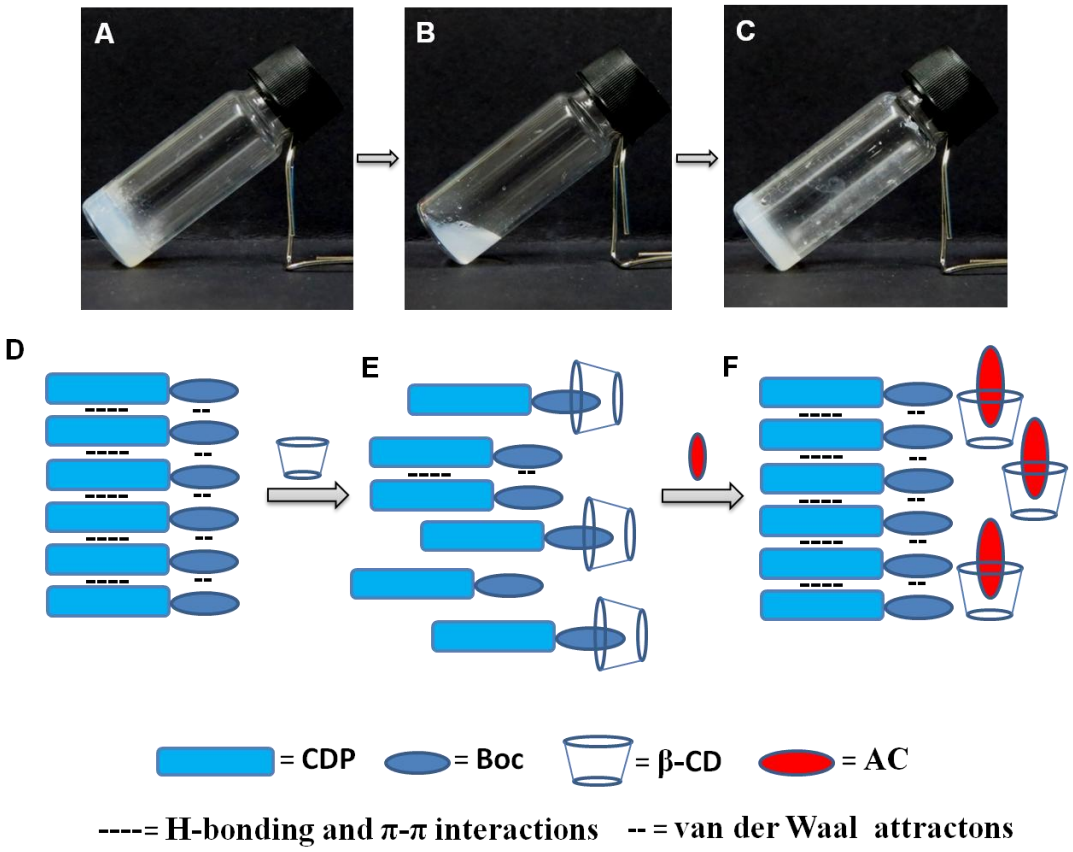

Figure 2.2.7 Host-guest induced reversible gelation studies of CDP **4**. Photographs of CDP **4** hydrogel (0.5 wt%) (A), transformed to sol after β-CD (50 mol%) addition (B) and reformed gel after the addition of AC (50 mol%) (C). Schematic representation of non-covalent molecular interactions in CDP **4** hydrogel (D), β-CD induced gel disruption by the host-guest interaction of β-CD and CDP **4** (E) and reformation of the gel by the addition of AC a known competitor to form stronger host-guest complex with β-CD. β-CD: beta-cyclodextrin, AC: 1-adamantane carboxylic acid.

spectroscopy analysis confirmed the presence of strong intermolecular hydrogen bonding in CDP **3** and **4**.

2.2.2.7 Host-guest interactions

The significant contribution of tertiary butyloxycarbonyl (Boc) moiety in driving the CDP hydrogelation through van der Waals interactions alongside hydrogen bonding of the core lactam ring was evaluated by using β-cyclodextrin (β-CD) based host-guest chemistry

experiments. β-Cyclodextrin was chosen as host to encapsulate CDP Boc-moiety. β-CD encapsulates selectively Boc-moiety over benzyl group, and 1-adamantane carboxylic acid (AC) was selected as competing guest to release the Boc-moiety from the β-CD cavity.[85] CDP **4** hydrogel (0.5 wt%) turned to sol upon the addition of β-CD (50 mol% of gel) and further attempts to convert it to gel were unsuccessful even after 24 h of incubation under the studied experimental conditions (Figure 2.2.7A, B). However, the hydrogel was effectively restored by the addition of competing guest such as AC (50 mol% of gel), which can release the bound CDP **4** by replacing Boc-moiety encapsulated in the β-CD cavity and re-facilitating the self-assembly of CDPs followed by gelation (Figure 2.2.7C). The loss of gelation ability upon the addition of β-CD indicates the host-guest complexation of CDP **4** with β-CD through the encapsulation of Boc-moiety in the β-CD cavity. This host-guest complexation was further confirmed by the recovery of gelation ability upon addition of competing guest AC to the sol as depicted in Figure 2.2.7D-F). Overall, the β-CD-CDP **4** host-guest study confirmed the contribution of Boc-moiety in driving the molecular gelation of CDPs (**3** and **4**) and further explains the inability of CDPs with free carboxylic acid groups (**3a** and **4a**) to form molecular gels.

2.2.2.8 *In situ* gelation studies

The ability to form *in situ* gels was evaluated by studying the gelation of CDPs upon injecting their *N*-methyl-2-pyrrolidone (NMP) solutions into PBS (10 mM, pH 7.4, 37 ºC). NMP was chosen as the preferred solvent to dissolve the CDPs and for *in situ* gelation studies because of its proven biocompatibility (FDA approved) and established use in subcutaneous injection formulations (ELIGARD™).[71-73] The concentration of CDPs in NMP was optimized to achieve *in situ* gelation upon injection into a vial containing PBS at 37 ºC. CDP **3** failed to form *in situ* gelation even at very high

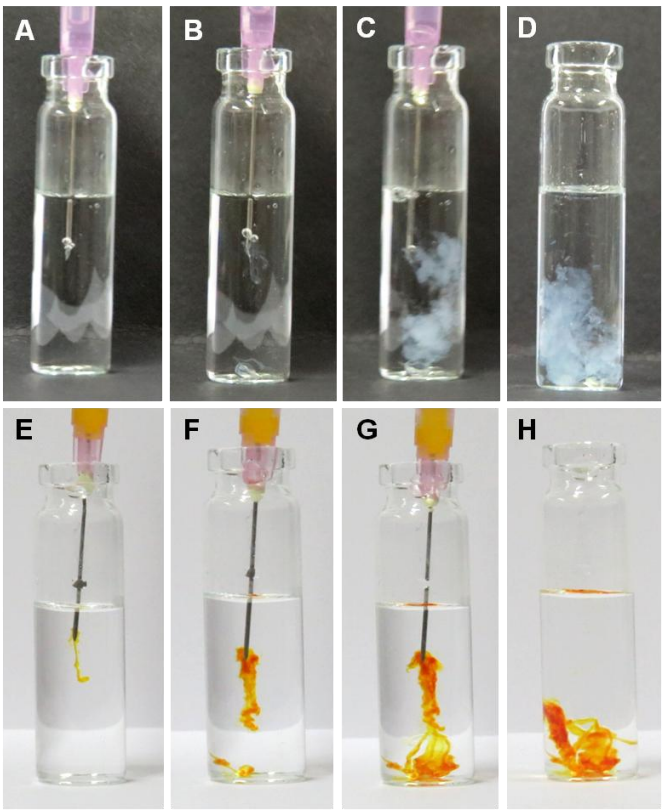

Figure 2.2.8 I*n-situ* gelation studies of CDP **4**. Photographs showing the formation of (A-D) pristine and (E-H) curcumin loaded (10 wt% of CDP) hydrogels of CDP **4** (2.8 wt%) in PBS (10 mM, pH 7.4, 37 ºC).

concentrations studied. On the other hand, CDP **4** (2.8 wt% in NMP) instantaneously formed a gel upon injection into PBS solution using a commercially available syringe (Figure 2.2.8A-D), and the solid gel formed in solution was found to be stable for months under ambient conditions. The inability of CDP **3** to form gels *in situ* is attributed to the differential self-assembly patterns of peptides containing phenylalanine and tyrosine, because of the variation in electron density on the side chain aromatic group (-H on Phe; -OH on Tyr).[86] The possible application of CDP **4** for the parenteral administration of biologically important molecules was demonstrated by loading hydrophobic curcumin, an anticancer molecule and the propensity for *in situ* gelation was studied. As shown in Figure 2.2.8E-H curcumin (10 wt% of CDP) loaded CDP **4** instantaneously formed *in situ*

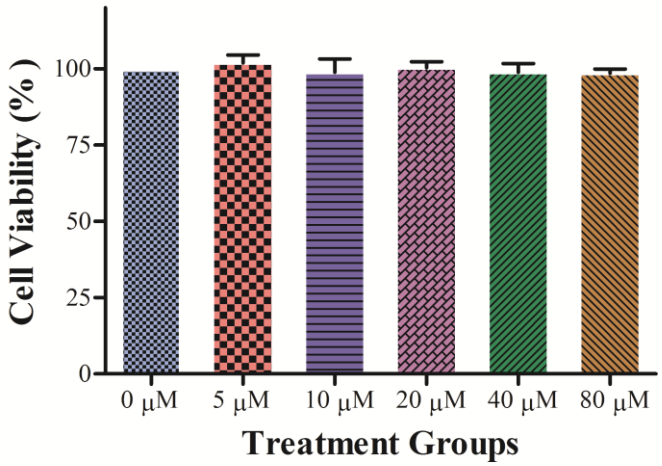

Figure 2.2.9 Cytocompatibility of CDP **4** studied in murine PC12 cells. MTT assay results showing % of viable cells treated with different concentration of CDP **4** for 24 h. All data points represent mean ± SD (n=3). MTT: 3-(4,5-dimethylthiazol-2-yl)-2,5-diphenyltetrazolium bromide.

gels in PBS solution upon injection. The ability of CDP **4** to form *in situ* gels alone and with loaded cargo (Figure 2.2.8A-H) highlighted its potential use for parenteral administration of drugs and biomolecules. The *in situ* formed gels may be employed as the local depot of drugs and biomolecules for their controlled and sustained long term release.

2.2.2.9 Cytotoxicity study

The cytocompatibility of CDP **4** was evaluated by mitochondrial activity 3(4,5-dimethylthiazol-2-yl)-2,5-diphenyltetrazolium bromide (MTT) assay in murine adrenal medulla derived PC12 (pheochromocytoma) cells. The metabolic activity of PC12 cells in presence of different concentrations of CDP **4** was assessed. Figure 2.2.9 show the results of cytotoxicity studies in PC12 cells treated with different concentration of CDP **4** after 24 h in culture. The viability of cells treated with CDP **4** for 24 h was found to comparable to the untreated control cells (Figure 2.2.9). The PC12 cells treated with CDP

4 showed >95% viability and hence confirmed its cytocompatible nature. Thus, the cytotoxicity study has clearly demonstrated that CDP **4** is a potential candidate for the applications involving live cells.

2.2.3 Conclusion

In summary, CDPs were designed by the minimalistic rational approach to obtain low molecular weight organic gelators. The significance of each functional moiety of CDP in driving the gelation is demonstrated in a range of organic- and aqueous solvents through structure-gelation studies. CDP **3** and **4** with optimal structural units were found to be the best gelator molecules. The self-assembly of CDPs into nanofibrous networks resulted in the formation of molecular gels as shown by vial inversion gelation experiments and scanning electron microscopy study. Concentration and variable temperature-dependent ^{1}H NMR studies were performed to demonstrate the presence of strong intermolecular hydrogen bonding which leads to the formation 3D network of nanofibers, which in turn encapsulates the solvent molecules to form a gel. The viscoelastic and thermal stability measurements asserted the formation stable organo- and hydrogels. Among all the CDPs, **4** found to be the supergelator in both organic- and aqueous solvents with *in situ* hydrogelation ability. The cytocompatibility of supergelator CDP **4** was demonstrated using murine brain PC12 cells *in vitro*. The ability of a small molecule to form *in situ* gels upon injection from their organic solutions under physiological temperature and pH in case of CDPs was demonstrated with CDP **4**. Further, we have successfully shown that bioactive molecules like curcumin can be loaded and used for *in situ* gelation, which is useful in creating local depots for long-term drug release. The ambidextrous supergelation and *in situ* hydrogelation ability of CDP **4** and associated good cytocompatibility may find potential applications in drug delivery and tissue engineering applications. This study

may inspire the design of injectable molecular supergelators for numerous biomedical applications.

2.2.4 Experimental Section

Materials. Fmoc-protected amino acids were obtained from Novabiochem, coupling reagents and other chemicals were obtained from Spectrochem India. All the solvents used for synthesis and gelation studies were spectroscopic grade and used as received from Spectrochem (India) without any further purification. Milli-Q water was used for extractions during synthesis, for gelation studies, and for the preparation of phosphate buffered saline (PBS) solutions. Thin Layer Chromatography (TLC) was performed using TLC Silica gel 60 F254 silica plates from Merck and visualization of the compounds was achieved using UV light (254 and 365 nm) and ninhydrin treatment. Purification of compounds by column chromatography was carried using 60-120 mesh Silica gel obtained from ACME chemicals.

NMR spectroscopy. ^{1}H and ^{13}C NMR spectra were recorded on a Bruker AV-400 spectrometer in $CDCl_3$, DMSO-d_6 or D_2O at 300 K. Chemical shifts (δ) are reported in parts per million (ppm) with respect to residual solvent peak and coupling constant (*J*) values are reported in hertz (Hz). The multiplicity of NMR signal are represented as s = singlet, d = doublet, t = triplet, q = quartet, dd = doublet of doublet and m = multiplet.

NMR experiments. Concentration-dependent ^{1}H NMR experiments of CDPs were performed by recording the NMR spectra with various defined concentrations of CDPs at 300 K in DMSO-d_6. Variable-temperature ^{1}H NMR (VT-NMR) experiments for CDPs were performed at temperatures 300, 310, 320, 330, 340 and 350 K using DMSO-d_6 as solvent at a specified concentration.

Elemental analysis. Elemental analysis of vacuum dried CDPs was carried out on a Thermo Scientific FLASH 2000 organic element analyzer.

Mass spectrometry (MS). Mass spectra were obtained on a Bruker Ultraflex II MALDI-TOF spectrometer and high resolution mass spectra (HRMS) were recorded on Agilent 6538 UHD HRMS/Q-TOF spectrometer either in acetonitrile or methanol using positive ion electrospray ionization method.

Absorption spectroscopy. UV-vis spectra were recorded on a Perkin Elmer Model Lambda 900 spectrophotometer. CDP solutions at specified concentrations were analyzed using a quartz cuvette of 10 mm path length under ambient conditions.

Fluorescence spectroscopy. Fluorescence spectra were recorded on a Perkin Elmer Model LS 55 spectrophotometer. CDP solutions at specified concentrations were analyzed using a quartz cuvette of 10 mm path length with the mentioned excitation and emission wavelengths under ambient conditions.

Preparation of CDP gels. CDP organogels were prepared using the heating-cooling method. Briefly, organogels of CDPs were prepared by dispersing the specified amount of CDP in one centimeter cube (1 mL) organic solvent and heated to get a clear solution. The obtained clear solution was cooled to room temperature under ambient conditions. The ability of CDPs to form gels was eventually determined qualitatively by inversion tube method. Upon the vial inversion, if there is no solvent flow under gravity the sample is assigned as a gel. Hydrogels were prepared by dissolving CDPs in DMSO (<10 vol%) at high concentration and then diluting to the required concentration using the aqueous solvents (water, PBS buffer, 50% glycerol). The obtained loose gels (semi-gels) were heated to get a clear solution and the resulting clear solution was allowed to cool to room temperature and the gelation was confirmed by inversion tube method.

Determination of minimal gelation concentration. Minimal gelation concentration (MGC) of organo- and hydrogels of CDPs were measured by preparing the gels at high concentration (1 wt%) and diluting the gels to a concentration where no gelation is observed through inversion tube method.

Determination of gel melting temperature. The gel melting temperature (T_g) was measured for varying gel concentrations in organic ($CHCl_3$) and aqueous (water) solvents using inversion tube method. Briefly, CDP organo-, hydrogel vials were immersed in a water bath and heated 5 min at each temperature measured and the temperature at which the gel started melting was assigned as its T_g, for each gel studied. It is to be noted that 15-30 min of heating is required at T_g to completely convert the gel to sol.

Rheology studies. The visco-elastic properties of CDP gels were characterized using oscillatory rheometry analysis. CDP gels (organo- and hydrogels) at 1 wt% gel concentration were placed in the gap between cone and plate of the rheometer (Anton Paar MCR 52) and the amplitude sweep between 0.1 rad/sec to 100 rad/sec was carried out at a fixed amplitude of 0.1% under ambient conditions.

Field emission scanning electron microscopy. Samples for field emission electron microscopy (FESEM) analysis were prepared by placing an aliquot of the CDP hot clear solution onto a clean, one side polished single crystalline silicon(111) surface, dried at ambient conditions overnight and then under vacuum before sample analysis. Microscopic imaging at nanoscale was carried out using FESEM, FEI Nova nanoSEM-600 equipped with field emission gun operating at 5 kV.

***In situ* gelation studies**. CDP gelators from *N*-methyl-2-pyrrolidone (NMP) were injected into phosphate buffered saline (PBS; pH 7.4, 37 ºC) at indicated concentrations using commercially available, disposable syringes under ambient conditions. The

formation of solid (gel-like) mass was evaluated through visual inspection. Similarly, drug loaded *in situ* gelation was studied by using a physical mixing of curcumin (10 wt% of CDP) with CDP **4** in NMP.

Cell culture. Murine adrenal medulla derived PC12 cells were used to evaluate the cytocompatibility of CDP **4**. The cells from cryopreserved stock were revived and grown in complete growth medium containing Roswell Park Memorial Institute (RPMI, Gibco) 1640 media supplemented with 10% heat-inactivated horse serum, 5% fetal bovine serum (Gibco), 1% antibiotic-antimycotic solution (Sigma). Cell cultures were maintained at 37 ºC, 95% humidity and 5% CO_2 using a humidified CO_2 incubator and the culture media was changed every alternate day of culture. Cells were detached from the tissue culture flasks upon reaching 70-80% of the confluence using 0.05% trypsin-EDTA (Gibco) and harvested by neutralizing with the complete media and centrifugation at 1500 rpm for 5 min. The cells were then subcultured for further use as required.

Cell viability studies. The cytotoxicity of CDP **4** was evaluated by measuring the viability of PC12 cells treated with increasing concentrations (0-80 µM) for 24 h in culture. MTT interacts with mitochondria of live cells and the resulting change in the optical density give the number of live cells. Approximately $l0^4$ cells/well were seeded into 96 well plate and incubated for 24 h in humidified CO_2 incubator. 10% MTT (5mg/mL, Sigma) reagent was added and incubated for 3 h at 37 ºC. The purple colored formazan crystals formed were solubilized using high purity DMSO (Merck) and the intensity of color was measured by recording the optical density (570 nm with 690 nm reference) using a microplate reader (Infinite® 200 PRO, TECAN). The measured optical intensity of CDP **4** treated cells containing wells in comparison to the control wells received only complete media gives the percentage of cell viability.

Preparation of Fmoc-*L*-Lys(Boc)-Gly-OCH_3 (1). Fmoc-*L*-Lys(*t*Boc)-OH (200.0 mg, 0.42 mmol), hydroxybenzotrizole (68.0 mg, 0.51 mmol) and 1-ethyl-3-(3-dimethylaminopropyl)carbodiimide hydrochloride (EDC. HCl; 98.0 mg, 0.51 mmol) were dissolved in dichloromethane (DCM; 8 mL) and cooled to 0 ºC. Glycine methyl ester hydrochloride (53.0 mg, 0.42 mmol) and *N*,*N*-diisopropylethylamine (DIPEA; 176.0 mg, 1.36 mmol) were added and the reaction mixture was stirred at ice cold temperature for 1 h and then at room temperature for 5 h. The reaction progress was monitored by thin layer chromatography (TLC). Reaction mixture was evaporated to dryness and extracted from dichloromethane, washed with water, dried over anhydrous sodium sulfate and purified using silicagel coloumn chromatography with MeOH/$CHCl_3$ (v/v: 0.8/99.2) as eluent to obtain **1** in quantitative yield (218.0 mg, 92%). ^{1}H NMR ($CDCl_3$, 400 MHz) δ_{ppm} 1.43 (s, 3H), 1.50 (b, 4H), 1.70 (s, 3H), 1.88 (s, 1H), 3.10-3.11 (d, *J* = 5.2 Hz, 2H), 3.73 (s, 3H), 4.03 (s, 2H), 4.19-4.22 (t, *J* = 6.4 Hz, 2H), 4.40 (s, 2H), 4.65 (s, 2H), 5.52 (s, 1H), 6.68 (s, 1H), 7.28-7.32 (dt, *J* = 7.6 Hz, *J* = 0.8 Hz, 2H), 7.37-7.41 (t, *J* = 7.6 Hz, 2H), 7.58-7.59 (d, *J* = 7.2 Hz, 2H), 7.75-7.76 (d, *J* = 7.6 Hz, 2H); ^{13}C NMR ($CDCl_3$, 100 MHz) δ_{ppm} 22.4, 28.5, 29.7, 32.0, 39.9, 41.2, 47.3, 52.5, 54.8, 67.2, 79.3, 120.1, 125.2, 127.2, 127.8, 141.4, 143.9, 156.3, 170.1, 172.1.

Preparation of *cyclo*(*L*-Lys(*t*Boc)-Gly) (CDP 1): The linear dipeptide Fmoc-*L*-Lys(*t*Boc)-Gly-OCH_3 (**1**) (200.0 mg, 0.37 mmol) was dissolved in piperidine-DCM (v/v, 20:80, 6 mL) and stirred at room temperature for 24 h and the reaction progress was monitored by thin layer chromatography. Reaction mixture was evaporated to dryness and purified using silicagel coloumn chromatography with MeOH/$CHCl_3$ (v/v: 1.6/98.4) as eluent to obtain CDP **1** in quantitative yield (65.0 mg, 62%). ^{1}H NMR (DMSO-d_6, 400 MHz). δ_{ppm} 1.20-1.33 (m, 4H), 1.36 (s, 9H), 1.59-168 (m, 2H), 2.86-2.91 (q, *J* = 2 Hz, 2H), 3.62-3.79 (m, 3H), 6.74-6.77 (t, *J* = 4.8 Hz, 1H), 7.97 (s, 1H), 8.14 (s, 1H); 13C

NMR (DMSO-d_6, 100 MHz) δ_{ppm} 21.3, 28.2, 29.2, 32.4, 44.2, 54.0, 77.3, 166.6, 167.9; MALDI-TOF-MS = m/z 288. 39 $[M+3H]^+$; Elemental analysis. Found: C 54.75, H 8.15, N 14.75, O 22.35; Calcd: C 54.72, H 8.12, N 14.73, O 22.43 for $C_{13}H_{23}N_3O_4$.

Preparation of *cyclo*(*L*-Lys-Gly) (2). *cyclo*(*L*-Lys(*t*Boc)-Gly) (CDP **1**) (100.0 mg, 0.35 mmol) was dissolved in trifluoroacetic acid-water (TFA; v/v, 1:1, 6 mL) and catalytic amount of triisopropylsilane (TIPS) was added and the resulting reaction mixture was stirred at room temperature for 4 h. The reaction progress was monitored by thin layer chromatography. Reaction mixture was evaporated to dryness and co-evaporated with toluene to obtain **2** in quantitative yield (99.0 mg, 95%). ^{1}H NMR (DMSO-d_6, 400 MHz) δ_{ppm} 1.27-1.490 (m, 2H), 1.50-1.62 (m, 2H), 1.63-1.74 (m, 2H), 3.66-3.80 (m, 3H), 7.74 (s, 3H), 8.01 (s, 1H), 8.51 (s, 1H); ^{13}C NMR (DMSO-d_6, 100 MHz) δ_{ppm} 20.9, 26.7, 32.1, 43.6, 44.2, 53.8, 166.0, 167.8.

Preparation of *cyclo*(*L*-Lys(Fmoc)-Gly) (CDP 2). Sodium hydrogen carbonate (56.0 mg, 0.66 mmol) was added to *cyclo*(*L*-Lys-Gly) (**2**) (100.0 mg, 0.33 mmol) in water (5 mL) and cooled to ice cold temperature. *N*-(9-Fluorenylmethoxycarbonyloxy) succinimide (Fmoc-OSu; 135.0 mg, 0.40 mmol) in 1,4-dioxane (5 mL) was added drop wise to the above solution over a period of 30 min under ice cold conditions. The resultant solution was stirred at 0 ºC for 30 min, then at room temperature for 4 h. Reaction progress was monitored by thin layer chromatography. The resultant solution was washed with ethylacetate thrice. Combined layers of ethylacetate were back extracted with saturated sodium hydrogen carbonate solution. Combined layers of sodium hydrogen carbonate, aqueous layers were combined and acidified to pH 1 using 10% HCl. The acidified solution was thrice extracted into ethylacetate, combined layers of ethylacetate were dried over anhydrous sodium sulfate evaporated to dryness and purified using

silicagel coloumn chromatography with MeOH/$CHCl_3$ (v/v: 1.8/98.2) as eluent to obtain CDP **2** in quantitative yield (130.0 mg, 96%). ^{1}H NMR (DMSO-d_6, 400 MHz) δ_{ppm} 1.23-1.42 (m, 2H), 1.59-1.70 (m, 2H), 2.94-2.99 (q, *J* = 6.4 Hz), 3.64-3.81 (m, 3H), 4.19-4.22 (t, *J* = 6.8 Hz, 1H), 4.28-4.30 (d, *J* = 6.8 Hz, 2H), 7.26-7.29 (t, *J* = 11.2 Hz, 1H), 7.31-7.35 (dt, *J* = 7.6 Hz, J = 1.2Hz, 2H), 7.39-7.43 (t, *J* = 7.6 Hz, 2H), 7.67-7.69 (d, *J* = 7.2 Hz), 7.88-7.89 (d, *J* = 7.6 Hz, 2H), 7.93 (s, 1H), 8.16 (s, 1H); ^{13}C NMR (DMSO-d_6, 100 MHz) δ_{ppm} 21.3, 29.0, 32.4, 44.2, 46.7, 54.0, 65.1, 120.1, 125.1, 127.0, 127.5, 140.7, 143.9, 156.0, 166.1, 167.9 ; MALDI-TOF-MS = *m/z* 430.18 $[M+Na]^+$, 446.16 $[M+K]^+$. Elemental analysis. Found: C 67.78, H 6.12, N 10.28, O 15.82; Calcd: C 67.80, H 6.18, N 10.31, O 15.71 for $C_{23}H_{25}N_3O_4$.

Preparation of Fmoc-*L*-Glu(OtBu)-*L*-Tyr-OCH_3 (4). Fmoc-*L*-Glu(OtBu)-OH (1.0 g, 2.4 mmol), 1-(3-dimethylaminopropyl)-3-ethylcarbodiimide hydrochloride (EDC. HCl; 0.75 g, 3.8 mmol), hydroxybenzotrizole (HOBt; 0.52 g, 3.8 mmol) and were dissolved in dichloromethane (40 mL) at ice cold temperature. *L*-Tyrosine methyl ester hydrochloride (**3**) (0.6 g, 2.6 mmol) and *N*,*N*-diisopropylethylamine (DIPEA; 0.92 g, 7.1 mmol) were added and the reaction mixture was stirred at ice cold temperature for 1 h and then continued at room temperature for 4 h. TLC was used to check the progress of reaction. Reaction mixture was evaporated to dryness and residue was extracted from dichloromethane, washed with water, dried over anhydrous sodium sulphate. Solvent was evaporated under vacuum and the crude product was purified on silicagel column chromatography with $CH_3OH/CHCl_3$ (v/v: 1.2/98.8) as eluent to obtain **4** as a white powder in moderate yield (0.71 g, 50%). ^{1}H NMR ($CDCl_3$, 400 MHz) δ_{ppm} 1.44 (s, 9H), 1.86-2.09 (m, 2H), 2.28-2.41 (m, 2H), 2.96-3.10 (m, 2H), 3.71 (s, 3H), 4.17-4.21 (m, 2H) 4.30-4.40 (m, 2H) 4.76-4.81 (m, 1H), 5.48 (b, 1H), 5.68 (b, 1H), 6.64-6.67 (d, *J* = 8.4 Hz, 2H), 6.82 (b, 1H), 6.93-6.95 (d, *J* = 8.04 Hz, 2H), 7.28-7.32 (t, *J* = 7. 44 Hz, 2H), 7.37-

7.41 (t, *J* = 7.4 Hz, 2H), 7.57-7.58 (m, 2H), 7.75-7.76 (d, *J* = 7.6 Hz, 2H); ^{13}C NMR ($CDCl_3$, 100 MHz) δ_{ppm} 28.2, 31.7, 37.1, 47.2, 52.5, 53.6, 54.2, 67.3, 81.3, 115.7, 120.1, 125.2, 127.2, 127.4, 127.8, 130.4, 141.4, 141.4, 143.9, 155.2, 171.2, 171.8, 173.0.

Preperation of *cyclo*(*L*-Glu(OtBu)-*L*-Tyr) (CDP 3). The linear dipeptide Fmoc-*L*-Glu(OtBu)-*L*-Tyr-OCH_3 (**4**) (0.4 g, 0.6 mmol) was dissolved in piperidine-DCM (v/v, 20:80, 10 mL) and stirred at room temperature for 12 h. TLC was used to monitor the progress of reaction. Solvent was evaporated under vacuum and the crude product was purified on silicagel column chromatography using $CH_3OH/CHCl_3$ (v/v: 4.0/96) as eluent to obtain CDP **3** as a white powder in good yield (0.18 g, 78%). ^{1}H NMR (DMSO-d_6, 400 MHz) δ_{ppm} 1.12-1.21 (m, 1H), 1.31-1.33 (m, 1H), 1.36 (s, 9H), 1.65-1.70 (m, 2H), 2.69-2.74 (dd, *J* = 4.76 Hz, 1H), 2.99-3.04 (dd, *J* = 3.8 Hz, 1H), 3.67-3.69 (m, 1H), 4.08-4.09 (m, 1H), 6.61-6.64 (d, *J* = 8.52 Hz, 2H), 6.91-6.93 (d, *J* = 8.48 Hz, 2H), 8.02 (b, 1H), 8.10 (b, 1H), 9.11 (s, 1H); ^{13}C NMR (DMSO-d_6, 100 MHz) δ_{ppm} 27.6, 28.6, 29.7, 37.1, 53.0, 55.4, 79.3, 114.7, 125.8, 131.1, 156. 3, 166.3, 166.4, 171.5. HRMS: m/z Found: 371.1563 $[M+Na]^+$, Calcd: 371.1583 $[M+Na]^+$. Elemental analysis. Found: C, 58.10; H, 6.45; N, 7.84; Calc: C, 58.21; H, 6.51; N, 7.54 for $C_{18}H_{24}N_2O_5$.

Preperation of *cyclo*(*L*-Glu-*L*-Tyr) (CDP 3a). *Cyclo*(*L*-Glu(OtBu)-*L*-Phe) (CDP **3**) (100.0 mg, 0.28 mmol) was dissolved in trifluoroacetic acid-water (v/v, 1:1 6 mL) at ice cold temperature and catalytic amount of triisopropylsilane (TIPS) was added to the resulting mixture. The reaction was then carried at room temperature for 4 h under N_2 atmosphere. TLC was used to monitor the progress of reaction. The obtained reaction mixture was evaporated to dryness and co-evaporated with toluene to obtain CDP **3a** in quantitative yield (80.5 mg, 96%). ^{1}H NMR(DMSO-d_6, 400 MHz) δ_{ppm} 1.13-1.23 (m, 1H), 1.31-1.40 (m, 1H), 1.80-1.84 (m, 2H), 2.71-2.76 (dd, *J* = 4.76 Hz, 1H), 2.97-3.02

(dd, *J* = 4.04 Hz, 1H), 3.68-3.70 (m, 1H), 4.07 (b, 1H), 6.62-6.64 (d, *J* = 8.4 Hz, 2H), 6.92-6.94 (d, *J* = 8.44 Hz, 2H), 8.04 (b, 1H), 8.6 (b, 1H); ^{13}C NMR (DMSO-d_6, 100 MHz) δ_{ppm} 17.8, 19.2, 28.6, 37.3, 53.0, 55.4, 114.7, 125.9, 131.0, 156.2, 166.5, 166.7, 173.7.

Preparation of Fmoc-*L*-Glu(OtBu)-*L*-Phe-OCH$_3$ (6). Fmoc-*L*-Glu(OtBu)-OH (1.50 g, 3.5 mmol), 1-(3-dimethylaminopropyl)-3-ethylcarbodiimide hydrochloride (EDC. HCl; 1.15 g, 5.82 mmol), hydroxybenzotrizole (HOBt; 0.79 g, 5.82 mmol) and were dissolved in dichloromethane (60 mL) at ice cold temperature. *L*-Phenylalanine methyl ester hydrochloride (**5**) (0.84 g, 3.9 mmol) and *N*,*N*-diisopropylethylamine (DIPEA; 1.4 g, 10.6 mmol) were added and the reaction mixture was stirred at ice cold temperature for 1 h and then continued at room temperature for 4 h. Thin layer chromatography (TLC) was used to monitor the progress of reaction. Reaction mixture was evaporated to dryness and residue was extracted from dichloromethane, washed with water, dried over anhydrous sodium sulphate. Solvent was evaporated under vacuum and the crude product was purified on silicagel column chromatography with $CH_3OH/CHCl_3$ (v/v, 0.8/99.2) as eluent to obtain peptide **6** as a white crystaline powder in very good yield (1.82 g, 88%). ^{1}H NMR ($CDCl_3$, 400 MHz) δ_{ppm} 1.44 (s, 9H), 1.87-1.94 (m, 1H), 2.01-2.08 (m, 1H), 2.31-2.43 (m, 2H), 3.04-3.18 (m, 2H), 3.71 (s, 3H), 4.18-4.22 (m, 2H), 4.35-4.37 (m, 2H), 4.81-4.86 (m, 1H), 5.65 (b, 1H), 6.79 (b, 1H), 7.10-7.121 (d, *J* = 7 Hz, 2 H), 7.19-7.24 (m, 3H), 7.29-7.33 (t, *J* = 7.84 Hz, 2 H), 7.38-7.42 (t, *J* = 7.44 Hz, 2H), 7.58-7.59 (d, *J* = 7.28 Hz, 2H), 7.75-7.77 (d, *J* = 7.52 Hz, 2H); ^{13}C NMR ($CDCl_3$, 100 MHz) δ_{ppm} 28.2, 28.3, 29.8, 31.7, 37.9, 47.2, 52.5, 53.5, 54.2, 67.3, 77.3, 81.2, 120.1, 125.2, 127.2, 127.3, 127.8, 128.7, 129.3, 135.8, 141.4, 143.9, 143.9, 171.0, 171.7, 173.0.

Preperation of *cyclo*(*L*-Glu(OtBu)-*L*-Phe) (CDP 4). The linear dipeptide Fmoc-*L*-Glu(OtBu)-*L*-Phe-OCH_3 (**6**) (1.6 g, 2.7 mmol) was dissolved in piperidine-DCM (v/v,

20:80, 30 mL) and stirred magnetically at room temperature for 12 h. TLC was used to monitor the progress of reaction. Solvent was evaporated under vacuum and the crude product was purified on silicagel column chromatography using $CH_3OH/CHCl_3$ (v/v, 4.0/96) as eluent to obtain CDP **4** as a white powder in good yield (0.64 g, 72%). ^{1}H NMR (DMSO-d_6, 400 MHz) δ_{ppm} 1.00-1.09 (m, 1H), 1.19-1.28 (m, 1H), 1.36 (s, 9H), 1.51-1.56 (m, 2H), 2.81-2.85 (dd, *J* = 4.92 Hz, 1H), 3.13-3.17 (dd, *J* = 3.68 Hz, 1H), 3.65-3.68 (m, 1H), 4.18-4.20 (m, 1H), 7.14-7.27 (m, 5H), 8.02 (b, 1H), 8.19 (b, 1H); ^{13}C NMR (DMSO-d_6, 100 MHz) δ_{ppm} 27.6, 28.4, 29.4, 37.9, 52.9, 55.2, 79.2, 126.7, 127.9, 130.2, 135.9, 166.0, 166.3, 171.4. HRMS: m/*z* Found: 355.1615 $[M+Na]^+$, Calcd: 355.1634 $[M+Na]^+$. Elemental analysis. Found: C, 60.65; H, 6.88; N, 8.10; Calcd: C, 60.83; H, 6.81; N, 7.88 for $C_{18}H_{24}N_2O_4$.

Preperation of *cyclo*(*L*-Glu-*L*-Phe) (CDP 4a). *Cyclo*(*L*-Glu(OtBu)-*L*-Phe) (CDP **4**) (100.0 mg, 0.30 mmol) was dissolved in trifluoroacetic acid-water (v/v, 1:1 6 mL) at ice cold temperature and catalytic amount of triisopropylsilane (TIPS) was added to the resulting mixture. The reaction was then carried at room temperature for 4 h under N_2 atmosphere. TLC was used to monitor the progress of reaction. The obtained reaction mixture was evaporated to dryness and co-evaporated with toluene to obtain CDP **4a** in quantitative yield (80.0 mg, 95%). ^{1}H NMR(DMSO-d_6, 400 MHz) δ_{ppm} 0.95-1.1 (m, 1H), 1.23-1.33 (m, 1H), 1.67-1.72 (m, 2H), 2.83-2.88 (dd, *J* = 4.9 Hz, 1H), 3.10-3.15 (dd, *J* = 3.92 Hz, 1H), 3.66-3.69 (m, 1H), 4.17-4.18 (m, 1H), 7.15-7.27 (m, 5H), 8.07 (b, 1H), 8.13 (b, 1H); ^{13}C NMR (DMSO-d_6, 100 MHz) δ = 28.6, 28.7, 37.9, 53.0, 55.2, 126.7, 127.9, 130.1, 136.0, 166.2, 166.6, 173.9.

Preparation of Fmoc-*L*-Asp(OtBu)-*L*-Phe-OCH_3 (8). Fmoc-*L*-Asp(OtBu)-OH (1.0 g, 2.4 mmol), 1-(3-dimethylaminopropyl)-3-ethylcarbodiimide hydrochloride (EDC. HCl;

0.75 g, 3.8 mmol), hydroxybenzotrizole (HOBt; 0.52 g, 3.8 mmol) and were dissolved in dichloromethane (40 mL) at ice cold temperature. *L*-Phenylalanine methyl ester hydrochloride (**7**) (0.6 g, 2.6 mmol) and *N*,*N*-diisopropylethylamine (DIPEA; 0.92 g, 7.1 mmol) were added and the reaction mixture was stirred at ice cold temperature for 1 h and then continued at room temperature for 4 h. Reaction progress was monitered by thin layer chromatography. Reaction mixture was evaporated to dryness and residue was extracted from dichloromethane, washed with water, dried over anhydrous sodium sulphate. Solvent was evaporated under vacuum and the crude product was purified on silicagel column chromatography with $CH_3OH/CHCl_3$ (v/v: 1.2/98.8) as eluent to obtain peptide **8** as a white powder in good yield (1.1 g, 79%). ^{1}H NMR ($CDCl_3$, 400 MHz) δ_{ppm} 1.44 (s, 9H), 2.58-2.64 (dd, *J* = 6.7 Hz, 1H), 2.86-2.91 (dd, *J* = 3.76 Hz, 1H), 3.05-3.16 (m, 2H), 3.69 (s, 3H), 4.20-4.23 (m, 1H), 4.33-4.42 (m, 2H), 4.54-4.55 (m, 1H), 4.79-4.84 (m, 1H), 5.93-5.95 (b, 1H), 7.02-7.03 (b, 1H), 7.13-7.15 (m, 2H), 7.20-7.33 (m, 5H), 7.39-7.42 (t, *J* = 7.44 Hz, 2H), 7.56-7.58 (d, *J* = 7.4 Hz, 2H), 7.76-7.78 (d, *J* = 7.56 Hz, 2H); ^{13}C NMR ($CDCl_3$, 100 MHz) δ_{ppm} 28.1, 37.4, 37.8, 47.2, 51.0, 52.3, 53.6, 67.4, 77.3, 82.0, 120.1, 125.1, 125.2, 127.2, 127.2, 127.8, 128.7, 129.3, 135.8, 141.4, 143.8, 143.8, 156.0, 170.3, 171.3, 171.4.

Preparation of *cyclo*(*L*-Asp(OtBu)-*L*-Phe) (CDP 5). The linear dipeptide Fmoc-*L*-Asp(OtBu)-*L*-Phe-OCH_3 (**8**) (0.4 g, 0.7 mmol) was dissolved in piperidine-DCM (v/v, 20:80, 10 mL) and stirred at room temperature for 12 h. Reaction progress was monitered by thin layer chromatography. Solvent was evaporated under vacuum and the crude product was purified on silicagel column chromatography using $CH_3OH/CHCl_3$ (v/v: 2.4/97.6) as eluent to obtain CDP **5** as a white powder in good yield (0.16 g, 75%). ^{1}H NMR (DMSO-d_6, 400 MHz) δ_{ppm} 1.35 (s, 9H), 1.53-1.58 (dd, *J* = 6.64 Hz, 1H), 1.79-1.84 (dd, *J* = 6.24 Hz, 1H), 2.89-2.93 (dd, *J* = 4.92 Hz, 1H), 3.07-3.12 (dd, *J* = 4.28 Hz, 1H),

3.96-3.99 (m, 1H), 4.20-4.22 (m, 1H), 7.16-7.30 (m, 5H), 7.90 (b, 1H), 8.12 (b, 1H); ^{13}C NMR (DMSO-d_6, 100 MHz) δ_{ppm} 27.6, 37.9, 38.8, 51.0, 55.2, 80.0, 126.6, 128.1, 130.1, 136.2, 166.5, 168.8. HRMS: m/z Found: 341.1457 $[M+Na]^+$, Calcd: 341.1477 $[M+Na]^+$. Elemental analysis. Found: C, 59.53; H, 6.68; N, 8.32; Calcd: C, 59.81; H, 6.50; N, 7.21 for $C_{17}H_{22}N_2O_4$.

Preparation of *cyclo*(*L*-Asp-*L*-Phe) (CDP 5a). *Cyclo*(*L*-Asp(OtBu)-*L*-Phe) (CDP **5**) (100.0 mg, 0.31 mmol) was dissolved in trifluoroacetic acid-water (v/v, 1:1, 6 mL) at ice cold temperature and catalytic amount of triisopropylsilane (TIPS) was added to the resulting mixture. The reaction was then carried at room temperature for 4 h under N_2 atmosphere. Reaction progress was monitered by thin layer chromatography. The obtained reaction mixture was evaporated to dryness and co-evaporated with toluene to obtain CDP **5a** in quantitative yield (78.5 mg, 95%). ^{1}H NMR(DMSO-d_6, 400 MHz) δ_{ppm} 1.53-1.59 (dd, *J* = 7 Hz, 1H), 2.01-2.06 (dd, *J* = 5.4 Hz, 1H), 2.90-2.95 (dd, *J* = 4.9 Hz, 1H), 3.07-3.11 (dd, *J* = 4.4 Hz, 1H), 4.01-4.04 (m, 1H), 4.19-4.22 (m, 1H), 7.17-7.30 (m, 5H), 7.86 (b, 1H), 8.11 (b, 1H), 12.25 (b, 1H); ^{13}C NMR (DMSO-d_6, 100 MHz) δ_{ppm} 37.8, 37.9, 50.9, 55.1, 126.6, 128.0, 130.0, 136.2, 166.4, 166.6, 171.3.

Preparation of Fmoc-*L*-Glu(OtBu)-*L*-Leu-OCH$_3$ (10). Fmoc-*L*-Glu(OtBu)-OH (1.0 g, 2.35 mmol), 1-(3-dimethylaminopropyl)-3-ethylcarbodiimide hydrochloride (EDC. HCl; 0.69 g, 3.6 mmol), hydroxybenzotrizole (HOBt; 0.48 g, 3.6 mmol) and were dissolved in dichloromethane (40 mL) at ice cold temperature. *L*-Leucine methyl ester hydrochloride (0.47 g, 2.6 mmol) and *N*,*N*-diisopropylethylamine (DIPEA; 0.92 g, 7.1 mmol) were added and the reaction mixture was stirred at ice cold temperature for 1 h and then continued at room temperature for 4 h. Reaction progress was monitered by thin layer chromatography. Reaction mixture was evaporated to dryness and residue was extracted

from dichloromethane, washed with water, dried over anhydrous sodium sulphate. Solvent was evaporated under vacuum and the crude product was purified on silicagel column chromatography with $CH_3OH/CHCl_3$ (v/v: 1.1/98.9) as eluent to obtain peptide **10** as a white powder in very good yield (1.17 g, 90%). ^{1}H NMR ($CDCl_3$, 400 MHz) δ_{ppm} 0.91-0.93 (d, *J* = 6.1 Hz, 6H), 1.46 (s, 9H), 1.54-1.68 (m, 3H), 1.90-1.99 (m, 1H), 2.05-2.13 (m, 1H), 2.39-2.49 (m, 2H), 3.72 (s, 3H), 4.19-4.30 (m, 2H), 4.36-4.38 (m, 2H), 4.55-4.61 (m, 1H), 5.72 (b, 1H), 6.81 (b, 1H), 7.29-7.32 (t, *J* = 7.4 Hz, 2H), 7.37-7.41 (t, *J* = 7.4 Hz, 2H), 7.58-7.60 (d, *J* = 7.4 Hz, 2H), 7.75-7.77 (d, *J* = 7.5 Hz, 2H); ^{13}C NMR ($CDCl_3$, 100 MHz) δ_{ppm} 21.9, 22.9, 25.0, 28.2, 28.6, 31.7, 41.3, 47.2, 51.1, 52.4, 54.0, 67.3, 81.3, 120.1, 125.2, 127.2, 127.8, 141.4, 141.4, 143.9, 144.0, 156.2, 171.2, 173.1, 173.2.

Preperation of *cyclo*(*L*-Glu(OtBu)-*L*-Leu) (CDP 6). The linear dipeptide Fmoc-*L*-Glu(OtBu)-*L*-Leu-OCH_3 (**10**) (0.4 g, 0.72 mmol) was dissolved in piperidine-DCM (v/v, 20:80, 10 mL) and stirred at room temperature for 12 h. Reaction progress was monitered by thin layer chromatography. Solvent was evaporated under vacuum and the crude product was purified on silicagel column chromatography using $CH_3OH/CHCl_3$ (v/v: 1.8/98.2) as eluent to obtain CDP **6** as a white powder in good yield (0.17 g, 80%). ^{1}H NMR (DMSO-d_6, 400 MHz) δ_{ppm} 0.84-0.89 (dd, *J* = 6.6 Hz, 6H), 1.39 (s, 9H), 1.42-1.49 (m, 1H), 1.57-1.64 (m, 1H), 1.77-1.86 (m, 2H), 1.89-1.98 (m, 1H), 2.27-2.31 (m, 2H), 3.73-3.76 (m, 1H), 3.79-3.82 (m, 1H), 8.10 (b, 1H), 8.19 (b, 1H); ^{13}C NMR (DMSO-d_6, 100 MHz) δppm 21.7, 22.9, 23.5, 27.7, 28.8, 30.6, 43.0, 52.5, 53.3, 79.6, 167.5, 168.4, 171.5. HRMS: m/*z* Found: 321.1769 $[M+Na]^+$, Calcd: 321.1790 $[M+Na]^+$. Elemental analysis. Found: C, 56.03; H, 8.18; N, 8.96; Calcd: C, 56.06; H, 8.15; N, 8.72 for $C_{15}H_{26}N_2O_4$.

Preperation of *cyclo*(*L*-Glu-*L*-Leu) (CDP 6a). *Cyclo*(*L*-Glu(OtBu)-*L*-Leu) (CDP **6**) (100.0 mg, 0.33 mmol) was dissolved in trifluoroacetic acid-water (v/v, 1:1, 6 mL) at ice cold temperature and catalytic amount of triisopropylsilane (TIPS) was added to the resulting mixture. The reaction was then carried at room temperature for 4 h under N_2 atmosphere. Reaction progress was monitered by thin layer chromatography. The obtained reaction mixture was evaporated to dryness and co-evaporated with toluene to obtain CDP **6a** in quantitative yield (88.0 mg, 96%). ^{1}H NMR(DMSO-d_6, 400 MHz) δ_{ppm} 0.84-0.89 (dd, J = 6.6 Hz, 6H), 1.42-1.49 (m, 1H), 1.57-1.64 (m, 1H), 1.77-1.86 (m, 2H), 1.90-1.99 (m, 1H), 2.30-2.36 (m, 2H), 3.73-3.77 (m, 1H), 3.80-3.83 (m, 1H), 8.13 (b, 1H), 8.18 (b, 1H); ^{13}C NMR (DMSO d_6, 100 MHz) δ_{ppm} 21.7, 22.9, 23.6, 28.7, 29.4, 42.9, 52.5, 53.3, 167.7, 168.5, 173.7.

2.2.5 Appendix

- ^{1}H NMR and ^{13}C NMR spectra of CDP **1**
- ^{1}H NMR and ^{13}C NMR spectra of CDP **2**
- ^{1}H NMR and ^{13}C NMR spectra of CDP **3**
- ^{1}H NMR and ^{13}C NMR spectra of CDP **4**
- ^{1}H NMR and ^{13}C NMR spectra of CDP **5**
- ^{1}H NMR and ^{13}C NMR spectra of CDP **6**

^{1}H NMR spectrum of CDP 1

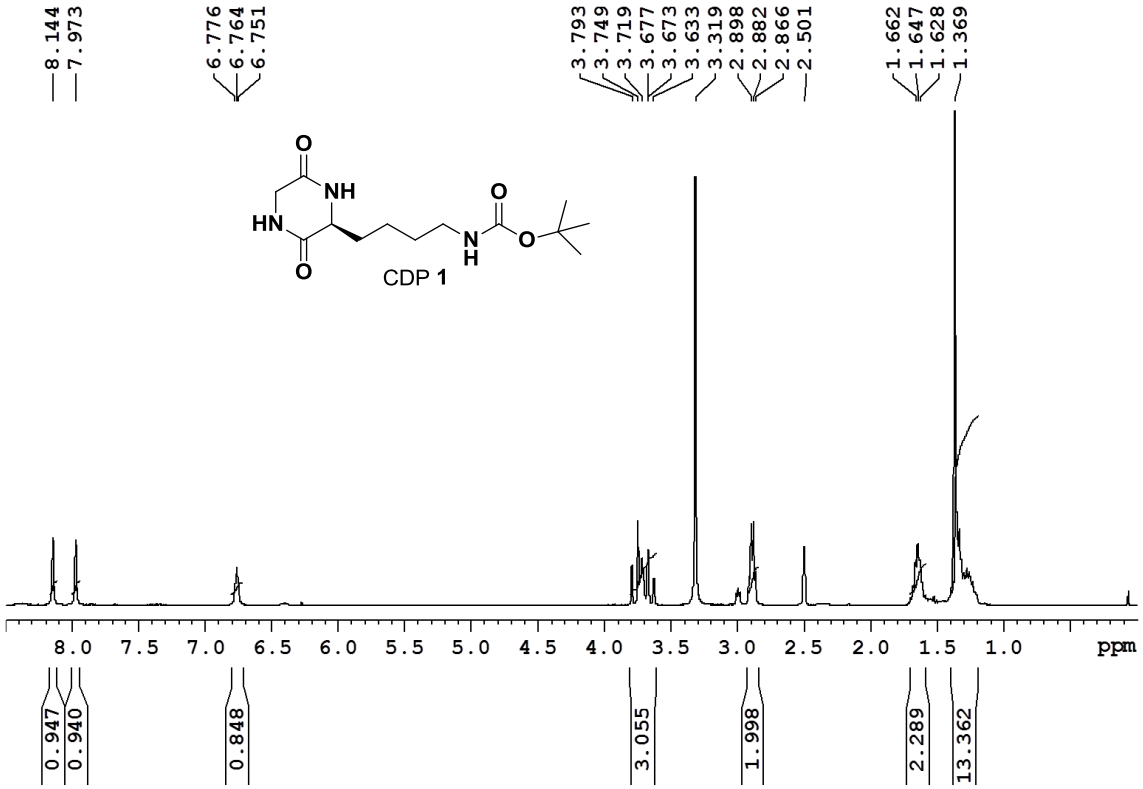

^{13}C NMR spectrum of CDP 1

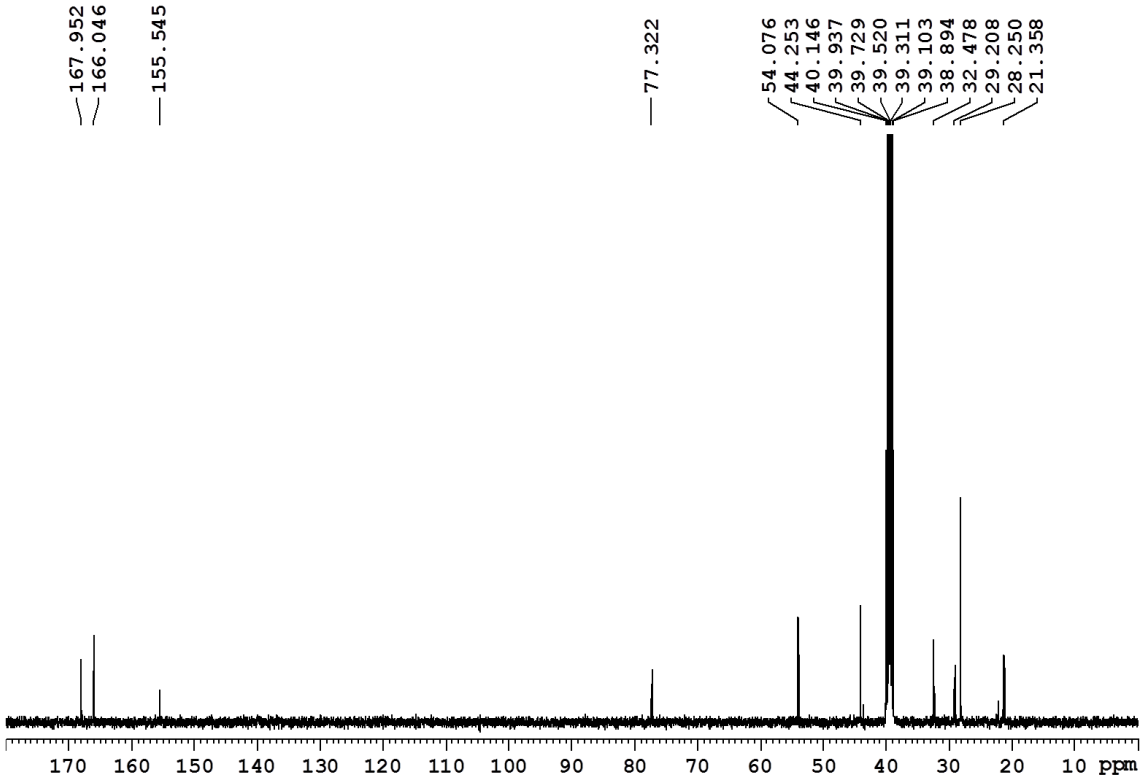

^{1}H NMR spectrum of CDP 2

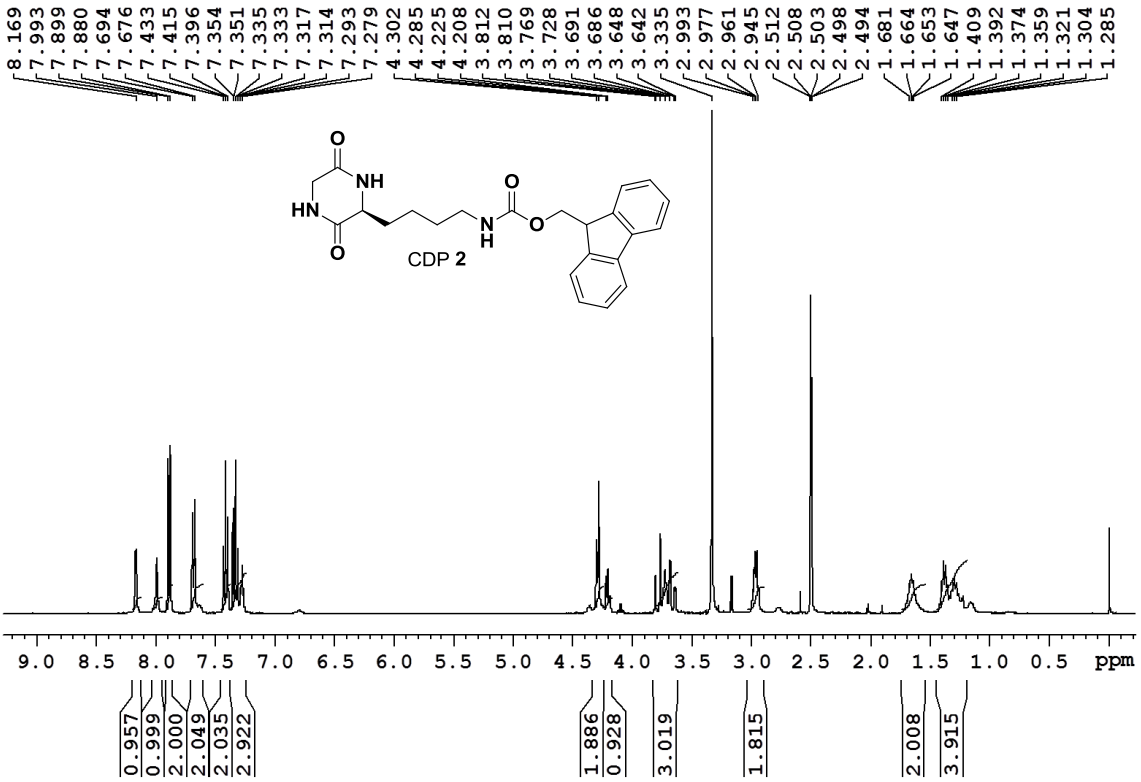

^{13}C NMR spectrum of CDP 2

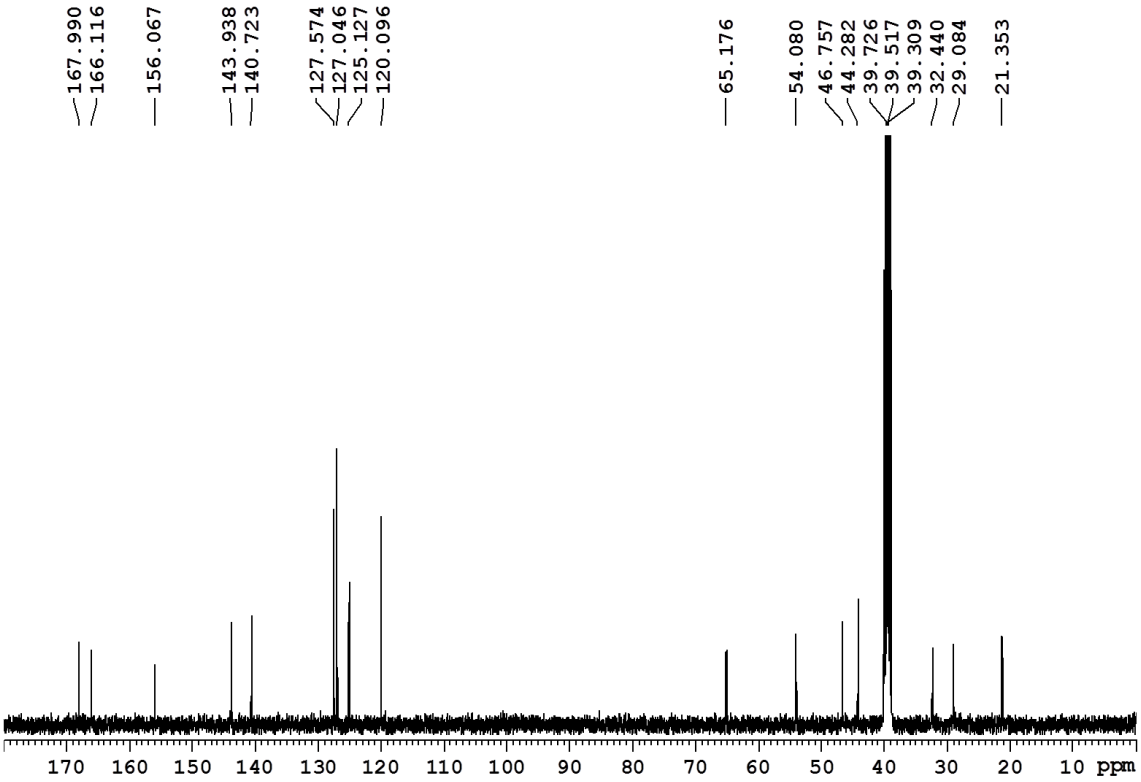

^{1}H NMR spectrum of CDP 3

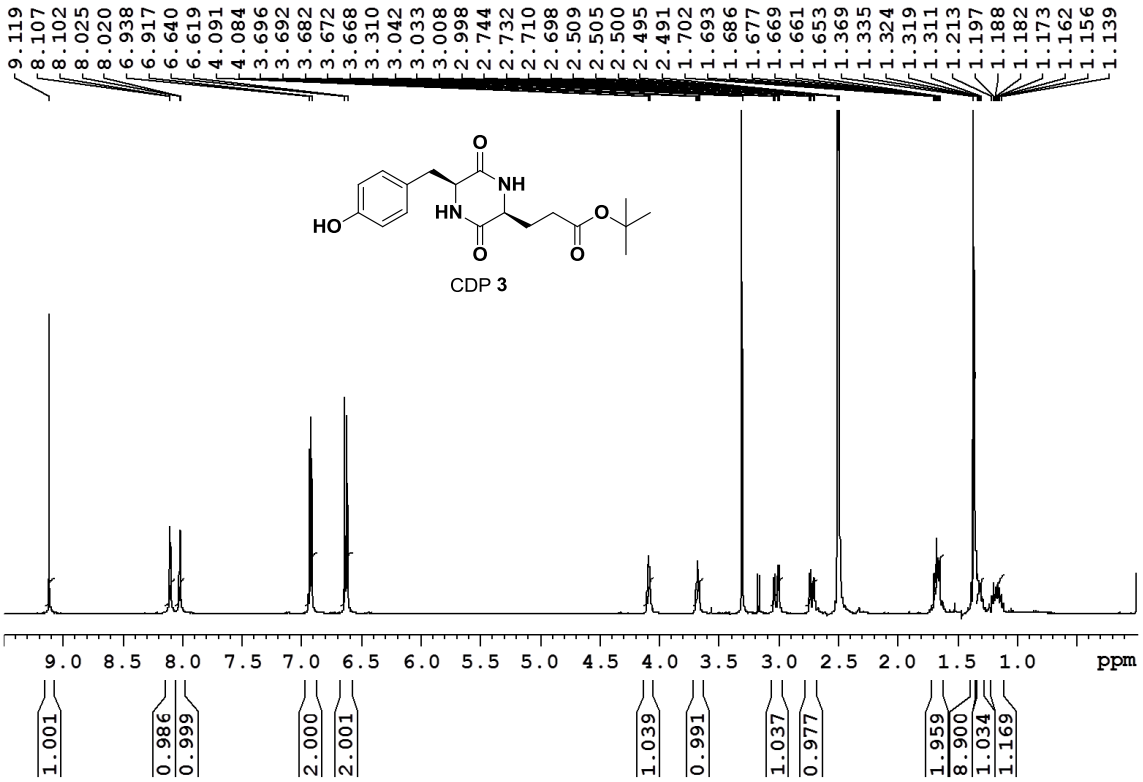

^{13}C NMR spectrum of CDP 3

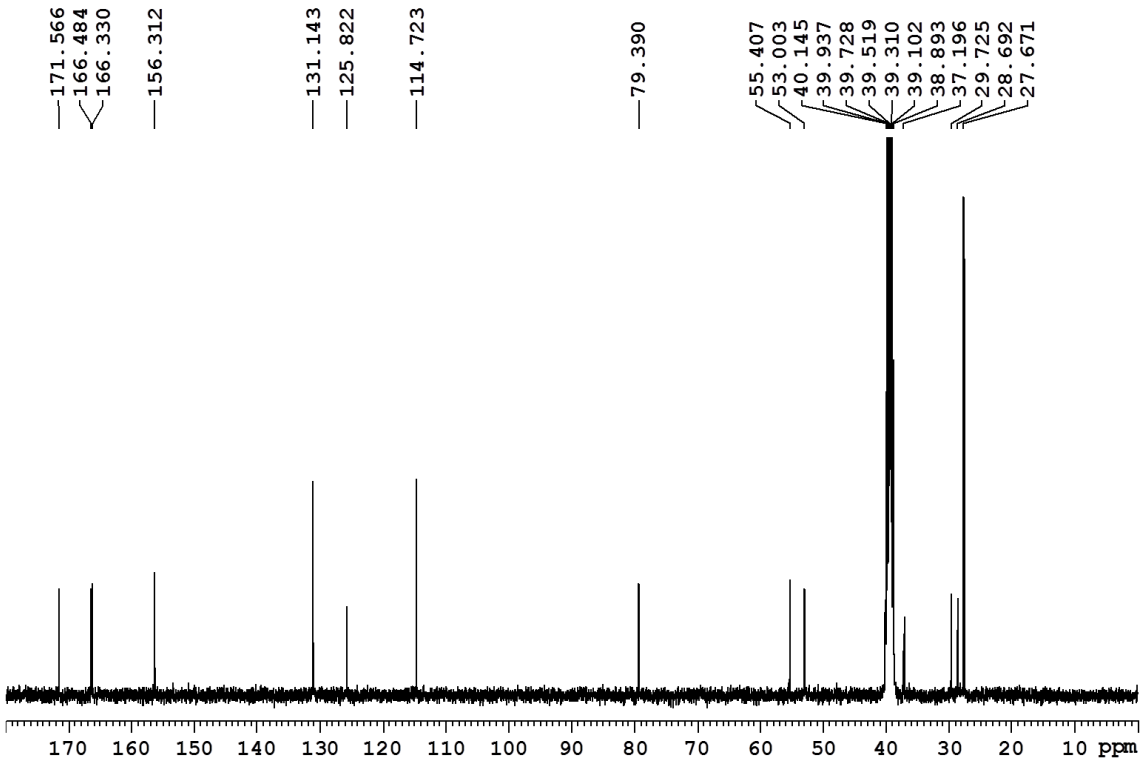

^{1}H NMR spectrum of CDP 4

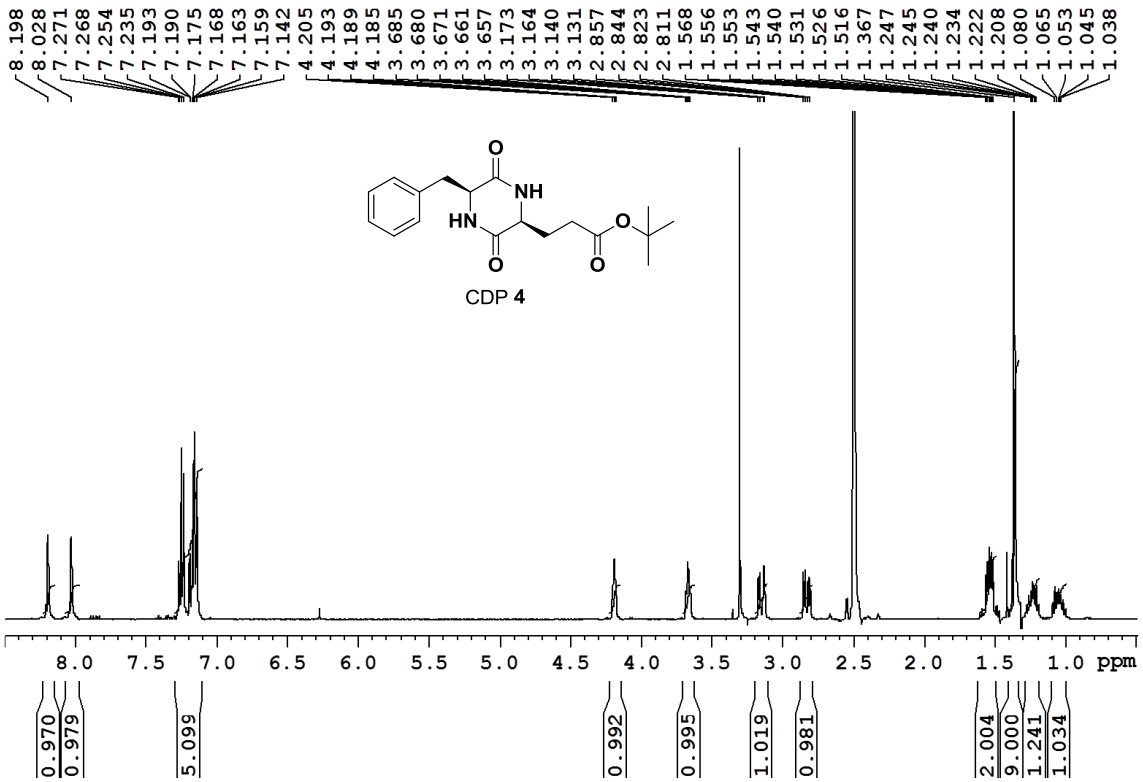

^{13}C NMR spectrum of CDP 4

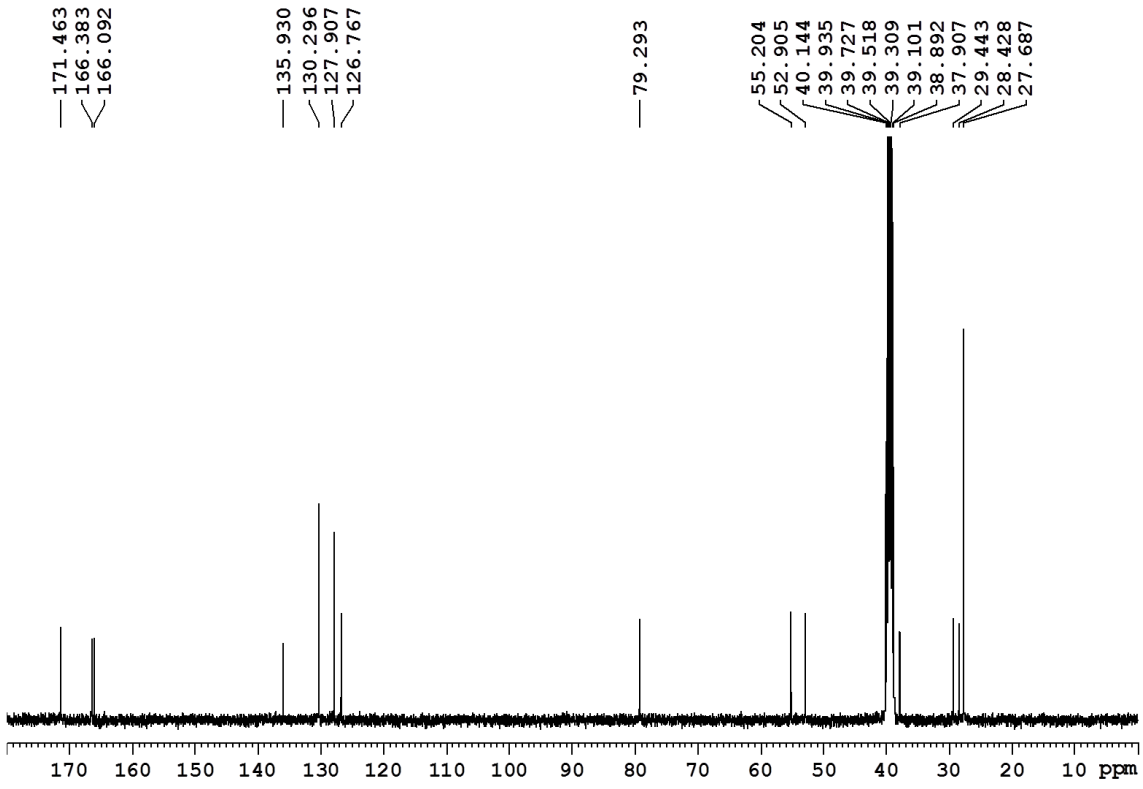

^{1}H NMR spectrum of CDP 5

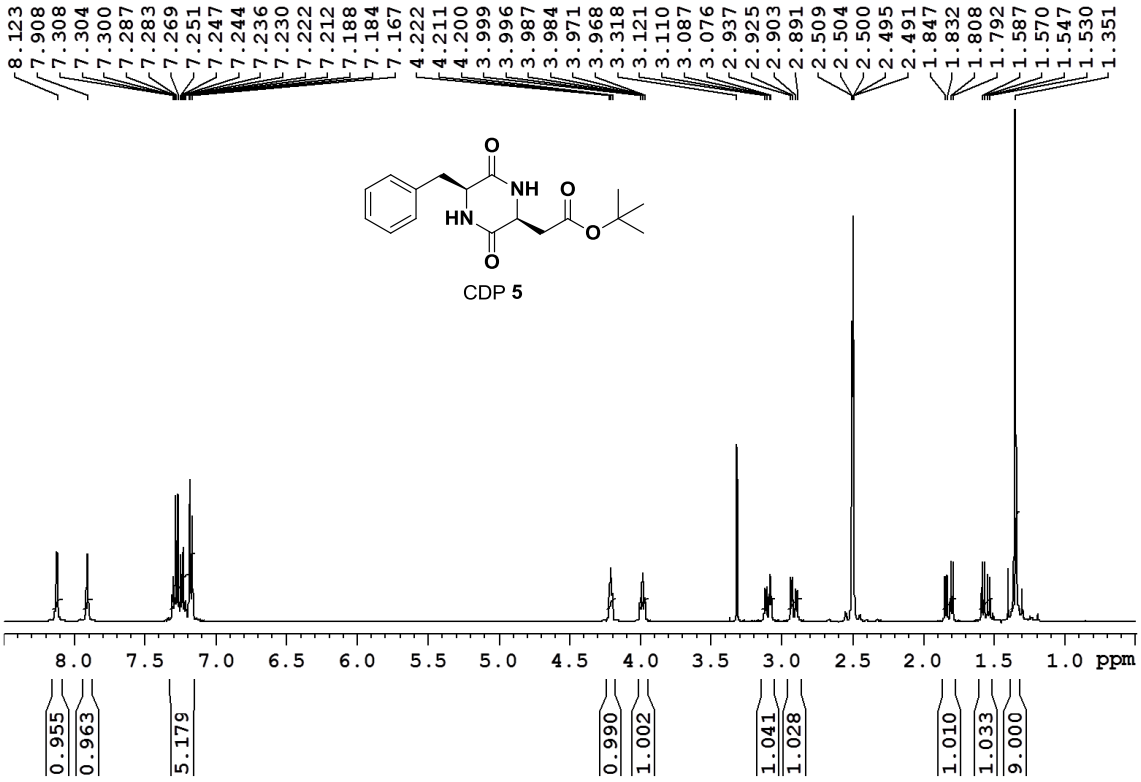

^{13}C NMR spectrum of CDP 5

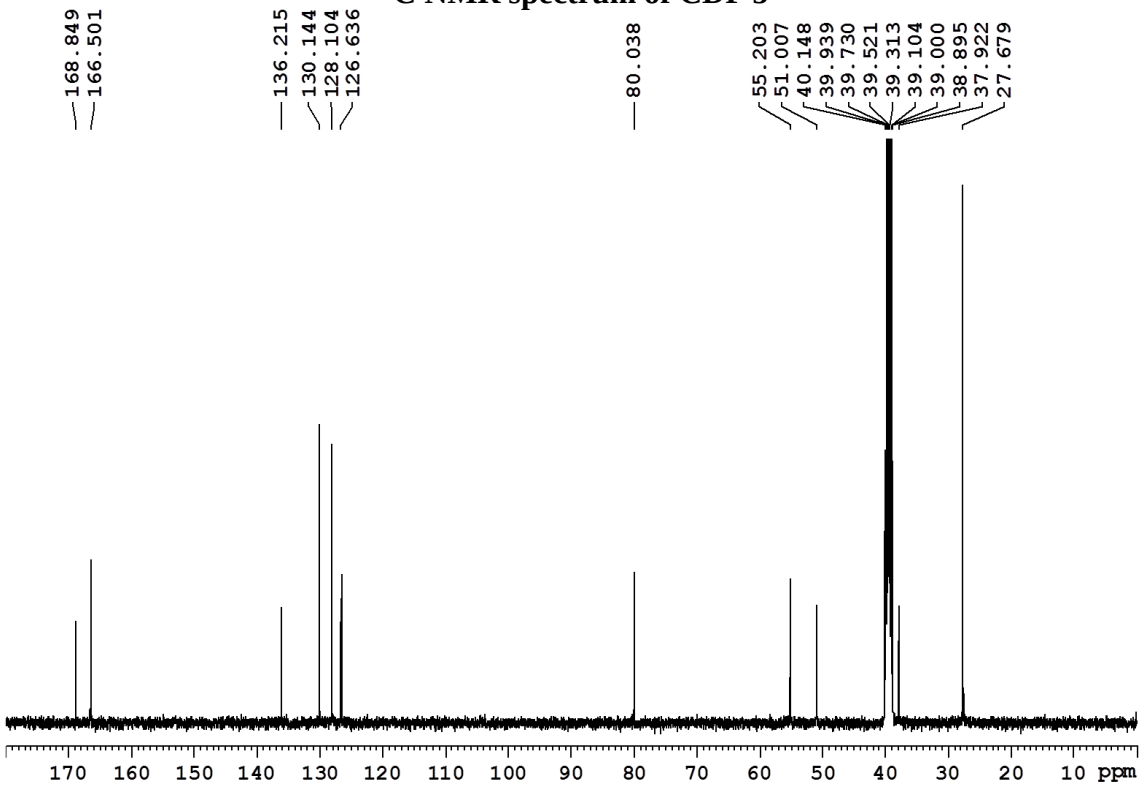

^{1}H NMR spectrum of CDP 6

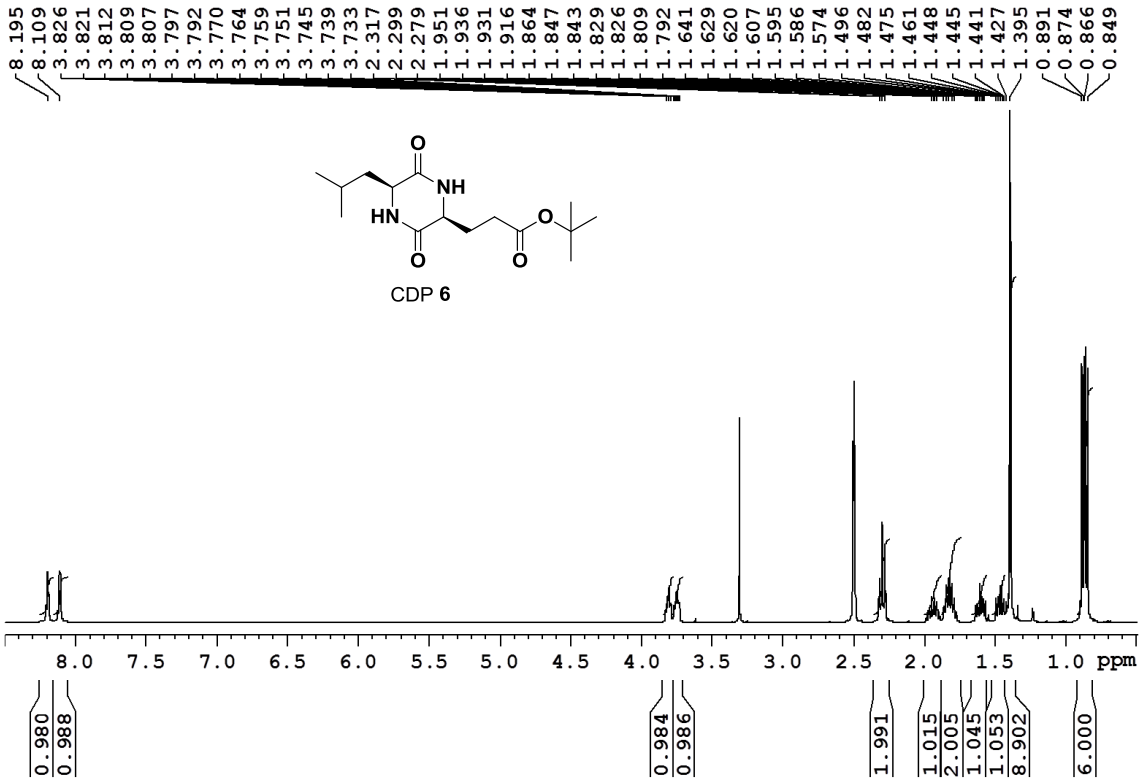

^{13}C NMR spectrum of CDP 6

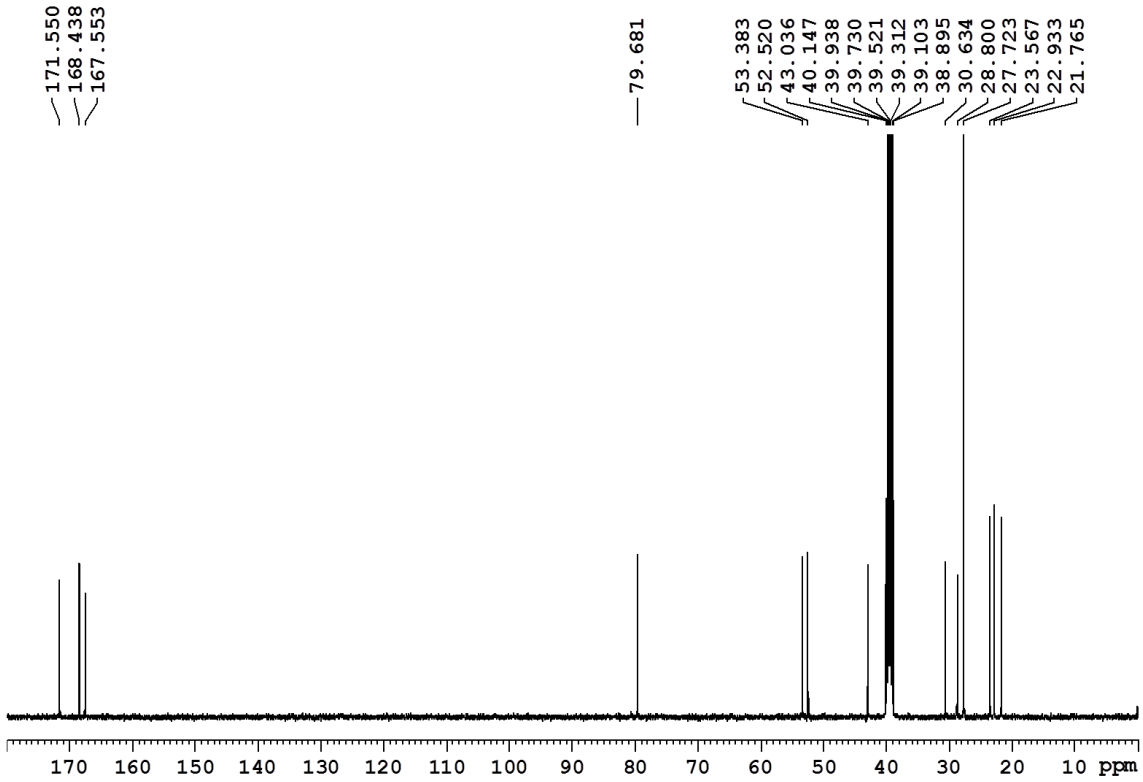

2.2.5 References

1. Terech, P.; Weiss, R. G. *Molecular gels: materials with self-assembled fibrillar networks*. Springer, Dordrecht, **2006**.

2. Binder, W. H.; Smrzka, O.W. Self-assembly of fibers and fibrils. *Angew. Chem. Int. Ed.* **2006**, *45*, 7324-7328.

3. Adams, D. J.; Topham, P. D. Peptide conjugate hydrogelators. *Soft Matter* **2010**, *6*, 3707-3721.

4. Steed, J. W. Supramolecular gel chemistry: developments over the last decade. *Chem. Commun.* **2011**, *47*, 1379-1383.

5. Johnson, E. L.; Adams, D. J.; Cameron, P. J. Peptide based low molecular weight gelators. *J. Mater. Chem.* **2011**, *21*, 2024-2027.

6. Xie, Z.; Zhang, A.; Ye, L.; Feng, Z. Organo- and hydrogels derived from cyclo(L-Tyr-L-Lys) and its 3-amino derivatives. *Soft Matter* **2009**, *5*, 1474-1482.

7. Yagai, S.; Nakajima, T.; Kishikiva, K.; Kohmoto, S.; Karatsu, T.; Kitamura, A. Hierarchical organization of photoresponsive hydrogen-bonded rosettes. *J. Am. Chem. Soc.* **2005**, *127*, 11134-11139.

8. Huang, Y.; Qiu, Z.; Xu, Y.; Shi, J.; Lin, H.; Zhang, Y. Supramolecular hydrogels based on short peptides linked with conformational switch. *Org. Biomol. Chem.* **2011**, *9*, 2149-2155.

9. Aggeli, A.; Bell, M.; Carrick, L. M.; Fishwick, C.W. G.; Harding, R.; Mawar, P. J.; Radford, S. E.; Strong, A. E.; Boden, N. pH as a trigger of peptide β-sheet self-assembly and reversible switching between nematic and isotropic phases. *J. Am. Chem. Soc.* **2003**, *125*, 9619-9628.

10. Khatua, D.; Maiti, R.; Dey, J. A supramolecular hydrogel that responds to biologically relevant stimuli. *Chem. Commun.* **2006**, 4903-4905.

11. Brinksma, J.; Feringa, B. L.; Kellogg, R. M.; Vreeker, R.; Esch, J. V. Rheology and thermotropic properties of bis-urea-based organogels in various primary alcohols. *Langmuir* **2000**, *16*, 9249-9255.

12. Percec, V.; Peterca, M.; Yurchenko, M. E.; Rudick, J. G.; Heiney, P. A. Thixotropic twin-dendritic organogelators. *Chem. Eur. J.* **2008**, *14*, 909-918.

13. Toledano, S.; Williams, R. J.; Jayawarna, V.; Uljin, R. V. Enzyme-triggered self-assembly of peptide hydrogels via reversed hydrolysis. *J. Am. Chem. Soc.* **2006**, *128*, 1070-1071.

14. Yang, Z.; Ho, P. L.; Liang, G.; Chow, K. H.; Wang, Q.; Cao, Y.; Guo, Z.; Xu, B. Using β-lactamase to trigger supramolecular hydrogelation. *J. Am. Chem. Soc.* **2007**, *129*, 266-267.

15. Uljin, R. V.; Smith, A. M. Designing peptide based nanomaterials. *Chem. Soc. Rev.* **2008**, *37*, 664-675.

16. Vintiloiu, A.; Leroux, J. C. Organogels and their use in drug delivery-a review. *J. Control. Release* **2008**, *125*, 179-192.

17. Park, K.H.; Na, K.; Chung, H. M. Enhancement of the adhesion of fibroblasts by peptide containing an Arg-Gly-Asp sequence with poly(ethylene glycol) into a thermo-reversible hydrogel as a synthetic extracellular matrix. *Biotechnol. Lett.* **2005**, *27*, 227-231.

18. Tibbitt, M. W.; Anseth, K. S. Hydrogels as extracellular matrix mimics for 3D cell culture. *Biotechnol. Bioeng.* **2009**, *103*, 655-663.

19. Debnath, S.; Anshupriya, S.; Dutta, S. Das, P. K. Dipeptide-based low-molecular-weight efficient organogelators and their application in water purification. *Chem. Eur. J.* **2008**, *14*, 6870-6881.

20. Tanmoy, K.; Debnath, S.; Das, D.; Anshupriya, S.; Das, P. K. Organogelation and hydrogelation of low-molecular-weight amphiphilic dipeptides: pH responsiveness in phase-selective gelation and dye removal. *Langmuir* **2009**, *25*, 8639-8648.

21. Kimura, M.; Kobayashi, S.; Kuroda, T.; Hanabusa, K.; Shirai, H. Assembly of gold nanoparticles into fibrous aggregates using thiol-terminated gelators. *Adv. Mater.* **2004**, *16*, 335-338.

22. Ray, S.; Das, A. K.; Banerjee, A. Smart oligopeptide gels: in situ formation and stabilization of gold and silver nanoparticles within supramolecular organogel networks. *Chem. Commun.* **2006**, 2816-2818.

23. Li, X.; Kuang, Y.; Lin, H. C.; Gao, Y.; Shi, J.; Xu, B. Supramolecular nanofibers and hydrogels of nucleopeptides. *Angew. Chem. Int. Ed.* **2011**, *50*, 9365-9369.

24. Adhikari, B.; Nanda, J.; Banerjee, A. Pyrene-containing peptide-based fluorescent organogels: inclusion of graphene into the organogel. *Chem. Eur. J.* **2011**, *17*, 11488-11496.

25. Kreplak, L.; Doucet, J.; Dumas, P.; Briki, F. New aspects of the α-helix to β-sheet transition in stretched hard α-keratin fibers. *Biophys. J.* **2004**, *87*, 640-647.

26. Keten, S.; Xu, Z.; Ihle, B.; Buehler, M. J. Nanoconfinement controls stiffness, strength and mechanical toughness of β-sheet crystals in silk. *Nat. Mater.* **2010**, *9*, 359-367.

27. Dobson, C. M. Protein folding and misfolding. *Nature* **2003**, *426*, 884-890.

28. Haswell, S. J.; Skelton, V. Chemical and biochemical microreactors. *Trends Anal. Chem.* **2000**, *19*, 389-395.

29. Babu, S. S.; Mahesh, S.; Kartha, K. K.; Ajayaghosh, A. Solvent-directed self-assembly of π gelators to hierarchical macroporous structures and aligned fiber bundles. *Chem. Asian J.* **2009**, *4*, 824-829.

30. Shastri, V. P.; Martin, I.; Langer, R. Macroporous polymer foams by hydrocarbon templating. *Proc. Natl. Acad. Sci. U. S. A.* **2000**, *97*, 1970-1975.

31. Hafkamp, R. J. H.; Feiters, M. C.; Nolte, R. J. M. Tunable supramolecular structures from a gluconamide containing imidazole. *Angew. Chem. Int. Ed. Engl.* **1994**, *33*, 986-987.

32. Yang, W. Y.; Ahn, J. H.; Yoo, Y. S.; Oh, N. K.; Lee, M. Supramolecular barrels from Amphiphilic rigid-flexible macrocycles. *Nat. Mater.* **2005**, *4*, 399-402.

33. Hanabusa, K.; Matsumoto, Y.; Miki, T.; Koyama, T.; Shirai, H. Cyclo(dipeptide)s as low-molecular-mass gelling agents to harden organic fluids. *J. Chem. Soc. Chem. Commun.* **1994**, 1401-1402.

34. Hanabusa, K.; Matsumoto, M.; Kimura, M.; Kakehi, A.; Shirai, H. Low molecular weight gelators for organic fluids: gelation using a family of cyclo(dipeptide)s. *J. Colloid Interface Sci.* **2000**, *224*, 231-244.

35. Benedetti, E.; Corradini, P.; Pedone, C. The crystal and molecular structure of trans-3,6-dimethyl-2,5-piperazinedione (L-alanyl-D-alanyl-2,5-diketopiperazine). *J. Phys. Chem.* **1969**, *73*, 2891-2895.

36. Joshi, K. B.; Verma, S. Participation of aromatic side chains in diketopiperazine ensembles. *Tetrahedron Lett.* **2008**, *49*, 4231-4234.

37. MacDonald, J. C.; Whitesides, G. M. Solid-state structures of hydrogen-bonded tapes based on cyclic secondary diamides *Chem. Rev.* **1994**, *94*, 2383-2420.

38. Govindaraju, T.; Pandeeswar, M.; Jayaramulu, K.; Jaipuria, G.; Atreya, H. S. Spontaneous self-assembly of designed cyclic dipeptide (Phg-Phg) into two-dimensional nano- and mesosheets. *Supramol. Chem.* **2011**, *23*, 487-492.

39. Govindaraju, T. Spontaneous self-assembly of aromatic cyclic dipeptide into fibre bundles with high thermal stability and propensity for gelation. *Supramol. Chem.* **2011**, *23*, 759-767.

40. Sasaki, Y.; Akutsu, Y.; Matsui, M.; Suzuki, K.; Sakurada, S.; Sato, T.; Kisara, K. Studies on analgesic oligopeptides: structure-activity relationship among thirty analogs of cyclic dipeptide, cyclo(-Tyr-Arg-). *Chem. Pharm. Bull.* **1982**, *30*, 4435-4443.

41. Prasad, C. Bioactive cyclic dipeptides. *Peptides* **1995**, *16*, 151-164.

42. Lucietto, F. R.; Milne, P. J.; Kilian, G.; Frost, C. L.; Venter, M. V. D. The biological activity of the histidine-containing diketopiperazines cyclo(His-Ala) and cyclo(His-Gly). *Peptides* **2006**, *27*, 2706-2714.

43. Tanaka, K.; Mori, A.; Inoue, S. The cyclic dipeptide cyclo [(S)-phenylalanyl-(S)-histidyl] as a catalyst for asymmetric addition of hydrogen cyanide to aldehydes. *J. Org. Chem.* **1990**, *55*, 181-185.

44. Kim, H. J.; Jackson, W. R. Polymer attached cyclic dipeptides as catalysts for enantioselective cyanohydrin formation. *Tetrahedron: Asymmetry* **1992**, *3*, 1421-1430.

45. Ressurreição, A. S. M.; Delatouche, R.; Gennari, C.; Piarulli, U. Bifunctional 2,5-diketopiperazines as rigid three-dimensional scaffolds in receptors and peptidomimetics. *Eur. J. Org. Chem.* **2011**, 217-228.

46. Smith, A. M.; Williams, R. J.; Tang, C.; Coppo, P.; Collins, R. F.; Turner, M. L.; Saiani, A.; Uljin, R. V. Fmoc-diphenylalanine self assembles to a hydrogel via a novel architecture based on π-π interlocked β-sheets. *Adv. Mater.* **2008**, *20*, 37-41.

47. Palmore, G. T. R.; Luo, T. J. M.; Wieser, M. T. M.; Picciotto, E. A.; Paz, C. M. R. Engineering crystalline architecture with diketopiperazines: an investigation of the strength of hydrogen-bonded tapes based on the cyclic dipeptide of (S)-aspartic acid. *Chem. Mater.* **1999**, *11*, 3315-3328.

48. Adams, D. J.; Topham, P. D. Peptide conjugate hydrogelators. *Soft Matter* **2010**, *6*, 3707-3721.

49. Fichman, G.; Gazit, E. Self-assembly of short peptides to form hydrogels: Design of building blocks, physical properties and technological applications. *Acta Biomater.* **2014**, *10*, 1671-1682.

50. Vagner, J.; Qu, H.; Hruby, V. J. Peptidomimetics, a synthetic tool of drug discovery. *Curr. Opin. Chem. Biol*. **2008**, *12*, 292-296.

51. Li, J.; Li, X.; Kuang, Y.; Gao, Y.; Du, X.; Shi, J.; Xu, B. Self-delivery multifunctional anti-HIV hydrogels for sustained release. *Adv. Healthcare Mater.* **2013**, *2*, 1586-1590.

52. Salick, D. A.; Pochan, D. J.; Schneider, J. P. Design of an Injectable *β*-hairpin peptide hydrogel that kills methicillin-resistant staphylococcus aureus. *Adv. Mater.* **2009**, *21*, 4120-4123.

53. Cui, H.; Webber, M. J.; Stupp, S. I. Self-assembly of peptide amphiphiles: From molecules to nanostructures to biomaterials. *Biopolymers* **2010**, *94*, 1-18.

54. Jung, J. P.; Gasiorowski, J. Z.; Collier, J. H. Fibrillar peptide gels in biotechnology and biomedicine. *Biopolymers* **2010**, *94*, 49-59.

55. Tomasini, C.; Castellucci, N. Peptides and peptidomimetics that behave as low molecular weight gelators. *Chem. Soc. Rev.* **2013**, *42*, 156-172.

56. Li, J.; Kuang, Y.; Gao, Y.; Du, X.; Shi, J.; Xu, B. D-amino acids boost the selectivity and confer supramolecular hydrogels of a nonsteroidal anti-inflammatory drug (NSAID). *J. Am. Chem. Soc.* **2013**, *135*, 542-545.

57. Wang, H.; Wei, J.; Yang, C.; Zhao, H.; Li, D.; Yin, Z.; Yang, Z. The inhibition of tumor growth and metastasis by self-assembled nanofibers of taxol. *Biomaterials* **2012**, *33*, 5848-5853.

58. Matson, J. B.; Stupp, S. I. Self-assembling peptide scaffolds for regenerative medicine. *Chem. Commun.* **2012**, *48*, 26-33.

59. Bhattacharya, S.; Samanta, S. K. Soft functional materials induced by fibrillar networks of small molecular photochromic gelators. *Langmuir* **2009**, *25*, 8378-8381.

60. Mart, R. J.; Osborne, R. D.; Stevens, M. M.; Ulijn. R. V. Peptide-based stimuli-responsive biomaterials. *Soft Matter* **2006**, *2*, 822-835.

61. Yang, X.; Zhang, G.; Zhang, D. Stimuli responsive gels based on low molecular weight gelators. *J. Mater. Chem.* **2012**, *22*, 38-50.

62. Basak, S.; Nanda, J.; Banerjee, A. Multi-stimuli responsive self-healing metallohydrogels: tuning of the gel recovery property. *Chem. Commun.* **2014**, *50*, 2356-2359.

63. Mahler, A.; Reches, M.; Rechter, M.; Cohen, S.; Gazit, E. Rigid, Self-assembled hydrogel composed of a modified aromatic dipeptide. *Adv. Mater.* **2006**, *18*, 1365-1370.

64. Martin, A. D.; Robinson, A. B.; Thordarson, P. Biocompatible small peptide super-hydrogelators bearing carbazole functionalities. *J. Mater. Chem. B* **2015**, *3*, 2277-2280.

65. Altunbas, A.; Lee, S. J.; Rajasekaran, S. A.; Schneider, J. P.; Pochan, D. J. Encapsulation of curcumin in self-assembling peptide hydrogels as injectable drug delivery vehicles *Biomaterials* **2011**, *32*, 5906-5914.

66. Zhang, S.; Greenfield, M. A.; Mata, A.; Palmer, L. C.; Bitton, R.; Mantei, J. R.; Aparicio, C.; de la Cruz, M. O.; Stupp, S. I. A self-assembly pathway to aligned monodomain gels. *Nat. Mater.* **2010**, *9*, 594-601.

67. Morales, M. E.; Gallardo, V.; Clares, B.; Garcia, M. B.; Ruiz, M. A. Study and description of hydrogels and organogels as vehicles for cosmetic active ingredients. *J. Cosmet. Sci.* **2009**, *60*, 627-636.

68. Geisler, I. M.; Schneider, J. P. Evolution-based design of an injectable hydrogel. *Adv. Funct. Mater.* **2012**, *22*, 529-537.

69. Lei, K.; Shen, W.; Cao, L.; Yu, L.; Ding, J. An injectable thermogel with high radiopacity. *Chem. Commun.* **2015**, *51*, 6080-6083.

70. Zhang, S.; Ermann, J.; Succi, M. D.; Zhou, A.; Hamilton, M. J.; Cao, B.; Korzenik, J. R.; Glickman, J. N.; Vemula, P. K.; Glimcher, L. H.; Traverso, G.; Langer, R.; Karp, J. M. An inflammation-targeting hydrogel for local drug delivery in inflammatory bowel disease. *Sci. Transl. Med.* **2015**, *7*, 300ra128.

71. Couffin-Hoarau, A. C.; Motulsky, A.; Delmas, P.; Leroux, J. C. In situ-forming pharmaceutical organogels based on the self-assembly of L-alanine derivatives. *Pharm. Res.* **2004**, *21*, 454-457.

72. Bastiat, G.; Leroux, J. C. Pharmaceutical organogels prepared from aromatic amino acid derivatives. *J. Mater. Chem.* **2009**, *19*, 3867-3877.

73. Bastiat, G.; Plourde, F.; Motulsky, A.; Furtos, A.; Dumont, Y.; Quirion, R.; Fuhrmann, G.; Leroux, J. C. Tyrosine-based rivastigmine-loaded organogels in the treatment of Alzheimer's disease. *Biomaterials* **2010**, *31*, 6031-6038.

74. Borthwick, A. D. 2,5-Diketopiperazines: synthesis, reactions, medicinal chemistry, and bioactive natural products. *Chem. Rev.* **2012**, *112*, 3641-3716.

75. Bellezza, I.; Peirce, M. J.; Minelli, A. Cyclic dipeptides: from bugs to brain. *Trends Mol. Med.* **2014**, *20*, 551-558.

76. Nishanth, S. K.; Nambisan, B.; Dileep, C. Three bioactive cyclic dipeptides from the Bacillus sp. N strain associated with entomopathogenic nematode. *Peptides* **2014**, *53*, 59-69.

77. Barman, A. K.; Verma, S. Solid state structures and solution phase self-assembly of clicked mannosylated diketopiperazines. *RSC Adv*. **2013**, *3*, 14691-14700.

78. Jeziorna, A.; Stopczyk, K.; Skorupska, E.; Durnas, K. L.; Oszajca, M.; Lasocha, W.; Gorecki, M.; Frelek, J.; Potrzebowski, M. J. Cyclic dipeptides as building units of nano- and microdevices: synthesis, properties, and structural studies. *Cryst. Growth Des.* **2015**, *15*, 5138-5148.

79. Furutani, M.; Kudo, K. Transformation of Gold(I)-cyclo[-Met-Met-] complex supramolecular fibers into aligned gold nanoparticles. *Chem. Lett.* **2013**, *42*, 601-603.

80. Manchineella, S.; Govindaraju, T. Hydrogen bond directed self-assembly of cyclic dipeptide derivatives: gelation and ordered hierarchical architectures. *RSC Adv.* **2012**, *2*, 5539-5542.

81. Manchineella, S.; Prathyusha, V.; Priyakumar, U. D.; Govindaraju, T. Solvent-induced helical assembly and reversible chiroptical switching of chiral cyclic-dipeptide-functionalized naphthalenediimides. *Chem. Eur. J.* **2013**, *19*, 16615-16624.

82. Avinash, M. B.; Raut, D.; Mishra, M. K.; Ramamurty, U.; Govindaraju, T. Bioinspired reductionistic peptide engineering for exceptional mechanical properties *Sci. Rep.* **2015**, *5*, 16070.

83. Hoshizawa, H.; Suzuki, M.; Hanabusa, K. Cyclo(L-aspartyl-L-phenylalanyl)-containing poly(dimethylsiloxane)-based thixotropic organogels. *Chem. Lett.* **2011**, *40*, 1143-1145.

84. Kleinsmann, A. J.; Nachtsheim, B. J. Phenylalanine-containing cyclic dipeptides - the lowest molecular weight hydrogelators based on unmodified proteinogenic amino acids. *Chem. Commun.* **2013**, *49*, 7818-7820.

85. Harada, A.; Takashima, Y.; Nakahata, M. Supramolecular polymeric materials via cyclodextrin-guest interactions. *Acc. Chem. Res.* **2014**, *47*, 2128-2140.

86. Pappas, C. G.; Mutasa, T.; Frederix, P. W. J. M.; Fleming, S.; Bai, S.; Debnath, S.; Kelly, S. M.; Gachagan, A.; Ulijn, R. V. Transient supramolecular reconfiguration of peptide nanostructures using ultrasound. *Mater. Horiz.* **2015**, *2*, 198-202.

Chapter 3

Solvent-induced Helical Assembly and Reversible Chiroptical Switching of Chiral Cyclic Dipeptide Functionalized Naphthalenediimides

3.1 Introduction

Helical chirality is ubiquitous in biological systems, as seen in DNA and proteins.[1-3] The helical conformations adopted by synthetic oligomers and polymers are pertinent to various applications, such as chiral recognition, asymmetric catalysis, chiral separation, and chiroptical switching.[4-6] In recent times, helical chirality in supramolecular polymers has attracted considerable interest due to the intrinsic dynamic nature of such materials and the ease with which their structural and functional properties may be tuned compared to covalent polymers.[7-10] The characteristic feature of such supramolecular polymers is the assembly of π-conjugated and aromatic monomer units with stabilization through hydrogen bonding and π-stacking interactions. Induction of helical chirality in supramolecular polymers through structural variations at the molecular self-assembly level is challenging due to the interplay of multiple noncovalent interactions. In general, the noncovalent synthesis of supramolecular polymers can be modulated through external stimuli capable of influencing the mode of molecular self-assembly. In this context, previous literature reports suggest that helical handedness in a self-assembly system can be achieved by employing similar external stimuli and chiral auxiliaries.[11-16] External stimuli such as temperature, light, solvent, and additives have been successfully used to control the chiral handedness of synthetic oligomers and polymers.[17-27] Some of the successful reports on chiral modulation in noncovalent systems have dealt with solvent-modulated supramolecular chirality of merocyanines, squarine dyes, and benzenetricarboxylic acid derivatives.[28-30]

Naphthalenediimide (NDI), the bis-imide derivative of 1,4,5,8-naphthalenetetracarboxylic dianhydride (NDA), is an extremely useful molecular platform with applications ranging from organic electronics to biomedicine.[31-35] The possibility of selective imide functionalization, high π-acidity, molecular planarity

conducive to strong π–π interactions, and ease of processability in solution has led to increased demand for the design of novel NDI-based supramolecular systems. Imide substituents studied have included alkyl chains, aromatic rings, amino acids, dipeptides, and a combination of alkyl chains and amino acids.[36-52] Recent work demonstrated the potential of a biomimetic strategy based on amino acid- and peptide-functionalized NDIs for designing 0D, 1D, and 2D molecular materials with interesting structural and functional properties.[35,49-52] The functional relevance of these biomimetic molecular materials varied from attolitre containers for miniaturized biological assays to organic electronics to self-cleaning functional molecular materials.[35,49-51] Furthermore, the amino acid- and dipeptide functionalized NDIs emphasized the significance of the chiral centre of the amino acid directly attached to the imide nitrogen in controlling the supramolecular helical chirality of the derived self-assembled structures.[52] Subsequently, the chiroptical properties of these systems revealed significant chiral transcription, amplification, and retentive helical memory with probable implications for the origin of homochirality in Nature.[3]

Cyclic dipeptides (CDPs) are the smallest possible cyclic forms of peptides, are known for their unique structural properties and diverse biological functions.[53-56] Because of their structural rigidity, propensity for strong intermolecular hydrogen bonding, molecular recognition, and resistance towards proteolytic enzymes, CDPs constitute good supramolecular synthons for the preparation of soft organogels, hydrogels, and well-defined nanoarchitectures for various applications.[57-63] We envisaged an inclusive molecular design based on NDI with CDP chiral auxiliaries as monomers for the noncovalent synthesis of helical supramolecular polymers. The NDI-CDP (NCDP) conjugates serve as model systems to evaluate the role of chiral centers on the imide substituent located several atoms away from the imide nitrogen, in inducing specific

helical assemblies of NDI. This study complements earlier works, in which the chiral center of the first amino acid directly attached as the imide substituent through the α-amino group was found to determine the outcome of the helical assembly of NDIs.[49-52] The NCDP molecular platform has also assisted our understanding of the influence of α-substituent and the corresponding chiral centers in CDP auxiliaries. In the present study, we report novel symmetrical NCDPs (**1**-**6**) as a new molecular platform to engineer NDI chiral assembly through aromatic (NDI) and hydrogen-bonding (CDP) interactions. Furthermore, this study emphasizes the significance of chiral auxiliaries and the decisive role played by solvent composition in modulating the helical supramolecular self-assembly of such systems.

3.2 Results and Discussion

3.2.1 Synthesis of NCDPs

CDPs [*cyclo*(*L*-Lys-*L*-Tyr) (**13**), *cyclo*(l-Lys-l-Phe) (**16**), *cyclo*(*L*-Lys-*L*-Leu) (**20**), *cyclo*(*L*-Lys-Gly) (**2**), *cyclo*(*L*-Lys-*D*-Tyr) (**24**), and *cyclo*(*L*-Lys-*D*-Phe) (**28**)] from the corresponding linear dipeptides, retaining *L*-lysine as one of the amino acids and varying the second amino acid, to obtain α-substituent with desired stereochemistry (*L* or *D*).[59] CDP auxiliaries were then condensed with naphthalenetetracarboxylic dianhydride (NDA) through ε-amine group of lysine to obtain NCDPs **1**-**6**, respectively, in good to excellent yields (Scheme 3.1-3.6). All the NCDPs were thoroughly characterized by NMR spectroscopy, elemental analysis, and mass spectrometry.

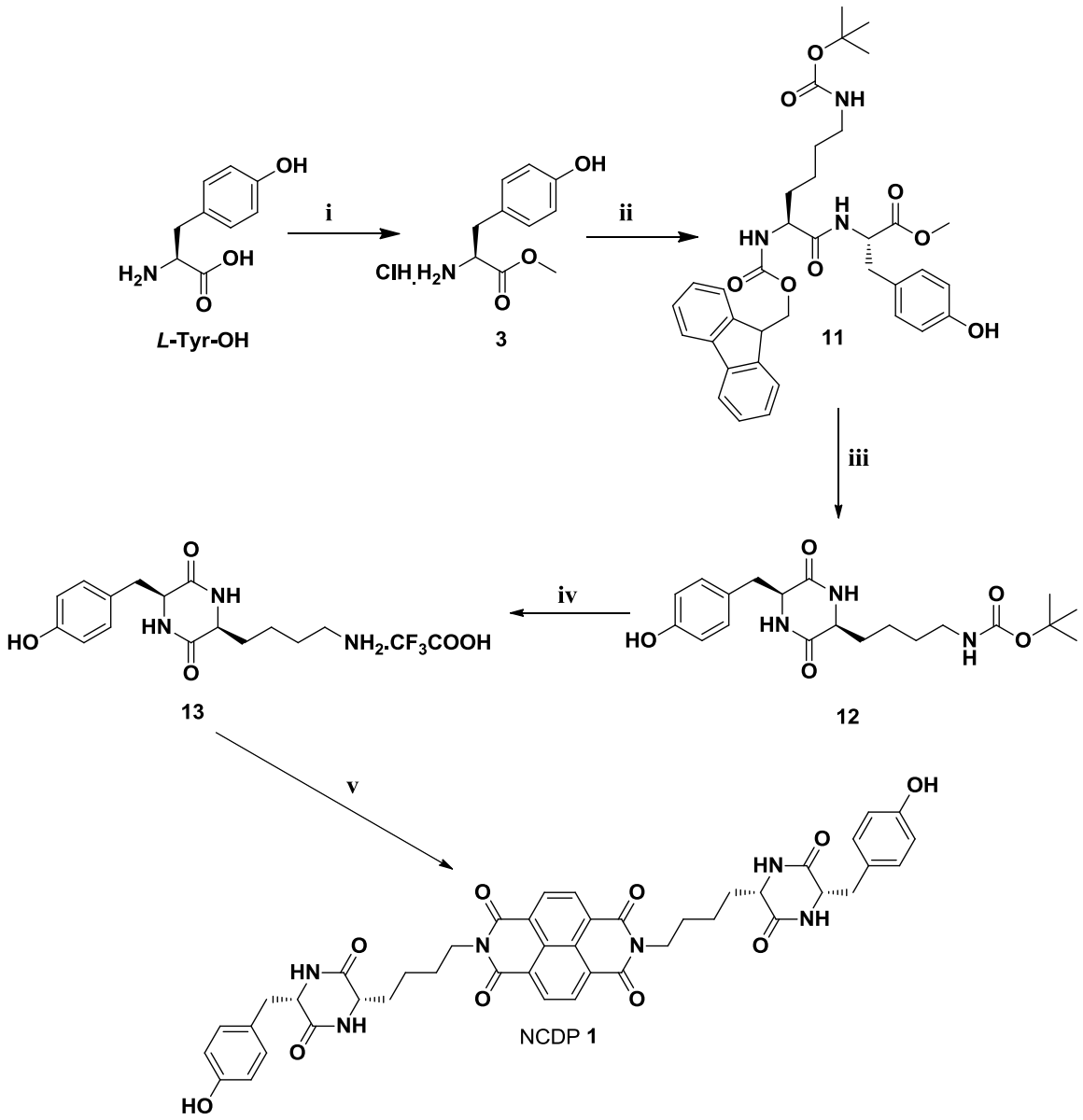

Scheme 3.1 Synthesis of NCDP **1**. Reagents and conditions: (i) $SOCl_2$, CH_3OH, 0-80 ºC, 4 h. (ii) Fmoc-*L*-Lys(*t*Boc)-OH, EDC.HCl, HOBt, DIPEA, DCM, 0 ºC 1 h, RT 3 h. (iii) piperidine:DCM (v/v, 20:80), RT, 8 h. (iv) TFA:DCM (v/v,1:1), TIPS, RT, 4 h. (v) 1,4,5,8-naphathalenetetracarboxylic dianhydride (NDA), DIPEA, DMF, 80 ºC, 14 h. EDC.HCl: 1-Ethyl-3-(3-dimethylaminopropyl)carbodiimide hydrochloride; HOBt: 1-hydroxybenzotriazole; DIPEA: *N*,*N*-diisopropylethylamine; DCM: dichloromethane; TFA: trifluoroacetic acid; DMF: *N*,*N*-dimethylformamide; RT: room temperature; TIPS: triisopropylsilane.

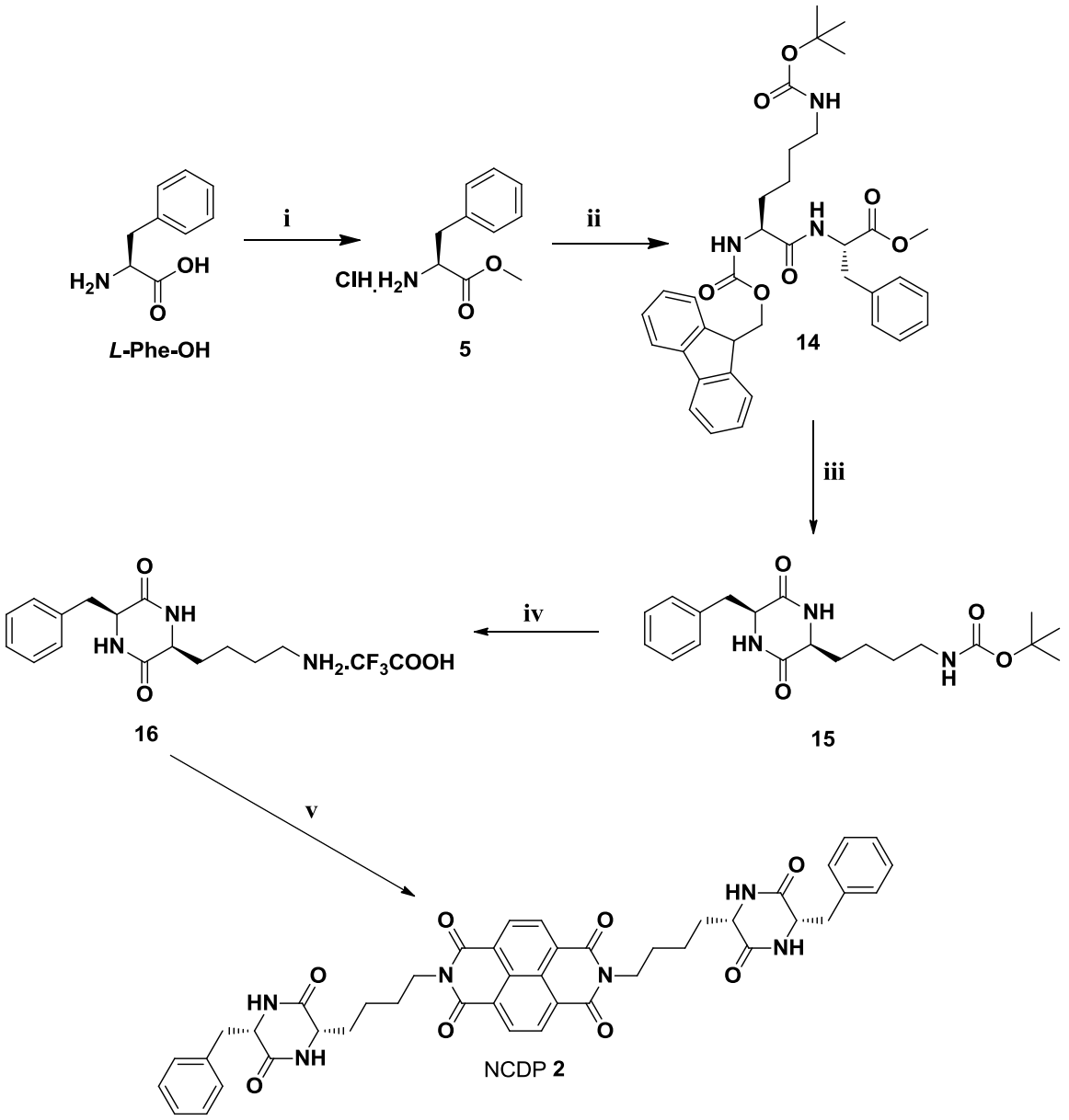

Scheme 3.2 Synthesis of NCDP **2**. Reagents and conditions: (i) $SOCl_2$, CH_3OH, 0-80 °C, 4 h. (ii) Fmoc-*L*-Lys(*t*Boc)-OH, EDC.HCl, HOBt, DIPEA, DCM, 0 °C 1 h, RT 4 h. (iii) piperidine:DCM (v/v, 20:80), RT, 6 h. (iv) TFA:DCM (v:v, 1:1), TIPS, RT, 4 h. (v) 1,4,5,8-naphathalenetetracarboxylic dianhydride, DIPEA, DMF, 80 °C, 12 h.

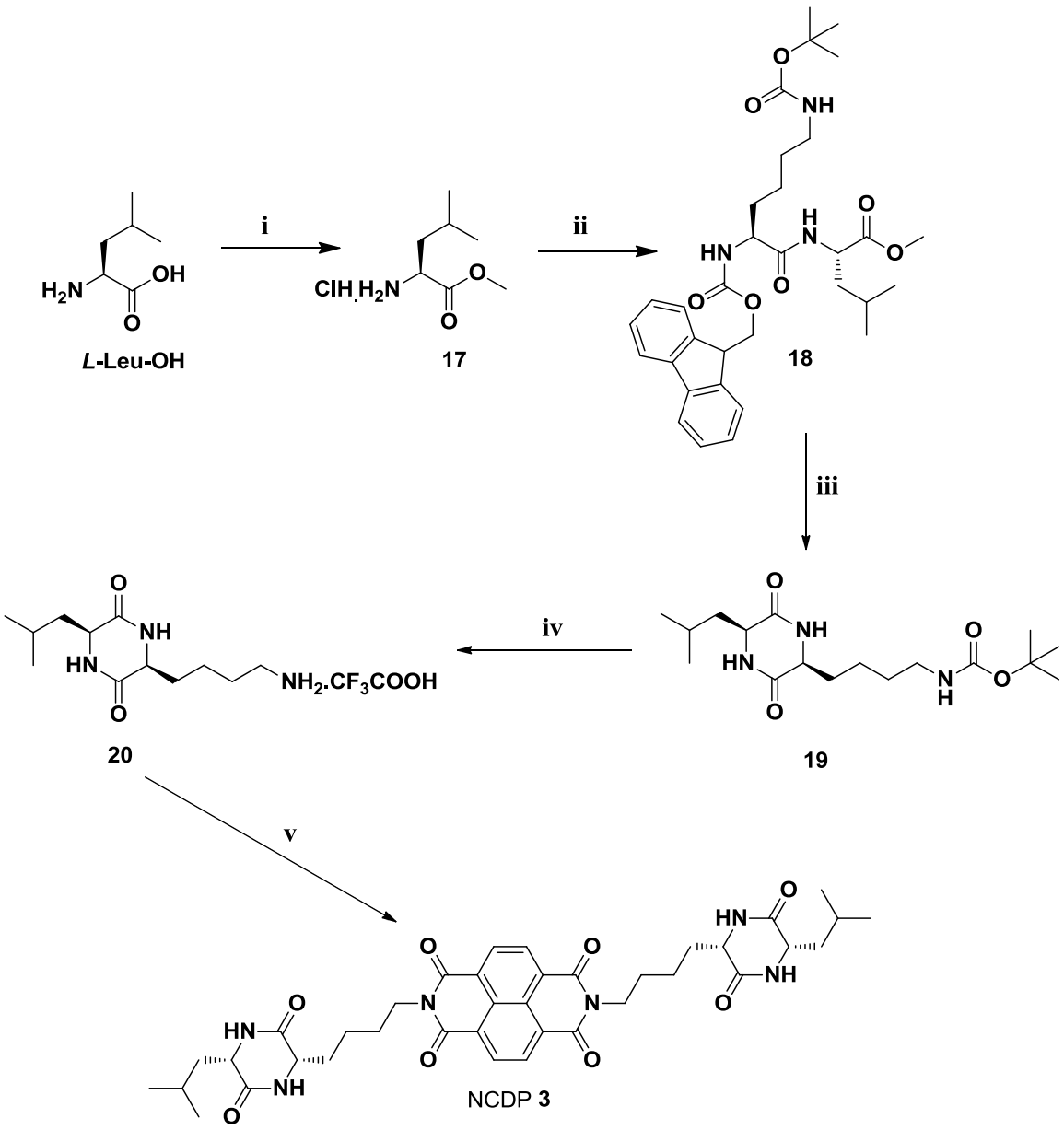

Scheme 3.3 Synthesis of NCDP **3**. Reagents and conditions: (i) $SOCl_2$, CH_3OH, 0-80 °C, 6 h. (ii) Fmoc-*L*-Lys(*t*Boc)-OH, EDC.HCl, HOBt, DIPEA, DCM, 0 °C 1 h, RT 4 h. (iii) piperidine:DCM (v/v, 20:80), RT, 8 h. (iv) TFA:DCM (v/v, 1:1), TIPS, RT, 4 h. (v) 1,4,5,8-naphathalenetetracarboxylic dianhydride, DIPEA, DMF, 80 °C, 12 h.

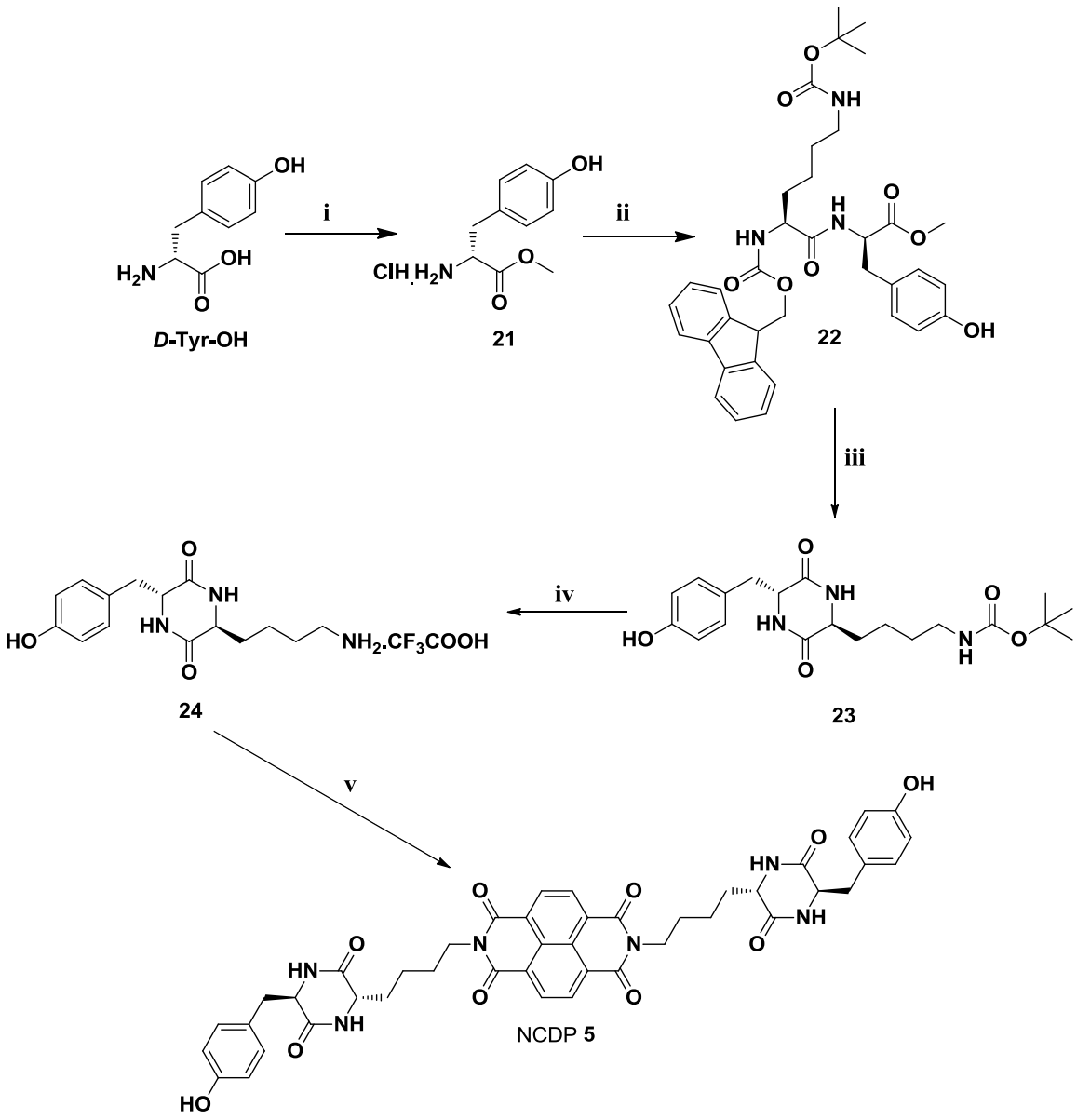

Scheme 3.4 Synthesis of NCDP **5**. Reagents and conditions: (i) $SOCl_2$, CH_3OH, 0-80 °C, 14 h. (ii) Fmoc-*L*-Lys(*t*Boc)-OH, EDC.HCl, HOBt, DIPEA, DCM, 0 °C 1 h, RT 8 h. (iii) piperidine:DCM (v/v, 20:80), RT, 10 h. (iv) TFA:DCM (v/v, 1:1), TIPS, RT, 8 h. (v) 1,4,5,8-naphathalenetetracarboxylic dianhydride, DIPEA, DMF, 80 °C, 16 h.

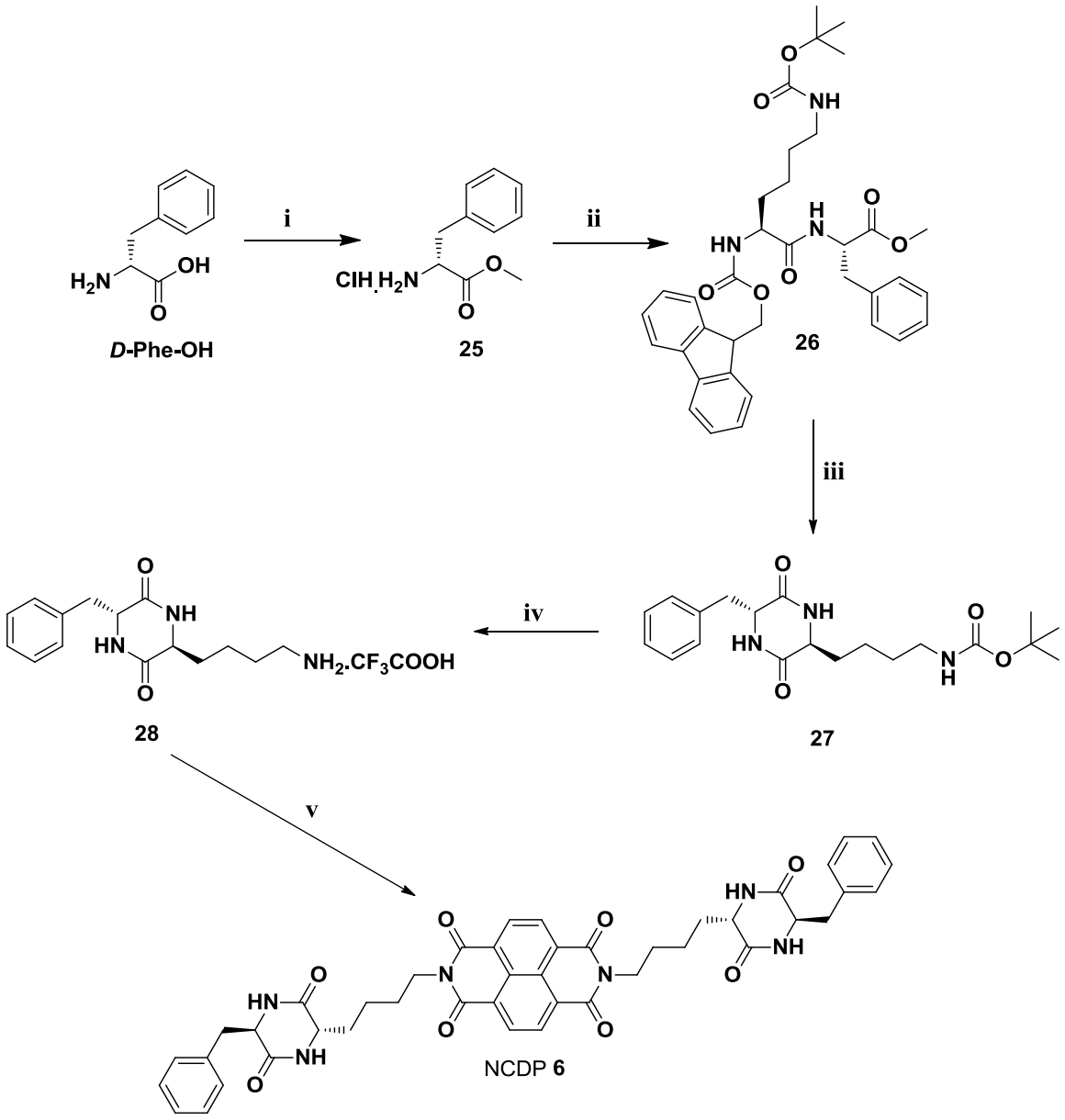

Scheme 3.5 Synthesis of NCDP **6**. Reagents and conditions: (i) $SOCl_2$, CH_3OH, 0-80 °C, 4 h. (ii) Fmoc-*L*-Lys(*t*Boc)-OH, EDC.HCl, HOBt, DIPEA, DCM, 0 °C 1 h, RT 6 h. (iii) piperidine:DCM (v/v, 20:80), RT, 11 h. (iv) TFA:DCM (v/v, 1:1), TIPS, RT, 8 h. (v) 1,4,5,8-naphathalenetetracarboxylic dianhydride, DIPEA, DMF, 80 °C, 15 h.

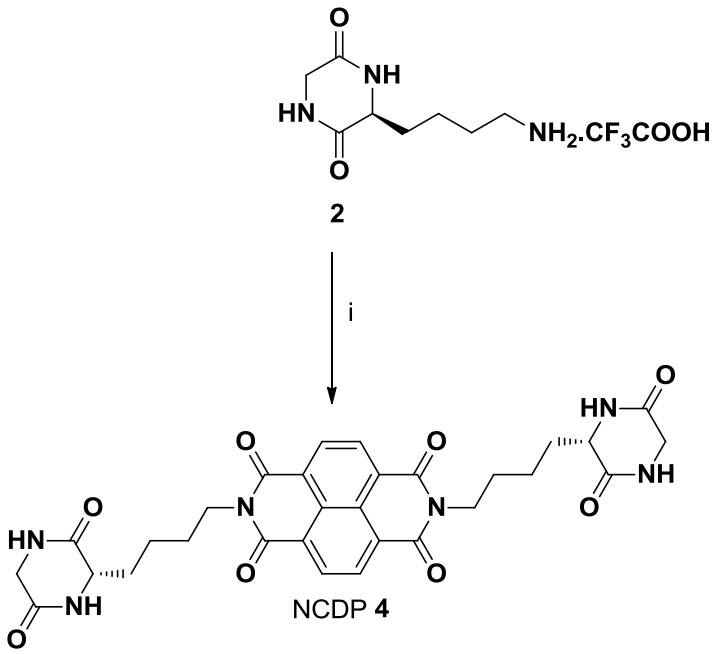

Scheme 3.6 Synthesis of NCDP **4**. Reagents and conditions: (i) 1,4,5,8-naphathalene tetracarboxylic dianhydride, DIPEA, DMF, 80 °C, 14 h.

3.2.2 NCDP helical assembly and chiroptical switching

NCDP **1** containing *L*-tyrosine as the second amino acid of the CDP auxiliary was chosen initially, for our detailed study owing to the characteristic self-assembling properties of *L*-tyrosine when present in polymer chains, and the proven strong intermolecular interactions among cyclo(*L*-Tyr-*L*-Lys) derivatives.[62,63] The molecular interactions and chiral aggregation properties of NCDP-1 were studied by UV/Vis absorption and CD spectroscopic measurements in hexafluoro-2-propanol (HFIP), dimethyl sulfoxide (DMSO), and mixtures thereof. Specifically, HFIP is known to stabilize helical conformations in peptides through various mechanisms.[64-66] The high solvent polarity, hydrogen-bond accepting properties, and localized hydrophobic solvating effects of methyl groups in DMSO are thought to facilitate solvophobic interactions, thereby inducing aggregation in binary solvent mixtures through diverse mechanisms.[67,68]

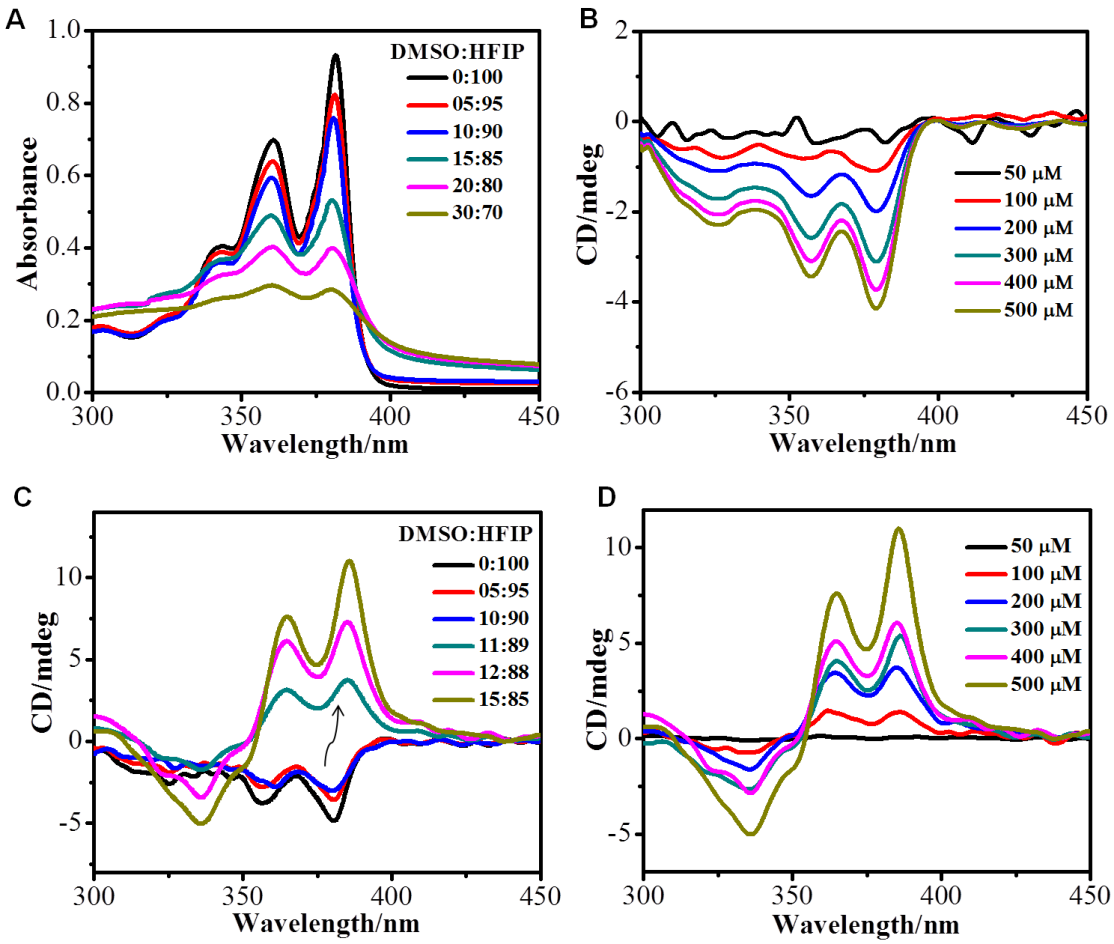

Figure 3.1 Photophysical and chiroptical studies of NCDP **1**. (A) UV-Vis absorption spectra of NCDP **1** (100 μM) in HFIP with increasing volume fraction of DMSO under ambient conditions. (B) CD spectra of NCDP **1** in HFIP with increasing concentration from 50 μM to 500 μM. (C) CD spectra of NCDP **1 (**500 μM) in HFIP with increasing volume fraction of DMSO. (D) CD spectra of NCDP **1** in DMSO:HFIP (15:85,v/v) with increasing concentration from 50 μM to 500 μM; DMSO: dimethylsulphoxide; HFIP: hexafluoro-2-propanol. The arrow in (C) indicates the chiroptical switching from *M*- to *P*-helical assembly.

NCDP **1** (100 μM) in HFIP showed absorption peaks in the region 300-400 nm, a characteristic band I absorption for NDI. The corresponding emission spectrum showed weak fluorescence characteristic of amino acid-functionalized NDIs (data not shown).[49-52] NCDP **1** exhibited aggregation-induced self-assembly with increasing volume fraction of DMSO (0-30%) in HFIP. A strong hypochromic effect and a slight hypsochromic shift

were observed for the NDI absorption band (300-400 nm) (Figure 3.1A). Circular dichroism (CD) studies were performed to gain insight into the chiroptical properties of NCDP **1**. In HFIP, at lower concentrations (<100 μM), NCDP **1** did not show any significant CD signals. However, a monosignate negative CD signal was obtained upon increasing the concentration of the solution to 100 μm, indicating *M*-helical (left-handed) assembly of NCDP **1** (Figure 3.1B). Negative Cotton signals were consistently observed for all the concentrations studied (100-500 μM), indicating the trivial effect of concentration on the chiral aggregation of NCDP **1**. Furthermore, it should be noted that the CD spectra on the molar ellipticity scale (data not shown) showed similar CD signal intensity, which clearly demonstrated that the chiroptical switching was independent of concentration. The observed M-helical bias of NCDP **1** may be ascribed to the aggregation of molecules (≥ 100 μM) and preferential stabilization of one of the helical forms (M type) by HFIP. It is presumed that in HFIP the *M*-helical assembly is the thermodynamically preferred arrangement of NCDP **1**. Semiempirical quantum chemical and density functional theory calculations on model structures were used to examine the relative stabilities of *M*- and *P*-helical assemblies, as discussed later.

Furthermore, we studied the effect of DMSO/HFIP solvent composition on the chiral aggregation of NCDP **1**. CD spectra of NCDP **1** (500 μM) were recorded as a function of increasing volume fraction of DMSO (v/v) in HFIP. There was no change in the negative Cotton signal upon increasing the volume fraction of DMSO up to 10% (v/v) in HFIP. However, the negative Cotton signal was transformed completely to a bisignate positive Cotton signal at volume fractions of DMSO>10% in HFIP, indicating a reversal of chiral assembly from *M*- to *P*-helicity (right handed). At 15% DMSO in HFIP (15:85, v/v), NCDP **1** exhibited maximum CD signal intensity, with a red-shift in λ_{max} (CD signal position), suggesting extended and more stable *P*-helical assembly as opposed to the

initially formed *M*-helical assembly in pure HFIP (Figure 3.1C). CD studies of NCDP **1** performed in DMSO alone and in HFIP containing co-solvents not isostructural with DMSO under similar conditions did not show any chiroptical switching properties (data not shown). Thus, DMSO in HFIP is responsible for the observed *M*- to *P*-helical inversion in the chiral self-assembly of NCDP **1**. The CD measurements performed on NCDP **1** at 50 μM both in HFIP and DMSO/HFIP (15:85, v/v) using 10 mm path length cuvettes to rule out the sensitivity related issues when using 1 mm path length cuvettes. This CD study using 10 mm path length cuvettes did not show any noteworthy additional signals, emphasizing the significance of minimum monomer concentration for aggregation of NCDP **1** (data not shown). To rule out linear dichroism (LD)-induced artifacts in the observed helical assembly and chiroptical switching properties of NCDP **1**, LD spectra were recorded under similar experimental conditions and showed no significant signals. The observed chiroptical switching from monosignate *M*-helical to bisignate *P*-helical handedness of NCDP **1** assembly is attributed to the strong excitonic interactions and preferential helical stabilization of this system in DMSO/HFIP (15:85, v/v). It is proposed that the DMSO molecules locally reorganize the HFIP solvent clusters around the NCDP. The methyl groups (-CH_3) of DMSO can preferentially solvate NCDP **1** to induce a hydrophobic effect, which subsequently drives the inversion of the *M*-helical to the thermodynamically more stable *P*-helical assembly of NCDP **1** in DMSO/HFIP. Concentration-dependent CD spectra were recorded in DMSO/HFIP (15:85, v/v) to study the effect of monomer concentration on the observed chiroptical switching of NCDP **1** helical assembly. The CD spectra of NCDP **1**, from 100 to 500 μM in DMSO/HFIP (15:85, v/v) showed bisignate positive Cotton signal (P-helical bias) regardless of the concentration (Figure 3.1D). This further emphasized the crucial role of the DMSO/HFIP (15:85, v/v) solvent composition in stabilizing the thermodynamically

more stable P-helical assembly of NCDP **1**. Variable-temperature CD studies were carried out to probe the effect of temperature on the chiroptical switching and stability of the *P*-helical assembly. CD spectra recorded for NCDP **1** (500 μM) in DMSO/HFIP (15:85, v/v) between 25 and 60 ºC showed no significant changes in the sign or intensity of the CD signal during the heating and cooling cycles (data not shown). Thus, variable-temperature CD study ruled out any influence of temperature on the observed chiroptical switching and asserted the stability of chiral aggregates at higher temperatures. The stability of P-helical aggregates of NCDP **1** can be attributed to strong intermolecular aromatic π–π interactions between the NDI cores supported by N-H···O hydrogen bonding between peripheral CDP auxiliaries.

3.2.3 Dynamic light scattering studies

Dynamic light-scattering (DLS) studies were carried out to obtain direct evidence for the self-assembly of NCDP **1** in solution. DLS analysis of NCDP **1** at 500 μM in solution showed the presence of aggregates, and the aggregate size was found to vary with solvent composition (Figure 3.2). The hydrodynamic sizes of the aggregates of NCDP **1** were found to be 37 nm in HFIP, and 210, 269, and 531 nm in 5% DMSO, 11% DMSO, and DMSO in HFIP, respectively. Furthermore, the observed chirality could be unequivocally attributed to self-assembled NCDP **1** (500 μM) aggregates in solution by recording CD spectra in DMSO/HFIP (15:85, v/v) before and after centrifugation and filtration of the solution through a 0.45 μm filter. The CD spectrum recorded from the as-prepared sample showed a strong bisignate CD signal, whereas the filtered solution did not show any CD signal, as the centrifugation and filtration process had removed the chiral aggregates. This study corroborated the observed chirality and its origin through intermolecular self-assembly of monomeric NCDP supramolecular synthons in solution.

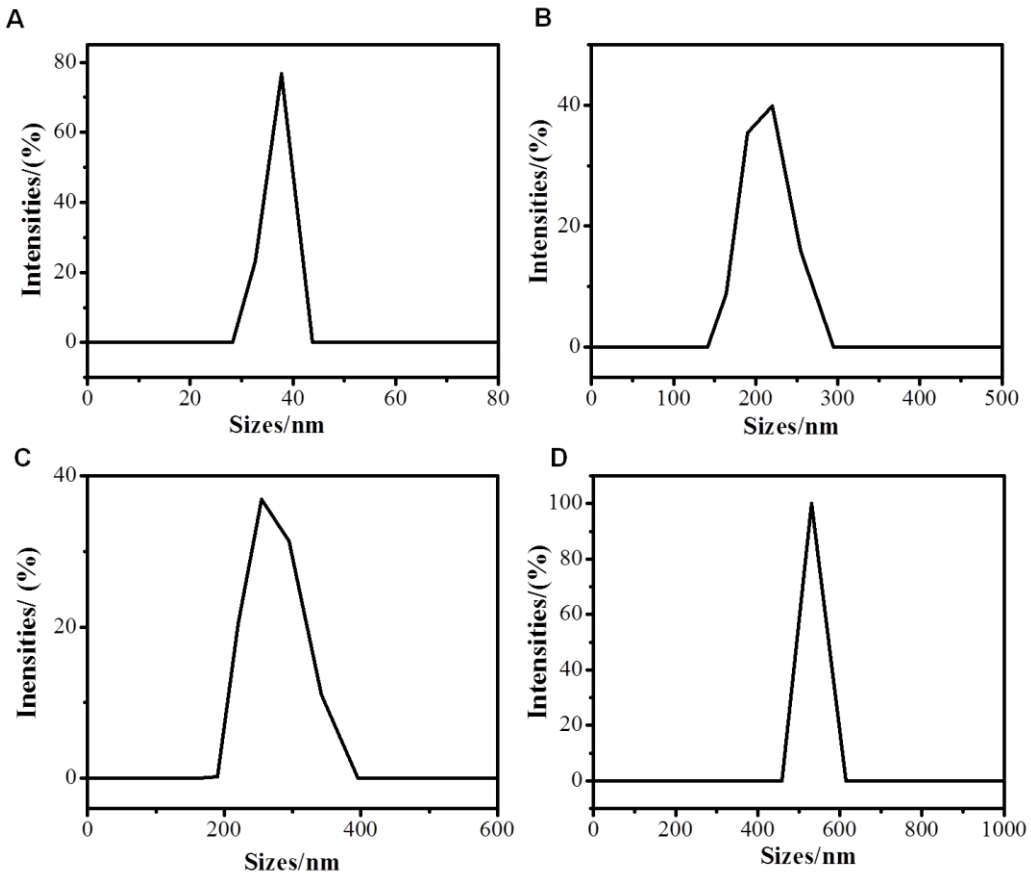

Figure 3.2 Dynamic light-scattering (DLS) studies of NCDP-1 at 500 mm (self-assembled chiral aggregates) in (A) HFIP (37 nm), (B) 5% DMSO in HFIP (210 nm), (C) 11% DMSO in HFIP (269 nm), and (D) 15% DMSO in HFIP (531 nm). Observed hydrodynamic size distributions are given in parentheses.

Quantum chemical calculations were carried out to further understand the magnitude of intermolecular interactions in all of the NCDP molecules (**1**-**6**) in their *M*- and *P*-helical supramolecular assembly states. Four dimer models were constructed for the *P*- and *M*-helices for NCDPs **1**-**6** from their respective monomers. The differences between the respective models lie in the conformational arrangement of the monomer units. Since these molecules have long linear side chains, several conformations are possible, of which four straightforward possibilities were considered. The interaction

Table 3.1 Relative energies (kcal/mol) of the *P*- and *M*- helical models of NCDP **1** dimers along with the interaction energies calculated at the PM7 (I_a) and M06/6-31+G* (I_b) levels of theory

Model	Relative energy	Interaction energy (I_a)	Interaction energy (I_b)
I-P	0.0(0.0)	-78.7	-74.9
II-P	15.7(16.1)	-63.0	-58.8
III-P	17.4(22.6)	-61.3	-52.3
IV-P	19.9(25.1)	-58.8	-49.8
I-M	17.4(18.0)	-61.2	-56.9
II-M	24.0(36.7)	-54.7	-38.2
III-M	43.7(56.8)	-35.0	-18.1
IV-M	51.5(65.6)	-27.2	-9.3

Relative energy values in parentheses correspond to the calculations carried out at M06/6-31+G level. I_a: Interaction energies calculated using the energies of the optimized dimers and those of the optimized monomer at PM7 level. I_b: Interaction energies calculated using the single point energy of the optimized dimers and those of the single point energy of the optimized monomer at M06/6-31+G* level (optimization done at PM7 level).

energies for all the models of the NCDP **1** molecule were calculated at the semiempirical PM7 and density functional M06/6-31+G* levels of theory. The results obtained at these two levels of theory were in reasonable agreement with each other (Table 3.1). The semiempirical PM7 method has been shown to reasonably capture nonbonded interactions involving both electrostatic and dispersion interactions.[69] Based on this, the other molecules were modeled at the computationally less expensive PM7 level of theory. The optimized geometries of the most stable *M*- and *P*-helical dimers for NCDP **1** are depicted in Figure 3.3. The interaction energies corresponding to the formation of such dimers

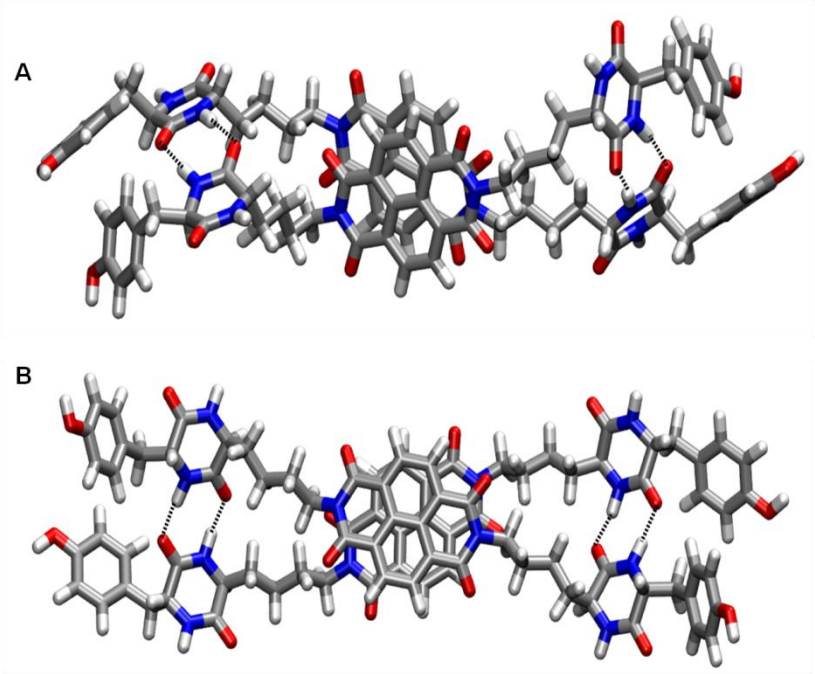

Figure 3.3 Optimized structures of (A) *P*-helical dimer (I-P) and (B) *M*-helical dimer (I-M) of NCDP **1**.

were found to be more favorable for the *P*-helices compared to the *M*-helices. Interestingly, the CD intensity of a P-helix at a given concentration of NCDP **1** in DMSO/HFIP was found to be higher than that of an M-helix of NCDP **1** in HFIP, indicating a higher stability of the former. Both the *P*- and *M*-helices of NCDP **1** dimer involve hydrogen-bonding interactions between the CDP amide groups. The hydroxyl groups of the tyrosine moieties in NCDP **1** are unlikely to form hydrogen bonds between them as the distance between the oxygen atoms of the two monomer units is about 4 Å. It should be noted that the *P*-helical models were found to be thermodynamically more stable than the *M*-helical assemblies. The stacking energy for the basic NDI stacked dimers was calculated to be 20 $kcalmol^{-1}$ at the M06/6-31+G* level of theory. Comparison of the interaction energies given in Table 3.1 indicates that the hydrogen-

Table 3.2 The interaction energies corresponding to the intermolecular hydrogen bonds formed between the monomers of the respective dimers which are the least energy conformers for all the six NCDP molecules under study using the second order perturbation analysis with the NBO method at HF/6-31G* level

	O1-NH	**O2-NH**	**O3-NH**	**O4-NH**
P_NCDP 1	22.10	26.03	31.87	22.57
P_NCDP 2	21.30	57.95	40.49	28.70
P_NCDP 3	21.68	31.66	34.74	22.16
P_NCDP 4	36.69	35.04	35.27	24.51
P_NCDP 5	17.89	30.02	25.88	14.23
P_NCDP 6	19.95	32.86	30.77	30.05
M_NCDP 1	26.76	25.32	29.95	25.26
M_NCDP 2	30.52	50.95	46.31	30.63
M_NCDP 3	22.18	26.52	22.43	17.12
M_NCDP 4	34.57	32.89	32.47	35.27
M_NCDP 5	21.87	28.80	32.05	20.04
M_NCDP 6	26.93	20.04	29.34	20.33

bonding interactions significantly contribute to the overall stability of the supramolecular assembly. The intermolecular hydrogen bonding between the amide groups of the constituent monomers of the corresponding dimers was also verified by calculating second-order perturbative interaction energies by means of natural bond orbital (NBO) analysis at the *ab initio* HF level using the 6-31+G* basis set. The interaction energies of the four amide groups are given in Table 3.2. From the data, it can be noted that there is strong intermolecular hydrogen bonding between the amide groups of the monomers.

Explicit calculations involving the solvent molecules are not practical to examine the role of the solvent in the *M*- to *P*-helical transition.

However, based on the computational results and experimental observations, possible determinants of the chiroptical switching may be proposed, as discussed below. The twist angles (helical twist between the two monomer units) calculated for the helical models were found to range between 35 and 40º. The hydrogen bond distances between the amide groups at either side of the monomer units were found to lie in the range 1.75-1.95 Å.

3.2.4 Effect of CDP substituent and chiral center on chiral helical assembly

Next, we probed the effect of α-substituent present in CDP chiral auxiliary, on the assembly properties of NCDPs. UV/Vis absorption studies of NCDPs **2**-**4** revealed aggregation characteristics similar to those of NCDP **1**. With increasing volume fraction of DMSO in HFIP increasing the volume fraction of DMSO in HFIP, NCDPs **2**-**4** (100 μM) showed decreases in absorbance and hypsochromic shifts in 300 - 400 nm region (Figure 3.4, 3.6A). NCDPs **2** and **3** (500 μM) showed monosignate negative CD signals in the region 300-400 nm in pure HFIP (*M*-helical assembly). Similar to NCDP **1**, NCDPs **2** and **3** showed chiroptical switching from a monosignate *M*-helical Cotton signal to a bisignate *P*-helical Cotton signal on increasing the volume fraction of DMSO in HFIP (Figure 3.5). Notably, the solvent compositions (DMSO/HFIP, v/v) giving the maximum positive Cotton signals were specifically different for NCDPs **1**-**3** (15:85, 30:70, and 40:60, respectively) (Figure 3.1C, 3.5). This variation in the solvent composition of DMSO/HFIP may be necessary to attain balanced polarity, hydrophobicity, and hydrogen bonding interactions to trigger chiroptical switching from *M*- to *P*-helical assemblies of

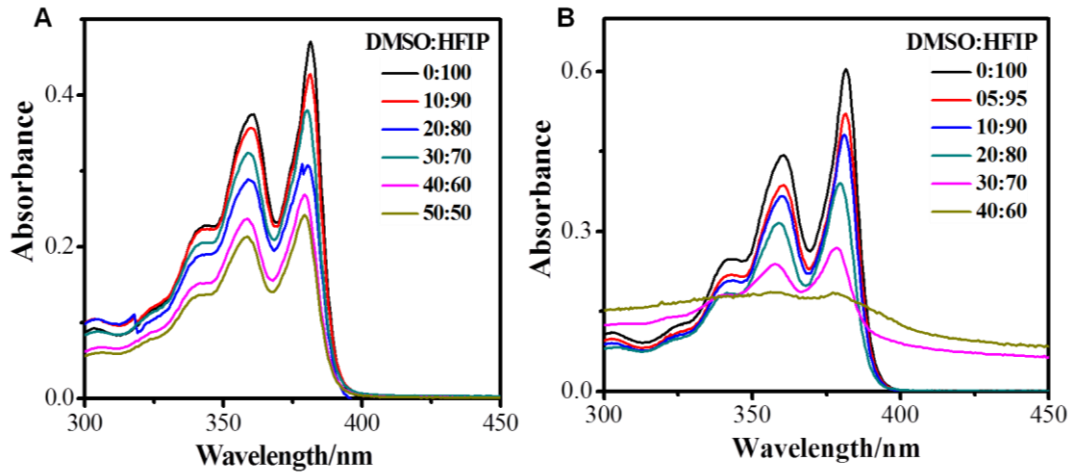

Figure 3.4 UV-Vis absorption spectra of (A) NCDP **2** and (C) NCDP **3** in HFIP at 100 μM concentration with increasing volume fraction of DMSO under ambient conditions.

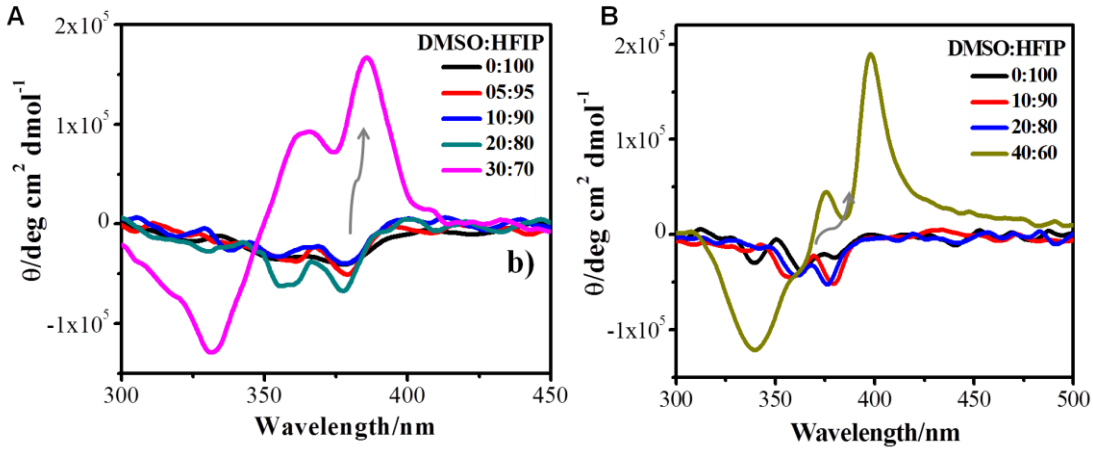

Figure 3.5 CD spectra of (A) NCDP **2** and (B) NCDP **3** in HFIP with increasing volume fractions of DMSO at 500 mm. Grey arrows indicate the chiroptical switching from *M*- to *P*-helical assemblies.

NCDPs **1-3** with different α-substituent. In general, these results suggest that the chiral assembly and chiroptical switching of NCDPs **1-3** is independent of the nature of the α-substituent (alkyl or aryl) of the second amino acid in CDP auxiliary.

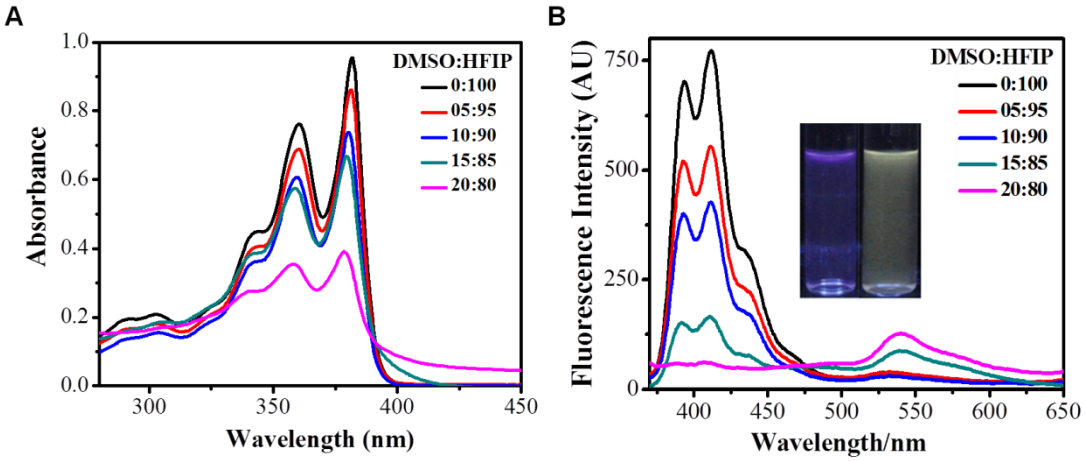

Figure 3.6 Photophysical studies of NCDP **4**. (A) UV-Vis absorption spectra of NCDP **4** in HFIP at 100 μM concentration with increasing volume fraction of DMSO under ambient conditions. (B) Fluorescence emission spectra of NCDP **4** in HFIP at 100 μM concentration with increasing volume fraction of DMSO under ambient conditions. Inset in (B) shows the photographs of NCDP-4 (100 μM) in HFIP (violet colour fluorescence) and in DMSO:HFIP (v/v 20:80) (yellow colour fluorescence).

The remarkable chiroptical switching phenomenon further encouraged us to investigate the effect of the chirality of the second amino acid in the CDP auxiliaries. Initially, we examined the effect of an achiral amino acid (Gly) on the chiral assembly and solvent-dependent chiroptical switching property of NCDPs. NCDP **4** with cyclo(*L*-Lys-Gly) served as an effective control to study the transfer of chiral information from a distant chiral center on *L*-lysine to the NDI core as well as to understand the influence of the second chiral center on the observed assembly properties of NCDPs **1-3**. In contrast to NCDPs **1-3**, NCDP **4** exhibited mirror image fluorescence emission in the region 380-450 nm in HFIP (Figure 3.6B). The monomeric emission band (380-450 nm) of NCDP **4** decreased with increasing volume fraction of DMSO in HFIP and subsequently, a new emission band at around 540 nm was observed, assigned to excimer-like aggregation.[59] At a solvent composition of DMSO/HFIP (v/v, 20:80), complete quenching of the

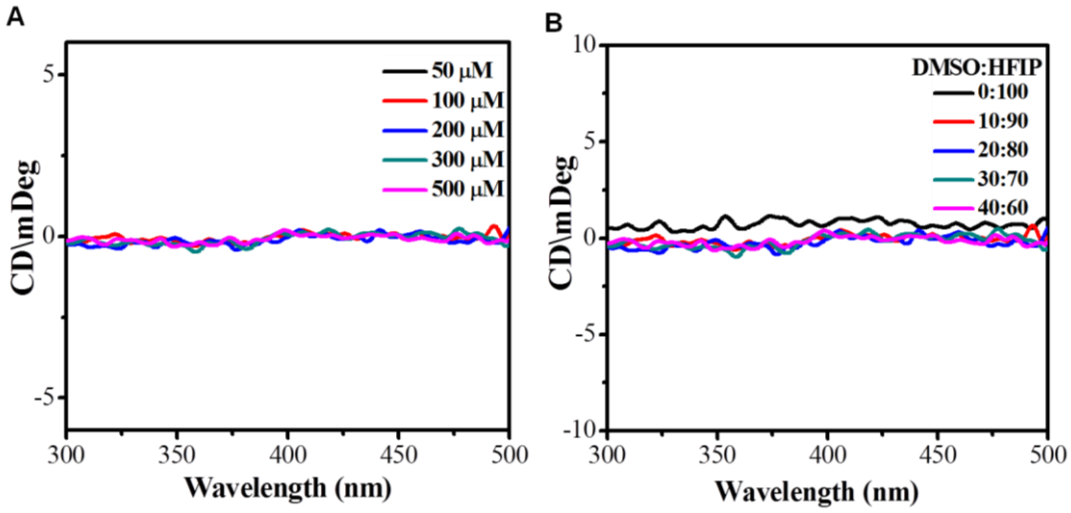

Figure 3.7 Chiroptical studies of NCDP **4**. **(**A) Concentration-dependent CD spectra of NCDP **4** (50-500 μM) in HFIP. (B) CD spectra of NCDP **4** in HFIP at 500 μM concentration with increasing volume fraction of DMSO.

monomeric emission band was observed, accompanied by a color change of the solution from violet (monomeric emission) to yellow (excimer-like emission) under UV light.

Flat CD signals were observed for NCDP **4** at all concentrations and solvent combinations of DMSO/HFIP studied, indicating the absence of chiral bias or switching property in its supramolecular assembly (Figure 3.7). The absence of any chiral bias and chiroptical switching in NCDP **4**, may be attributed to the perfectly symmetrical nature of the resultant assembly. The absence of a bulky α-substituent and chiral center on the second amino acid of CDP auxiliary lead to insignificant interconversion energy between the *M*- and *P*-helical assemblies. These results clearly emphasize the crucial role of chiral center as well as the bulky α-substituent on the CDP auxiliary second amino acid with regard to the solvent-induced preferential helical bias and chiroptical switching behavior of NCDP supramolecular assemblies.

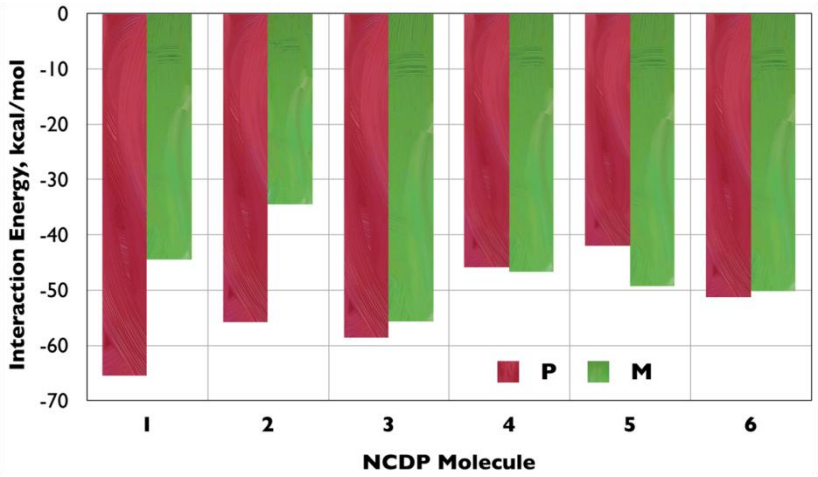

Figure 3.8 Average interaction energies for the *P*- and *M*-helical dimers for all six molecules (NCDPs **1**-**6**) calculated at the PM7 level of theory.

The origin of the distinct behavior of NCPD **4** compared to the other three NCDPs (**1**-**3**) discussed above were examined by further quantum chemical calculations. The average interaction energies for the four *P*- and *M*-type helical dimer models of the six NCDP molecules are represented in Figure 3.8. From the data, it is observed that for NCDPs **2** and **3**, the *P*-helical dimer is thermodynamically more stable than the *M*-helical dimer as in the case of NCDP **1**. The structures of the most stable *P*- and *M*-helical dimers at the PM7 level of theory, along with the hydrogen bonds between the amide groups (data not shown). The twist angles and the hydrogen-bonding distances between the cyclic dipeptide moieties calculated for the other models were found to be similar to those obtained for NCDP **1**. Interaction energy calculations on dimers of NCDP **4** indicated comparable stabilities for both the *P*- and *M*-forms (Figure 3.8). Visual inspection of the modeled structures indicates that the *P*- and *M*-forms of the supramolecular assembly of NCDP **4** are very similar (Figure 3.9). Hence, molecules of NCDP **4** are likely to be arranged almost equally in both forms, resulting in no CD signal, as observed experimentally. The intermolecular hydrogen-bonding interaction energies for the most

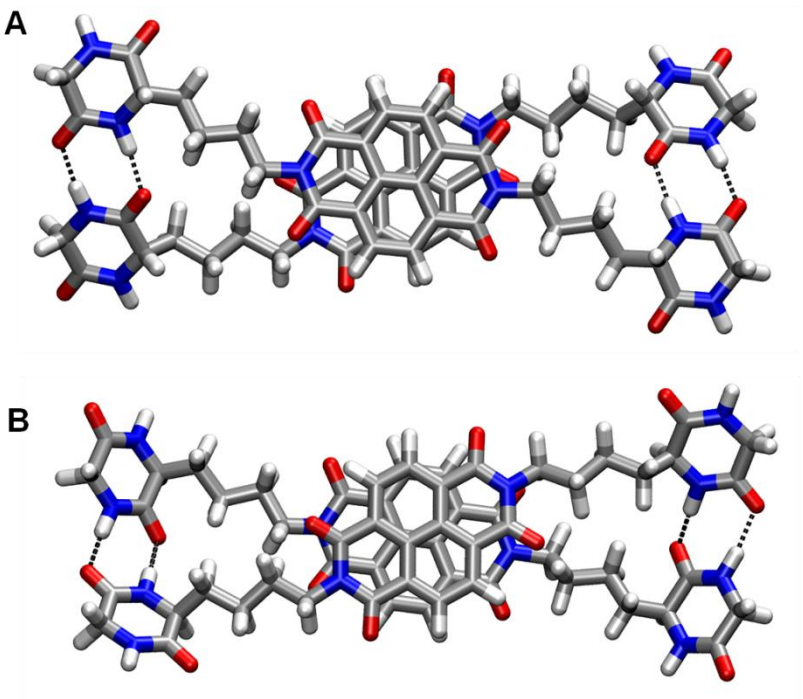

Figure 3.9 Optimized structures of a) *P*-helical dimer (I-P) and b) *M*-helical dimer (I-M) of NCDP **4**.

stable dimers of the above molecules are given in Table 3.2.

We further investigated, the effect of a change in chirality of second amino acid in the CDP auxiliary over the solvent-dependent chiral assembly and chiroptical switching of the NCDP aggregates. NCDPs **5** and **6** (epimers of NCDP **1** and **2**) with *D*-Tyr and *D*-Phe, respectively, at 100 µM concentration exhibited a decrease in the absorbance intensity and a slight hypsochromic shift with increasing volume fraction (v/v) of DMSO in HFIP, due to solvent-induced aggregation (Figure 3.10). The CD spectra of NCDPs **5** and **6** at 500 µM in HFIP showed flat CD signals in the region 300-400 nm, indicating no specific helical bias in their molecular assemblies. NCDPs **5** and **6** did not show any significant spectral changes upon increasing the volume fraction of DMSO (v/v) in HFIP, except that the flat CD signals in HFIP gradually became weak negative CD signals (Figure 3.11). The average interaction energies for NCDPs **5** and **6** are given in Figure 3.8

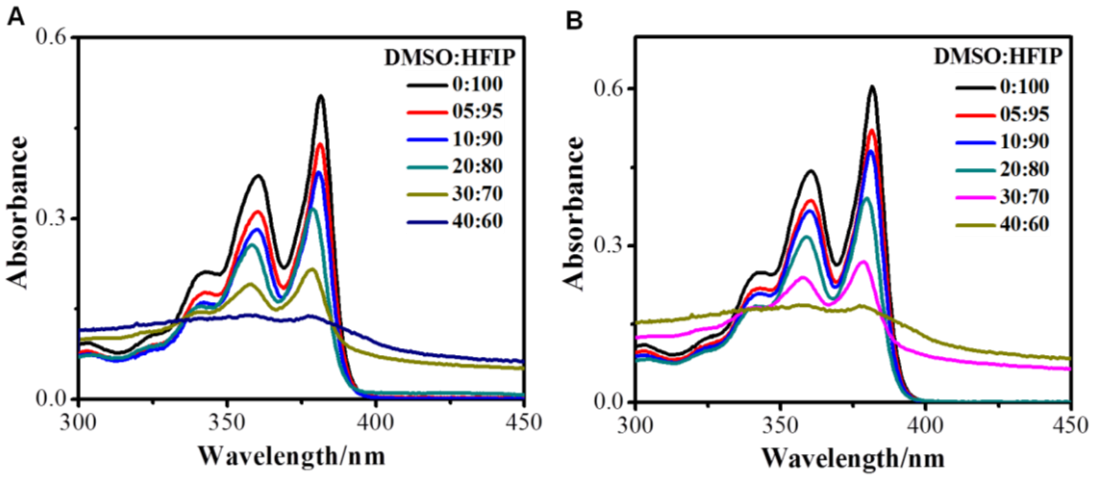

Figure 3.10 Photophysical studies of NCDPs **5** and **6**. UV-Vis absorption spectra of NCDP **5** (A) and NCDP **6** (B) in HFIP at 100 μM concentration with increasing volume fraction of DMSO under ambient conditions.

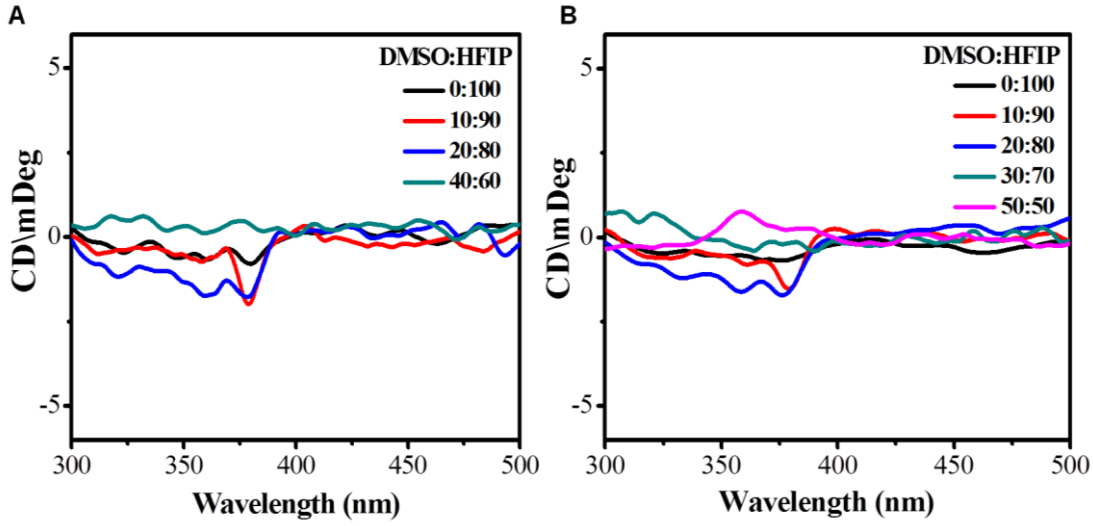

Figure 3.11 Chiroptical studies of NCDPs **5** and **6**. CD spectra of NCDP **5** (A) and NCDP **6** (B) in HFIP at 500 μM concentration with increasing volume fraction of DMSO.

from which it is apparent that the *M*-helical dimer was marginally more stable than the *P*-helical dimer in both cases. The helical angles and hydrogen-bonding distances were in similar ranges to those of the other molecules. Intermolecular hydrogen bonding interaction energies for the amides of the two (Table 3.2) are indicative of strong

bonding between them, leading to dimers, in addition to π-stacking interactions.

NCDPs **5** and **6** with *D*-amino acids in the second position of their CDP auxiliaries did not display significant CD signals due to mismatched chiral centers on the two amino acids of the CDP auxiliary, resulting in random aggregation. Thus, NCDPs **4**-**6** with no significant CD features in HFIP did not exhibit chiroptical switching in the mixed solvent (DMSO/HFIP). This confirmed that α-substituent and the chirality of the amino acid play an essential role in the solvent-induced helical chirality and chiroptical switching of the supramolecular assemblies of NCDPs. Therefore, the observed chiral aggregation of NCDPs **1**-**3** in HFIP is due to the clustering and stabilization of *M*-type helical assemblies, which is influenced by the α-substituent and the chirality (*L*) of amino acids in the CDP auxiliary. The chiroptical switching behavior of NCDPs **1**-**3** in DMSO/HFIP can be attributed to an effective local contribution of DMSO through the hydrophobic effect of its methyl groups and possible hydrogen bonding as an acceptor in reorganizing the HFIP clusters around the NCDP assembly, among other bulk effects of the mixed solvent.[70]

3.2.5 NMR studies

Intermolecular hydrogen bonding (CDP auxiliary) in NCDP **4** was validated through temperature dependent NMR studies. Variable-temperature ^{1}H NMR spectra were recorded. NCDP **4** showed upfield shifts of the CDP amide signals at δ = 8.18 and 7.98 ppm to δ = 7.91 and 7.72 ppm, respectively, on increasing the temperature from 25 to 80 ºC, which confirmed the hydrogen bonding network in its assembled structure (Figure 3.12). Similar upfield shifts of the amide signals from δ = 8.05 and 8.01 ppm to δ = 7.78 and 7.67 ppm on increasing the temperature from 25 to 80 ºC were observed for NCDP **1**

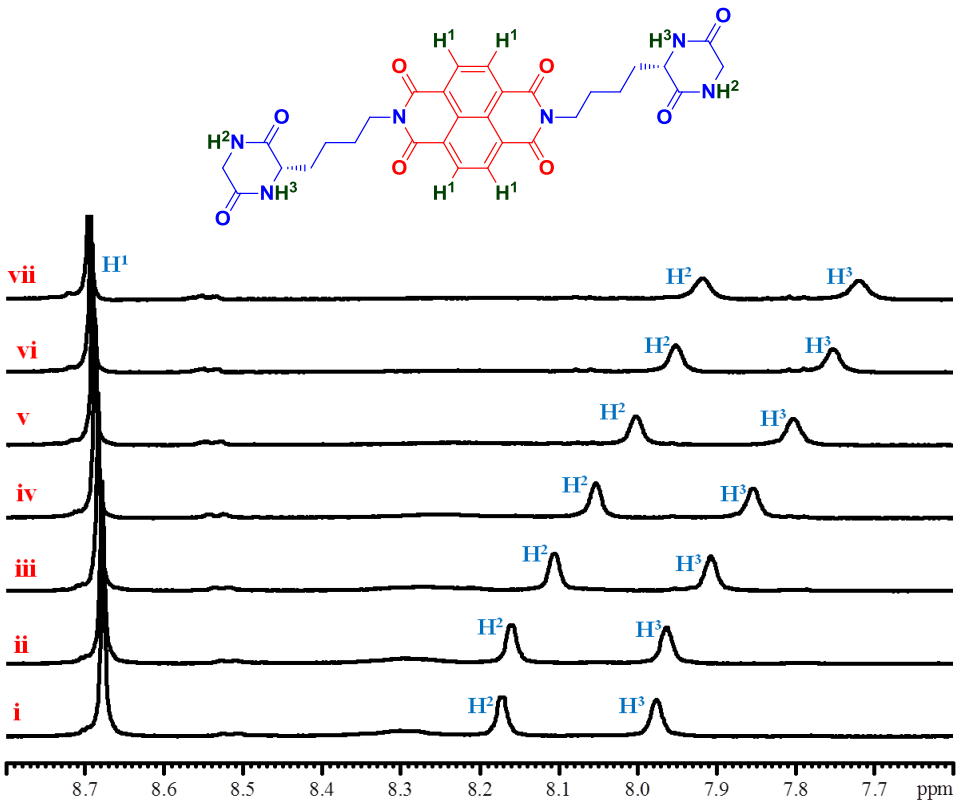

Figure 3.12 Temperature dependent ^{1}H NMR spectra (partial) of NCDP **4 (**5.97 mM) in DMSO-d_6. i: 25 ºC, ii: 30 ºC, iii: 40 ºC, iv: 50 ºC, v: 60 ºC, vi: 70 ºC, vii: 80 ºC.

(Figure 3.13A). Concentration-dependent ^{1}H NMR spectra of NCDP **1** in DMSO-d_6 revealed the presence of strong intermolecular π-π stacking of the NDI chromophores and hydrogen-bonding between the CDP units of NCDP, as evidenced by a downfield shift of the CDP amide proton signals accompanied by an upfield shift of the NDI chromophore proton signals with increasing concentration (Figure 3.13B).

3.2.6 Reversible chiroptical switching studies

We further investigated the reversibility of observed chiroptical switching of NCDP **1** between *M*- and *P*-type helical assemblies by carrying out CD studies in HFIP and DMSO/HFIP (15:85, v/v) in cycles. Specifically, the CD spectrum of NCDP-1 (500 µM

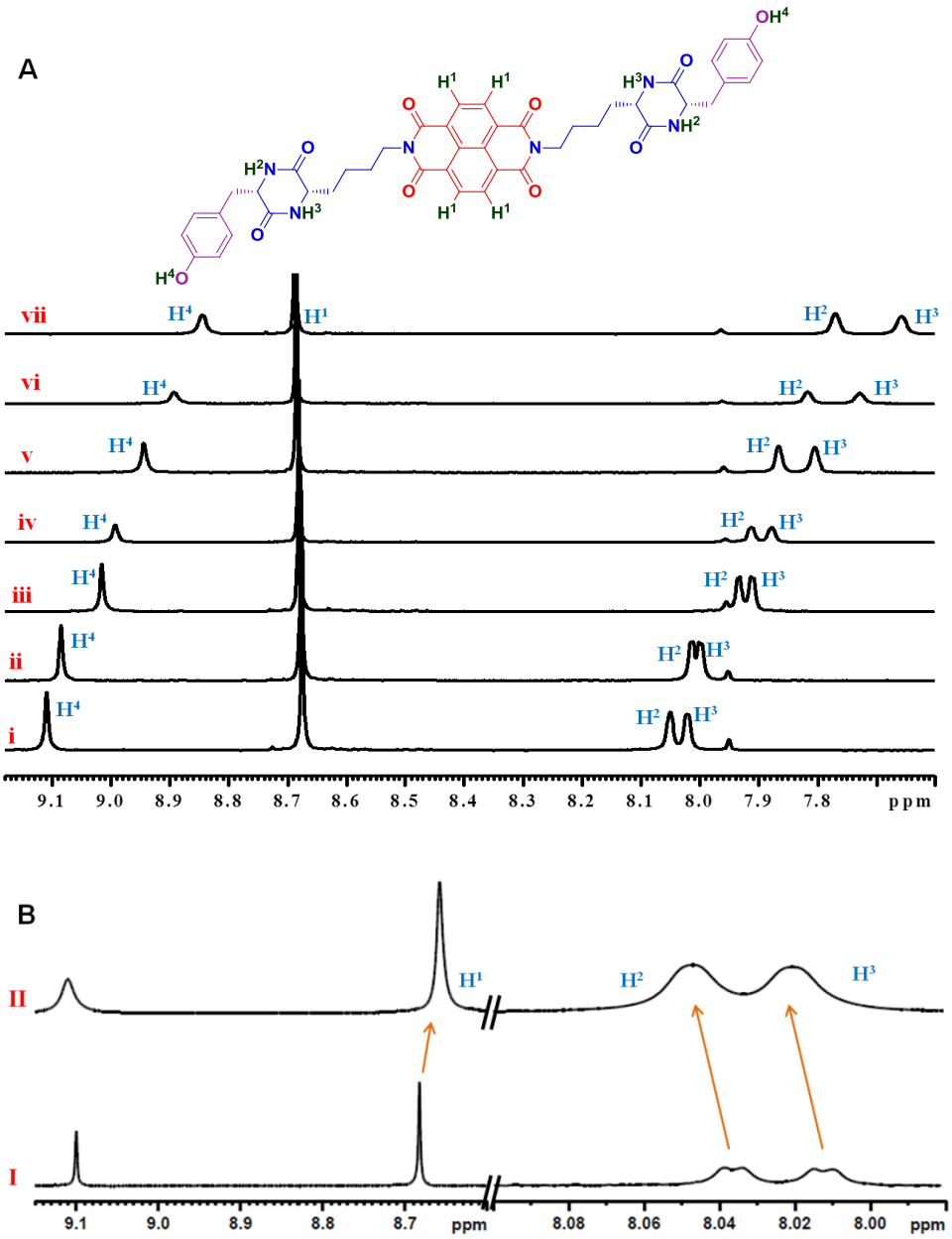

Figure 3.13 NMR studies of NCDP **1**. (A) Temperature dependent ^{1}H NMR spectra (partial) of NCDP **1** (4.02 mM) in DMSO-d_6. (B) Concentration dependent ^{1}H NMR spectra of NCDP **1**. i: 25 °C, ii: 30 °C, iii: 40 °C, iv: 50 °C, v: 60 °C, vi: 70 °C, vii: 80 °C.; I: 0.18 mM, II: 13.8 mM.

in HFIP) was recorded and the solvent was removed in vacuum. The residue was re-dissolved in DMSO/HFIP (15:85, v/v) and CD spectrum recorded to complete the first cycle. For the next cycle, the mixed solvent (DMSO/HFIP) was removed in vacuum, the residue was redissolved in HFIP, and the CD spectrum was recorded. This procedure was

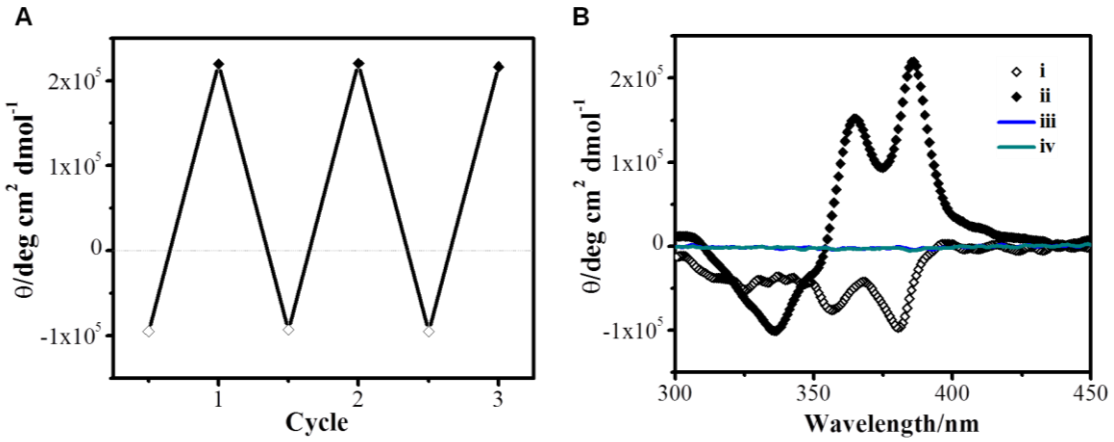

Figure 3.14 Solution and drop-cast thin film CD spectra of NCDP **1**. (A) CD intensity spotted against each cycle of study for NCDP **1** at 500 μM concentration in HFIP (◊ λ = 380 nm) and DMSO: HFIP (v/v 15:85, ♦ λ = 385 nm). (B) CD spectra of NCDP **1** at 500 μM in solution (i and ii) and drop-cast thin films (iii and iv, solid lines). NCDP **1** (500 μM) in solution i: HFIP, ii: DMSO:HFIP(v/v 15:85) and thin films (drop cast) from iii: HFIP and iv: DMSO:HFIP (v/v 15:85).

followed over further cycles and the complete data is shown in Figure 3.14A. This study clearly demonstrated the reversibility of the solvent-induced chiroptical switching, as reflected by the retention of CD features for NCDP **1** in HFIP (*M*-helicity) and DMSO/HFIP (*P*-helicity) even after three cycles of solvent removal and redissolution (Figure 3.14A). In addition, CD spectra of NCDP **1** thin films were recorded to further ascertain the observed solvent-induced reversible chiroptical switching. Thin films were prepared by drop-casting NCDP **1** from the corresponding solutions from HFIP and DMSO/HFIP (v/v, 15:85) onto quartz substrates. The CD spectra of the thin films showed flat signals indicating the absence of chiral bias in the solid state, further emphasizing the crucial role of the solvent in helical assembly and reversible chiroptical switching of the NCDPs (Figure 3.14B).

Table 3.3 Molecular structures of various solvents which induced chiral switching of *M*-helical aggregates of NCDP **1** (500 μM) in HFIP and % volume fractions of each solvent in HFIP to achieve maximum positive Cotton signal upon chiral inversion.

Solvent	Solvent Structure	% Volume fraction of cosolvent in HFIP (at maximum inversion)
Dimethyl sulfoxide		15%
Acetone		25%
2-Pentanone	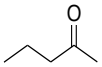	25%
3-Pentanone	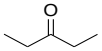	25%
Cyclopentanone	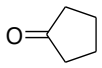	25 %
Cyclohexanone	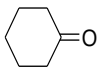	30 %
Isopropanol		35%

3.2.7 Isostructural solvent effects

The intriguing solvent (DMSO/HFIP)-induced chiroptical switching of self-assembled chiral aggregates of NCDPs prompted us to further generalize this effect in other solvent systems. The addition of solvents such as chloroform, dichloromethane, or *N*-methyl-2-pyrrolidone (NMP) failed to induce chiroptical switching of the *M*-helical aggregates of NCDP **1** in HFIP. Next, we examined isostructural (ketone and alcohol) solvents such as acetone, 2-pentanone, 3-pentanone, cyclopentanone, and cyclohexanone, as they possess variable linear or cyclic alkyl substituents on the C=O functionality (Table 3.3), as well as

2-propanol (isopropanol). The CD spectra of NCDP **1** (500 μM) in HFIP with varying volume fractions of the above-mentioned solvents were recorded. Remarkably, all of these solvents showed chiroptical switching similar to that seen in the DMSO/HFIP system (data not shown). Interestingly, the volume fractions required to obtain the maximum positive Cotton signal upon chiral inversion varied with each solvent combination (25% acetone, 25% 2-pentanone, 25% 3-pentanone, 25% cyclopentanone, 30% cyclohexanone, and 35% isopropanol in HFIP). These results revealed that the solvent composition required to induce the maximum chiral inversion was the same for all of the ketones (except cyclohexanone), that is, 25% in HFIP. Notably, isopropanol, the nonfluorinated isostructural analog of HFIP, exhibited a completely opposite effect by inducing chiroptical switching of the *M*-helical assembly of NCDP **1** in HFIP to the thermodynamically more stable *P*-helical assembly (Figure 3.15). This result may have broader implications for understanding the distinct role of fluorinated solvents compared to their non-fluorinated analogs. Overall, the above CD data are in agreement with the changes observed for NCDP **1** in DMSO/HFIP and show the generality of the chiroptical switching phenomena in HFIP containing solvents isostructural to DMSO.

Though the *P*-helical dimer was found to be thermodynamically more stable in the case of NCDPs **1**-**3**, *M*-helical supramolecular complexes were observed in the CD spectroscopic studies in HFIP. However, with the gradual addition of DMSO, the *P*-helical complexes were formed. It is proposed that hydrogen-bond dynamics and hydrophobic effects within the supramolecular complex and with the solvent play major roles in this chiral reversal. Based on quantum chemical/DFT calculations and spectroscopic studies, it has been proposed that the helix-stabilizing effect of specific compositions of HFIP in peptides can be attributed to a clustering and coating effect, entropic and enthalpic factors, and variations in the kinetics of conformational

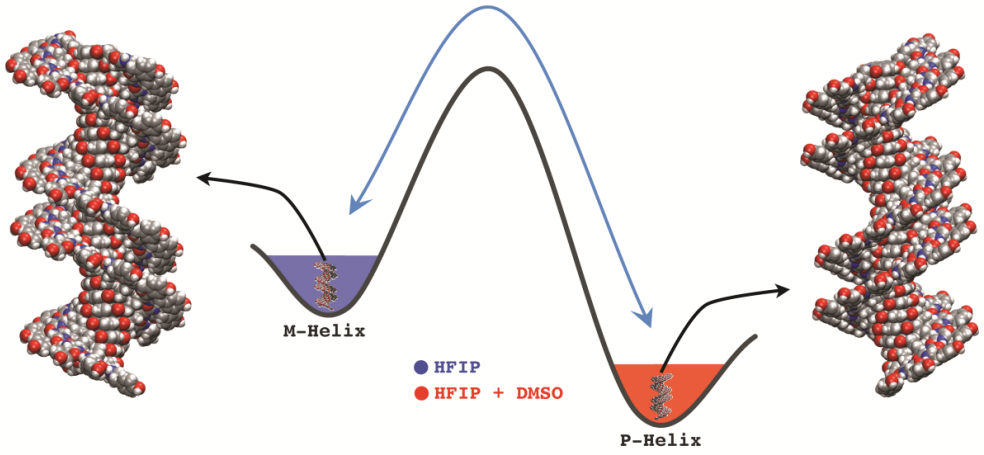

Figure 3.15 Schematic showing the solvent dependent reversible chiral helical assembly of NCDP **1**.

changes.[64-66] It is reasonable to postulate that similar effects are operative in the initial stabilization of the *M*-helical assemblies of NCDPs **1**-**3**. It is possible that the amide groups (both C=O and N-H) of NCDP in the less stable *M*-helix may form intermolecular hydrogen bonds, both with each other and with the solvent cluster. In such a scenario, the energy difference between the M- and P-helices will be compensated by the hydrogen bonding with the solvent, as well as by entropic and enthalpic factors. In the mixed solvent, the DMSO molecules reorganize the solvent cluster of HFIP through hydrogen bonding and localized hydrophobic effects, which drive the switching from the initial *M*-type to the thermodynamically more stable *P*-type helical assembly. Chiral reversal is not observed in NCDP **5** and **6** since the energy differences between the two states are calculated to be not so significant (Figure 3.8). In these two cases, the marginally more stable *M*-helical form is observed experimentally. Similar findings were observed by Faul *et al.* in a symmetrical sugar-based perylenediimide derivative, whereby a *P*-helical model was thermodynamically more stable than the *M*-helix.[16]

3.3 Conclusion

In summary, symmetrical naphthalenediimides with CDP chiral auxiliaries (NCDPs) have been designed, synthesized and studied to orchestrate the preferential supramolecular helical assembly. The contributions of intermolecular aromatic π-stacking and hydrogen-bonding interactions have been established by various experimental studies and quantum chemical calculations. The solvent-dependent helical supramolecular assembly and chiroptical switching (*M*- to *P*-type) of NCDP assemblies have been validated through a series of concentration-, solvent-, and temperature-dependent CD studies. NCDPs **1**-**3** formed *M*-helical assemblies in HFIP, which underwent chiral inversion to form thermodynamically more stable P-helical assemblies in DMSO/HFIP mixtures. Further CD studies revealed the significance of α-substituent and the chirality of corresponding peripheral amino acid in the CDP auxiliary with regard to solvent-induced helical assembly and the chiroptical switching properties of NCDPs. The characteristic chiroptical switching of the helical assembly of NCDP is reversible and can be reversibly transformed between *M*- and *P*-helices by solvent exchange cycles. Overall, the remarkable helical assembly characteristics of the NCDPs reported herein demonstrate the crucial role of the CDP chiral auxiliary. We hope that the present study might inspire the development of novel chiral auxiliaries to master the art of preferential helical assembly of designed supramolecular synthons so as to obtain smart self-assembled systems and materials, as well as for chiroptical applications.

3.4 Experimental Section

Materials. Amino acids and coupling reagents were obtained from Novabiochem (Merck) and Spectrochem India, respectively. All other chemicals, solvents, and analytical grade reagents were obtained either from Sigma-Aldrich or Spectrochem and

were used as received without any further purification unless otherwise mentioned specifically. Ultrapure milli-Q water was used for extractions during synthesis. Thin Layer Chromatography (TLC) was performed using TLC Silica gel 60 F254 silica plates from Merck and visualization of the compounds was achieved using UV light (254 and 365 nm) and ninhydrin treatment

NMR spectroscopy. ^{1}H and ^{13}C NMR spectra were recorded on a Bruker AV-400 spectrometer in $CDCl_3$, DMSO-d_6 or D_2O at 300 K. Chemical shifts (δ) are reported in parts per million (ppm) with respect to residual solvent peak and coupling constant (*J*) values are reported in hertz (Hz). The multiplicity of NMR signal are represented as s = singlet, d = doublet, t = triplet, q = quartet, dd = doublet of doublet and m = multiplet.

NMR experiments. Concentration-dependent ^{1}H NMR experiments for NCDPs was performed by recording the NMR spectra with various defined concentrations of NCDPs at 300 K in DMSO-d_6. Variable-temperature ^{1}H NMR (VT-NMR) experiments for NCDPs were performed at temperatures 25, 30, 40, 50 60 70 and 80 ºC using DMSO-d_6 as solvent at a specified concentration.

Elemental analysis. Elemental analysis of vacuum dried NCDPs was carried out on a Thermo Scientific FLASH 2000 organic element analyzer.

Mass spectrometry (MS*)*. Mass spectra were obtained on a Bruker Ultraflex II MALDI-TOF spectrometer.

Absorption spectroscopy. UV-vis spectra were recorded on a Perkin Elmer Model Lambda 900 spectrophotometer. NCDP solutions at specified concentrations were analyzed using a quartz cuvette of 1 mm path length under ambient conditions.

Fluorescence spectroscopy. Fluorescence spectra were recorded on a Perkin Elmer Model LS 55 spectrophotometer. NCDP solutions at specified concentrations were analyzed using a quartz cuvette of 1 mm path length with the mentioned excitation and emission wavelengths under ambient conditions.

Circular and linear dichroism. NCDP solution, thin-film circular dichroism (CD) and linear dichroism (LD) measurements were performed on a JASCO J-815 spectropolarimeter under N_2 atmosphere using 1 mm or 10 mm path length quartz cuvettes.

Dynamic light-scattering. Dynamic light-scattering (DLS) measurements were carried out on a NanoZS analyzer (Malvern, UK) under ambient conditions.

Computational details. The monomers for all six models under study (NCDPs **1**-**6**) were modeled using the GaussView 05 program.[71] *P*- and *M*-helical dimers were modeled from the initial monomer structure. The *P*-helical dimers were modeled by placing the second monomer at a distance of 3 Å from the first monomer and then rotating the second monomer in the anticlockwise direction by 30º. A twist angle of 30º was chosen on the basis of M06/6–31+G* optimization of the dimer of naphthalenediimide. Similarly, the *M*-helical dimer was also modeled in the same way by rotating the second monomer in the clockwise direction. The monomer and the two resultant dimers were then optimized at the PM7 level of theory using the MOPAC 2012 program.[72] Based on test calculations, we considered up to four different conformations for each molecule under study. Furthermore, the optimized monomer and the dimers of NCDPs **1** and **2** were further subjected to single-point energy calculations at the M06 level of theory using the 6-31+G* basis set and the Gaussian 09 program.[73,74] The interaction energies were calculated as the differences between the energies of the dimers and the monomers. The

donor-acceptor interactions between the individual monomers resulting in the formation of the dimers were analyzed for all of the NCDP molecules under study using natural bond orbital (NBO) analysis carried out at the ab initio HF level of theory using the 6-31+G* basis set. The NBO analysis was carried out using the NBO program 3.1 included in the G09 suite of programs.[75]

Preparation of *L*-Tyr-OCH$_3$.HCl (3). Methanol (20 mL) was taken in a two-necked round-bottomed flask fitted with a reflux condenser and an addition funnel, cooled to ice cold temperature. *L*-Tyrosine (1.0 g, 5.51 mmol) was dispersed in above ice-cooled methanol and thionyl chloride ($SOCl_2$) (0.98 g, 8.27 mmol) was added dropwise, stirred at ice cold temperature for 30 min and then refluxed at 80 ºC for 4 h. The reaction progress was monitored by thin layer chromatography (TLC), after the completion of reaction solvent was removed under vacuum to yield **7** as white solid in quantitative yield (1.22 g, 96% yield). ^{1}H NMR (DMSO-d_6, 400 MHz) δ_{ppm} 2.96-3.09 (m, 2H), 3.67 (s, 1H), 4.13-4.16 (t, J = 6.3 Hz, 1H), 6.71-6.73 (d, J = 8.5, 2H), 6.9-7.0 (d, J = 8.5, 2H), 8.61 (s, 3H), 9.46 (s, 1H); ^{13}C NMR (DMSO-d_6, 100 MHz) δppm 35.0, 52.5, 53.4, 115.4, 124.3, 130.3, 156.6, 169.4.

Preparation of Fmoc-*L*-Lys(*t*Boc)-*L*-Tyr-OCH$_3$.HCl (11). Fmoc-*L*-Lys(*t*Boc)-OH (0.80 g, 1.70 mmol), hydroxybenzotrizole (0.34 g, 2.56 mmol) and 1-(3-dimethylaminopropyl)-3-ethylcarbodiimide hydrochloride (0.49 g, 2.56 mmol) were dissolved in dichloromethane (20 mL) and cooled to ice temperature. *L*-tyrosine methyl ester hydrochloride (**3**) (0.47 g, 2.04 mmol) and *N*,*N*-diisopropylethylamine (1.54 g, 11.95mmol) were added and the reaction mixture was stirred at ice temperature for 1 h and then at room temperature for 3 h. The reaction progress was monitored by TLC. Reaction mixture was evaporated to dryness and residue was extracted from

dichloromethane, washed with water, dried over anhydrous sodium sulphate. Solvent was evaporated under vacuum and the crude product was purified on silicagel column chromatography with MeOH/$CHCl_3$ (v/v: 1.2/98.8) as eluent to obtain **11** as a white powder in very good yield (0.94 g, 86%). ^{1}H NMR ($CDCl_3$, 400 MHz) δ_{ppm} 1.08-1.21(m, 2H), 1.44 (s, 9H), 1.50-1.73 (m, 5H), 3.00-3.11 (m, 4H), 3.71 (s, 3H), 4.02 (b, 1H), 4.18-4.21 (t, *J* = 6.5 Hz, 1H), 4.39-4.43 (m, 2H), 4.68 (b, 1H), 4.80 (b, 1H), 5.38 (b, 1H), 6.50 (b, 1H), 6.71-6.73 (d, *J* = 7.1 Hz, 2H), 6.91-6.93 (d, *J* = 8.4 Hz, 2H), 7.28-7.32 (t, *J* = 7.4 Hz, 2H), 7.37-7.41 (t, *J* = 7.4 Hz, 2H), 7.57-7.58 (d, *J* = 6.8 Hz, 2H), 7.74-7.76 (d, *J* = 6.8 Hz, 2H); ^{13}C NMR ($CDCl_3$, 100 MHz) δ_{ppm} 22.4, 28.5, 29.7, 32.2, 37.0, 40.2, 47.2, 52.5, 67.2, 77.3, 115.9, 120.1, 125.2, 125.2, 127.1, 127.2, 127.9, 130.4, 141.4, 143.9, 156.2, 156.6, 171.3, 172.0.

Preparation of *cyclo*(*L*-Lys(*t*Boc)-*L*-Tyr) (12). The linear dipeptide Fmoc-*L*-Lys(*t*Boc)-*L*-Tyr-OCH_3 (**11**) (0.80 g, 1.21 mmol) was dissolved in piperidine-DCM (v/v, 20:80, 20 mL) and stirred at room temperature for 8 h. The reaction progress was monitored by TLC. The precipitate formed was filtered washed with methanol, acetonitrile and dried under vacuum to yield **12** in good yield as a white powder (0.36 g, 76%). ^{1}H NMR (DMSO-d_6, 400 MHz) δ_{ppm} 0.69-0.86 (m, 3H), 1.06-1.16 (m, 3H), 1.36 (s, 9H), 2.70-2.78 (m, 3H), 2.98-3.0 (m, 1H), 3.53 (b, 1H), 4.06 (b, 1H), 6.62-6.64 (d, *J* = 8.4, 3H), 6.91-6.93 (d, *J* = 8.4, 2H), 7.97 (b, 1H), 8.00 (b, 1H), 9.13 (b, 1H); ^{13}C NMR (DMSO-d_6, 100 MHz) δ_{ppm} 21.1, 25.7, 28.2, 29.0, 33.1, 37.4, 53.7, 55.5, 77.3, 114.7, 126.0, 131.1, 155.4, 156.2, 166.3, 167.0.

Preparation of *cyclo*(*L*-Lys-*L*-Tyr)-NDI-*cyclo*(*L*-Lys-*L*-Tyr) (NCDP 1). *cyclo*(*L*-Lys(*t*Boc)-*L*-Tyr) (**12**) (0.20 g, 0.25 mmol) was dissolved in TFA-DCM (v/v, 1:1, 5 mL), triisopropylsilane (TIPS, 0.2 mL) and the resulting reaction mixture was stirred at room

temperature for 4 h. The reaction progress was monitored by TLC. Reaction mixture was evaporated to dryness and co-evaporated thrice with toluene to yield **13** as a white solid in an excellent yield (0.20 g, 95%) and used as such without any further purification. 1,4,5,8-naphthalenetetracarboxylic dianhydride (60 mg, 0.22 mmol) and *cyclo*(*L*-Lys-*L*-Tyr)(10) (0.20 g, 0.49 mmol) were dissolved in *N*,*N*-dimethylformamide (20 mL). *N*,*N*-diisopropylethylamine (60 mg, 0.49 mmol) was added and refluxed at 80 ºC for 12 h. The reaction progress was monitored by TLC. Reaction mixture was cooled to room temperature and the precipitate was filtered, washed with methanol, acetonitrile and dried under vacuum to yield NCDP **1** as dark brown solid in good yield (130 mg, 76%). ^{1}H NMR (DMSO-d_6, 400 MHz) δ_{ppm} 0.92-0.93 (m, 6H), 1.12-1.21 (m, 4H), 1.42 (b, 4H), 2.98-3.30 (m, 2H), 3.62 (b, 2H), 3.88-3.92 (t, *J* = 7.4, 4H), 4.07 (b, 2H), 6.61-6.63 (d, *J* = 8.3, 4H), 6.92-6.94 (d, *J* = 8.3, 4H), 8.02 (s, 2H), 8.04 (s, 2H), 8.66 (s, 4H), 9.10 (s, 2H); MALDI-TOF = m/*z* 837.29 $[M+Na]^+$, 853.26 $[M+K]^+$; Elemental analysis. Found: C, 64.84; H, 5.27; N, 10.30; Calcd: C, 64.86; H, 5.20; N, 10.31 for $C_{44}H_{42}N_6O_{10}$.

Preparation of *L*-Phe-OCH$_3$.HCl (5). Methanol (20 mL) was taken in a two-necked round-bottomed flask fitted with a reflux condenser and an addition funnel, cooled to ice cold temperature. *L*-Phenylalanine (1.0 g, 6.20 mmol) was dispersed in above ice-cooled methanol and thionyl chloride ($SOCl_2$) (1.10 g, 9.30mmol) was added dropwise, stirred at ice cold temperature for 30 min and then refluxed at 80 C for 4 h. The reaction progress was monitored by TLC, after the completion of reaction solvent was removed under vacuum to yield **5** as white solid in quantitative yield (1.28 g, 98%). ^{1}H NMR (D_2O, 400 MHz) δ_{ppm} 3.25-3.41 (m, 2H), 3.88 (s, 3H), 4.46-4.49 (m, 1H), 7.33-7.35 (m, 2H), 7.41-7.50 (m, 3H); ^{13}C NMR (D_2O, 100 MHz) δ_{ppm} 35.6, 53.5, 54.1, 128.1, 129.3, 129.4, 133.7, 170.1.

Preparation of Fmoc-*L*-Lys(*t*Boc)-*L*-Phe-OCH$_3$ (14). Fmoc-*L*-Lys(*t*Boc)-OH (1.0 g, 2.13 mmol), 1-(3-dimethylaminopropyl)-3-ethylcarbodiimide hydrochloride (EDC. HCl; 0.61 g, 3.2 mmol) and hydroxybenzotrizole (0.43 g, 3.20 mmol) were dissolved in dichloromethane (25 mL) and cooled to ice temperature. *L*-Phenylalanine methyl ester hydrochloride (**5**) (0.50 g, 2.34 mmol) and *N*,*N*-diisopropylethylamine (0.82 g, 6.40 mmol) were added and the reaction mixture was stirred at ice temperature for 1 h and then at room temperature for 4 h. The reaction progress was monitored by TLC. Reaction mixture was evaporated to dryness and residue was extracted from dichloromethane, washed with water, dried over anhydrous sodium sulphate. Solvent was evaporated under vacuum and the crude product was purified on silicagel column chromatography with MeOH/$CHCl_3$ (v/v: 1.0/99.0) as eluent to obtain **14** as a white powder in very good yield (1.18 g, 88%). ^{1}H NMR ($CDCl_3$, 400 MHz) δ_{ppm} 1.25-1.36 (m, 2H), 1.43 (s, 9H), 1.63 (s, 2H), 1.81 (b, 1H), 3.04-3.17 (m, 4H), 3.71 (s, 3H), 4.12-4.22 (m, 2H), 4.33-4.42 (m, 2H), 4.61 (b, 1H), 4.82-4.87 (q, *J* = 6.1 Hz, 1H), 5.37 (b, 1H), 6.38 (b, 1H), 7.07-7.09 (d, *J* = 6.8 Hz, 2H), 7.18-7.23 (m, 4H), 7.29-7.33 (t, *J* = 7.4 Hz, 2H), 7.38- 7.42 (t, *J* = 7.4 Hz, 2H), 7.57 (b, 2H), 7.75-7.77 (d, *J* = 7.5 Hz, 2H); ^{13}C NMR ($CDCl_3$, 100 MHz) δ_{ppm} 22.4, 28.5, 29.7, 32.1, 37.9, 40.0, 47.3, 52.5, 53.3, 67.2, 120.1, 125.2, 127.2, 127.3, 127.8, 128.7, 129.3, 135.7, 141.4, 143.9, 156.2, 171.3, 171.8.

Preparation of *cyclo*(*L*-Lys(*t*Boc)-*L*-Phe) (15). The linear dipeptide Fmoc-*L*-Lys(*t*Boc)-*L*-Phe-OMe (**14**) (1.0 g, 1.58mmol) was dissolved in piperidine-DCM (v/v, 20:80, 16 mL) and stirred at room temperature for 6 h. The reaction progress was monitored by TLC. The precipitate formed was filtered washed with methanol, ether and dried under vacuum to yield **15** in very good yield as a white powder (0.50 g, 84%). ^{1}H NMR (DMSO-d_6, 400 MHz) δ = 0.59-077 (m, 3H), 1.00-1.11 (m, 3H), 1.37 (s, 9H), 2.68-2.73 (q, *J* = 5.8 Hz, 2H), 2.81-2.86 (dd, *J* = 13.3 Hz, *J* = 4.9 Hz, 1H), 3.11-3.15 (dd, *J* = 13.6 Hz, *J* = 3.8 Hz,

1H), 3.54 (b, 1H), 4.17 (b, 1H), 6.61-6.64 (t, *J* = 5.0 Hz, 1H), 7.14-7.16 (m, 2H), 7.19-7.27 (m, 3H), 7.99 (b, 1H), 8.10 (b, 1H); ^{13}C NMR (DMSO-d_6, 100 MHz) δ_{ppm} 20.9, 28.2, 28.9, 33.0, 38.1, 53.7, 55.2, 77.2, 126.6, 127.9, 130.3, 136.1, 155.4, 166.1, 166.9.

Preparation of *cyclo*(*L*-Lys-*L*-Phe)-NDI-*cyclo*(*L*-Lys-*L*-Phe) (NCDP 2). *Cyclo*(*L*-Lys(*t*Boc)-*L*-Phe) (**15**), (0.80 g, 1.27 mmol) was dissolved in TFA-DCM (v/v, 1:1, 10 mL), triisopropylsilane (TIPS, 0.5 mL) and the resulting reaction mixture was stirred at room temperature for 4 h. The reaction progress was monitored by TLC. Reaction mixture was evaporated to dryness and co-evaporated thrice with toluene to yield **16** as a white solid in excellent yield (0.81 g, 98%) and used as such without any further purification. 1,4,5,8-naphthalenetetracarboxylic dianhydride (60 mg, 0.23 mmol) and *cyclo*(*L*-Lys-*L*-Phe) (**16**) (0.20 g, 0.51 mmol) were dissolved in *N*,*N*-dimethylformamaide (20 mL). *N*,*N*-diisopropylethylamine (60 mg, 0.51 mmol) was added and refluxed at 80 ^{o}C for 12 h. Reaction mixture was cooled to room temperature and the precipitate was filtered washed with methanol, acetonitrile and dried under vacuum to yield NCDP **2** as brown solid in a good yield (120 mg, 70%). ^{1}H NMR (DMSO-d_6, 400 MHz) δ_{ppm} 0.77-0.83 (m, 6H), 1.12-1.18 (m, 2H), 1.36-1.39 (m, 4H), 2.82-2.86 (m, 2H), 3.11-3.15 (m, 2H), 3.61 (b, 2H), 3.85-3.88 (t, *J* = 7.5 Hz, 4H), 4.17 (b, 2H), 7.14-7.27 (m, 10H), 8.02 (b, 2H), 8.11 (b, 2H), 8.67 (s, 4H); MALDI-TOF = m/*z* 805.29 $[M+Na]^+$, 821.25 $[M+K]^+$. Elemental analysis. Found: C, 67.50; H, 5.45; N, 10.73. Calcd: C, 67.51; H, 5.41; N, 10.74 for $C_{44}H_{42}N_6O_8$.

Preparation of *L*-Leu-OCH$_3$.HCl (17). Methanol (30 mL) was taken in a two-necked round-bottomed flask fitted with a reflux condenser and an addition funnel, cooled to ice cold temperature. *L*-Leucine (2.0 g, 15.24 mmol) was dispersed in above ice-cooled methanol and thionyl chloride ($SOCl_2$) (2.72 g, 22.86 mmol) was added dropwise, stirred

at ice cold temperature for 30 min and then refluxed at 80 ºC for 6 h. The reaction progress was monitored by TLC, after the completion of reaction solvent was removed under vacuum to yield **17** as white solid in quantitative yield (2.68 g, 97% yield). ^{1}H NMR (D_2O, 400 MHz) δ_{ppm} 0.98-1.01 (m, 6H), 1.73-1.84 (m, 2H), 1.86-1.95 (m, 1H), 3.88 (s, 3H), 4.17-4.21 (t, *J* = 13.8 Hz, 1H); ^{13}C NMR (D_2O, 100 MHz) δ_{ppm} 21.0, 21.4, 23.9, 38.8, 51.4, 53.5, 171.3.

Preparation of Fmoc-*L*-Lys(*t*Boc)-*L*-Leu-OCH$_3$ (18). Fmoc-*L*-Lys(*t*Boc)-OH (1.28 g, 2.75 mmol), 1-(3-dimethylaminopropyl)-3-ethylcarbodiimide hydrochloride (0.87 g, 4.60 mmol) and hydroxybenzotrizole (0.62 g, 4.60 mmol) were dissolved in dichloromethane (25 mL) and cooled to ice temperature. *L*-Leucine methyl ester hydrochloride (**17**) (0.60 g, 3.30 mmol) and *N*,*N*-diisopropylethylamine (1.17 g, 9.07 mmol) were added and the reaction mixture was stirred at ice temperature for 1 h and then at room temperature for 3 h. The reaction progress was monitored by TLC. Reaction mixture was evaporated to dryness and residue was extracted from dichloromethane, washed with water, dried over anhydrous sodium sulphate. Solvent was evaporated under vacuum and the crude product was purified on silicagel column chromatography using MeOH/$CHCl_3$ (v/v: 0.8/99.2) as eluent to obtain **18** as a white powder in very good yield (1.46 g, 89%). ^{1}H NMR ($CDCl_3$, 400 MHz) δ_{ppm} 0.89-0.90 (d, *J* = 4.5 Hz, 6H), 1.42 (s, 9H), 1.51-1.65 (m, 8H), 1.92 (b, 1H), 3.05-3.15 (b, 2H), 3.71 (s, 3H), 4.18-4.21 (t, *J* = 6.9 Hz, 2H), 4.36-4.37 (d, *J* = 6.8 Hz, 2H), 4.56-4.62 (m, 1H), 4.74 (b, 1H), 5.58 (b, 1H), 6.57 (b, 1H), 7.27-7.31 (t, *J* = 7.4 Hz, 2H), 7.36-7.40 (t, *J* = 7.4 Hz, 2H), 7.57-7.59 (d, *J* = 7.3 Hz, 2H), 7.74-7.76 (d, *J* = 5 Hz, 2H); ^{13}C NMR ($CDCl_3$, 100 MHz) δ_{ppm} 21.9, 22.3, 22.8, 24.9, 28.5, 29.5, 32.3, 39.9, 41.3, 47.2, 50.9, 52.4, 54.6, 67.2, 79.2, 120.0, 125.1, 127.1, 127.8, 141.3, 143.8, 143.9, 156.3, 171.7, 173.3.

Preperation of *cyclo*(*L*-Lys(*t*Boc)-*L*-Leu) (19). The linear dipeptide Fmoc-*L*-Lys(*t*Boc)-*L*-Leu-OMe (**18**) (0.80 g, 2.34 mmol) was dissolved in piperidine-DCM (v/v, 20:80, 16 mL) and stirred at room temperature for 8 h. The reaction progress was monitored by TLC. Reaction mixture was evaporated to dryness and residue was extracted with dichloromethane, washed with water, dried over anhydrous sodium sulphate. Solvent was evaporated under vacuum and the crude product was purified on silicagel column chromatography using MeOH/$CHCl_3$ (v/v: 1.4/98.6) as eluent to obtain **19** as a white powder in fair yield (0.28 g, 62%). ^{1}H NMR (DMSO-d_6, 400 MHz) δ_{ppm} 0.84-0.88 (m, 6H), 1.23-1.33 (m, 4H), 1.36 (s, 9H), 1.42-1.48 (m, 1H), 1.56-1.87 (m, 4H), 2.86-2.91 (q, *J* = 6.4 Hz, 2H), 3.72-3.75 (m, 2H), 6.70-6.72 (t, *J* = 5.2 Hz, 1H), 8.09 (b, 1H), 8.14 (b, 1H); ^{13}C NMR (DMSO-*d6*, 100 MHz) δ_{ppm} 21.7, 22.9, 23.5, 28.2, 29.1, 33.1, 43.2, 52.5, 54.0, 77.3, 155.5, 167.8, 168.3.

Preparation of *cyclo*(*L*-Lys-*L*-Leu)-NDI-*cyclo*(*L*-Lys-*L*-Leu) (NCDP 3). *Cyclo*(*L*-Lys(*t*Boc)-*L*-Leu) (**19**), (0.25 g, 0.73 mmol) was dissolved in TFA-DCM (v/v, 1:1, 10 mL), triisopropylsilane (TIPS, 0.2 mL) and the resulting reaction mixture was stirred at room temperature for 4 h. The reaction progress was monitored by TLC. The reaction mixture was evaporated to dryness and co-evaporated thrice with toluene to yield **20** as a white solid in an excellent yield (0.25 g, 96%) and used as such without any further purification. 1,4,5,8-naphthalenetetracarboxylic dianhydride (80 mg, 0.32 mmol) and *cyclo*(*L*-Lys-*L*-Leu) (**20**) (0.25 g, 0.70 mmol) were dissolved in *N*,*N*-dimethylformamide (20 mL). *N*,*N*-diisopropylethylamine (90 mg, 0.70 mmol) was added and refluxed at 80 ºC for 12 h. The reaction progress was monitored by TLC. The reaction mixture was cooled to room temperature, precipitated with ether and the precipitate was filtered, washed with methanol, acetonitrile and dried under vacuum to yield NCDP **3** as dark brown solid in fair yield (120 mg, 63%). ^{1}H NMR (DMSO-d_6, 400 MHz) δ_{ppm} 0.84-0.89

(m, 12H), 1.40-1.49 (m, 6H), 1.56-1.85 (m, 12H), 3.73-3.77 (m, 4H), 4.05-4.08 (t, *J* = 14.2 Hz, 4H),8.10-8.11 (d, *J* = 2.2 Hz, 2H), 8.13-8.14 (d, *J* = 2.3 Hz, 2H), 8.67 (s, 4H); MALDI-TOF = m/*z* 737.31 $[M+Na]^+$, 753.25 $[M+K]^+$. Elemental analysis. Found: C, 63.83; H, 6.51; N, 11.75. Calcd: C, 63.85; H, 6.49; N, 11.76 for $C_{38}H_{46}N_6O_8$.

Preparation of *cyclo*(*L*-Lys-Gly)-NDI-*cyclo*(L-Lys-Gly) (NCDP 4). 1,4,5,8-naphthalenetetracarboxylic dianhydride (40 mg, 0.16 mmol) and *cyclo*(*L*-Lys-Gly) (**2**) (100 mg, 0.33 mmol) were dissolved in *N*,*N*-dimethylformamaide (10 mL). *N*,*N*-diisopropylethylamine (40 mg, 0.33 mmol) was added and the resultant reaction mixture was refluxed at 80 ºC for 15 h. Reaction mixture was cooled to room temperature, precipitated with ether and the precipitate was filtered, washed with methanol, acetonitrile and dried under vacuum to yield NCDP **4** as a brown coloured solid in moderate yield (60 mg, 62%). ^{1}H NMR (DMSO-*d6*, 400 MHz) δ = 1.38-1.56 (m, 8H), 3.01 (b, 4H), 3.64-3.79 (m, 6H), 4.04-4.08 (t, *J* = 7.0, 4H), 7.96 (b, 2H), 8.15 (b, 2H), 8.67 (s, 4H); MALDI-TOF = m/*z* 625.18$[M+Na]^+$, 641.15$[M+K]^+$; Elemental analysis. Found: C, 59.78; H, 5.08; N, 13.94. Calcd: C, 59.79; H, 5.02; N 13.95 for $C_{30}H_{30}N_6O_8$.

Preparation of *D*-Tyr-OCH$_3$.HCl (21). Methanol (20 mL) was taken in a two-necked round-bottomed flask fitted with a reflux condenser and an addition funnel, cooled to ice cold temperature. *D*-Tyrosine (0.80 g, 4.41 mmol) was dispersed in above ice-cooled methanol and thionyl chloride ($SOCl_2$) (0.78 g, 6.62 mmol) was added dropwise, stirred at ice cold temperature for 30 min and then refluxed at 80 ºC for 14 h. The reaction progress was monitored by TLC, after the completion of reaction solvent was removed under vacuum to yield **21** as white solid in quantitative yield (1.01 g, 99% yield). ^{1}H NMR (DMSO-d_6, 400 MHz) δ_{ppm} 2.96-3.07 (m, 2H), 3.66 (s, 3H), 4.15 (s, 1H), 6.71-6.73

(d, J = 8.2 Hz, 2H), 6.99-7.01 (d, J = 8.4 Hz, 2H), 8.64 (b, 3H), 9.47 (b, 1H); ^{13}C NMR (DMSO-d_6, 100 MHz) δ_{ppm} 35.0, 52.5, 53.4, 115.4, 124.3, 130.3, 156.6, 169.4.

Preparation of Fmoc-*L*-Lys(*t*Boc)-*D*-Tyr-OCH$_3$ (22). Fmoc-*L*-Lys(*t*Boc)-OH (1.0 g, 2.13 mmol), 1-(3-dimethylaminopropyl)-3-ethylcarbodiimide hydrochloride (0.61 g, 3.2 mmol) and hydroxybenzotrizole (0.43 g, 3.2 mmol) were dissolved in dichloromethane (25 mL) and cooled to ice temperature. *D*-Tyrosine methyl ester hydrochloride (**21**) (0.59 g, 2.56 mmol) and *N*,*N*-diisopropylethylamine (0.82 g, 6.4 mmol) were added and the reaction mixture was stirred at ice temperature for 1 h and then at room temperature for 8 h. The reaction progress was monitored by TLC. Reaction mixture was evaporated to dryness and residue was extracted from dichloromethane, washed with water, dried over anhydrous sodium sulphate. Solvent was evaporated under vacuum and the crude product was purified on silicagel column chromatography using MeOH/$CHCl_3$ (v/v: 1.2/98.8) as eluent to obtain **22** as a white powder in very good yield (1.15 g, 84%). ^{1}H NMR ($CDCl_3$, 400 MHz) δ_{ppm} 0.71-0.93 (m, 2H), 1.14-1.31 (m, 3H), 1.47 (s, 9H), 1.52-1.60 (m, 2H), 2.70-2.87 (m, 2H), 3.00-3.14 (m, 2H), 3.77 (s, 3H), 4.12-4.19 (m, 2H), 4.32-4.34 (m, 2H), 4.71 (b, 1H), 4.82-4.88 (m, 1H), 5.58-5.60 (d, J = 7.2 Hz, 1H), 6.611-6.13 (d, J = 8.1 Hz, 1H), 6.82-6.84 (d, J = 8.0 Hz, 2H), 6.96-6.98 (d, J = 8.2 Hz, 2H), 7.27-7.31 (t, J = 7.4 Hz, 2H), 7.36-7.40 (t, J = 7.4 Hz, 2H), 7.55-7.57 (d, J = 7.4 Hz, 2H), 7.74-7.76 (d, J = 7.4 Hz, 2H); ^{13}C NMR ($CDCl_3$, 100 MHz) δ_{ppm} 22.6, 27.9, 29.4, 32.0, 36.8, 40.5, 47.1, 52.5, 67.2, 77.3, 116.8, 120.1, 125.2, 125.4, 127.1, 127.2, 127.9, 130.4, 141.5, 143.9, 156.4, 156.6, 171.5, 172.6.

Preparation of *cyclo*(*L*-Lys(*t*Boc)-*D*-Tyr) (23). The linear dipeptide Fmoc-*L*-Lys(*t*Boc)-*D*-Tyr-OCH_3 (**22**) (1.0 g, 1.58 mmol) was dissolved in DCM-piperidine (v/v: 80:20, 20 mL) and stirred at room temperature for 10 h. The reaction progress was monitored by

TLC. Reaction mixture was evaporated to dryness and residue was extracted with dichloromethane, washed with water, dried over anhydrous sodium sulphate. Solvent was evaporated under vacuum and the crude product was purified on silicagel column chromatography using MeOH/$CHCl_3$ (v/v: 1.2/98.8) as eluent to obtain **23** as a white powder in fair yield (0.33 g, 55%). ^{1}H NMR (DMSO-d_6, 400 MHz) δ_{ppm} 1.04-1.27 (m, 5H), 1.35 (s, 9H), 2.73-3.01 (m, 6H), 4.01 (b, 1H), 6.62-6.64 (d, *J* = 8.3 Hz, 2H), 6.69-6.72 (t, *J* = 5.3 Hz, 1H), 6.93-6.95 (d, *J* = 8.3 Hz, 2H), 7.89 (s, 1H), 8.01 (s, 1H), 9.22 (b, 1H); ^{13}C NMR (DMSO-d_6, 100 MHz) δ_{ppm} 20.7, 28.2, 29.2, 31.3, 37.8, 52.9, 55.7, 77.3, 114.8, 125.7, 131.0, 155.5, 156.1, 167.5, 167.5.

Preparation of *cyclo*(*L*-Lys-*D*-Tyr)-NDI-*cyclo*(*L*-Lys-*D*-Tyr) (NCDP 5). *cyclo*(*L*-Lys(*t*Boc)-*D*-Tyr) (**23**), (0.27 g, 0.70 mmol) was dissolved in TFA-DCM (v/v, 1:1, 10 mL), triisopropylsilane (TIPS, 0.2 mL) and the resulting reaction mixture was stirred at room temperature for 8 h. The reaction progress was monitored by TLC. Reaction mixture was evaporated to dryness and co-evaporated thrice with toluene to yield **24** as a white solid in excellent yield (0.27 g, 98%) and used as such without any further purification. 1,4,5,8-naphthalenetetracarboxylic dianhydride (60 mg, 0.22 mmol) and *cyclo*(*L*-Lys-*D*-Tyr) (**24**) (0.20 g, 0.49 mmol) were dissolved in *N*,*N*-dimethylformamaide (20 mL). *N*,*N*-diisopropylethylamine (60 mg, 0.49 mmol) was added and refluxed at 80 ºC for 16 h. The reaction progress was monitored by TLC. Reaction mixture was cooled to room temperature, precipitated with ether and the precipitate was filtered washed with methanol, acetonitrile and dried under vacuum to yield NCDP **5** as yellowish brown solid in good yield (0.14 g, 78 %). ^{1}H NMR (DMSO-*d6*, 400 MHz) δ_{ppm} 1.19-1.35 (m, 6H), 1.48-1.64 (m, 8H), 2.90-2.92 (m, 2H), 2.96-3.01 (m, 2H), 3.97-4.01 (m, 6H), 6.61-6.64 (d, *J* = 8.4 Hz, 4H), 6.92-6.94 (d, *J* = 8.4 Hz, 4H), 7.94 (b, 2H), 8.03 (b, 2H), 8.64 (b, 4H), 9.21 (s, 2H); MALDI-TOF = m/*z*837.26 $[M+Na]^+$, 853.22 $[M+K]^+$; Elemental

analysis. Found: C, 64.85; H, 5.24; N, 10.30; Calcd: C, 64.86; H, 5.20; N, 10.31 for $C_{44}H_{42}N_6O_{10}$.

Preparation of *D*-Phe-OCH$_3$.HCl (25). Methanol (20 mL) was taken in a two-necked round-bottomed flask fitted with a reflux condenser and an addition funnel, cooled to ice cold temperature. *D*-Phenylalanine (1.0 g, 6.20 mmol) was dispersed in above ice-cooled methanol and thionyl chloride ($SOCl_2$) (1.10 g, 9.32 mmol) was added dropwise, stirred at ice cold temperature for 30 min and then refluxed at 80 ºC for 4 h. The reaction progress was monitored by TLC, after the completion of reaction solvent was removed under vacuum to yield **25** as white solid in quantitative yield (1.29 g, 99%). ^{1}H NMR (D_2O, 400 MHz) δ_{ppm} 3.26-3.42 (m, 2H), 3.88 (s, 3H), 4.47-4.50 (t, *J* = 7.2 Hz, 1H), 7.33-7.35 (m, 2H), 7.44-7.50 (m, 3H); ^{13}C NMR (D_2O, 100 MHz) δ_{ppm} 35.6, 53.6, 54.1, 128.1, 129.3, 129.4, 133.7, 170.1.

Preparation of Fmoc-*L*-Lys(*t*Boc)-*D*-Phe-OCH$_3$ (26). Fmoc-*L*-Lys(*t*Boc)-OH (1.97 g, 4.21 mmol), 1-(3-dimethylaminopropyl)-3-ethylcarbodiimide hydrochloride (1.33 g, 6.95 mmol) and hydroxybenzotrizole (0.93 g, 6.95 mmol) were dissolved in dichloromethane (25 mL) and cooled to ice temperature. *D*-Phenylalanine methyl ester hydrochloride (**25**) (1.0 g, 4.63 mmol) and *N*,*N*-diisopropylethylamine (1.79 g, 13.91 mmol) were added and the reaction mixture was stirred at ice temperature for 1 h and then at room temperature for 6 h. The reaction progress was monitored by TLC. Reaction mixture was evaporated to dryness and residue was extracted with dichloromethane, washed with water, dried over anhydrous sodium sulphate. Solvent was evaporated under vacuum and the crude product was purified on silicagel column chromatography using MeOH/$CHCl_3$ (v/v: 0.8/99.2) as eluent to obtain **26** as a white powder in very good yield (2.25 g, 85%). ^{1}H NMR ($CDCl_3$, 400 MHz) δ_{ppm} 1.25 (b, 2H), 1.43 (s, 9H), 1.52-1.75 (m, 4H), 3.01-3.18

(m, 4H), 3.71 (s, 3H), 4.15-4.20 (m, 2H), 4.36 (b, 2H), 4.56 (b, 1H), 4.86 (b, 1H), 5.42 (b, 1H), 6.49 (b, 1H), 7.08-7.09 (d, *J* = 6.8 Hz, 2H), 7.18-7.23 (m, 3H), 7.28-7.32 (t, *J* = 7.4 Hz, 2H), 7.37-7.41 (t, *J* = 7.4 Hz, 2H), 7.56-7.59 (t, *J* = 6.4 Hz, 2H), 7.75-7.77 (d, *J* = 7.5 Hz, 2H); ^{13}C NMR ($CDCl_3$, 100 MHz) δ_{ppm} 22.4, 28.5, 29.7, 32.2, 38.0, 39.9, 47.2, 52.5, 53.2, 54.9, 67.3, 79.3, 120.1, 125.2, 127.2, 127.3, 127.8, 128.7, 129.3, 135.8, 141.4, 143.9, 156.2, 171.4, 171.8.

Preparation of *cyclo*(*L*-Lys(*t*Boc)-*D*-Phe) (27). The linear dipeptide Fmoc-*L*-Lys(*t*Boc)-*D*-Phe-OCH_3 (**26**) (1.0 g, 1.54 mmol) was dissolved in piperidine-DCM (v/v, 20:80, 25 mL) and stirred at room temperature for 10 h. The reaction progress was monitored by TLC. Reaction mixture was reduced to half and toluene (20 mL) was added to precipitate the compound. The precipitate was washed with methanol, ether and dried under vacuum to yield **27** a white powder in fair yield (0.34 g, 58%). ^{1}H NMR (DMSO-d_6, 400 MHz) δ_{ppm} 1.04-1.27 (m, 4H), 1.36 (s, 9H), 1.46-1.56 (m, 2H), 2.81-2.93 (m, 4H), 3.09-3.13 (m, 1H), 4.11 (b, 1H), 6.70-6.73 (t, *J* = 5.4 Hz, 1H), 7.16-7.18 (m, 2H), 7.22-7.28 (m, 3H), 7.95 (s, 1H), 8.09 (s, 1H); ^{13}C NMR (DMSO-d_6, 100 MHz) δ_{ppm} 20.8, 28.2, 29.2, 31.5, 38.4, 53.0, 55.4, 77.3, 126.6, 128.0, 130.0, 135.9, 155.5, 167.3, 167.5.

Preparation of *cyclo*(*L*-Lys-*D*-Phe)-NDI-*cyclo*(*L*-Lys-*D*-Phe) (NCDP 6): *cyclo*(*L*-Lys(*t*Boc)-*D*-Phe) (**27**), (0. 20 g, 0.52 mmol) was dissolved in TFA-DCM (v/v, 1:1, 10 mL), triisopropylsilane (TIPS, 0.2 mL) and the resulting reaction mixture was stirred at room temperature for 8 h. The reaction progress was monitored by TLC. Reaction mixture was evaporated to dryness and co-evaporated thrice with toluene to yield **28** as a white solid in an excellent yield (0.20 g, 98 %) and used as such without any further characterization. 1,4,5,8-naphthalenetetracarboxylic dianhydride (40 mg, 0.17 mmol) and *cyclo*(*L*-Lys-*D*-Phe) (**28**) (0.20 g, 0.51 mmol) were dissolved in *N*,*N*-dimethylformamaide

(20 mL). *N*,*N*-diisopropylethylamine (60 mg, 0.51 mmol) was added and refluxed at 80 ºC for 16 h. The reaction progress was monitored by TLC. Reaction mixture was cooled to room temperature and the precipitate was filtered, washed with methanol, acetonitrile and dried under vacuum to yield NCDP **6** as pale brown solid in a good yield (90 mg, 72 %). ^{1}H NMR (DMSO-d_6, 400 MHz) δ_{ppm} 1.19-1.37 (m, 4H), 1.50-1.64 (m, 8H), 2,86-2.90 (dd, *J* = 13.5 Hz, *J* = 4.8 Hz, 2H), 2.94-2.96 (t, *J* = 4.6 Hz, 2H), 3.08-3.12 (dd, *J* = 13.6 Hz, *J* = 4.3 Hz, 2H), 3.97-4.01 (t, *J* = 7.3 Hz, 4H), 4.10-4.11 (m, 2H), 7.16-7.18 (m, 4H), 7.19-7.28 (m, 6H), 7.98 (b, 2H), 8.10 (b, 2H), 8.64 (s, 4H); MALDI-TOF = m/z 805.27$[M+Na]^+$, m/z 821.24$[M+K]^+$; Elemental analysis. Found: C, 67.50; H, 5.45; N, 10.73; Calcd: C, 67.51; H, 5.41; N, 10.74 for $C_{44}H_{42}N_6O_8$.

3.5 Appendix

- ^{1}H NMR and MALDI-TOF spectrum of NCDP **1**
- ^{1}H NMR and MALDI-TOF spectrum of NCDP **2**
- ^{1}H NMR and MALDI-TOF spectrum of NCDP **3**
- ^{1}H NMR and MALDI-TOF spectrum of NCDP **4**
- ^{1}H NMR and MALDI-TOF spectrum of NCDP **5**
- ^{1}H NMR and MALDI-TOF spectrum of NCDP **6**

^{1}H NMR spectrum of NCDP 1

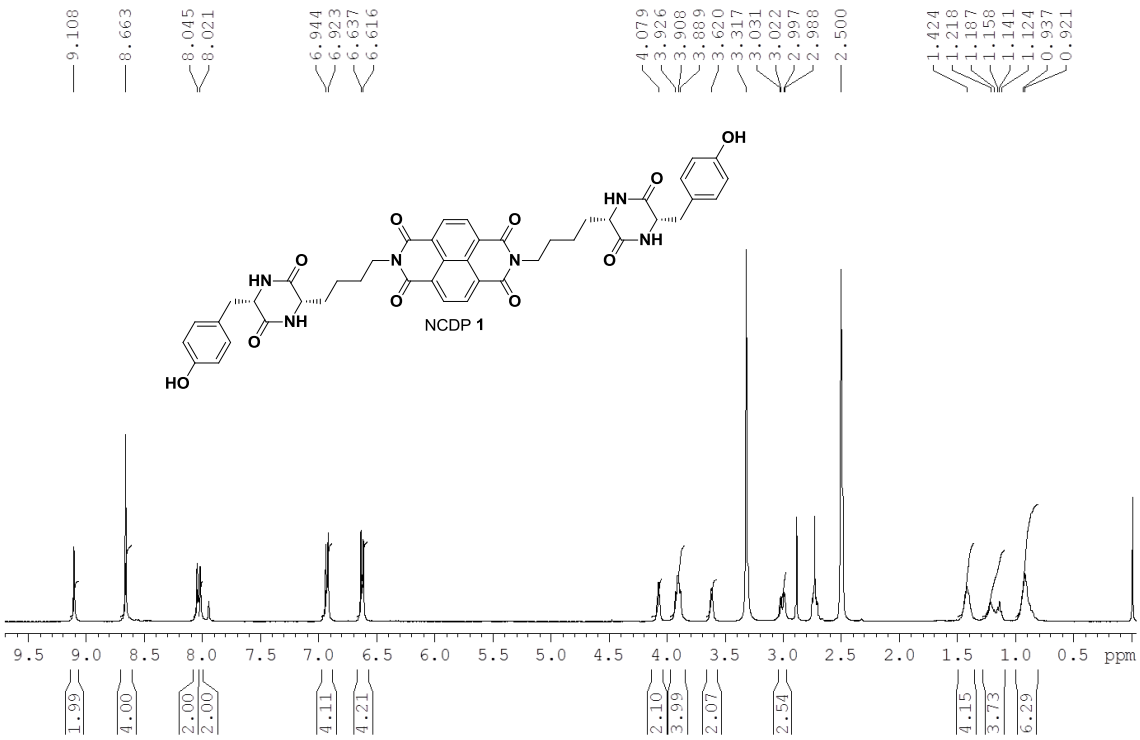

MALDI-TOF mass spectrum of NCDP 1

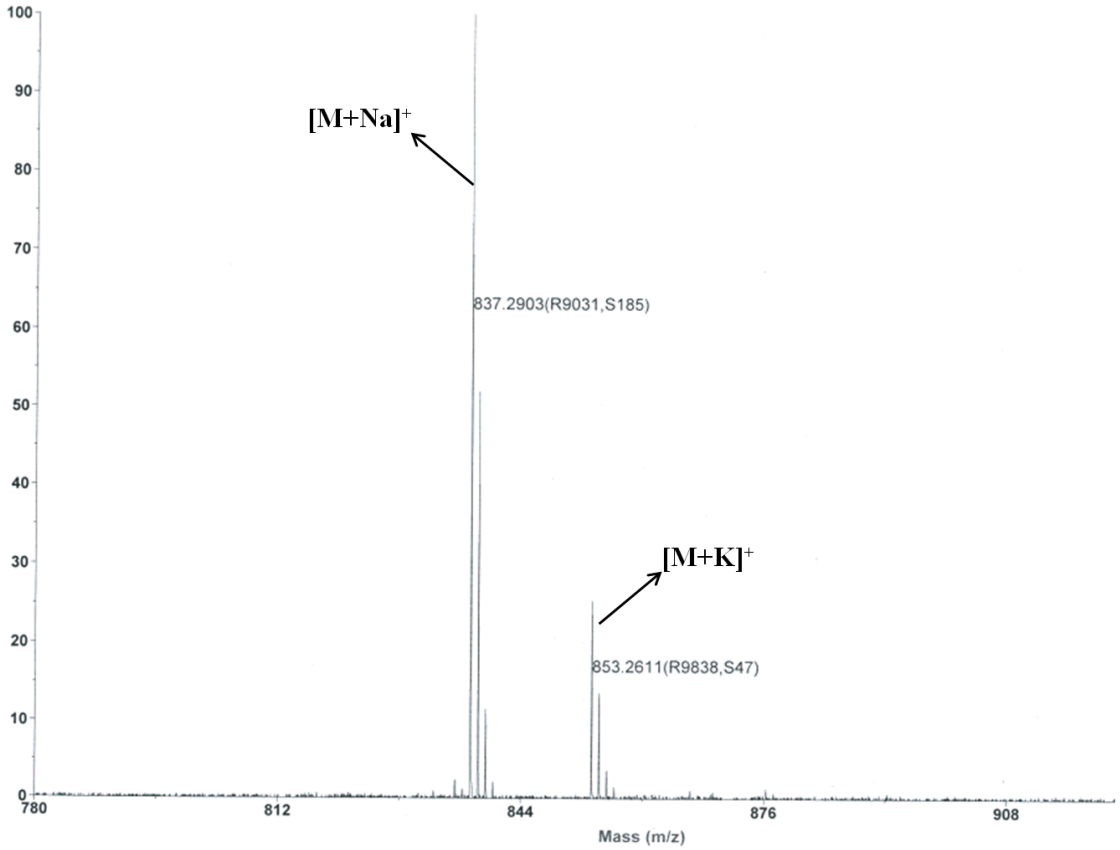

^{1}H NMR spectrum of NCDP 2

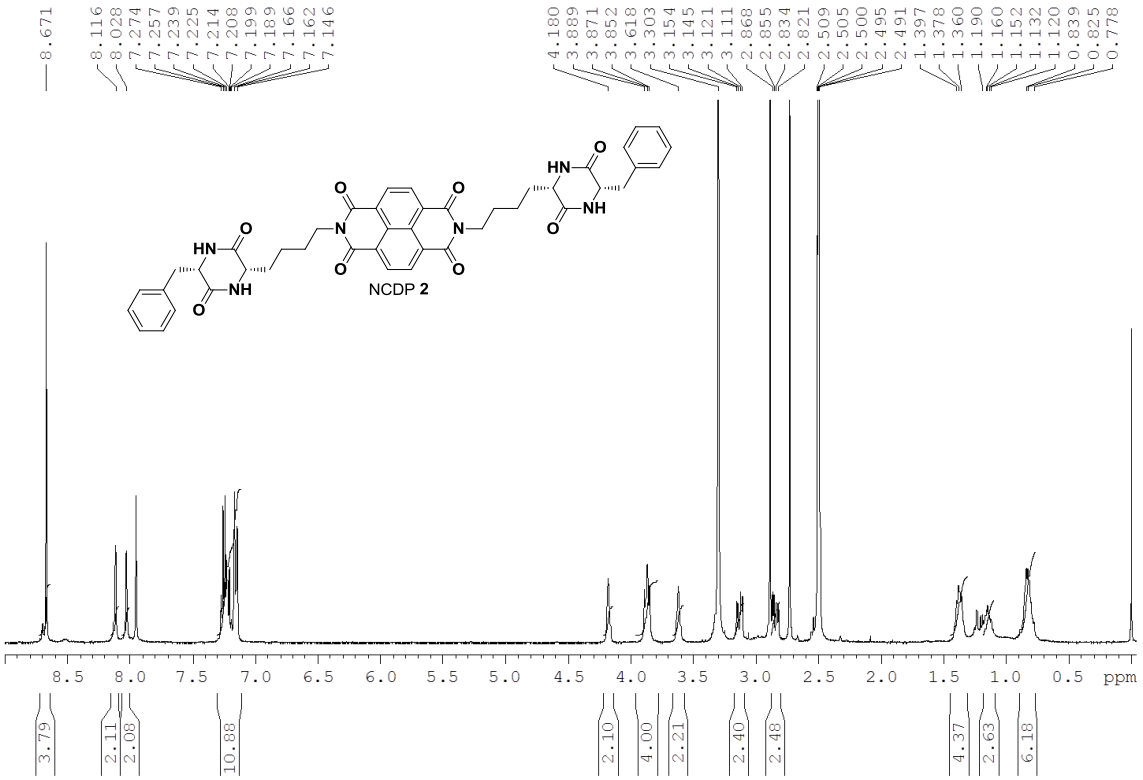

MALDI-TOF mass spectrum of NCDP 2

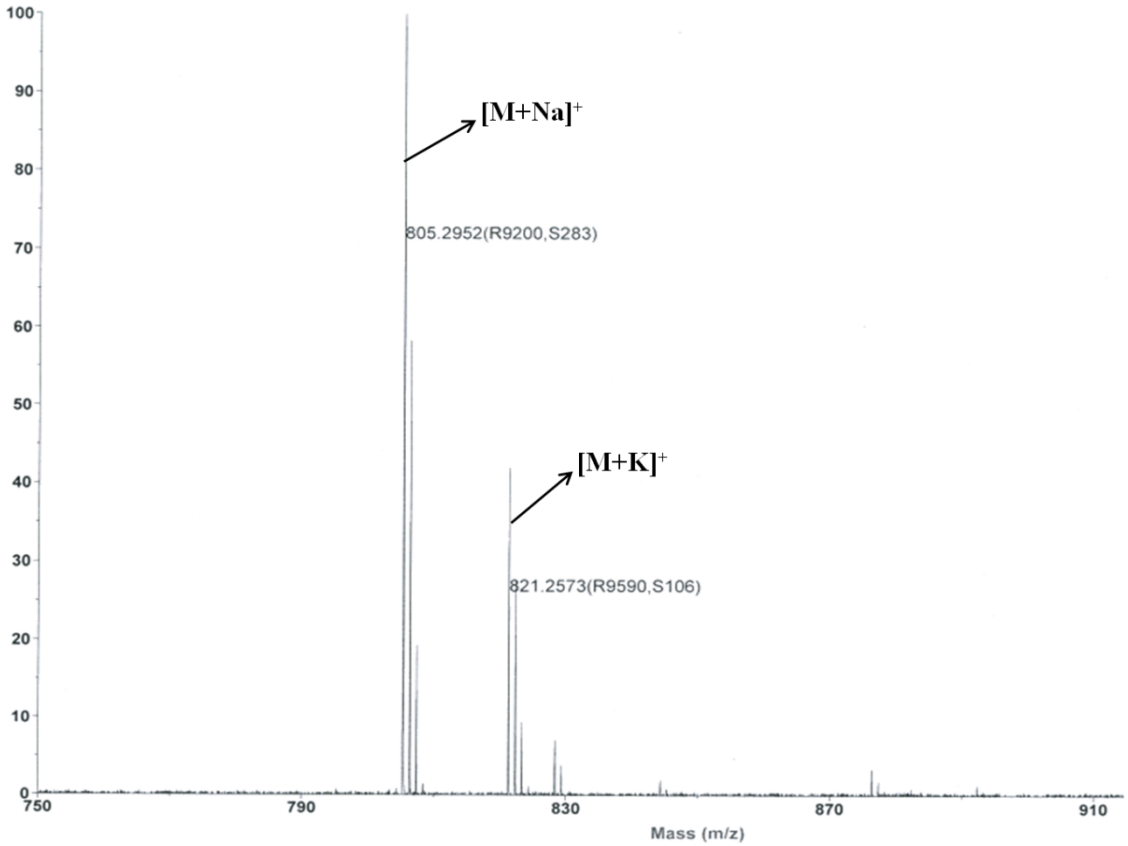

^{1}H NMR spectrum of NCDP 3

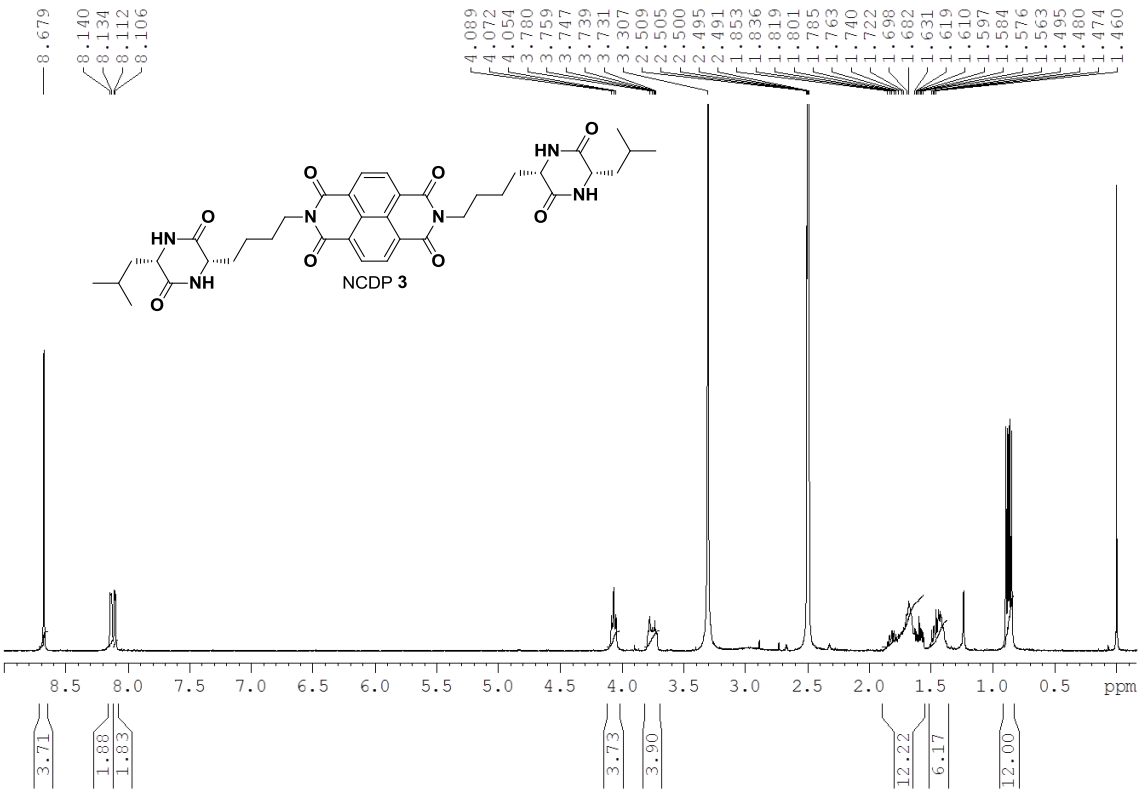

MALDI-TOF mass spectrum of NCDP 3

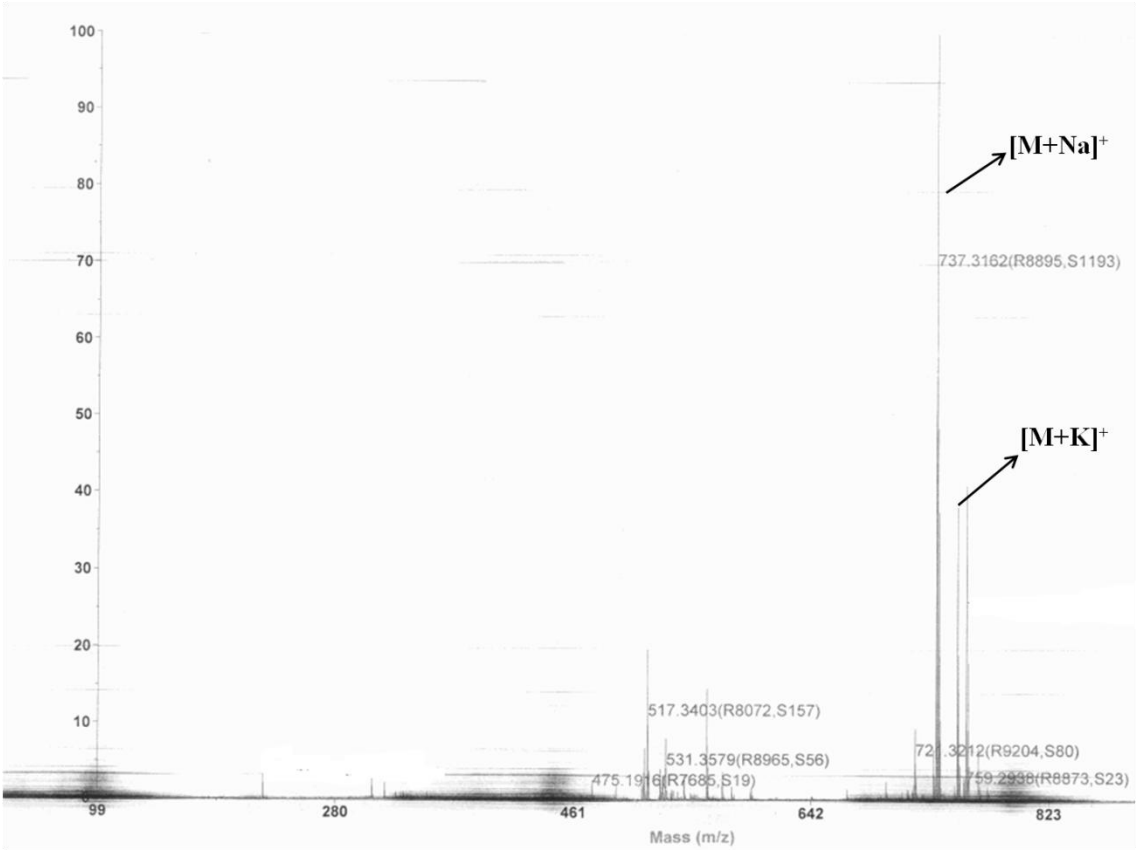

^{1}H NMR spectrum of NCDP 4

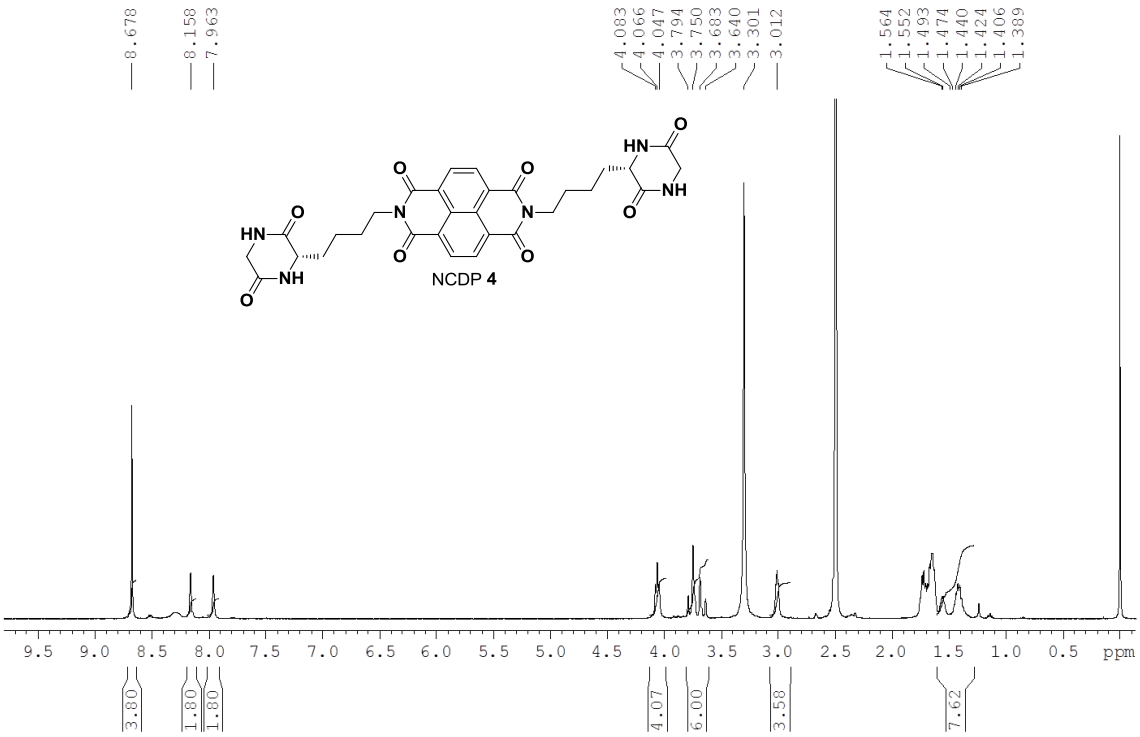

MALDI-TOF mass spectrum of NCDP 4

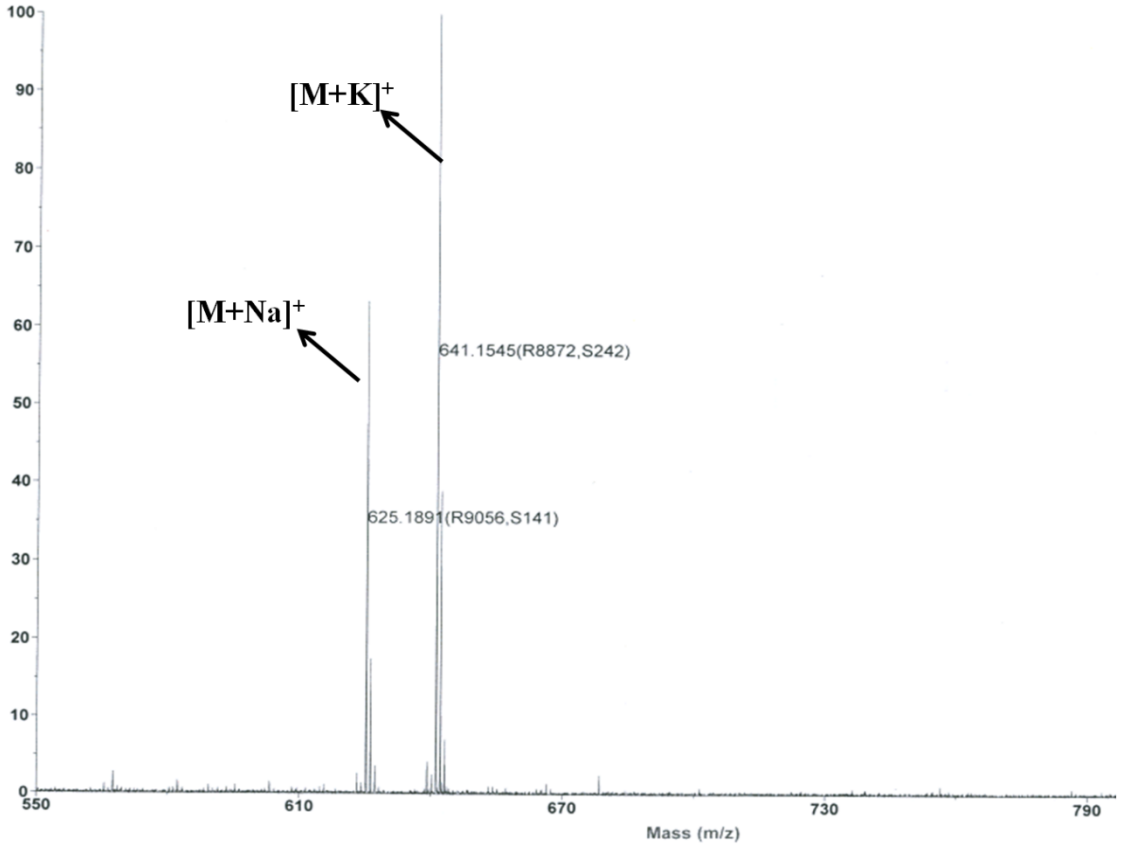

^{1}H NMR spectrum of NCDP 5

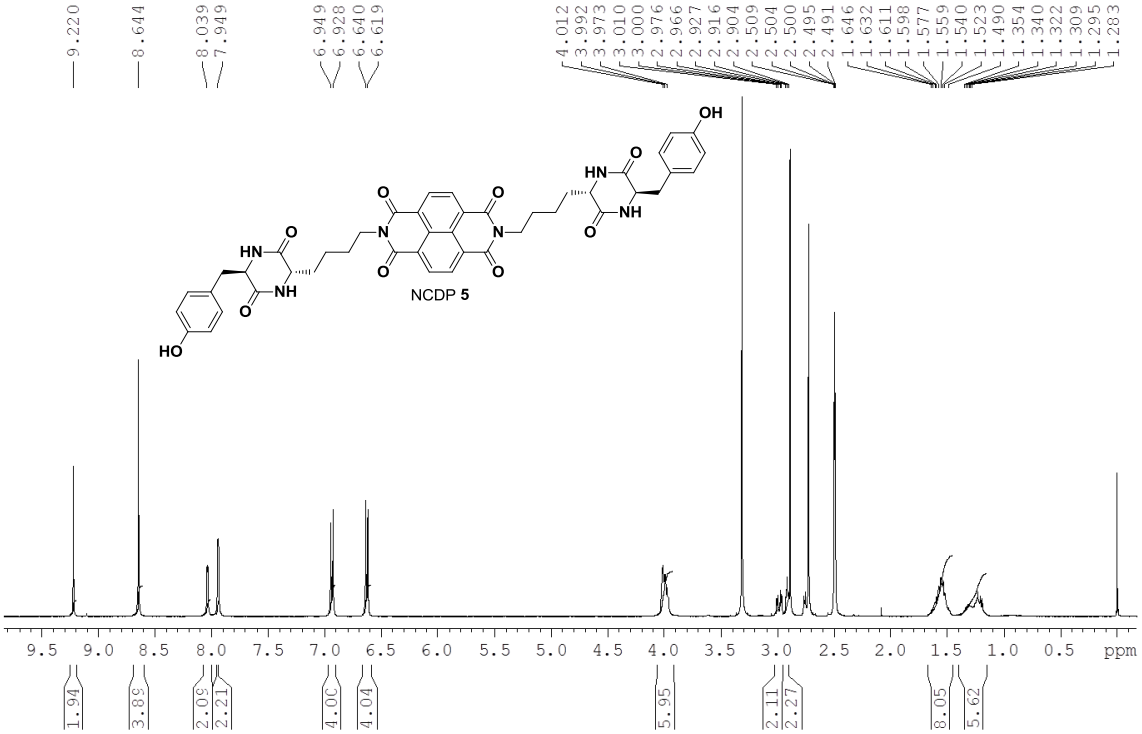

MALDI-TOF mass spectrum of NCDP 5

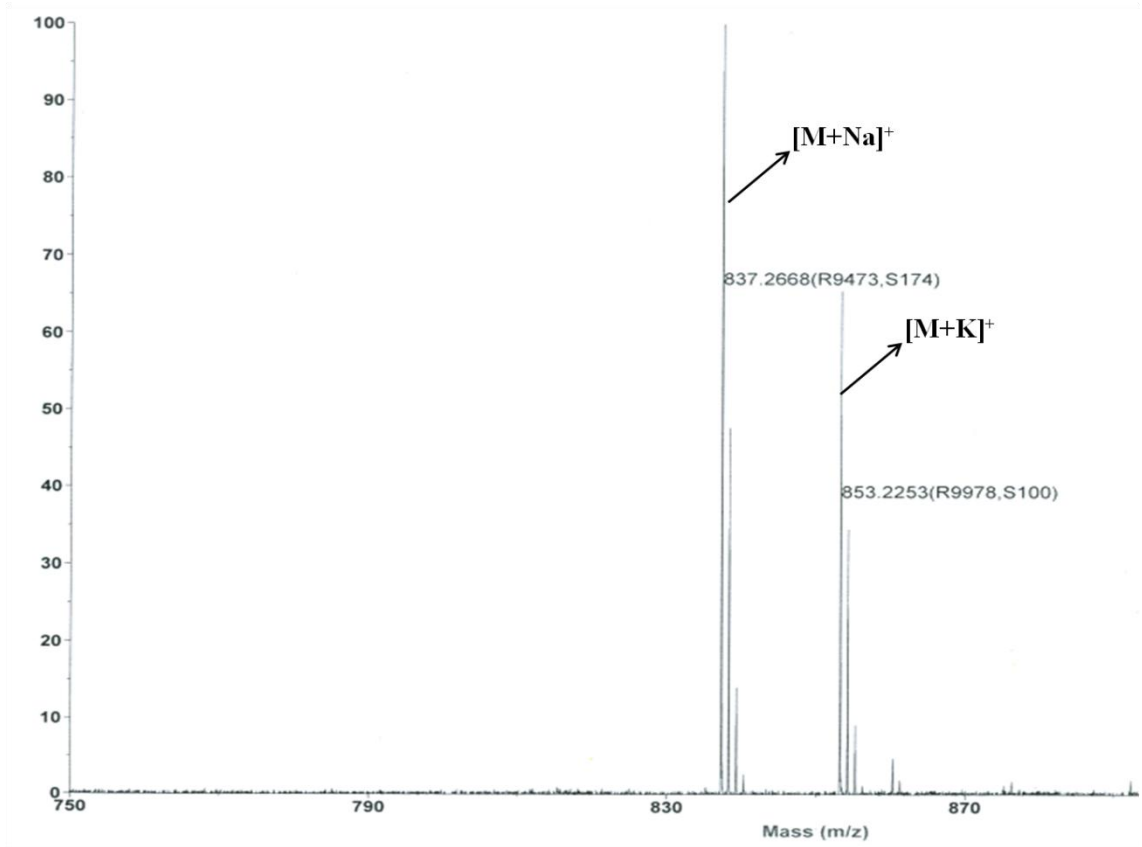

^{1}H NMR spectrum of NCDP 6

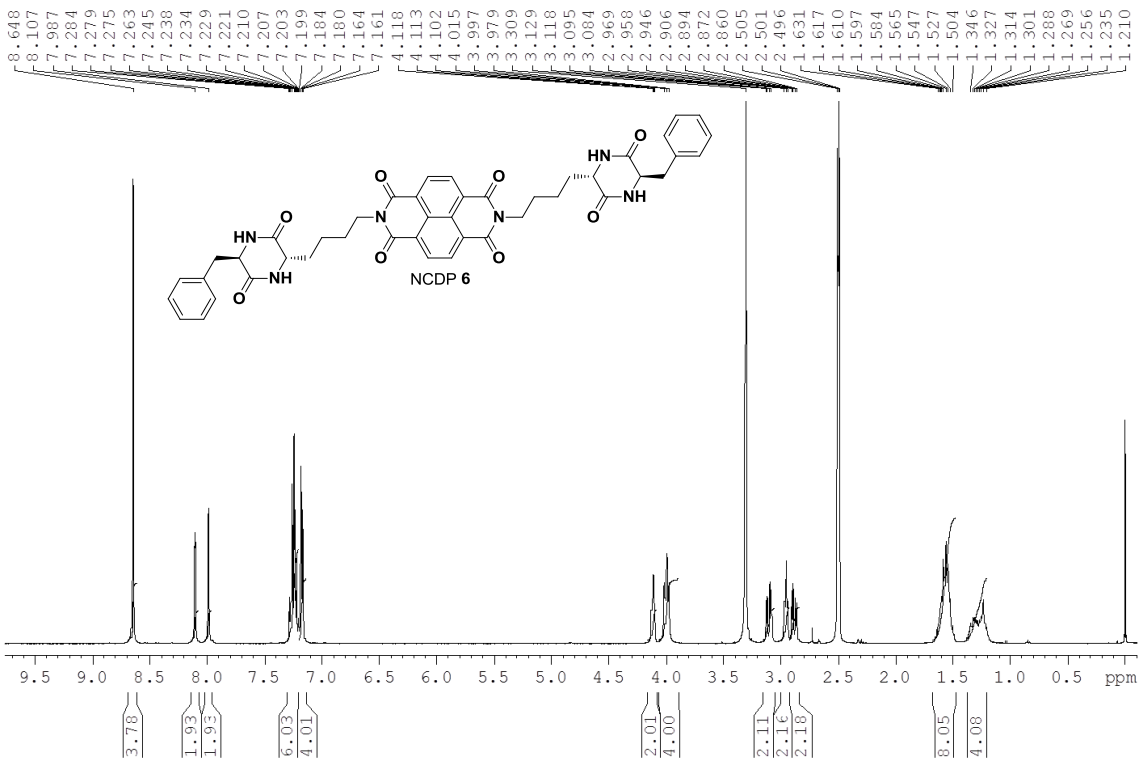

MALDI-TOF mass spectrum of NCDP 6

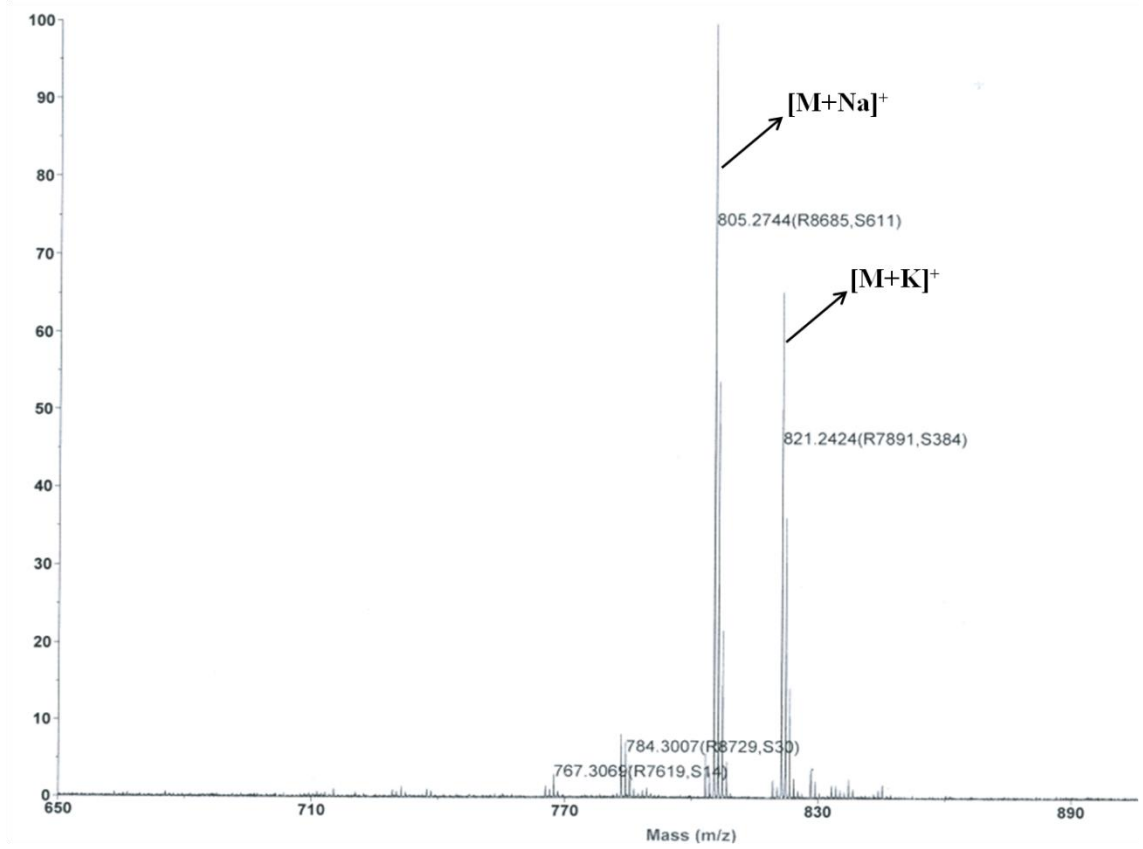

3.6 References

1. Watson, J. D.; Crick, F. H. C. Molecular structure of nucleic acids: a structure for deoxyribose nucleic acid. *Nature* **1953**, *171*, 737-738.

2. Pauling, L.; Corey, R. B.; Branson, H. R. The structure of proteins: two hydrogen-bonded helical configurations of the polypeptide chain. *Proc. Natl. Acad. Sci. USA* **1951**, *37*, 205-211.

3. Hein, J. E.; Blackmond, D. G. On the origin of single chirality of amino acids and sugars in biogenesis. *Acc. Chem. Res.* **2012**, *45*, 2045-2054.

4. Yashima, E.; Maeda, K.; Iida, H.; Furusho, Y.; Nagai, K. Helical polymers: synthesis, structures, and functions. *Chem. Rev.* **2009**, *109*, 6102-6211.

5. Feringa, B. L.; Delden, R. A. V.; Koumura, N.; Geertsema, E. M. Chiroptical molecular switches. *Chem. Rev.* **2000**, *100*, 1789-1816.

6. Canary, J. W. Redox-triggered chiroptical molecular switches. *Chem. Soc. Rev.* **2009**, *38*, 747-756.

7. Rowan, A. E.; Nolte, R. J. M. Helical molecular programming. *Angew. Chem. Int. Ed.* **1998**, *37*, 63-68.

8. Serrano, J. L.; Sierra, T. Helical supramolecular organizations from metal-organic liquid crystals. *Coord. Chem. Rev.* **2003**, *242*, 73-85.

9. Mateos-Timoneda, M. A.; Crego-Calama, M.; Reinhoudt, D. N. Supramolecular chirality of self-assembled systems in solution. *Chem. Soc. Rev.* **2004**, *33*, 363-372.

10. Wang, Y.; J. Xu, Wang, Y.; Chen, H. Emerging chirality in nanoscience. *Chem. Soc. Rev.* **2013**, *42*, 2930-2962.

11. Engelkamp, H.; Middelbeek, S.; Nolte, R. J. M. Self-assembly of disk-shaped molecules to coiled-coil aggregates with tunable helicity. *Science* **1999**, *284*, 785-788.

12. Nakashima, H.; Fujiki, M.; Koe, J. R.; Motonaga, M. Solvent and temperature effects on the chiral aggregation of poly(alkylarylsilane)s bearing remote chiral groups. *J. Am. Chem. Soc.* **2001**, *123*, 1963-1969.

13. Brizard, A.; Aim, C.; Labrot, T.; Huc, I.; Berthier, D.; Artzner, F.; Desbat, B.; Oda, R. Counterion, temperature, and time modulation of nanometric chiral ribbons from gemini-tartrate amphiphiles *J. Am. Chem. Soc.* **2007**, *129*, 3754-3762.

14. J. Cui, A. Liu, Y. Guan, J. Zhang, Z. Shen, X. Wan, Tuning the helicity of self-assembled structure of a sugar-based organogelator by the proper choice of cooling rate. *Langmuir* **2010**, *26*, 3615-3622.

15. Huang, Y. W.; Hu, J. C.; Kuang, W. F.; Wei, Z. X.; Faul, C. F. J. Modulating helicity through amphiphilicity-tuning supramolecular interactions for the controlled assembly of perylenes. *Chem. Commun.* **2011**, *47*, 5554-5556.

16. Hu, J. C.; Kuang, W. F.; Deng, K.; Zou, W. J.; Huang, Y. W.; Wei, Z. X.; Faul, C. F. J. Self-assembled sugar-substituted perylene diimide nanostructures with homochirality and high gas sensitivity. *Adv. Funct. Mater.* **2012**, *22*, 4149-4158.

17. Fujiki, M. Helix Magic: thermo-driven chiroptical switching and screw-sense inversion of flexible rod helical polysilylenes. *J. Am. Chem. Soc.* **2000**, *122*, 3336-3343.

18. Fujiki, M.; Koe, J. R.; Motonaga, M.; Nakashima, H.; Terao, K.; Teramoto, A. Computing handedness: quantized and superposed switch and dynamic memory of helical polysilylene. *J. Am. Chem. Soc.* **2001**, *123*, 6253-6261.

19. Schenning, A. P. H. J.; Fransen, M.; Meijer, E. W. Side-chain-functionalized polyacetylenes: liquid crystalline and stereomutational properties. *Macromol. Rapid Commun.* **2002**, *23*, 265-270.

20. Mayer, S.; Maxein, G.; Zentel, R. Correlation between the isomerization of side groups and the helical main chain in chiral polyisocyanates. *Macromolecules* **1998**, *31*, 8522-8525.

21. Green, M. M.; Khatri, C.; Peterson, N. C. A macromolecular conformational change driven by a minute chiral solvation energy. *J. Am. Chem. Soc.* **1993**, *115*, 4941-4942.

22. Yashima, E.; Maeda, K.; Sato, O. Switching of a macromolecular helicity for visual distinction of molecular recognition events. *J. Am. Chem. Soc.* **2001**, *123*, 8159-8160.

23. Sakajiri, K.; Sugisaki, T.; Moriya, K.; Kutsumizu, S. Solvent-induced chirality inversion involving supramolecular helix transformation and color-tunable fluorescence of a C_6-symmetric hexakis(phenylethynyl)benzene derivative. *Org. Biomol. Chem.* **2009**, *7*, 3757-3762.

24. Goto, H.; Yashima, E.; Okamoto, Y. Unusual solvent effects on chiroptical properties of an optically active regioregular polythiophene in Solution. *Chirality* **2000**, *12*, 396-399.

25. Yamada, T.; Nagata, Y.; Suginome, M. Non-hydrogen-bonding-based, solvent-dependent helix inversion between pure P-helix and pure M-helix in poly(quinoxaline-2,3-diyl)s bearing chiral side chains *Chem. Commun.* **2010**, *46*, 4914-4916.

26. Nagata, Y.; Nishikawa, T.; Suginome, M. Solvent-dependent fluorescence and circular dichroism properties of poly(quinoxaline-2,3-diyl)s bearing pyrene pendants *Chem. Commun.* **2012**, *48*, 11193-11195.

27. Qi, T.; Maurizot, V.; Noguchi, H.; Charoenraks, T.; Kauffmann, B.; Takafuji, M.; Ihara, H.; Huc, I. Solvent dependence of helix stability in aromatic oligoamide foldamers. *Chem. Commun.* **2012**, *48*, 6337-6339.

28. Lohr, A.; Lysetska, M.; Würthner, F. Thermodynamic self-assembly of helical merocyanine dye nanorods. *Angew. Chem.* **2005**, *117*, 5199-5202.

29. Jyothish, K.; Hariharan, M.; Ramaiah, D. Chiral supramolecular assemblies of a squaraine dye in solution and thin films: concentration-, temperature-, and solvent-induced chirality inversion. *Chem. Eur. J.* **2007**, *13*, 5944-5951.

30. Cantekin, S.; Nakano, Y.; Everts, J. C.; van der Schoot, P.; Meijer, E.W.; Palmans, A. R. A. A stereoselectively deuterated supramolecular motif to probe the role of solvent during self-assembly processes. *Chem. Commun.* **2012**, *48*, 3803-3805.

31. Guelev, V. M.; Harting, M. T.; Lokey, R. S.; Iverson, B. L. Altered sequence specificity identified from a library of DNA-binding small molecules. *Chem. Biol.* **2000**, *7*, 1-8.

32. Guha, S.; Saha, S. Fluoride ion sensing by an anion-π interaction. *J. Am. Chem. Soc.* **2010**, *132*, 17674-17677.

33. Holman, G. G.; Zewail-Foote, M.; Smith, A. R.; Johnson, K. A.; Iverson, B. L. A sequence-specific threading tetra-intercalator with an extremely slow dissociation rate constant. *Nat. Chem.* **2011**, *3*, 875-881.

34. Collie, G. W.; Promontorio, R.; Hampel, S. M.; Micco, M.; Neidle, S.; Parkinson, G. N. Structural basis for telomeric G-quadruplex targeting by naphthalene diimide ligands. *J. Am. Chem. Soc.* **2012**, *134*, 2723-2731.

35. Avinash, M. B.; Govindaraju, T. Engineering molecular organization of naphthalenediimides: large nanosheets with metallic conductivity and attoliter containers. *Adv. Funct. Mater.* **2011**, *21*, 3875-3882.

36. Alp, S.; Erten, S.; Karapire, C.; Koz, B.; Doroshenko, A. O.; Ìcli, S. Photoinduced energy-electron transfer studies with naphthalene diimides. *J. Photochem. Photobiol. A* **2000**, *135*, 103-110.

37. Erten, B.; Posokhov, Y.; Alp, S.; Ìcli, S. The study of the solubility of naphthalene diimides with various bulky flanking substituents in different solvents by UV-vis spectroscopy. *Dyes Pigm.* **2005**, *64*, 171-178.

38. Pengo, P.; Pantos, G. D.; Otto, S.; Sanders, J. K. M. Efficient and mild microwave-assisted stepwise functionalization of naphthalenediimide with α-amino acids. *J. Org. Chem.* **2006**, *71*, 7063-7066.

39. Shao, H.; Seifert, J.; Romano, N. C.; Gao, M.; Helmus, J. J.; Jaroniec, C. P.; Modarelli, D. A.; Parquette, J. R. Amphiphilic self-assembly of an n-type nanotube. *Angew. Chem.* **2010**, *122*, 7854-7857; *Angew. Chem. Int. Ed.* **2010**, *49*, 7688-7691.

40. Shao, H.; Nguyen, T.; Romano, N. C.; Modarelli, D. A.; Parquette, J. R. Self-assembly of 1-D n-type nanostructures based on naphthalene diimide-appended dipeptides. *J. Am. Chem. Soc.* **2009**, *131*, 16374-16376.

41. Shao, H.; Parquette, J. R. A π-conjugated hydrogel based on an Fmoc-dipeptide naphthalene diimide semiconductor. *Chem. Commun.* **2010**, *46*, 4285-4287.

42. Shao, H.; Gao, M.; Kim, S. H.; Jaroniec, C. P.; Parquette, J. R. Aqueous self-assembly of L-lysine-based amphiphiles into 1D n-type nanotubes. *Chem. Eur. J.* **2011**, *17*, 12882-12885.

43. Horne, W. S.; Ashkenasy, N.; Ghadiri, M. R. Modulating charge transfer through cyclic D, L-α-peptide self-assembly. *Chem. Eur. J.* **2005**, *11*, 1137-1144.

44. Bell, T. D. M.; Yap, S.; Jani, C. H.; Bhosale, S. V.; Hofkens, J.; Schryver, F. C. D.; Langford, S. J.; Ghiggino, K. P. Synthesis and photophysics of core-substituted naphthalene diimides: fluorophores for single molecule applications. *Chem. Asian J.* **2009**, *4*, 1542-1550.

45. Durban, M. M.; Kazarinoff, P. D.; Luscombe, C. K. Synthesis and characterization of thiophene-containing naphthalene diimide n-type copolymers for OFET applications. *Macromolecules* **2010**, *43*, 6348-6352.

46. Molla, M. R.; Das, A.; Ghosh, S. Chiral induction by helical neighbour: spectroscopic visualization of macroscopic-interaction among self-sorted donor and acceptor π-stacks. *Chem. Commun.* **2011**, *47*, 8934-8936.

47. Molla, M. R.; Ghosh, S. Hydrogen-bonding-mediated J-aggregation and white-light emission from a remarkably simple, single-component, naphthalenediimide chromophore. *Chem. Eur. J.* **2012**, *18*, 1290-1294.

48. Avinash, M. B.; Govindaraju, T. Amino acid derivatized arylenediimides: a versatile modular approach for functional molecular materials. *Adv. Mater.* **2012**, *24*, 3905-3922.

49. Avinash, M. B.; Govindaraju, T. A bio-inspired design strategy: organization of tryptophan-appended naphthalenediimide into well-defined architectures induced by molecular interactions. *Nanoscale* **2011**, *3*, 2536-2543.

50. Avinash, M. B.; Verheggen, E.; Schmuck, C.; Govindaraju, T. Self-cleaning functional molecular materials. *Angew. Chem.* **2012**, *124*, 10470-10474.

51. Avinash, M. B.; Govindaraju, T. Extremely slow dynamics of an abiotic helical assembly: unusual relevance to the secondary structure of proteins. *J. Phys. Chem. Lett.* **2013**, *4*, 583-588.

52. Pandeeswar, M.; Avinash, M. B.; Govindaraju, T. Chiral transcription and retentive helical memory: probing peptide auxiliaries appended with naphthalenediimides for their one-dimensional molecular organization. *Chem. Eur. J.* **2012**, *18*, 4818-4822.

53. MacDonald, J. C.; Whitesides, G. M. Solid-state structures of hydrogen-bonded tapes based on cyclic secondary diamides. *Chem. Rev.* **1994**, *94*, 2383-2420.

54. Prasad, C. Bioactive cyclic dipeptides. *Peptides* **1995**, *16*, 151-164.

55. Prakash, K. R. C.; Tang, Y.; Kozikowski, A. P.; Flippen-Anderson, J. L.; Knoblach, S. M.; Faden, A. I. Synthesis and biological activity of novel neuroprotective diketopiperazines. *Bioorg. Med. Chem.* **2002**, *10*, 3043-3048.

56. Martins, M. B.; Carvalho, I. Diketopiperazines: biological activity and synthesis. *Tetrahedron* **2007**, *63*, 9923-9932.

57. Hanabusa, K.; Matsumoto, Y.; Miki, T.; Koyama, T.; Shirai, H. Cyclo(dipeptide)s as low-molecular-mass gelling agents to harden organic fluids. *J. Chem. Soc. Chem. Commun.* **1994**, 1401-1402.

58. Bergeron, R. J.; Phanstiel, O.; Yao, G. W.; Milstein, S.; Weimar, W. R. Macromolecular self-assembly of diketopiperazine tetrapeptides. *J. Am. Chem. Soc.* **1994**, *116*, 8479-8484.

59. Manchineella, S.; Govindaraju, T. Hydrogen bond directed self-assembly of cyclic dipeptide derivatives: gelation and ordered hierarchical architectures. *RSC Adv.* **2012**, *2*, 5539-5545.

60. Govindaraju, T.; Pandeeswar, M.; Jayaramulu, K.; Jaipuria, G.; Atreya, H. S. Spontaneous self-assembly of designed cyclic dipeptide (Phg-Phg) into two-dimensional nano- and mesosheets. *Supramol. Chem.* **2011**, *23*, 487-492.

61. Govindaraju, T. Spontaneous self-assembly of aromatic cyclic dipeptide into fibre bundles with high thermal stability and propensity for gelation. *Supramol. Chem.* **2011**, *23*, 759-767.

62. Measey, T. J.; Smith, K. B.; Decatur, S. M.; Zhao, L. M.; Yang, G. L.; Stenner, R. S. Self-aggregation of a polyalanine octamer promoted by its C-terminal tyrosine and probed by a strongly enhanced vibrational circular dichroism signal. *J. Am. Chem. Soc.* **2009**, *131*, 18218-18219.

63. Xie, Z.; Zhang, A.; Ye, L.; Feng, Z. Organo- and hydrogels derived from cyclo(L-tyr-L-lys) and its ε-amino derivatives. *Soft Matter* **2009**, *5*, 1474-1482.

64. Hong, D. P.; Hoshino, M.; Kuboi, R.; Goto, Y. Clustering of fluorine-substituted alcohols as a factor responsible for their marked effects on proteins and peptides. *J. Am. Chem. Soc.* **1999**, *121*, 8427-8433.

65. Andersen, N. H.; Dyer, R. B.; Fesinmeyer, R. M.; Gai, F.; Liu, Z. H.; Neidigh, J. W.; Tong, H. Effect of hexafluoroisopropanol on the thermodynamics of peptide secondary structure formation. *J. Am. Chem. Soc.* **1999**, *121*, 9879-9880.

66. Jha, A.; Narayan, S.; Udgaonkar, J. B.; Krishnamoorthy, G. Solvent-induced tuning of internal structure in a protein amyloid protofibril. *Biophys. J.* **2012**, *103*, 797-806.

67. McKerrow, A. J.; Buncel, E.; Kazmaier, P. M. Aggregation of squaraine dyes: structure-property relationships and solvent effects. *Can. J. Chem.* **1995**, *73*, 1605-1615.

68. Gayathri, B. R.; Mannekutla, J. R.; Inamdar, S. R. Effect of binary solvent mixtures (DMSO/water) on the dipole moment and lifetime of coumarin dyes. *J. Mol. Struct.* **2008**, *889*, 383-393.

69. Stewart, J. J. P. Optimization of parameters for semiempirical methods VI: more modifications to the NDDO approximations and re-optimization of parameters. *J. Mol. Model.* **2013**, *19*, 1-32.

70. Hembury, G. A.; Borovkov, V. V.; Inoue, Y. Chirality-sensing supramolecular systems. *Chem. Rev.* **2008**, *108*, 1-73.

71. Dennington, R.; Keith, T.; Millam, J. Semichem Inc., Shawnee Mission KS, *GaussView Version 5*, **2009**.

72. Stewart, J. J. P. *Stewart computational chemistry*, Colorado Springs, CO, USA, *MOPAC2012*, **2012**.

73. Zhao, Y.; Truhlar, D. G. The M06 suite of density functionals for main group thermochemistry, thermochemical kinetics, noncovalent interactions, excited states, and transition elements: two new functionals and systematic testing of four M06-class functionals and 12 other functionals. *Theor. Chem. Acc.* **2008**, *120*, 215-241.

74. Frisch, M. J.; Trucks, G. W.; Schlegel, H. B.; Scuseria, G. E.; Robb, M. A.; Cheeseman, J. R.; Scalmani, G.; Barone, V.; Mennucci, B.; Petersson, G. A.; Nakatsuji, H.; Caricato, M.; Li, X.; Hratchian, H. P.; Izmaylov, A. F.; Bloino, J.; Zheng, G.; Sonnenberg, J. L.; Hada, M.; Ehara, M.; Toyota, K.; Fukuda, R.; Hasegawa, J.; Ishida, M.; Nakajima, T.; Honda, Y.; Kitao, O.; Nakai, H.; Vreven, T.; Montgomery, J. A.; Peralta, J. E.; Ogliaro, F.; Bearpark, M.; Heyd, J. J.; Brothers, E.; Kudin, K. N.; Staroverov, V. N.; Kobayashi, R.; Normand, J.; Raghavachari, K.; Rendell, A.; Burant, J. C.; Iyengar, S. S.; Tomasi, J.; Cossi, M.; Rega, N.; Millam, J. M.; Klene, M.; Knox, J. E.; Cross, J. B.; Bakken, V.; Adamo, C.; Jaramillo, J.; Gomperts, R.; Stratmann, R. E.; Yazyev, O.; Austin, A. J.; Cammi, R.; Pomelli, C.; Ochterski, J. W.; Martin, R. L.; Morokuma, K.; Zakrzewski, V. G.; Voth, G. A.; Salvador, P.; Dannenberg, J. J.; Dapprich, S.; Daniels, A. D. F.; Foresman, J. B.; Ortiz, J. V.; Cioslowski, J.; Fox, D. J. Gaussian 09, Revision C.01, *Gaussian, Inc.* Wallingford CT, **2009**.

75. F. L. Weinhold, C. R. Landis. *Valency and bonding: a natural bond orbital donor-acceptor perspective*. Cambridge University Press, Cambridge, **2005**.

Chapter 4

Antioxidant Phenolic Cyclic Dipeptides

4.1 Introduction

Oxidative stress caused by excessive free radicals has a detrimental effect on overall well-being and implicated in a number of pathological conditions and aging of humans.[1,2] A critical amount of free radicals is essential to maintain certain biochemical functions under normal physiological conditions. However, the presence of excessive reactive radical species beyond the critical concentration that cannot be controlled by natural antioxidant mechanisms involving superoxide dismutases, catalases, glutathione, and peroxidins adversely affect almost every organ function and pose severe health problems.[3-8] Oxidative stress causes cellular and tissue damage leading to cancer, inflammatory bowel disease and responsible for various neurodegenerative disorders including Alzheimer's disease (AD), Parkinson disease (PD), multiple sclerosis, amyotrophic lateral sclerosis (ALS) leading to memory loss and dementia.[9,10] Among all the neurodegenerative disorders, AD is the most common form of dementia epitomized by the progressive impairment of cognitive ability leading to death.[10,11] Aggregation and deposition of toxic Aβ (amyloid beta), hyperphosphorylation of tau protein and formation of neurofibrillary tangles (NFTs) are the hallmark changes observed in AD. Furthermore, AD is associated with the production of excessive reactive oxygen species by metal associated Aβ aggregates. The toxicity in AD is multifactorial and many *in vitro* studies on disease models and clinical studies have demonstrated that Aβ aggregate-induced oxidative stress plays a key role in the loss of cognitive function and disease progression leading to death.[11,12] Natural polyphenolic compounds such as non-flavonoid curcumin, resveratrol, tannic acid, melanins and flavonoid quercetin, epigallocatechin gallate (EGCG), silibinin and few synthetic polyphenolic compounds have been studied for modulating the oxidative stress associated toxicity in AD.[13-15] The major problem associated with the existing natural or synthetic molecules for controlling oxidative stress

in various disease conditions such as AD is their limited bioavailability, blood brain barrier (BBB) crossing ability along with other unwanted health effects.

Cyclic dipeptides (CDPs) also known as 2,5-diketopiperazines (DKPs) are the smallest cyclic form of peptides containing a 6-membered heterocyclic lactam core. CDPs are secondary metabolites that are conserved through evolution and ubiquitously present in nature ranging from bacteria to humans with diverse biological functions.[16] Cyclodipeptide synthases (CDPSs) and nonribosomal peptide synthetases (NRPSs) facilitates the non-ribosomal biosynthesis of a number of unmodified and modified CDPs.[17,18] CDP derivatives obtained either from natural sources or chemical synthesis are important class of active molecules with diverse biological functions such as bacterial quorum sensing, antibacterial, antimicrobial, anticancer properties, neuroprotective functions and even as carriers for biologically important molecules across the blood brain barrier.[19-22] CDPs owing to their rigid cyclic structure are stable towards enzymatic degradation, which further augments the possibility of developing CDP derived systems for oral delivery. Inspired by the beneficial properties of polyphenolic antioxidant molecules and unique properties of CDPs, we have designed a series of aromatic CDPs (**7-12**) with varying proteinogenic and non-proteinogenic phenolic amino acid composition and examined their antioxidant property. Free radical scavenging property against 2,2-diphenyl-1-picrylhydrazyl (DPPH) radicals, cytocompatibility with murine adrenal-derived PC12 cells and disaggregation of preformed $A\beta_{1-42}$ were studied. To the best of our knowledge, this is the first report on a systematic study of the structure-property relation of CDPs for antioxidant property with potential biomedical applications.

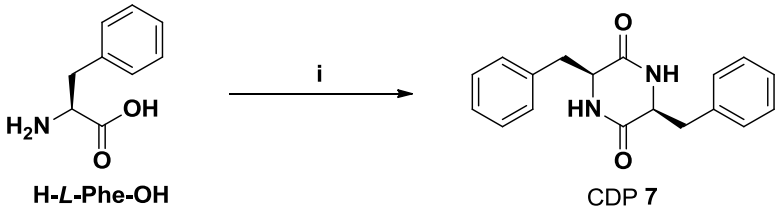

Scheme 4.1. Synthesis of CDP **7**. Reagents and conditions: (i) 1,2-ethanediol, reflux, 18 h.

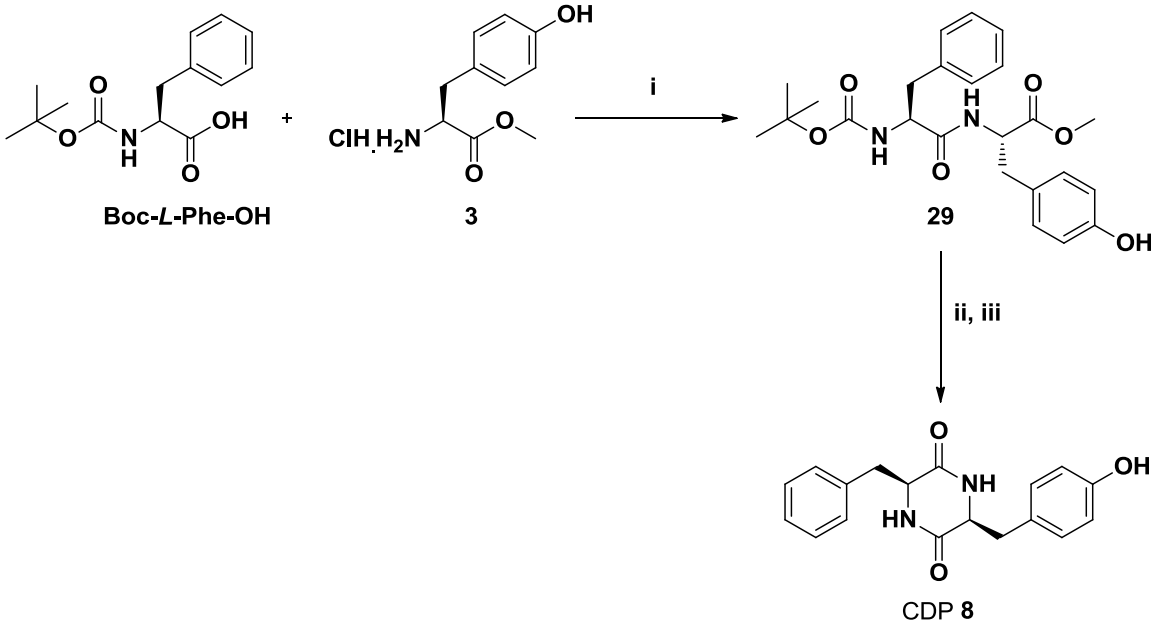

Scheme 4.2. Synthesis of CDP **8**. Reagents and conditions: (i) EDC.HCl, HOBt, DIPEA, DCM, 0 ºC- RT, 6 h. (ii) TFA-H_2O (v/v; 1:1), TIPS, RT, 4 h. (iii) NMM, 0.1M CH_3COOH, *Sec*-BuOH, 100 ºC, 6 h. EDC.HCl = 1-Ethyl-3-(3-dimethylaminopropyl)carbodiimide hydrochloride, HOBt = 1-hydroxybenzotriazole, DIPEA = *N*,*N*-diisopropylethylamine, DCM = dichloromethane, TFA = trifluoroacetic acid, NMM = *N*-methyl morpholine.

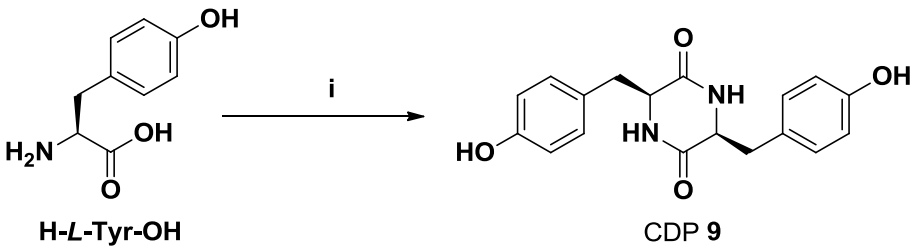

Scheme 4.3. Synthesis of CDP **9**. Reagents and conditions: (i) 1,2-ethanediol, reflux, 24 h.

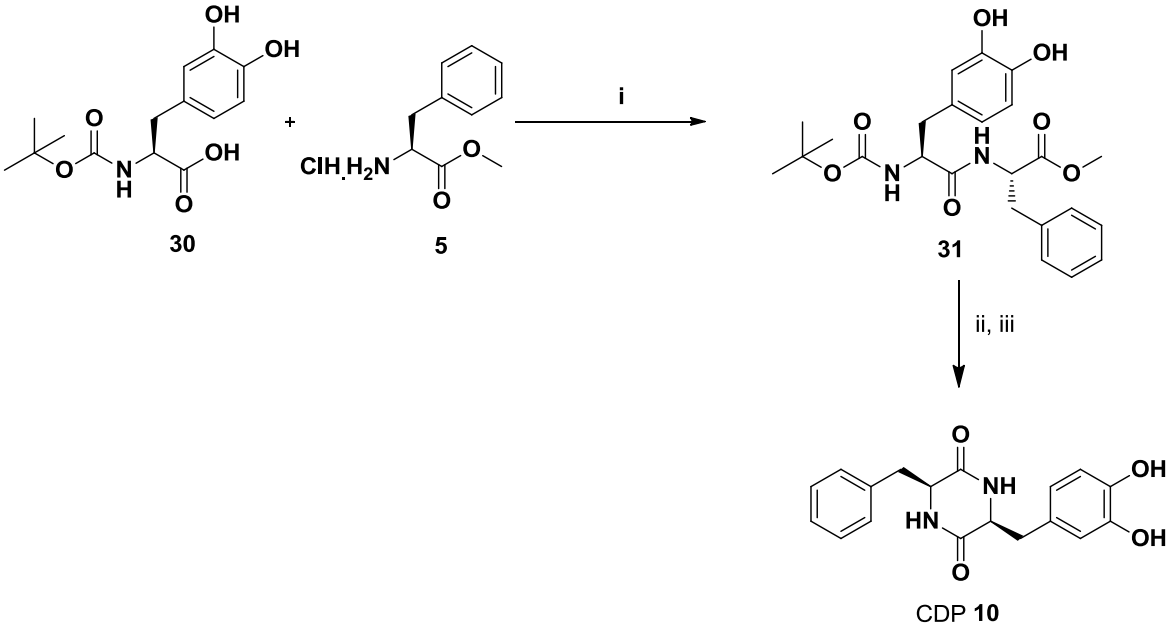

Scheme 4.4 Synthesis of CDP **10**. Reagents and conditions: (i) Di-tert-butyl dicarbonate, NaOH, 1,4-dioxane-H_2O, 24 h, RT. (ii) EDC.HCl, HOBt, DIPEA, H-*L*-Phe-OCH_3.HCl, DCM, 0 ºC- RT, 6 h. (iii) TFA-H_2O (v/v; 1:1), TIPS, RT, 4 h. (iv) NMM, 0.1M CH_3COOH, *Sec*-BuOH, 100 ºC, 6 h. DOPA: 3,4-dihydroxyphenylalanine.

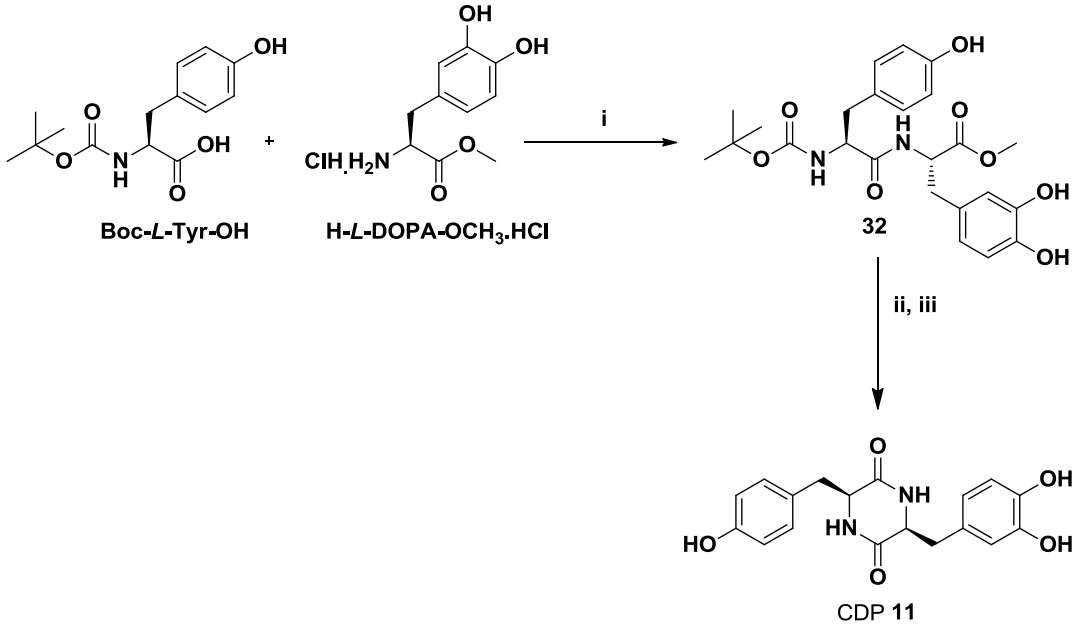

Scheme 4.5. Synthesis of CDP **11**. Reagents and conditions: (i) EDC.HCl, HOBt, DIPEA, DCM, 0 ºC- RT, 5 h. (ii) TFA-H_2O (v/v; 1:1), TIPS, RT, 4 h. (iii) NMM, 1M CH_3COOH, *Sec*-BuOH, 100 ºC, 6 h.

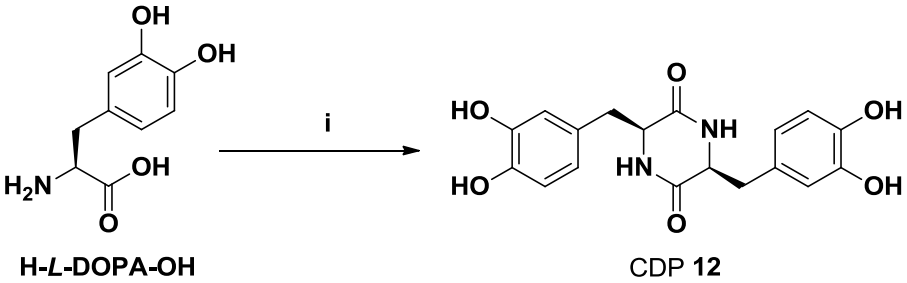

Scheme 4.6. Synthesis of CDP **12**. Reagents and conditions: (i) 1,2-ethanediol, reflux, 24 h.

4.2 Results and Discussion

4.2.1 Synthesis of CDPs

Cyclic dipeptides **7** [*cyclo*(*L*-Phe-*L*-Phe], **9** [*cyclo*(*L*-Tyr-*L*-Tyr] and CDP **12** [*cyclo*(*L*-DOPA-*L*-DOPA] were prepared by the condensation of corresponding amino acids in ethylene glycol under reflux conditions (Schemes 4.1, 4.3. 4.6).[23,24] While, CDPs **8** [*cyclo*(*L*-Phe-*L*-Tyr], **10** [*cyclo*(*L*-Phe-*L*-DOPA] and **11** [*cyclo*(*L*-Tyr-*L*-DOPA] were prepared through the synthesis of linear dipeptides followed by the cyclization under reflux conditions in *sec*-butanol (Schemes 4.2, 4.4, 4.5).[25] Synthesis protocols (condensation and cyclization) were optimized for each CDP to obtain the maximum possible yields with minimum synthesis steps (Scheme 4.1-4.6). Chemical purity and integrity of the prepared peptides and CDPs was evaluated using NMR, mass spectrometry, and elemental analysis.

4.2.2 Antioxidant activity

The potential of CDPs **7-12** to scavenge the free radicals was evaluated colorimetrically by using 2,2-diphenyl-1-picrylhydrazyl (DPPH) radicals.[26] The aqueous ethanol solution of DPPH radicals shows a deep violet colour with strong absorption in the visible region (460-560 nm) with a direct correlation of the colour intensity to the concentration of radicals and hence serves as a measure to calculate the radical scavenging property of

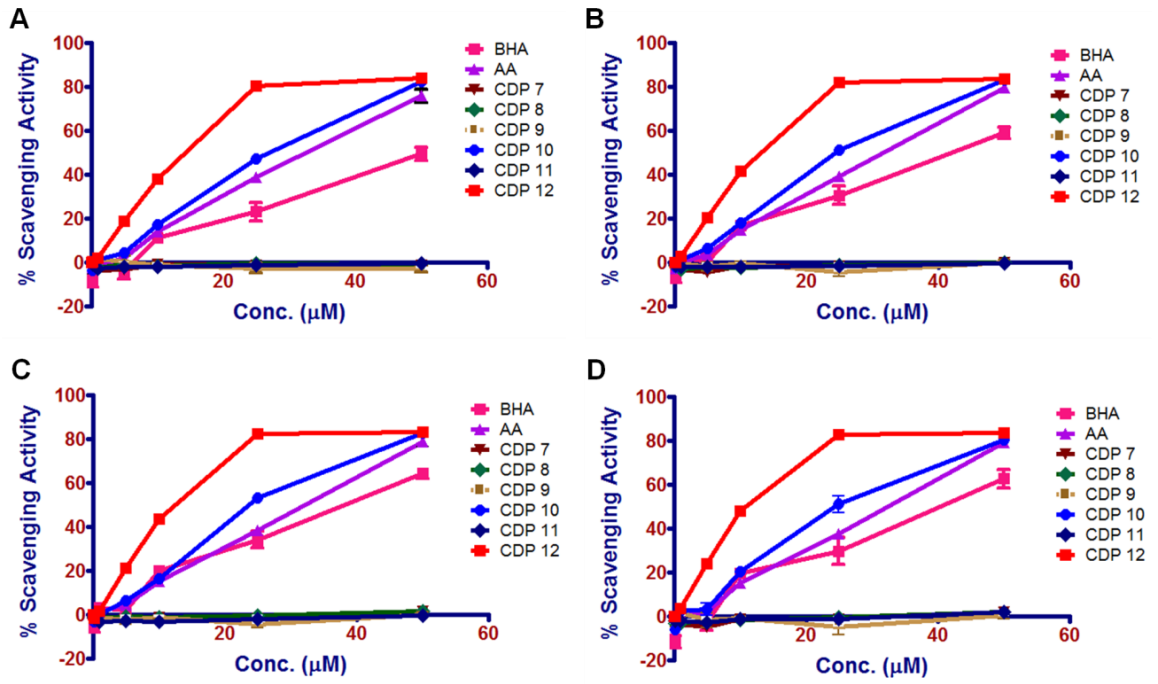

Figure 4.1 Antioxidant assay of CDPs **7-12**. Concentration-dependent radical scavenging property of CDPs **7-12** against DPPH free radicals after (A) 30 min, (B) 60 min, (C) 90 min and (D) 120 min of incubation at room temperature under dark conditions. The absorbance was measured at 490 nm. Values shown are means ± SEM of three independent experiments performed in three to four replicates.

CDPs. Natural antioxidant molecule ascorbic acid (AA, vitamin C) that is present in diet and helps in maintaining the physiological hemostasis, and butylated hydroxyanisole (BHA) a synthetic antioxidant that is used commercially in the food industry were used as positive controls and untreated DPPH as a negative control to study the antioxidant efficacy of CDPs. Increasing concentrations (0-50 µM) of CDPs (**7-12**) were incubated with a degassed aqueous ethanol solution of DPPH (100 µM) at room temperature under dark conditions. The change in concentration of DPPH radicals was calculated by measuring the colorimetric intensity at 490 nm using a microplate reader at regular intervals of 30, 60, 90 and 120 min of incubation (Figure 4.1). The untreated DPPH samples at each time point served as control and the antioxidant efficacy of CDPs was

calculated with respect to the control. After 30 min of incubation, lower concentrations of CDPs (< 5µM) did not show significant antioxidant activity, similar results were observed for the positive controls AA and BHA. However, significant radical scavenging activity was observed at CDP concentrations above 5 µM in an amino acid side chain dependent manner. CDPs **7, 8** and **9** containing either phenylalanine or tyrosine in the structure did not show any radical scavenging property under the studied conditions at all time points (Figure 4.1). CDPs **10** and **12** containing one and two DOPA amino acids respectively showed very good activity which is better than the positive controls. Surprisingly, CDP **11** with tyrosine and DOPA did not show any significant radical scavenging property under the studied conditions. CDPs **10** and **12** showed superior radical scavenging i.e. antioxidant properties compared to AA and BHA at corresponding concentrations at 60, 90 and 120 min incubation. The observed radical scavenging property of CDP **10** and **12** was attributed to the ability of DOPA to undergo keto-enol tautomerization and neutralize the DPPH radicals similar to the mechanism observed in natural phenolic antioxidant molecules curcumin and melanin.[14,27,28] Among CDP **10** and **12**, CDP **12** showed higher radical scavenging property which is attributed to the presence of two DOPA moieties in CDP **12**. Overall, this study confirmed the phenolic amino acid composition dependent antioxidant activity of CDPs and DOPA-containing CDPs **10** and **12** found to be potential antioxidant compounds (Figure 4.1).

4.2.3 Cytotoxicity analysis

Murine adrenal medulla derived PC12 (pheochromocytoma) cells were chosen for assessing the cytotoxicity of CDPs (**7-12**) *in vitro*. The viability of PC12 treated with various concentrations of CDPs was evaluated using 3-(4,5-dimethylthiazol-2-yl)-2,5-diphenyltetrazolium bromide (MTT) assay. Cell permeable MTT is a tetrazolium

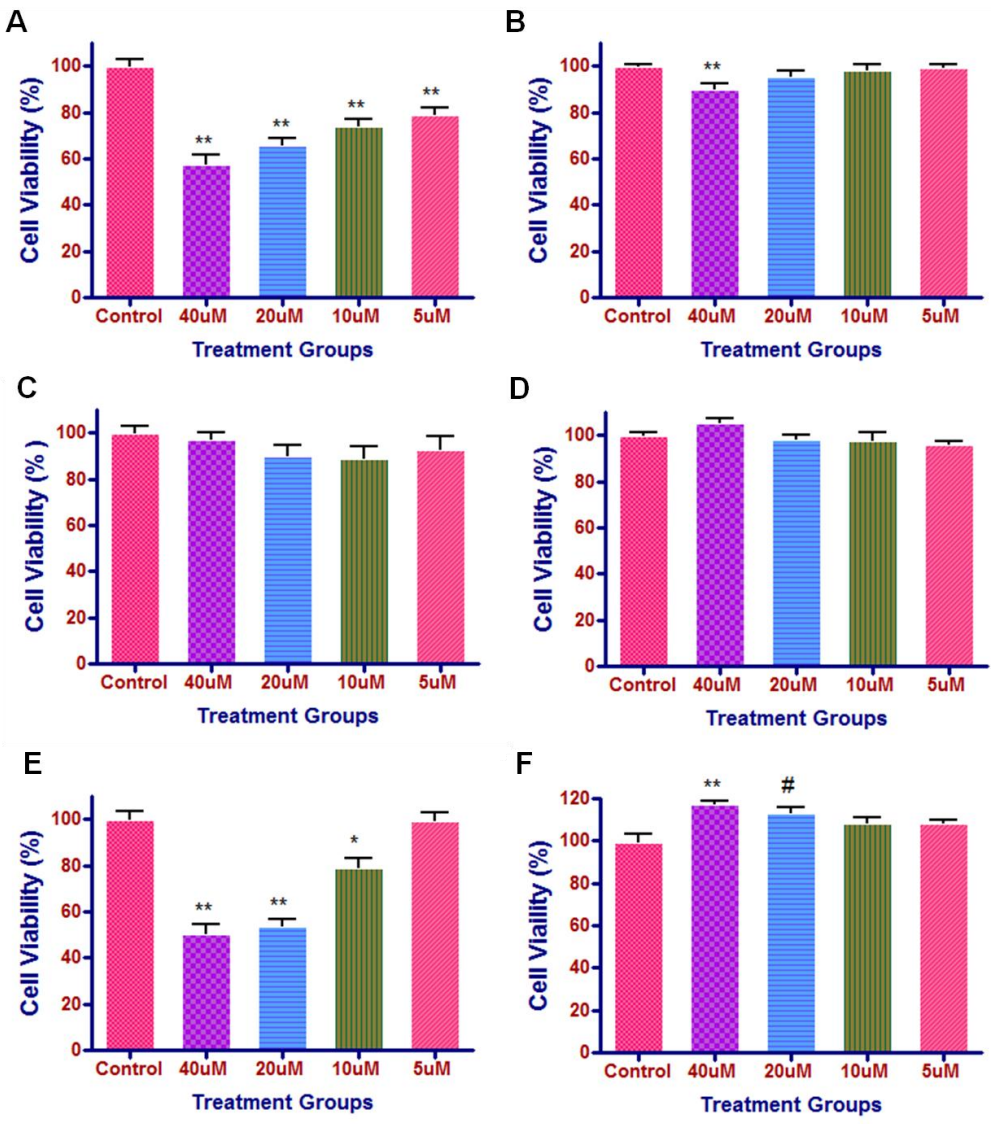

Figure 4.2 Cytotoxicity study of CDPs **7-12**. MTT assay results showing % of viable cells treated with different concentration of (A) CDP **7**, (B) CDP **8**, (C) CDP **9**, (D) CDP **10**, (E) CDP **11** and (F) CDP **12** for 24 h. All data points represent mean ± SEM (n=3). #($p < 0.05$), * ($p < 0.01$) and ** ($p < 0.001$) denotes significant difference compared to control. MTT: 3-(4,5-dimethylthiazol-2-yl)-2,5-diphenyltetrazolium bromide.

derivative and is reduced by mitochondrial oxidoreductases of live cells to purple-colored formazan crystals. Thus, the amount of purple-colored formazan produced is measured by a change in the optical density at 570 nm, which is a direct correlation to the cell viability. The measured optical intensity of wells containing CDP treated cells, in comparison to the control wells that received only complete media was calculated as the percentage of

cell viability and hence the toxicity of the CDPs. Untreated cells served as a positive control to calculate the percentage cell viability. PC12 cells were treated with increasing concentrations of CDPs **7-12** (0-50 µM) for 24 h and the cell viability calculated using MTT and the results are shown Figure 4.2. All the CDPs (**7-12)** showed good cell viability with more than 50% viable cells at concentrations less than 20 µM. CDPs **7** and **11** exhibited cytotoxicity at higher concentrations (≥40 µM) (Figure 4.2A,E). CDPs **8**, **9**, **10** and **12** showed good cell viability with PC12 cells for all the concentrations studied after 24 h of treatment (Figure 4.2B,C,D,F). Altogether, the *in cellulo* study exemplified the non-cytotoxic nature of CDPs, especially the free radical scavenging lead molecules CDP **10** and **12**.

4.2.4 $A\beta_{1-42}$ disaggregation study

Aβ aggregates were prepared from the $A\beta_{1-42}$ peptide and studied their disaggregation in presence of varying equivalents of CDPs **10** and **12**. CDPs **10** and **12** were chosen among the other CDPs because of their potential antioxidant property and cytocompatibility with PC12 cells (Figure 4.1 and 4.2). Briefly, the aggregation was induced by incubating the regenerated $A\beta_{1-42}$ in slightly acidic conditions for 24 h at 37 ºC and the aggregation of $A\beta_{1-42}$ into fibrillar structures was confirmed by transmission electron microscopy (TEM) analysis (data not shown).

The disaggregation efficacy of CDPs **10** and **12** towards the $A\beta_{1-42}$ aggregates was measured using thioflavin T (ThT) fluorescence assay and the results are expressed as a percentage of Aβ disaggregation with respect to the control or untreated $A\beta_{1-42}$ aggregates. As shown in Figure 4.3, one equivalent of CDPs ($A\beta_{1-42}$/CDP, 1:1) showed no significant disaggregation of preformed $A\beta_{1-42}$ aggregates. However, five equivalents of CDPs **10**

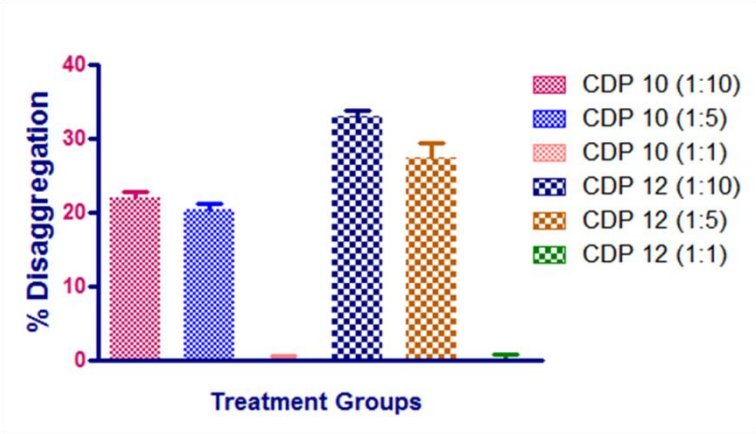

Figure 4.3 Thioflavin T (ThT) fluorescence assay showing the results of disaggregation of $A\beta_{1-42}$ aggregates treated with different equivalents of CDPs **10** and **12** for 24 h at 37 ºC. Values shown are means ± SEM of three independent experiments performed in three to four replicates.

and **12** showed an average 20% and 27% disaggregation of preformed $A\beta_{1-42}$ aggregates, respectively. A similar trend is observed with increasing the concentration of CDPs to 10 equivalents, and an average disaggregation of 22% and 33% $A\beta_{1-42}$ aggregates was observed for CDPs **10** and **12**, respectively (Figure 4.3). CDP **12** showed better disaggregation properties in comparison to CDP **10** for all the concentrations studied, which highlights the structure-activity relationship with respect to the amino acid composition. Overall, the disaggregation studies of illustrated the potential of CDPs **10** and **12** to disaggregate or dissolve the toxic aggregates of $A\beta_{1-42}$. Further studies to validate the antioxidant effect of CDP **10** and **12** and inhibition of multifaceted AB-toxicity is under progress in our laboratory.

4.3 Conclusion

In summary, we have designed and synthesized aromatic CDPs containing both proteinogenic and non-proteinogenic amino acids with a variable number of phenolic hydroxyl moieties. CDPs **7**-**12** were rationally designed based on the superior biological

activities observed with natural polyphenolic compounds such as curcumin, EGCG, and melanin. The significance of amino acid composition on the radical scavenging property of CDPs was examined systematically using DPPH-based calorimetric assay. CDPs with catechol (DOPA) moiety (**10** and **12**) emerged as the potential antioxidant molecules with better activity compared to other CDPs. The antioxidant property of CDPs **10** and **12** was found to be superior to the natural ascorbic acid (AA) and synthetic antioxidant (BHA) molecules. The cytocompatible nature of CDPs was demonstrated using murine brain PC12 cells and antioxidant CDPs were found to be non-toxic in nature. The potential applications of radical scavenging CDPs in modulating the toxicity of Alzheimer's disease (AD) was demonstrated in dissolving the Aβ aggregates. The preliminary studies on disaggregation of preformed $A\beta_{1-42}$ aggregates demonstrated the potential of CDPs **10** and **12** to dissolve the toxic protein aggregates. In general, DOPA-containing CDPs **10** and **12** showed strong antioxidant, good cytocompatibility and potential to dissolve aggregates of $A\beta_{1-42}$. CDP **12** showed overall better antioxidant and Aβ disaggregation properties compared to CDP **10** and therefore has the potential to modulate the multifaceted toxicity caused by protein aggregates which further aggravated by the reactive radical species. A detailed study exploring the potential applications of antioxidant CDPs is currently underway in our laboratory.

4.4 Experimental Section

Materials. Amino acids, coupling reagents and other chemicals were obtained from Spectrochem (India), Boc-protected amino acids were obtained from Sigma-Aldrich. All the solvents used for synthesis and spectroscopy studies were of spectroscopic grade and used as received from Spectrochem (India) without any further purification. Milli-Q water was used for extractions during synthesis, spectroscopic studies for gelation studies and

for the preparation of phosphate buffered saline (PBS) solutions. Thin Layer Chromatography (TLC) was performed using TLC Silica gel 60 F254 silica plates obtained from Merck and visualization of the compounds was achieved using UV light (254 and 365 nm) and ninhydrin treatment. Purification of compounds by column chromatography was carried using 60-120 mesh Silica gel obtained from ACME chemicals.

NMR spectroscopy. ^{1}H and ^{13}C NMR spectra were recorded on a Bruker AV-400 spectrometer in $CDCl_3$, DMSO-d_6 or D_2O at 300 K. Chemical shifts (δ) are reported in parts per million (ppm) with respect to residual solvent peak and the coupling constant (*J*) values are reported in hertz (Hz). The multiplicity of NMR signal are represented as s = singlet, d = doublet, t = triplet, q = quartet, dd = doublet of doublet and m = multiplet.

Elemental analysis. Elemental analysis of vacuum dried CDPs was carried out on a Thermo Scientific FLASH 2000 organic element analyzer.

High resolution mass spectrometry (HRMS*)*. HRMS spectra were recorded on Agilent 6538 UHD HRMS/Q-TOF spectrometer either in acetonitrile or methanol using positive ion electrospray ionization method.

Antioxidant assay. The inherent antioxidant property of CDPs was evaluated against the scavenging of 2,2-diphenyl-1-picrylhydrazyl (DPPH) radicals. The potential of CDPs to scavenge radicals was evaluated by incubating the different concentrations of CDPs with DPPH (100 µM) radicals in aqueous ethanol for different time points and the amount of un-scavenged radicals was calculated by measuring the intensity at 490 nm using a microplate reader (Infinite® 200 PRO, TECAN). Ascorbic acid (AA, vitamin C), butylhydroxyanisole (BHT) were used as positive control and untreated DPPH was used as negative control to measure the antioxidant efficiency of CDPs. The antioxidant

efficacy of CDPs was expressed in terms of percentage of free radical scavenging activity as a function of concentration and incubation time using the formula,

$$\%\ scavenging\ activity\ = \frac{(absorbance\ of\ control - absorbance\ of\ sample)}{\text{absorbance of control}} \times 100$$

Cell culture. Murine adrenal medulla derived PC12 cells were used to evaluate the cytocompatibility of CDPs **7-12**. Cells from cryopreserved stock were revived and grown in complete growth medium containing Roswell Park Memorial Institute (RPMI, Gibco) 1640 media supplemented with 10% heat-inactivated horse serum, 5% fetal bovine serum (Gibco), 1% antibiotic-antimycotic solution (Sigma). Cell cultures were maintained at 37 ºC, 95% humidity and 5% CO_2 using a humidified CO_2 incubator and the culture media was changed every alternate day of culture. Cells were detached from the tissue culture flasks upon reaching 70-80% of the confluence using 0.05% trypsin-EDTA (Gibco), harvested by neutralizing with complete media and centrifugation at 1500 rpm for 5 min. The cells were then subcultured for further use as required.

Cell viability study. The cytotoxicity of CDPs was evaluated by measuring the viability of PC12 cells treated with increasing concentrations (0-40 μM) for 24 h in culture using MTT assay. Approximately $l0^4$ cells/well of PC12 cells were seeded into 96 well plate and incubated for 24 h in humidified CO_2 incubator. 10% MTT (5 mg/mL, Sigma) reagent was added and incubated for 3 h at 37 ºC. The purple colored formazan crystals formed were solubilised using high purity dimethyl sulfoxide (DMSO; Merck) and the intensity of color was measured by recording the optical density (570 nm with 690 nm reference) using a microplate reader (Infinite® 200 PRO, TECAN). The measured optical intensity of CDP treated cells containing wells, in comparison to the control wells that received only complete media was calculated as the percentage of cell viability.

Preparation of $A\beta_{1-42}$ aggregates. $A\beta_{1-42}$ peptide (0.25 mg) (Calbiochem, Merck) was dissolved in hexafluoro-2-propanol (HFIP, 0.3 mL) and incubated at room temperature for 1 h. The solution was then sonicated at room temperature for 10 min and the obtained clear colorless HFIP solution was aliquoted into three 0.5 mL micro-centrifuge tubes (each tube receiving 0.083 mg of $A\beta_{1-42}$). HFIP was removed in a fume hood overnight followed by vacuum drying at room temperature for 3-4 h in a desiccator. The regenerated $A\beta_{1-42}$ samples were stored at -20 ºC until further use. Regenerated $A\beta_{1-42}$ peptide was dissolved in DMSO at a concentration of 5 mM and the clear solutions were then diluted to final concentration of 100 µM using 10 mM HCl, vortexed for 15-30 sec and incubated for 24 h at 37 ºC. The formation of $A\beta_{1-42}$ aggregates was confirmed by thioflavin T (ThT) fluorescence assay and transmission electron microscopy (TEM).

$A\beta_{1-42}$ disaggregation studies. The preformed $A\beta_{1-42}$ aggregates were incubated with increasing equivalents of CDPs (**9** and **11**) with respect to aggregates (1:1 to 1:10) in phosphate buffered saline (1X, pH ~7) for 24 h at 37 ºC. Control samples received only PBS without any CDPs. ThT fluorescence assay was performed to calculate the percentage disaggregation or dissolution of preformed $A\beta_{1-42}$ aggregates and expressed as % dissolution as a function of the ratio of $A\beta_{1-42}$ aggregates to CDPs.

Thioflavin T fluorescence assay. A ThT concentration of 10 µM in PBS (1X, pH ~7.2) was used to measure the spectral changes of CDP treated and untreated preformed $A\beta_{1-42}$ aggregates. Fluorescence measurements were carried for the samples in a 384 flat bottom black well plate, the emission intensity was recorded at 485 nm with an excitation at 440 nm using a microplate reader (Infinite® 200 PRO, TECAN) at room temperature.

Statistical analysis. Results are reported as mean ± standard deviation and the statistical analysis was carried out using one-way ANOVA analysis.

Preparation of *cyclo*(*L*-Phe-*L*-Phe) (CDP 7). H-*L*-Phe-OH (1.0 g, 6.05 mmol) was dispersed in ethylene glycol (10 mL) and refluxed at 195 ºC for 18 h under inert conditions. The reaction mixture was cooled to room temperature, the white precipitate was filtered, washed thoroughly with ethylene glycol (2x30 mL) and recrystalized from ethanol to obtain in CDP **7** in good yield (0.64 g, 72%). ^{1}H NMR (DMSO-d_6, 400 MHz). δ_{ppm} 2.20-2.25 (dd, J_1 = 8.6 Hz, J_2 = 3.8 Hz, 2H), 2.54-2.59 (dd, J_1 = 8.4 Hz, J_2 = 3.0 Hz, 2H), 3.95-3.98 (m, 2H), 7.02-7.04 (m, 2H), 7.18-7.30 (m, 6H), 7.92 (b, 4H); ^{13}C NMR (DMSO-d_6, 100 MHz) δ_{ppm} 54.6, 114.5, 125.6, 130.8, 155.8, 166.8; HRMS: m/z Found: 295.1432 $[M+H]^+$, Calcd: 295.1447 $[M+H]^+$,. Elemental analysis. Found: C, 73.22; H, 6.40; N, 9.75; Calcd: C, 73.45; H, 6.16; N, 9.52 for $C_{18}H_{18}N_2O_2$.

Preparation of *cyclo*(*L*-Phe-*L*-Tyr) (CDP 8). Boc-*L*-Phe-OH (0.50 g, 1.8 mmol), hydroxybenzotrizole (0.38 g, 2.8 mmol) and 1-ethyl-3-(3-dimethylaminopropyl)carbodiimide hydrochloride (EDC. HCl; 0.54 g, 2.81 mmol) were dissolved in dichloromethane (DCM; 40 mL) and cooled to 0 ºC. L-Tyrosine methyl ester hydrochloride (**3**) (0.44 g, 1.90 mmol) and *N*,*N*-diisopropylethylamine (DIPEA; 0.73 g, 5.62 mmol) were added and the reaction mixture was stirred at ice cold temperature for 1 h and then at room temperature for 5 h. The reaction progress was monitored by thin layer chromatography (TLC). The reaction mixture was evaporated to dryness and extracted with dichloromethane, washed with water, dried over anhydrous sodium sulfate and the obtained Boc-dipeptide (**29**) was used for cyclization without any purification. Boc-*L*-Phe-*L*-Tyr-OCH_3.HCl (0.30 g, 0.68 mmol) (**29**) was dissolved in dichloromethane-trifluoroacetic acid mixture (DCM:TFA, v/v: 1:1, 8 mL) at ice-cold temperature and a catalytic amount of triisopropylsilane (TIPS. 0.2 mL) was added and the resulting reaction mixture was stirred at room temperature for 4 h. Reaction progress was monitored using thin layer chromatography. The reaction mixture was evaporated to

dryness and co-evaporated thrice with toluene to obtain H-*L*-Phe-*L*-Tyr-OCH_3.HCl as a white solid and is used for cyclization as such without any further characterization. *N*-Methylmorpholine (76 mg, 0.75 mmol) and acetic acid (0.1 M) in *sec*-butanol (15 mL) were added to the linear dipeptide H-*L*-Phe-*L*-Tyr-OCH_3.HCl and refluxed at 100 ºC for 6 h under inert conditions. The reaction mixture was cooled to room temperature, the precipitate was filtered and washed with ice-cold ethanol (3x30 mL) and dried under vacuum to obtain CDP **8** in good yield (0.26 g, 75%). ^{1}H NMR (DMSO-d_6, 400 MHz). δ_{ppm} 2.14-2.21 (m, 2H), 2.25-2.60 (m, 2H), 3.88-3.94 (b, 2H), 6.66-6.68 (d, J = 5.2 Hz, 2H), 6.82-6.84 (d, J = 5.2 Hz, 2H), 7.02-7.04 (d, J = 4.4 Hz, 2H), 7.18-7.29 (m, 3H), 7.85 (b, 2H), 9.21 (s, 1H); ^{13}C NMR (DMSO-d_6, 100 MHz) δ_{ppm} 55.3, 55.7, 115.0, 126.4, 128.1, 129.7, 130.8, 136.6, 156.0, 166.1, 166.2. HRMS: m/z Found: 311.1380 $[M+H]^+$, Calcd: 311.1396 $[M+H]^+$. Elemental analysis. Found: C, 69.35; H, 6.82; N, 9.55; Calcd: C, 69.66; H, 5.85; N, 9.03 for $C_{18}H_{18}N_2O_3$.

Preparation of *cyclo*(*L*-Tyr-*L*-Tyr) (CDP 9). H-*L*-Tyr-OH (1.0 g, 5.5 mmol) was dispersed in ethylene glycol (10 mL) and refluxed at 195 ºC for 24 h under inert conditions. The reaction mixture was cooled to room temperature, the off-white solid was filtered, washed thoroughly with ethylene glycol (2x30 mL) and recrystalized from ethanol to obtain CDP **9** in moderate yield (0.45 g, 50%). ^{1}H NMR (DMSO-d_6, 400 MHz). δ_{ppm} 2.56-2.61 (dd, J_1 = 8.7 Hz, J_2 = 2.9 Hz, 2H), 2.86-2.91 (dd, J_1 = 8.6 Hz, J_2 = 2.1 Hz, 2H), 3.30 (b, 2H), 6.60-6.62 (d, J = 5.2 Hz, 4H), 6.89-6.91 (d, J = 5.2 Hz, 4H), 7.91 (b, 2H), 9.20 (b, 2H); ^{13}C NMR (DMSO-d_6, 100 MHz) δ_{ppm} 36.9, 54.8, 114.7, 125.8, 131.0, 156.0, 167.0.; HRMS: m/z Found: 327.1330 $[M+H]^+$, Calcd: 327.1345 $[M+H]^+$, Elemental analysis. Found: C, 66.15; H, 5.80; N, 8.68; Calcd: C, 66.25; H, 5.56; N, 8.58 for $C_{18}H_{18}N_2O_4$.

Preparation of *cyclo*(*L*-Phe-*L*-DOPA) (CDP 10). Boc-*L*-DOPA-OH (0.65 g, 2.18 mmol) (**30**), hydroxybenzotrizole (HOBt, 0.45 g, 3.28 mmol) and 1-ethyl-3-(3-dimethylaminopropyl)carbodiimide hydrochloride (EDC. HCl; 0.63 g, 3.28 mmol) were dissolved in dichloromethane (DCM; 60 mL) and cooled to 0 ºC. *L*-Phenylalanine methyl ester hydrochloride (**5**) (0.47 g, 2.18 mmol) and *N*,*N*-diisopropylethylamine (DIPEA; 0.85 g, 6.56 mmol) were added and the reaction mixture was stirred at ice cold temperature for 1 h and then at room temperature for 5 h. The reaction progress was monitored by thin layer chromatography (TLC). The reaction mixture was evaporated to dryness and extracted with dichloromethane, washed with water, dried over anhydrous sodium sulfate and the obtained Boc-dipeptide (**31**) was used for cyclization. Boc-*L*-Phe-*L*-DOPA-OCH_3.HCl (**31**) (0.40 g, 0. 87 mmol) was dissolved in dichloromethane-trifluoroacetic acid mixture (DCM:TFA, v/v: 1:1, 10 mL) at ice-cold temperature and a catalytic amount of triisopropylsilane (TIPS. 0.4 mL) was added and the resulting reaction mixture was stirred at room temperature for 4 h. Reaction progress was monitored using thin layer chromatography. The reaction mixture was evaporated to dryness and co-evaporated thrice with toluene to obtain H-*L*-DOPA-*L*-Phe-OCH_3.HCl as a white solid and is used for cyclization as such without any further characterization. *N*-Methylmorpholine (97 mg, 0.96 mmol) and acetic acid (0.1 M) in *sec*-butanol (15 mL) were added to the linear dipeptide H-*L*-Phe-*L*-Tyr-OCH_3.HCl and refluxed at 100 ºC for 6 h under inert conditions. The reaction mixture was cooled to room temperature, the precipitate was filtered and washed with ice-cold ethanol (3x30 mL) and dried under vacuum to obtain CDP **10** in moderate yield (0.12 g, 40%). ^{1}H NMR (DMSO-d_6, 400 MHz). δ_{ppm} 2.04-2.09 (dd, J_1 = 8.5 Hz, J_2 = 3.9 Hz, 1H), 2.17-2.22 (dd, J_1 = 8.3 Hz, J_2 = 4.2 Hz, 1H), 2.44-2.45 (m, 1H), 2.57-2.61 (dd, J_1 = 8.6 Hz, J_2 = 3.1 Hz, 1H), 3.84 (b, 1H), 3.92 (b, 1H), 6.29-6.31 (m, 1H), 6.47-6.48 (m, 1H), 6.61-6.63 (d, J = 5.1 Hz, 1H), 7.04-7.06 (m, 2H), 7.18-

7.29 (m. 3H), 7.77-7.79 (m, 2H), 8.65 (s, 1H), 8.79 (s 1H); ^{13}C NMR (DMSO-d_6, 100 MHz) δ_{ppm} 55.4, 55.8, 115.2, 117.3, 120.6, 126.3, 127.0, 128.1, 129.7, 136.6, 144.0, 144.6, 166.0, 166.2. HRMS: m/z Found: 327.1330 $[M+H]^+$, Calcd: 327.1345 $[M+H]^+$. Elemental analysis. Found: C, 66.08; H, 5.85; N, 8.84; Calcd: C, 66.25; H, 5.56; N, 8.58 for $C_{18}H_{18}N_2O_4$.

Preparation of *cyclo*(*L*-Tyr-*L*-DOPA) (CDP 11). Boc-*L*-Tyr-OH (1.29 g, 4.28 mmol), hydroxybenzotrizole (HOBt; 0.93 g, 6.87 mmol) and 1-ethyl-3-(3-dimethylaminopropyl)carbodiimide hydrochloride (EDC. HCl; 1.32 g, 6.87 mmol) were dissolved in dichloromethane (DCM; 60 mL) and cooled to 0 ºC. *L*-DOPA methyl ester hydrochloride (1.25 g, 5.04 mmol) and *N*,*N*-diisopropylethylamine (DIPEA; 0.98 g, 7.56 mmol) were added and the reaction mixture was stirred at ice cold temperature for 1 h and then at room temperature for 5 h. The reaction progress was monitored by thin layer chromatography (TLC). The reaction mixture was evaporated to dryness and extracted from dichloromethane, washed with water, dried over anhydrous sodium sulfate and the obtained Boc-dipeptide used for cyclization without any further purification. Boc-*L*-Tyr-*L*-DOPA-OCH_3.HCl (**32**) (0.50 g, 1.05 mmol) was dissolved in dichloromethane-trifluoroacetic acid mixture (DCM:TFA, v/v: 1:1, 10 mL) at ice-cold temperature and a catalytic amount of triisopropylsilane (TIPS. 0.4 mL) was added and the resulting reaction mixture was stirred at room temperature for 4 h. Reaction progress was monitored using thin layer chromatography. The reaction mixture was evaporated to dryness and co-evaporated thrice with toluene to obtain H-*L*-Tyr-*L*-DOPA-OCH_3.HCl as an off-white solid and is used for cyclization as such without any further characterization. *N*-Methylmorpholine (0.12 g, 1.16 mmol) and acetic acid (0.1 M) in *sec*-butanol (15 mL) were added to the linear dipeptide H-*L*-Tyr-*L*-DOPA-OCH_3.HCl and refluxed at 100 ºC for 6 h under inert conditions. The reaction mixture was cooled to room temperature, the

precipitate was filtered and washed with ice-cold ethanol (3x30 mL) and dried under vacuum to obtain CDP **11** in good yield (0.11 g, 65%). ^{1}H NMR (DMSO-d_6, 400 MHz). ^{1}H NMR (DMSO-d_6, 400 MHz). δ_{ppm} 2.03-2.13 (m, 2H), 2.46-2.47 (m, 1H), 2.54-2.55(m, 1H), 3.81 (b, 3H), 6.29-6.32 (m, 1H), 6.49 (m, 1H), 6.62-6.68 (m, 2H), 6.84-6.86 (m, 2H), 7.65 (b, 2H), 8.61 (s, 1H), 8.73 (s, 1H), 9.14 (s, 1H); δ_{ppm} 106.4, 109.7, 119.7, 125.3, 127.5, 129.0, 142.7

Preparation of *cyclo*(*L*-DOPA-*L*-DOPA) (CDP 12). H-*L*-DOPA-OH (1.0 g, 5.07 mmol) was dispersed in ethylene glycol (10 mL) and refluxed at 195 ºC for 24 h under inert conditions. The reaction mixture was cooled to room temperature, the off-white solid was filtered, washed thoroughly with ethylene glycol (2x30 mL) and recrystallized from ethanol to obtain CDP **12** in fair yield (0.36 g, 40%). ^{1}H NMR (DMSO-d_6, 400 MHz). δ_{ppm} 2.02-2.07 (dd, J_1 = 8.3 Hz, J_2 = 4,3 Hz, 2H), 2.46-2.47 (m, 2H), 3.79 (b, 2H), 6.29-6.32 (m, 2H), 6.48-6.49 (m, 2H), 6.62-6.64 (d, J = 4.9 Hz, 2H), 7.65-7.66 (m, 2H), 8.65 (b, 2H), 8.72 (b, 2H); ^{13}C NMR (DMSO-d_6, 100 MHz) δ_{ppm} 39.2, 55.9, 115.2, 117.1, 120.6, 127. 1, 143.9, 144.9, 1661.1. HRMS: m/z Found: 359.1228 $[M+H]^+$, Calcd: 359.1233 $[M+H]^+$. Elemental analysis. Found: C, 60.25; H, 5.36; N, 7.68; Calcd: C, 60.33; H, 5.06; N, 7.82 for $C_{18}H_{18}N_2O_6$.

4.5 Appendix

- ^{1}H NMR and ^{13}C NMR spectra of CDP **7**
- ^{1}H NMR and ^{13}C NMR spectra of CDP **8**
- ^{1}H NMR and ^{13}C NMR spectra of CDP **9**
- ^{1}H NMR and ^{13}C NMR spectra of CDP **10**
- ^{1}H NMR and ^{13}C NMR spectra of CDP **11**
- ^{1}H NMR and ^{13}C NMR spectra of CDP **12**

^{1}H NMR spectrum of CDP 7

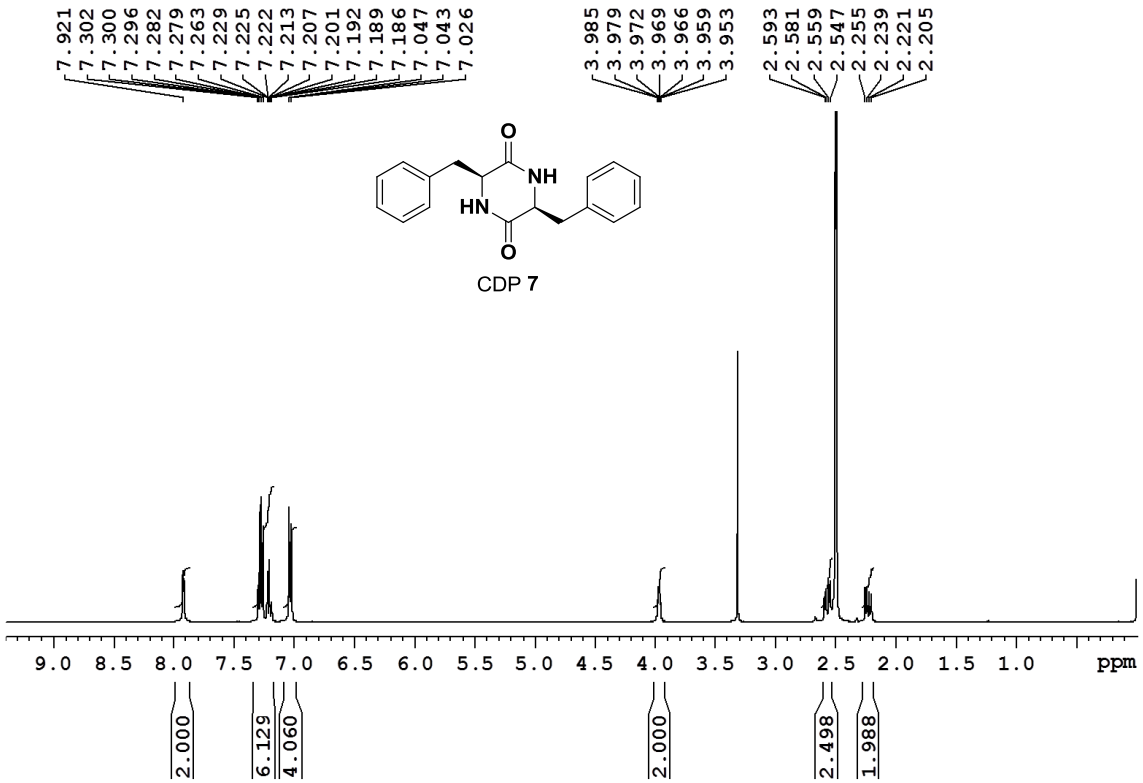

^{13}C NMR spectrum of CDP 7

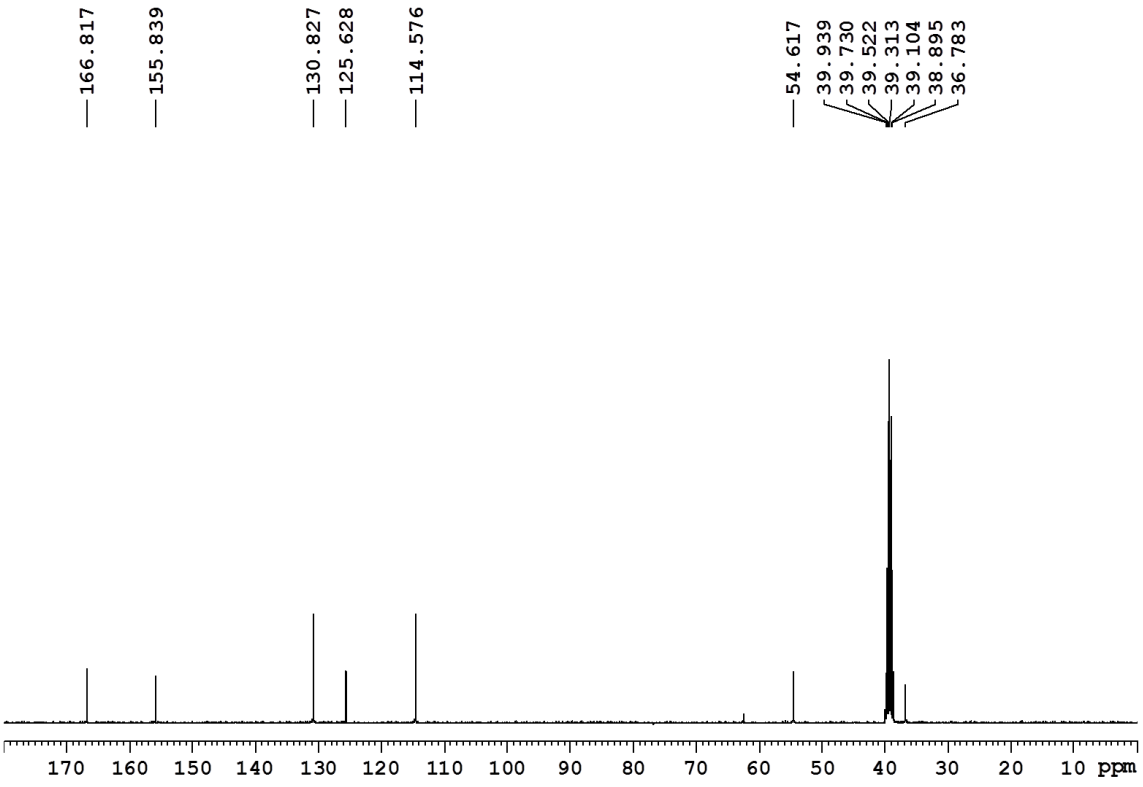

^{1}H NMR spectrum of CDP 8

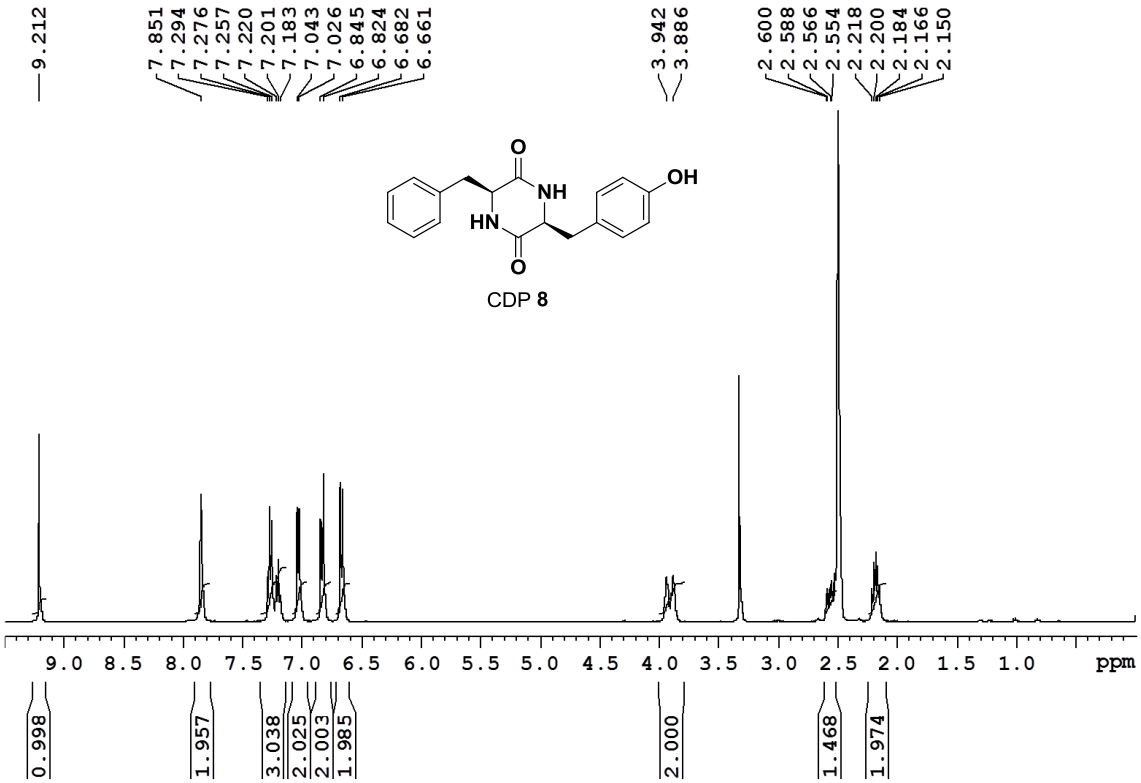

^{13}C NMR spectrum of CDP 8

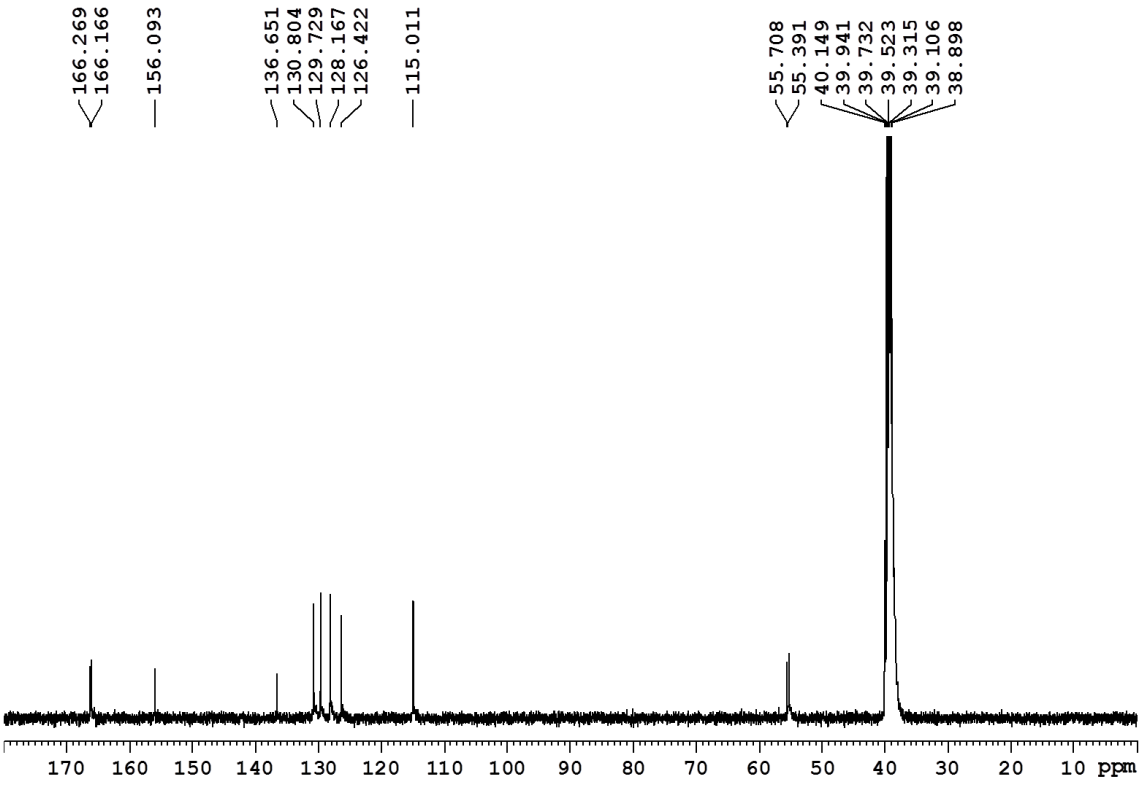

^{1}H NMR spectrum of CDP 9

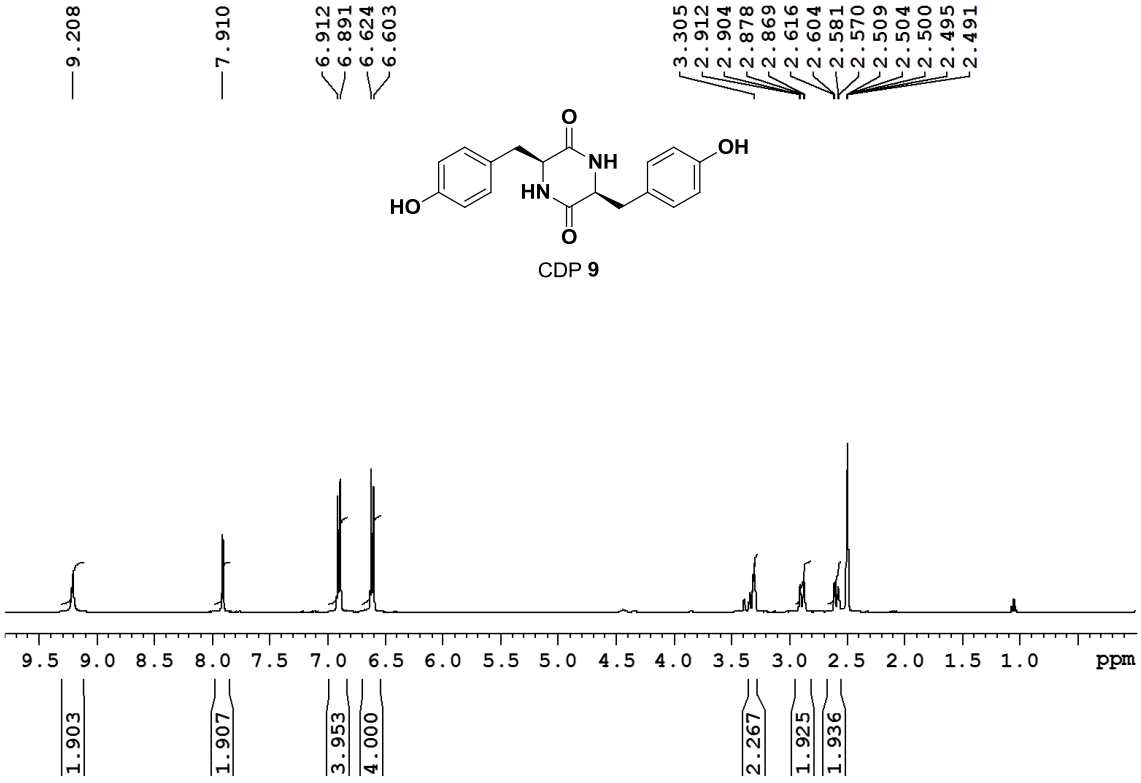

CDP **9**

^{13}C NMR spectrum of CDP 9

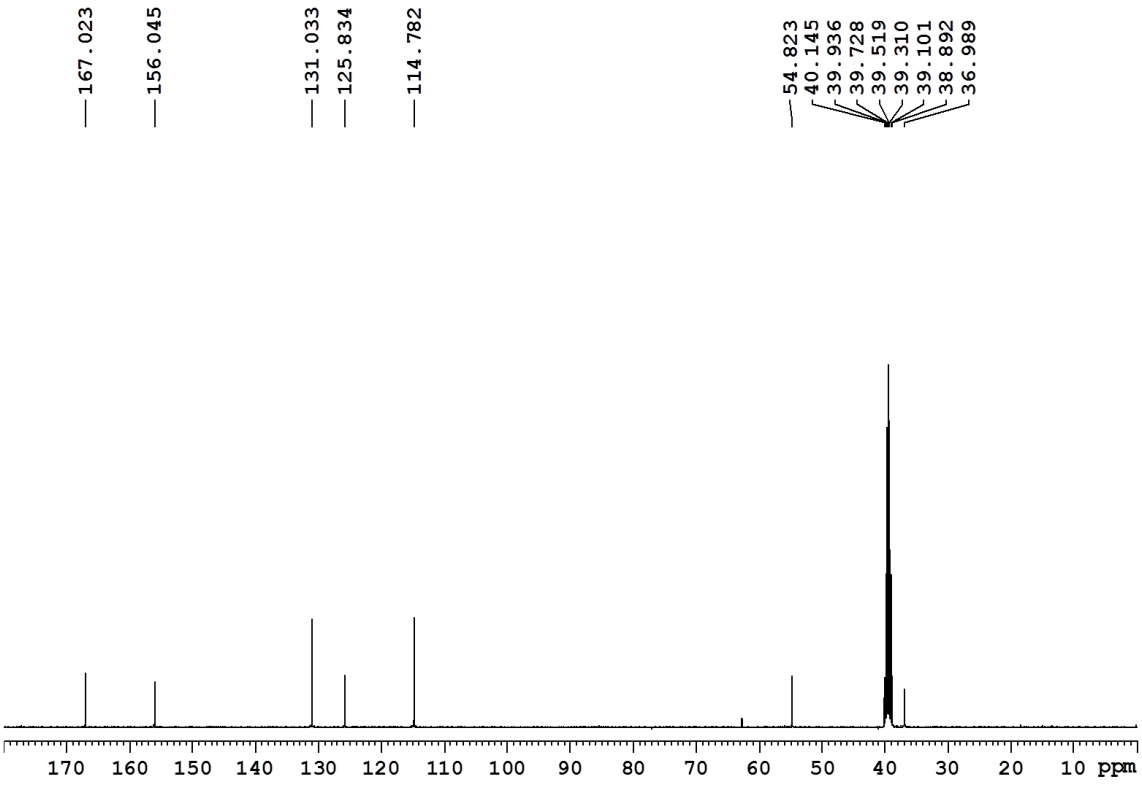

^{1}H NMR spectrum of CDP 10

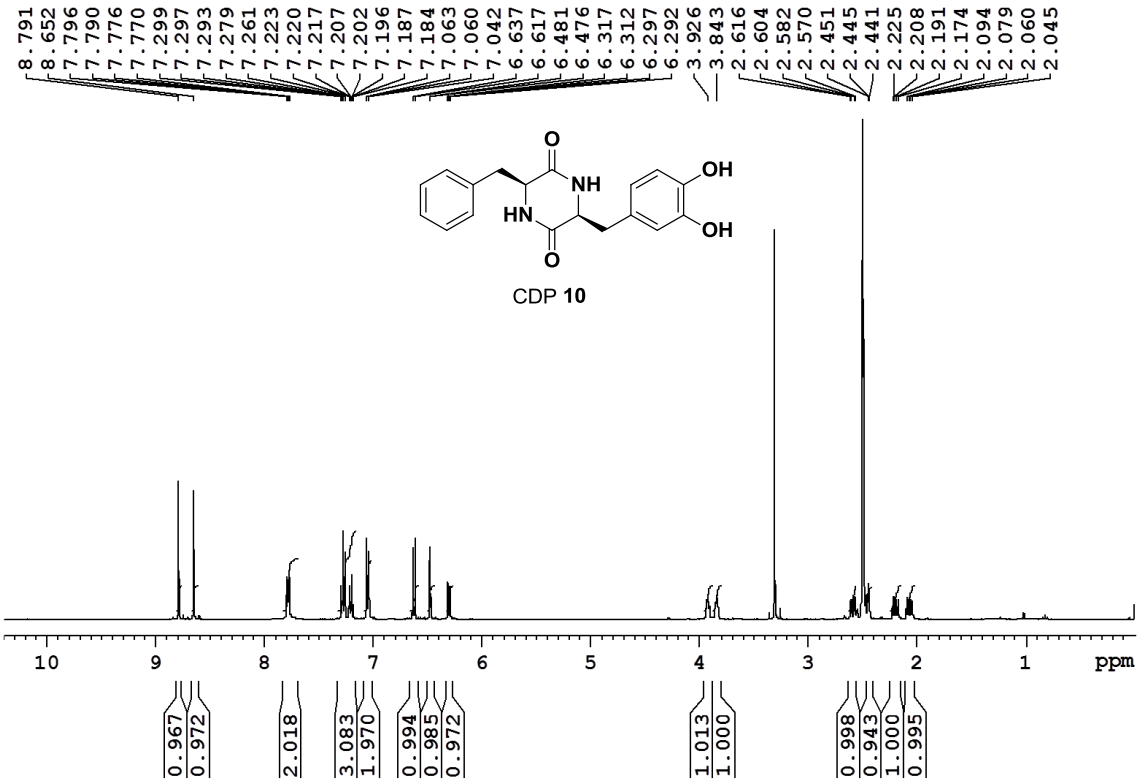

^{13}C NMR spectrum of CDP 10

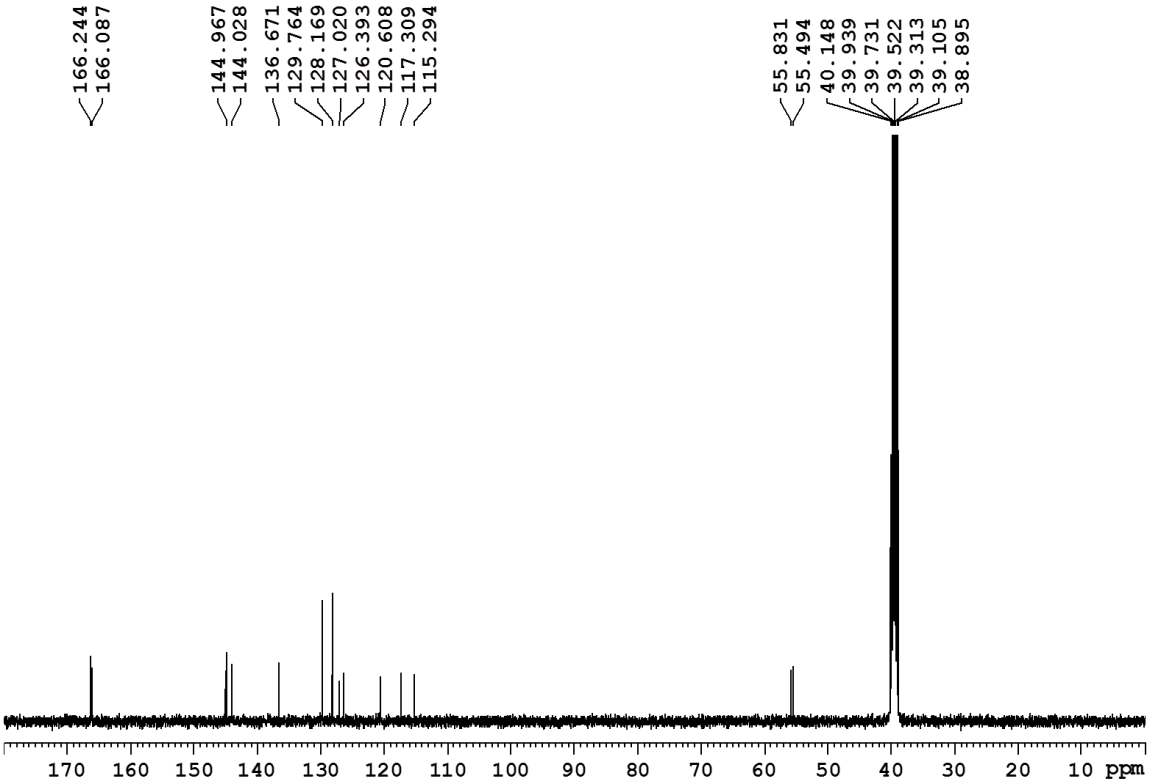

^{1}H NMR spectrum of CDP 11

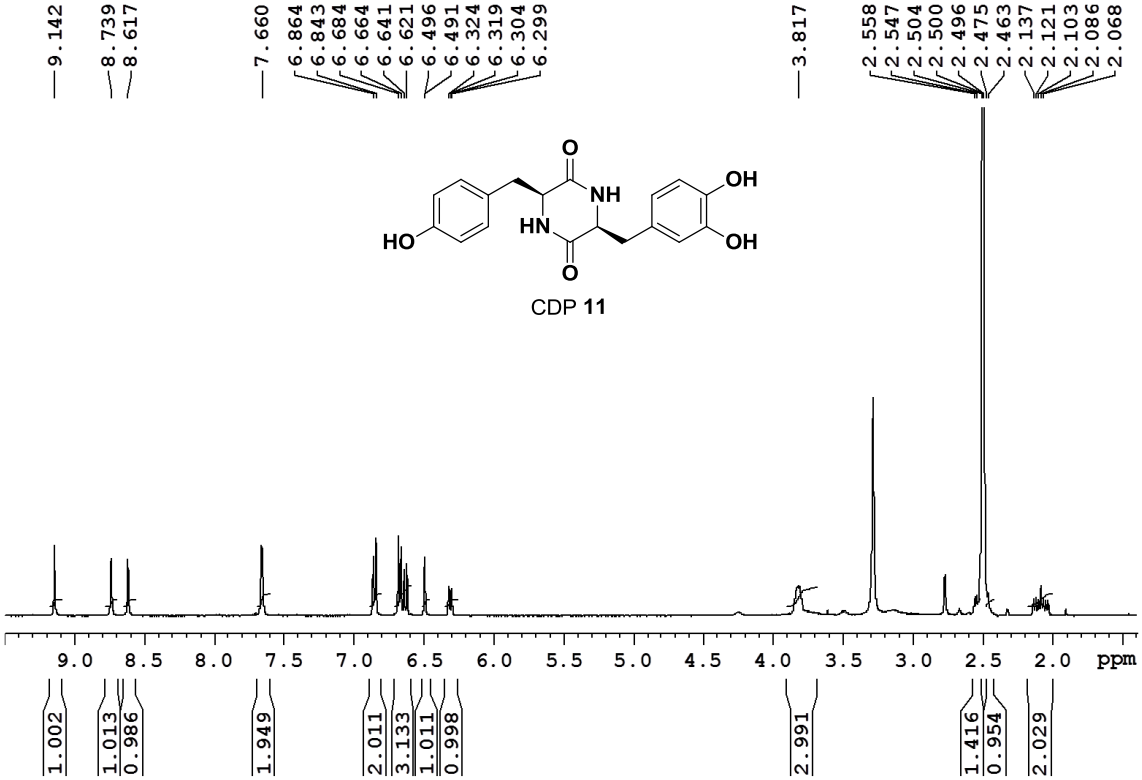

^{13}C NMR spectrum of CDP 11

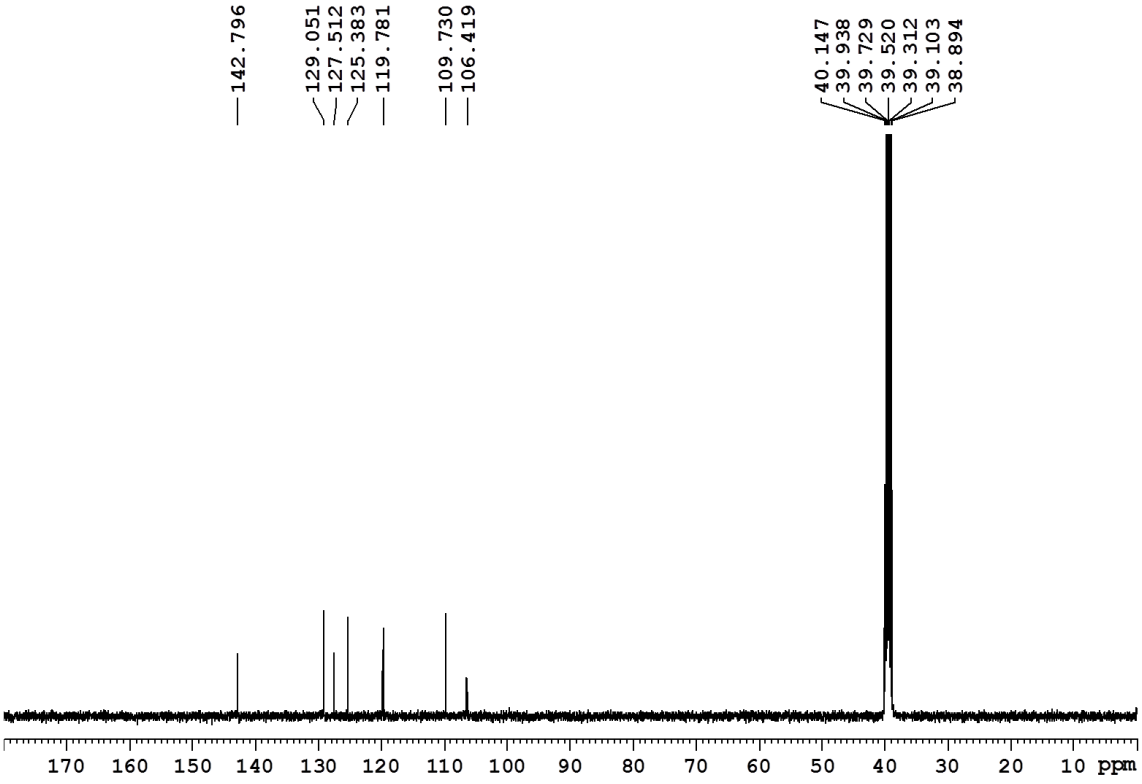

^{1}H NMR spectrum of CDP 12

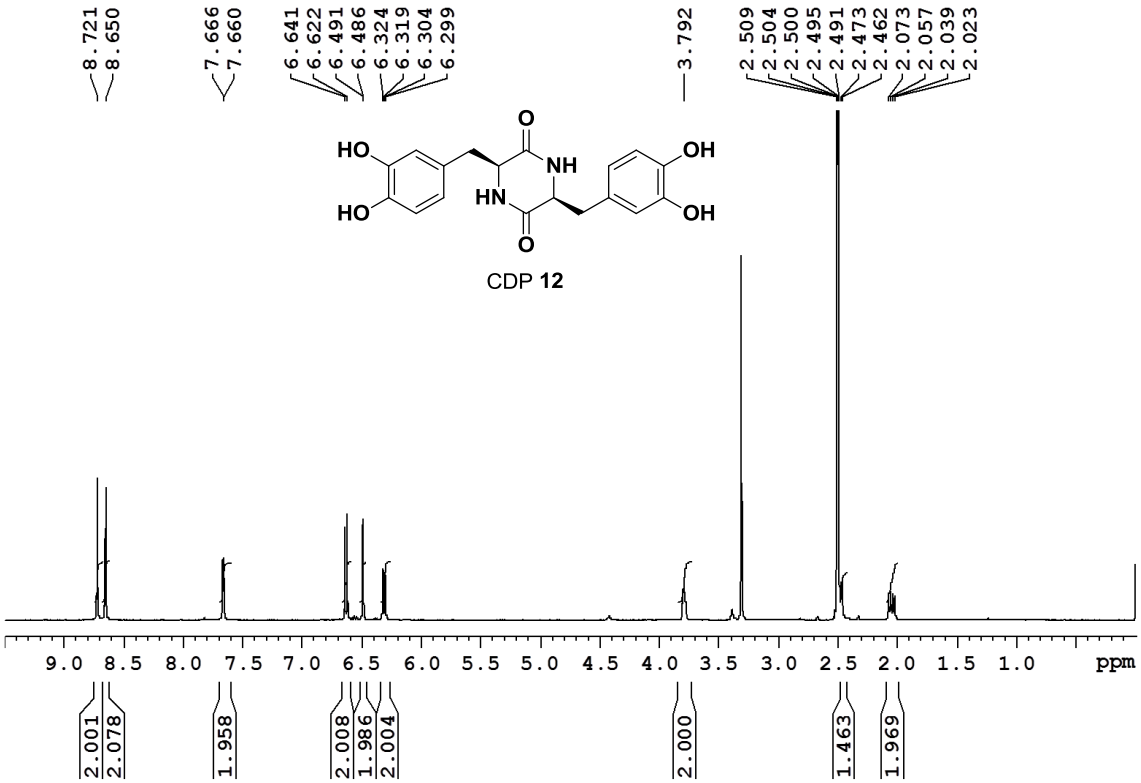

^{13}C NMR spectrum of CDP 12

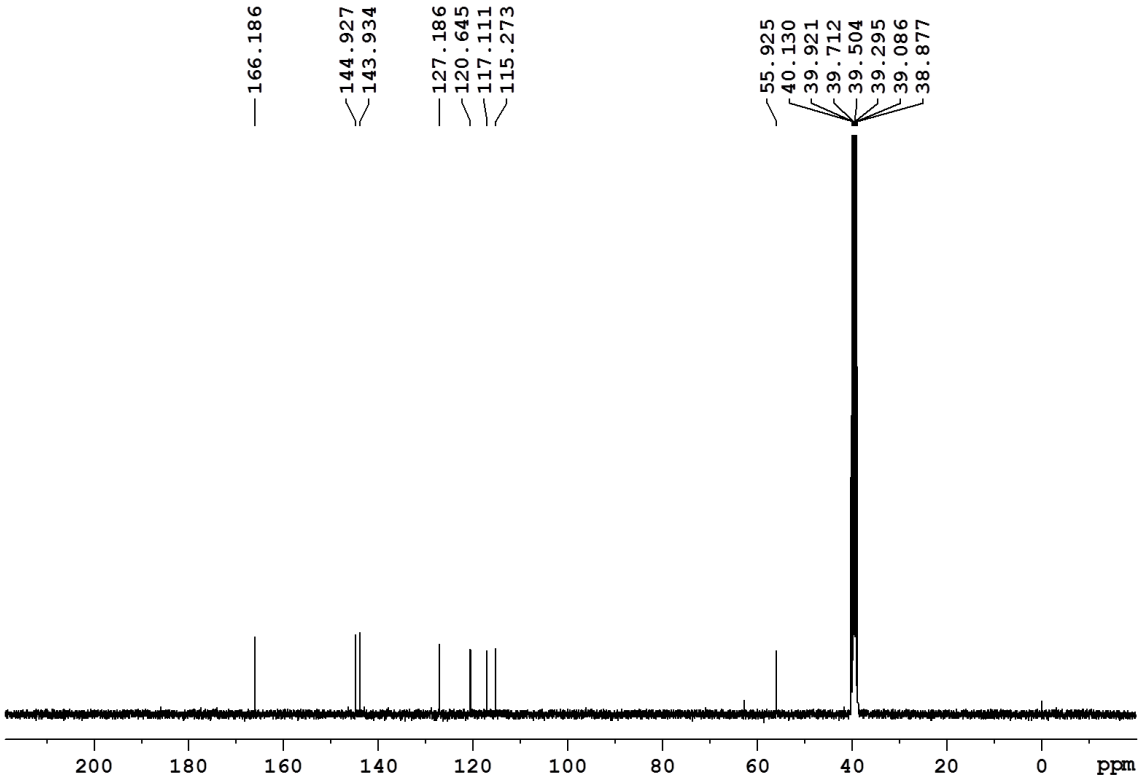

4.6 References

1. Valko, M.; Leibfritz, D.; Moncol, J.; Cronin, M. T. D.; Mazur, M.; Telser, J. Free radicals and antioxidants in normal physiological functions and human disease. *Int. J. Biochem. Cell Biol.* **2007**, *39*, 44-84.

2. Pham-Huy, L. A.; He, H.; Pham-Huy, C. Free radicals, antioxidants in disease and health. *Int. J Biomed. Sci.* **2008**, *4*, 89-96.

3. Wattamwar, P. P.; Mo, Y.; Wan, R.; Palli, R.; Zhang, Q.; Dziubla, T. D. Antioxidant activity of degradable polymer poly(troloxester) to suppress oxidative stress injury in the cells. *Adv. Funct. Mater*. **2010**, *20*, 147-154.

4. Liu, W. F.; Ma, M.; Bratlie, K. M.; Dang, T. T.; Langer, R.; Anderson, D. G. Real-time in vivo detection of biomaterial-induced reactive oxygen species. *Biomaterials* **2011**, *32*, 1796-1801.

5. Potter-Baker, K. A.; Capadona, J. R. Reducing the "stress": antioxidative therapeutic and material approaches may prevent intracortical microelectrode failure. *ACS Macro Lett.* **2015**, *4*, 275-279.

6. Pham-Huy, L. A.; He, H.; Pham-Huy, C. Free radicals, antioxidants in disease and health. *Int. J. Biomed. Sci.* **2008**, *4*, 89-96.

7. Essick, E. E.; Sam, F. Oxidative stress and autophagy in cardiac disease, neurological disorders, aging and cancer. *Oxid. Med. Cell. Longevity* **2010**, *3*, 168-177.

8. Reuter, S.; Gupta, S. C.; Chaturvedi, M. M.; Aggarwal, B. B. Oxidative stress, inflammation, and cancer: How are they linked? *Free Radical Biol. Med.* **2010**, *49*, 1603-1616.

9. Zhao, Y.; Zhao, B. Oxidative stress and the pathogenesis of Alzheimer's disease. *Oxid. Med. Cell Longev.* **2013**, *2013*, 10.

10. Sutherland, G. T.; Chami, B.; Youssef, P.; Witting, P. K. Oxidative stress in Alzheimer's disease: primary villain or physiological by-product? *Redox Report*, **2013**, *18*, 134-141.

11. Guilloreau, L.; Combalbert, S.; Sournia-Saquet, A.; Mazarguil, H.; Faller, P. Redox chemistry of copper–amyloid-β: The generation of hydroxyl radical in the presence of ascorbate is linked to redox-potentials and aggregation state. *ChemBioChem* **2007**, *8*, 1317-1325.

12. Rajasekhar, K.; Chakrabarti, M.; Govindaraju, T. Function and toxicity of amyloid beta and recent therapeutic interventions targeting amyloid beta in Alzheimer's disease. *Chem. Commun.* **2015**, *51*, 13434-13450.

13. Dimitrios, B. Sources of natural phenolic antioxidants. *Trends Food Sci. Tech.* **2006**, *17*, 505-512.

14. d'Ischia, M.; Wakamatsu, K.; Cicoira, F.; Mauro, E. D.; Garcia-Borron, J. C.; Commo, S.; Galván, I.; Ghanem, G.; Kenzo, K.; Meredith, P.; Pezzella, A.; Santato, C.; Sarna, T.; Simon, J. D.; Zecca, L.; Zucca, F. A.; Napolitano, A.; Ito, S. Melanins and melanogenesis: from pigment cells to human health and technological applications. *Pigm. Cell Melanoma Res.* **2015**, *28*, 520-544.

15. Ju, K. Y.; Lee, Y.; Lee, S.; Park, S. B.; Lee, J. K. Bioinspired polymerization of dopamine to generate melanin-like nanoparticles having an excellent free-radical-scavenging property. *Biomacromolecules* **2011**, *12*, 625-632.

16. Bellezza, I.; Peirce, M. J.; Minelli, A. Cyclic dipeptides: from bugs to brain. *Trends Mol. Med.* **2014**, *20*, 551-558.

17. Belin, P.; Moutiez, M.; Lautru, S.; Seguin, J.; Pernodet, J-L.; Gondry, M. The nonribosomal synthesis of diketopiperazines in tRNA-dependent cyclodipeptide synthase pathways. *Nat. Prod. Rep.* **2012**, *29*, 961-979.

18. Giessen, T. W. Marahiel, M. A. The tRNA-dependent biosynthesis of modified cyclic dipeptides. *Int. J. Mol. Sci.* **2014**, *15*, 14610-14631.

19. Prasad, C. Bioactive cyclic dipeptides. *Peptides* **1995**, *16*, 151-164.

20. Martins, M. B.; Carvalho, I. Diketopiperazines: biological activity and synthesis. *Tetrahedron*, **2007**, *63*, 9923-9932.

21. Mollica, A.; Costante, R.; Fioritoa, S.; Genovese, S.; Stefanucci, A.; Mathieu, V.; Kiss, R.; Epifano, F. Synthesis and anti-cancer activity of naturally occurring 2,5-diketopiperazines. *Fitoterapia* **2014**, *98*, 91-97.

22. Nishanth, S. K.; Nambisan, B.; Dileep, C. Three bioactive cyclic dipeptides from the Bacillus sp. N strain associated with entomopathogenic nematode. *Peptides*, **2014**, *53*, 59-69.

23. Govindaraju, T. Spontaneous self-assembly of aromatic cyclic dipeptide into fibre bundles with high thermal stability and propensity for gelation. *Supramol. Chem.* **2011**, *23*, 759-767.

24. Govindaraju, T.; Pandeeswar, M.; Jayaramulu, K.; Jaipuria, G.; Atreya, H. S. Spontaneous self-assembly of designed cyclic dipeptide (Phg-Phg) into two-dimensional nano- and mesosheets. *Supramol. Chem.* **2011**, *23*, 487-492.

25. Cook, B.; Hill, R. R.; Jeffs, G. E. Efficient one-step synthesis of diastereoisomeric cyclic dipeptides from amino acids: three diastereoisomers of cyclo-*L*-isoleucyl-*L*-isoleucine. *J. Chem. Soc. Perkin. Trans.* **1992**, 1199-1201.

26. Manchineella, S.; Thrivikraman, G.; Khanum, K. K.; Ramamurthy, P. C.; Basu, B.; Govindaraju, T. Pigmented silk nanofibrous composite for skeletal muscle tissue engineering. *Adv. Healthcare Mater.* **2016**, *5*, 1222-1232.

27. Menon, V. P.; Sudheer, A. R. Antioxidant and anti-inflammatory properties of curcumin. *Adv. Exp. Med. Biol.* **2007**, *595*, 105-125.

28. Gülçin, I. Antioxidant and radical scavenging properties of curcumin. *Chem. Biol. Interact.* **2008**, *174*, 27-37.

Chapter 5

Pigmented Silk Nanofibrous Composite for Skeletal Muscle Tissue Engineering

5. 1 Introduction

Biomaterial scaffold characteristics such as stiffness, wettability, topography, magnetic, and conducting properties along with soluble growth factors play a pivotal role in cellular adhesion, proliferation, and differentiation for tissue engineering (TE) applications.[1,2] Electroactive biomaterial scaffolds have drawn enormous attention in tissue engineering and regenerative medicine applications for tissues, whose functions are highly coordinated by endogenously generated electric fields (bioelectricity).[3,4] Cardiac myocytes, skeletal myoblasts, neurons, and osteoblasts are the examples of cells that respond to electric stimuli.[5-7] Another crucial aspect that needs to be addressed at the host tissue-biomaterial interface is the development of oxidative stress by cells and tissues, which leads to cell death, tissue injury, and maximizes the inflammation.[8-11] Moreover, oxidative stress is also associated with several pathological conditions and delayed wound healing.[12-15] Recently, many research groups have involved in developing antioxidant biomaterials through physical mixing and covalent chemical modification of the polymeric scaffolds with small molecules with antioxidant properties, although only meeting with moderate success.[16-19] Given this background, biomaterial scaffolds with inherent antioxidant activity along with other preferred physical and chemical cues are very much in demand for tissue engineering and regenerative medicine owing to their synergistic benefits.

Skeletal muscle tissue engineering (SMTE) involves the design of biomaterial scaffolds that can promote myogenic differentiation in myoblasts to generate functional myotubes and offers potential applications in repairing and regenerating the impaired muscle tissues. Developing such scaffolds has potential applications both in understanding the myotube assembly process in vitro and in regenerating the damaged muscle tissue in vivo.[20,21] Skeletal myoblasts are electroactive in nature and the myogenic

differentiation into myotubes can be modulated using electroactive biomaterial scaffolds when coupled with optimal signaling molecules (biochemical cues).[22-24] Mimicking the extracellular matrix (ECM) of muscle cells in designing novel biomaterial scaffolds for SMTE has drawn the attention of several researchers. Synthetic conducting polymers (CPs) such as polyaniline, polypyrrole, poly(3,4-ethylenedioxythiophene), and multiwall carbon nanotubes (MWNTs) mixed with synthetic and natural polymers in electrospun scaffold form and bioceramics with conducting properties have been used for promoting myogenic differentiation in vitro.[25-30] In spite of the promising applications in modulating cellular functions, CPs have limited use for long-term in vivo TE applications because of the problems of biocompatibility, toxicity, and non-biodegradability along with difficulty in fabricating different 3D scaffold formats. Further, the scaffolds prepared from the CP-synthetic polymer blends require additional biofunctionalization with biomolecules to make the scaffolds suitable for cell adhesion and proliferation.[31,32]

The scaffold material for SMTE should be biocompatible, biodegradable, moldable to various desired material formats, and should be readily available for large-scale applications. Silk fibroin, extracted from silkworm cocoons, is characterized by its superior biocompatibility, biodegradability, and easy processability into various scaffold formats and such material has been chosen as the base polymer for making scaffolds in the present study. Given its unique properties, silk fibroin has been extensively used in various biomedical, tissue engineering, electronic, and bioelectronic applications.[33-44] The electrical conducting properties were imparted to the otherwise non-conducting silk scaffolds with melanin incorporation. Melanin was chosen specifically over other additives such as graphene oxide and MWNTs because of its proven biocompatibility, biodegradability and conducting properties along with its excellent antioxidant property under physiological conditions.[45-50] Melanin is the naturally occurring polymeric pigment

having functionalities ranging from structural coloration to protection from sunlight and radicals.[51] Chemically, melanins are heterocyclic in nature and contain repeating units of 5,6-dihydroxyindole and 5,6-dihydroxyindole-2-carboxylic acid formed through the oxidation of tyrosine.[52,53] Melanin alone or in conjunction with synthetic polymers has rarely been used for biomaterial preparation and its potential in tissue engineering has not been evaluated to the full extent.[54]

In the present study, we illustrate the strategy of combining silk fibroin and melanin to develop antioxidant and electroactive biomaterial scaffolds for SMTE applications in order to overcome the limitations associated with scaffolds made from blends of synthetic and conducting polymers. Herein, we constructed biomaterial scaffold films and electrospun fiber mats using silk/melanin composite (SM) material with characteristic intrinsic antioxidant and conductivity properties in order to study the effect of topography along with conducting nature of the scaffold on myogenesis. The results of murine skeletal myoblast C2C12 cell attachment, proliferation, and differentiation into myotubes on SM films and mats in vitro exemplified the significance of scaffold conductivity and topography in modulating aligned myotube formation and potential of SM electrospun scaffolds in SMTE applications.

5.2 Results and Discussion

5.2.1 Fabrication of silk and silk/melanin composite scaffolds

Silk fibroin (silk; SF) was extracted from the cocoons of domesticated mulberry silkworm Bombyx mori using previously reported protocol (Scheme 5.1).[55] Pristine SF and melanin blend (SM; wt/wt 90:10)-regenerated silk fibroin solutions made from hexafluoro-2-propanol (HFIP) were used to fabricate biomaterial scaffold films and

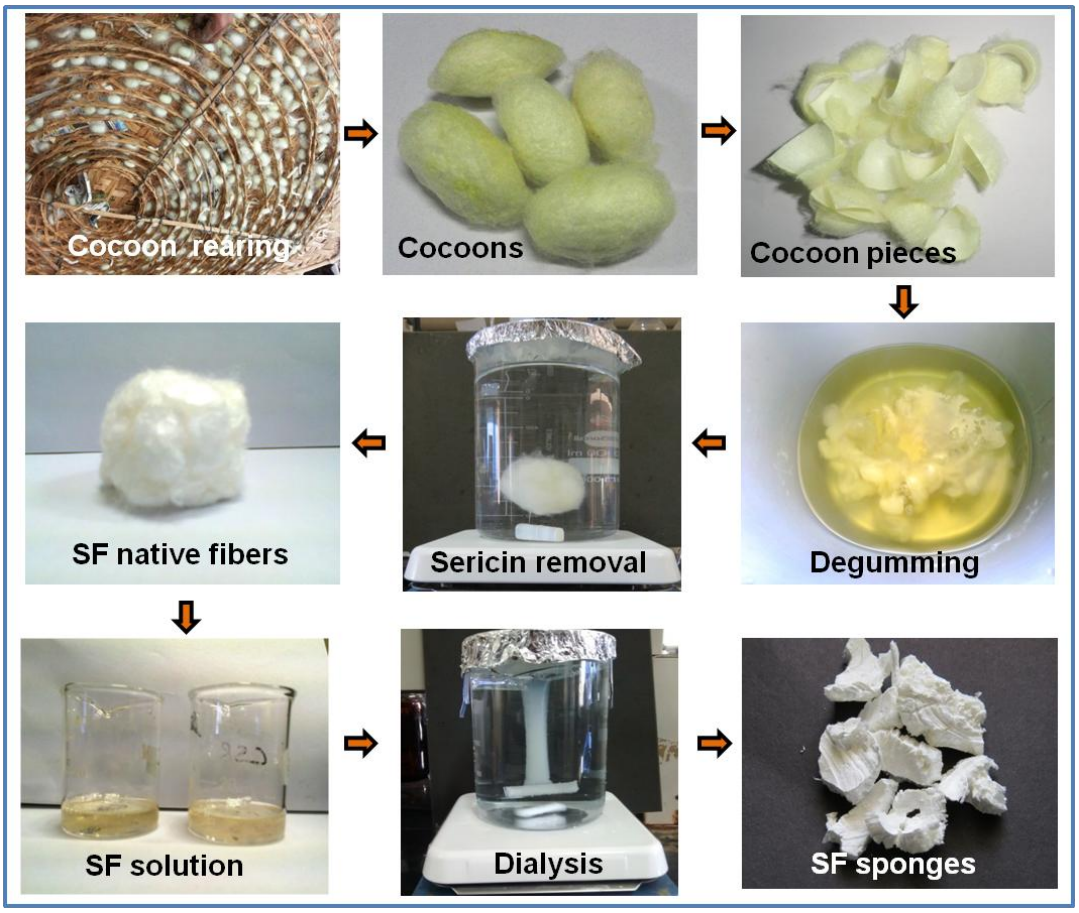

Scheme 5.1 Silk fibroin extraction from *Bombyx mori* cocoons and preparation of silk fibroin sponges.

electrospun nonwoven mats. HFIP was chosen as the solvent owing to its unique properties of dissolving most of the high molecular weight proteins at room temperature and its widespread use in the preparation of biomaterial scaffolds from various synthetic polymers as well as biopolymers.[56,57] Free-standing, flexible, and peelable 2D films were fabricated by drop-casting the respective solutions onto polystyrene substrates.

ECM-mimicking nonwoven, nanofibrous 3D fiber mats were prepared from pristine and melanin-blended silk fibroin using robust electrospinning technique. Electrospinning was chosen over the other fiber forming techniques (such as phase separation and self-assembly), because of its versatility and compatibility with a wide

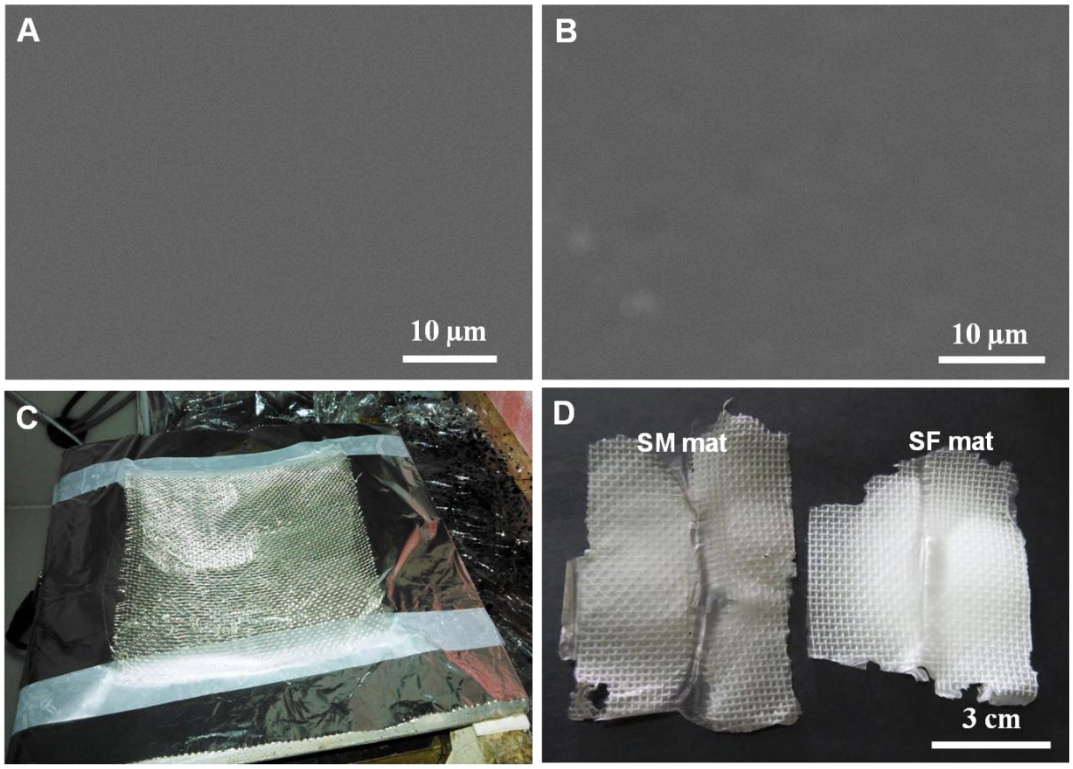

Figure 5.1 Scanning electron microscopy (SEM) micrographs of SF (A) and SM films (B). Photographs of In-house, custom modified stationary collector with SS mesh (C) and free standing silk/melanin composite (SM) and pristine (SF) electrospun mats (D).

range of synthetic and biopolymers and solvent systems, as well as its easy scalability.[58-66] The key electrospinning working parameters such as solvent, concentration, and composition (collectively known as solution parameters), voltage, needle diameter, flow rate, collector type and collector distance from the tip of the needle (collectively known as process parameters), and temperature and humidity (collectively known as ambient parameters) were optimized for the preparation of bead-free, uniform, and reproducible fiber mats.[62-64] A custom-designed stationary collector modified with stainless steel iron mesh stuck on non-stick aluminum foil (grounded) was used for the collection of fiber mat during the electrospinning (Figure 1C). Custom modification of the collector facilitated the fabrication of large-area, easily peelable, and free-standing fiber mats from

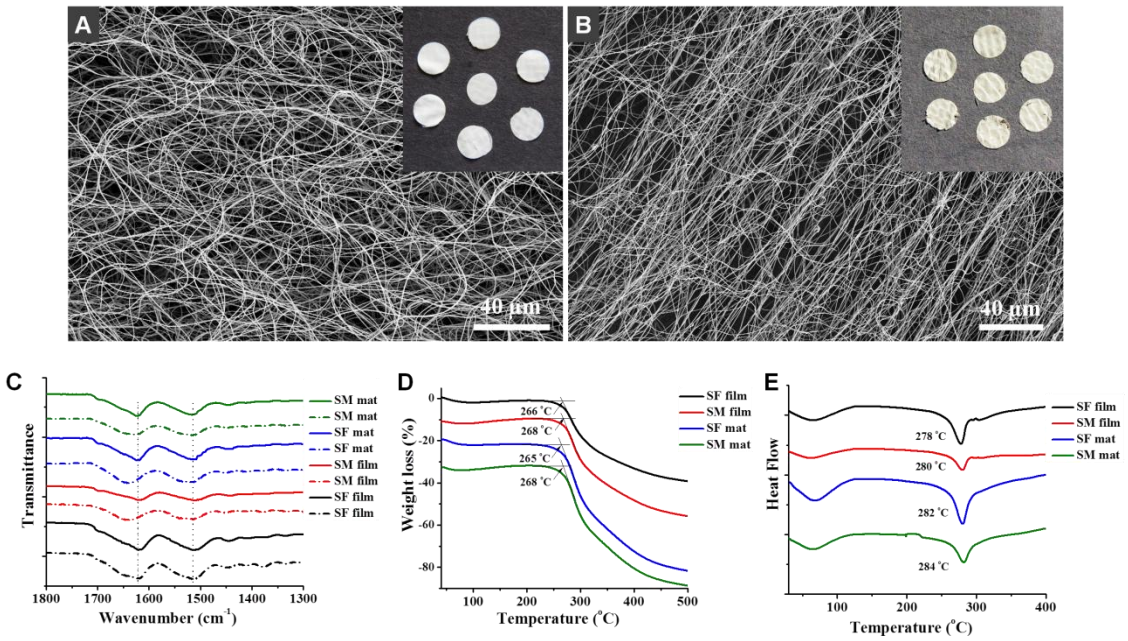

Figure 5.2 Fabrication and characterization of scaffolds. Scanning electron microscopy (SEM) micrographs of SF mat (fiber diameter 470 ± 45 nm) (A) and SM mat (fiber diameter 343 ± 40 nm) (B). Insets in (A) and (B) shows 6 mm discs cut from the corresponding electrospun mats for cell culture experiments. FT-IR analysis of as prepared and methanol treated films and mats (C). Broken lines represent as prepared and solid lines represent methanol treated scaffolds. Vertical dotted lines are inserted to visualize, shift in the silk fibroin amide absorption before after methanol treatment. Thermal stability of scaffolds. TG (D) and DSC (E) of SF film, SM film, SF mat and SM mat. Increased thermal stability is observed with the addition of melanin for both drop-cast films and electrospun mats. TG: thermogravimetric analysis, DSC: differential scanning calorimetry.

SF and SM solution in 10-15 min, unlike the case of conventional non-stick aluminum foil that takes 4-8 h to obtain free-standing fiber mats (Figure 1D).[65,66] Thus prepared films and electrospun mats were treated with a methanol–water mixture (v/v 90:10) for obtaining more stable scaffolds through induced β-sheet formation in silk.

5.2.2 Characterization of scaffolds

The surface morphology, topography of the drop-casted films, and electrospun fiber mats were analyzed using scanning electron microscopy (SEM). Pristine SF and composite SM films showed uniform surface texture without any cracks in the structure (Figure 5.1A, B). Crack-free films signify the uniform distribution of the protein in the case of pristine SF films and thorough blending of silk and melanin in the case of SM films. Biomaterial scaffold films with concurrent macro and microscopic cracks will be of the least significance for tissue engineering applications, because of the absence of uniform physical properties throughout the film. SEM analysis of SF electrospun mats revealed the presence of bead-free, randomly aligned porous submicron diameter fiber networks, as shown in Figure 5.2A. The fibers were obtained with very narrow size distribution and had an average diameter of 470 ± 45 nm, measured using ImageJ software. Similarly, SM electrospun fiber mats were obtained with uniformly distributed network of fibers with narrow size distributions. Interestingly, the formation of relatively aligned fiber mats was observed with silk/melanin blend solution under similar conditions (Figure 5.2B). The formation of bead-free and predominantly aligned fiber mats with relatively smaller fiber diameter (343 ± 40 nm) from SM was attributed to the increased conductivity of the electrospinning solution with melanin blending.[67-69] The electrospun mats were flexible for cutting or punching to attain the required scaffold dimensions for tissue engineering applications (insets in Figure 5.2A, B).

The secondary structure of the base polymer, silk fibroin in as-prepared films, electrospun mat scaffolds, and the induced β-sheet formation through methanol treatment was analyzed by monitoring the amide bond vibration frequencies in IR spectrum (Figure 5.2C). Fourier transform infrared (FTIR) spectrum of as-prepared SF films showed characteristic peaks at 1650 and 1621 cm^{-1} in amide-I region (C=O stretching) and 1514

Table 5.1 FT-IR amide-I and amide-II absorption frequencies of as prepared and methanol treated SF film, SM film, SF mat, and SM mats.

Characteristic absorption	SF Film		SM Film		SF mat		SM mat	
	As-made	Methanol treated	As-made	Methanol treated	As-spun	Methanol treated	As-spun	Methanol treated
Amide-I	1650 cm-$^{-1}$	1699 cm^{-1}	1642 cm^{-1}	1699 cm^{-1}	1640 cm-$^{-1}$	1699 cm^{-1}	1636 cm^{-1}	1699 cm^{-1}
	1621 cm-$^{-1}$	1620 cm^{-1}		1619 cm^{-1}		1622 cm^{-1}		1623 cm^{-1}
Amide-II	1514 cm^{-1}	1512 cm^{-1}	1516 cm^{-1}	1512 cm^{-1}	1526 cm^{-1}	1514 cm^{-1}	1524 cm^{-1}	1515 cm^{-1}

cm^{-1} in the amide-II region (N-H stretching), indicating the coexistence of random helical and β-sheet conformations in the films. SF films, after methanol treatment, showed shifted peaks at 1699, 1619, and 1512 cm^{-1} assigned to the β-sheet conformation of silk (silk-II). The similar vibrational frequency shift of characteristic amide-I and II peaks from the random coil and helical conformation to β-sheet conformation was observed for SM films, and SF and SM mats with methanol treatment. The characteristic vibration frequencies of the amide bonds of as-prepared film and mats samples (1642 and 1516 cm^{-1} for SM film and 1636 and 1524 cm^{-1} for SM mat) exhibited a shift corresponding to silk-II conformation upon the methanol treatment (1699, 1619, and 1512 cm^{-1} for SM film and 1699, 1623, and 1515 cm^{-1} for SM mat; Table 5.1). Electrospun mats exhibited more random and α-helical (silk I) structure in as-prepared SF and SM mats compared to the corresponding films, as seen from the amide bond absorption positions. The observed difference in the amide absorption peaks of as-prepared films and mats is attributed to the fact that the secondary structure of silk fibroin is strongly influenced by both fabrication method and the biomaterial format.[70] FTIR analysis clearly suggested the zero interference of melanin incorporation in the secondary structure of silk fibroin in scaffolds.

Table 5.2 Hydrophilicity of pristine silk fibroin and silk/melanin composites. Contact angle values and images of water and DMEM droplets on the surface of SF and SM spin coated scaffolds.

Sample	Contact angle		Images of drops	
	Water	DMEM	Water	DMEM
SF film	57 ± 0.2	57 ± 1.2	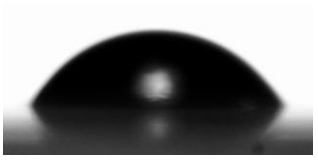	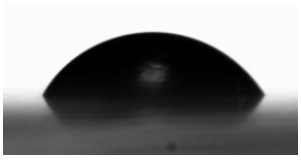
SM film	60 ± 0.2	61 ± 0.4	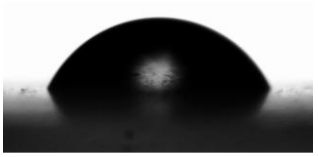	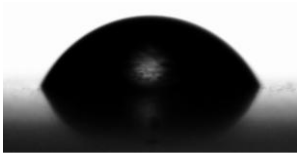

The hydrophilic properties, as reflected in their contact angles, affect cellular adhesion and proliferation on the scaffolds. The influence of melanin blending on the surface wettability was evaluated by measuring the contact angles using Milli-Q water and Dulbecco's modified Eagle's medium (DMEM) cell culture media, under ambient conditions, using the sessile drop method. Melanin blending had no profound effect on the hydrophilicity of the silk fibroin spin coated films (57 ± 0.2 for water, 57 ± 1.2 for DMEM) and only a marginal increase in the contact angles was observed with melanin addition, owing to the oligomeric aromatic nature of melanin (60 ± 0.2 for water, 61 ± 0.4 for DMEM) (Table 5.2). The scaffolds (both SF and SM) are hydrophilic, as evidenced by the wettability behavior, and are well in the suitable range for cell adhesion.

The thermal decomposition behavior of the SF and SM films and electrospun fiber mats (SF mat and SM mat) was studied by thermogravimetric (TG) and differential scanning calorimetric (DSC) analysis.[71,72] Representative TG graphs of SF and SM scaffolds are shown in Figure 5.2D. The initial weight loss around 100 °C for all the

scaffolds is due to the loss of water. TG curves of SF film, SM film, SF mat, and SM mat showed decomposition temperature at 264.9 ± 1.7, 268 ± 0.2, 265.2 ± 0.2, and 268.5 ± 0.6 °C, respectively. The decomposition temperature of melanin-incorporated films and electrospun mats was apparently higher than the corresponding pristine SF scaffolds. The higher thermal stability, as reflected in decomposition temperatures of SM scaffolds, can be attributed to the increased stability of scaffolds with the incorporation of melanin with the aromatic backbone. The higher thermal stability of melanin-incorporated scaffolds was further confirmed by carrying out DSC analysis. DSC curves showed higher degradation temperature for SM film and SM mat at 279.6 ± 0.7 and 283.7 ± 0.1 °C than that of the SF film and SF mat at 276.4 ± 1.8 and 281.9 ± 0.4 °C, respectively (Figure 5.2E).[72]

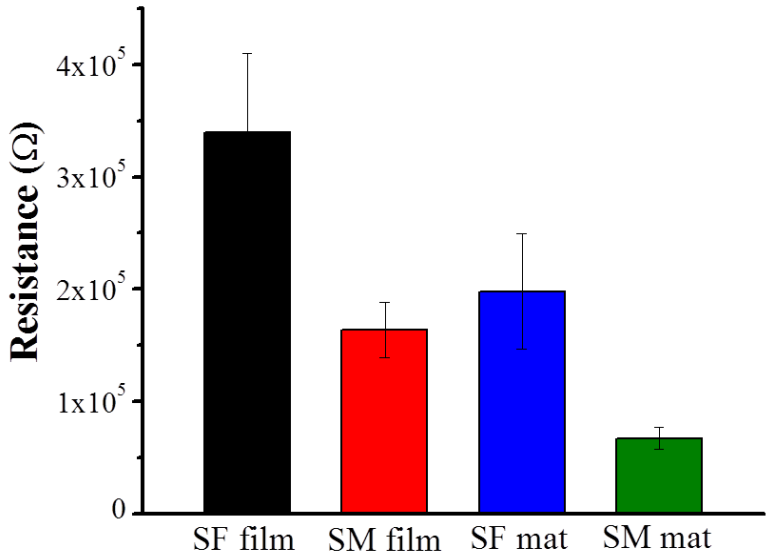

Figure 5.3 Electrical conducting properties of SF film, SM film, SF mat and SM mat. Sheet resistance values of scaffolds studied under physiological (humid) conditions.

The electrical conducting property of silk/melanin composites in comparison with silk alone was evaluated using a two-point resistivity probe at 25 °C and under humid conditions. SM spin-coated and electrospun samples exhibited characteristic linear variation of current with voltage, as indicated by I-V curves compared to the pristine SF scaffolds. The slope of I-V curve became more prominent in the case of SM samples under the studied humid conditions (data not shown). Sheet resistance values for SF, SM spin-coated, and electrospun scaffolds measured under physiological conditions are shown in Figure 5.3. Sheet resistance values were used to estimate the improvement in electroactive nature of scaffolds with melanin incorporation, instead of conductivity values owing to the porous nature of electrospun scaffolds. The spin-coated SM samples showed half of the sheet resistance values compared to the corresponding SF spin-coated samples, highlighting the contribution from melanin. Electrospun SM scaffolds displayed a further decrease in the sheet resistance values under the same conditions and as much as 2.5 times less sheet resistance was observed (1.64E + 05 Ω for SM films to 6.72E + 04 Ω for SM mats; Figure 5.3). The observed lowest sheet resistance values for SM mats as compared to SM films and SF scaffolds can be attributed to the porous nature, increased hydration, and hydration-dependent conductivity of melanin.[49] The improved conductivity (i.e., decreased sheet resistance) values of the scaffolds containing melanin support the hypothesis of preparation of conducting biomaterial scaffolds by blending melanin with silk fibroin.

The radical scavenging capacity of silk/melanin solutions and scaffolds was evaluated against the inhibition of lipophilic radicals (1,1-diphenyl-2-picrylhydrazyl (DPPH)) over a time period of 60 h. The results of antioxidant activity are shown in Figure 5.4A, as percentage inhibition of radicals by scaffolds with time. Highest radical scavenging activity was shown by silk/melanin solutions with 88% inhibition, followed

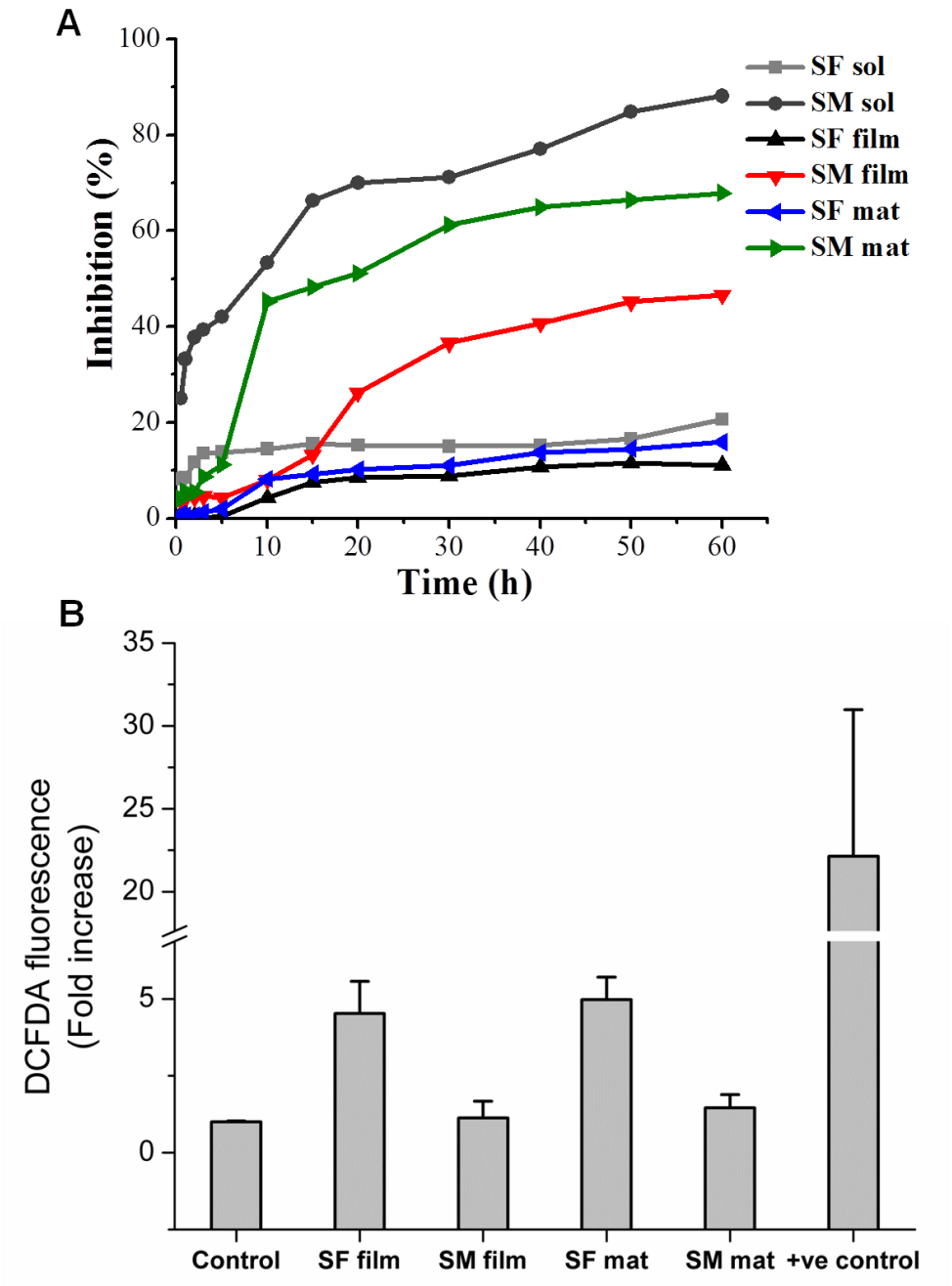

Figure 5.4 Free radical scavenging properties of scaffolds. (A) Radical scavenging property of SF, SM solutions and scaffolds (films and mats) against DPPH free radicals. DPPH: 1,1-diphenyl-2-picrylhydrazyl. (B) Cellular reactive oxygen species detection assay. Fluorescence from myoblasts cultured on TCPS control, SF film, SM film, SF mat and SM mat after 48 h of culture and treatment with CM-H2DCFDA. Fluorescence monitored at 535 nm with the excitation at 485 nm. CM-DCFDA: 5-(and-6)-chloromethyl-2′,7′-dichlorodihydrofluorescein diacetate.

by SM mats and SM films with 68% and 46% of radical inhibition, respectively. Notably, SM solutions showed rapid radical scavenging activity compared to the corresponding scaffolds, while the film and mat scaffolds of SM exhibited persistent activity over a prolonged time period compared to SM solutions, the desired property for cell culture applications. The rapid radical scavenging activity of SM solutions can be attributed to the increased availability of SM material for radical inhibition. Silk fibroin solutions, films, and electrospun mats have shown very little antioxidant activity as compared to SM scaffolds under the studied experimental conditions. The consistent radical scavenging activity of SM solutions and scaffolds was assigned to the strong antioxidant property of incorporated melanin.

5.2.3 Cytocompatibility of scaffolds

The suitability of scaffolds for muscle tissue engineering was evaluated by measuring the viability, cytotoxicity, and proliferation of myoblasts seeded onto the scaffolds through MTT, LIVE/DEAD, and cell proliferation assays, respectively. The viability of cells grown on the scaffolds was evaluated for their mitochondrial reductase activity of live cells using MTT assay. The metabolic activity of mouse myoblast cells (C2C12) on different SF and SM scaffolds was evaluated after 24, 48, and 72 h using MTT assay. As shown in Figure 5.5A, consistent yet statistically significant increase in the number of viable cells was observed from day 1 to day 3. There was no significant difference in the cell number on the scaffolds on all the days. The cytotoxicity of pristine and silk/melanin composite scaffolds (films and mats) on myoblasts was calculated by LIVE/DEAD assay. Representative images of cells cultured on SF and SM scaffolds stained with fluorescein diacetate (FDA)/propidium iodide (PI) dye combination are shown in Figure 5.5B-F.

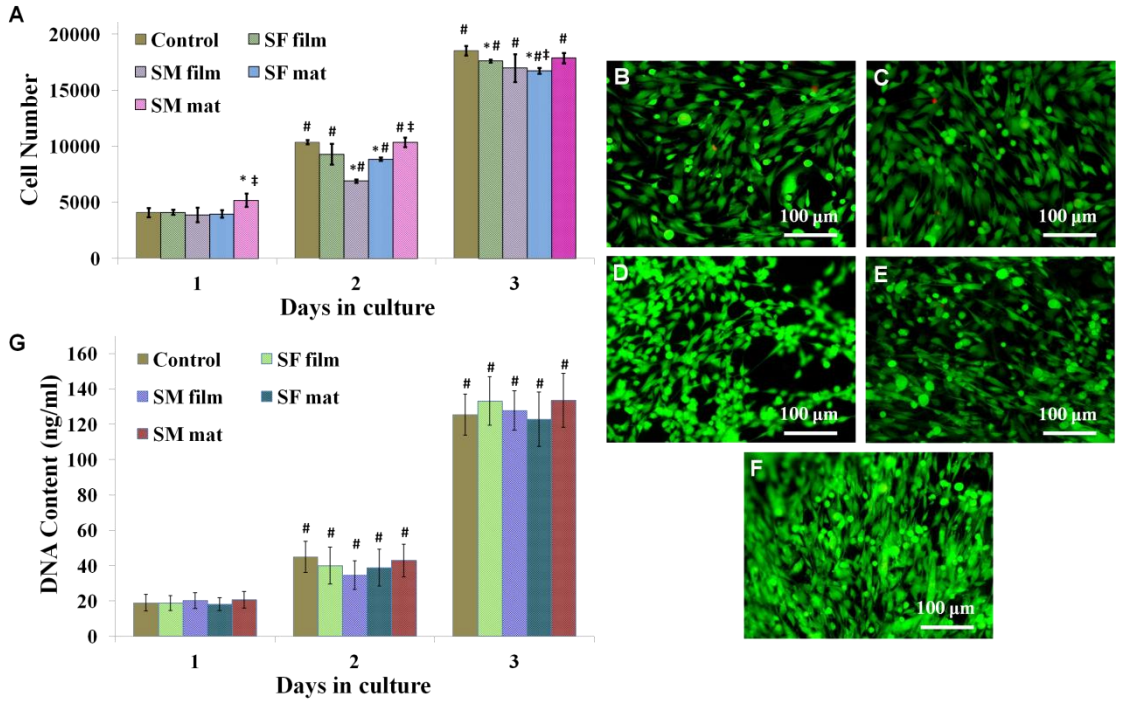

Figure 5.5 Cell viability and proliferation studies of myoblasts on scaffolds. (A) MTT assay results showing number of viable cells on SF film, SM film, SF mat and SM mat samples cultured for a time period of 1, 2 and 3 days respectively. '*' denotes statistically significant difference ($p < 0.05$) in cell number with respect to the corresponding control within each group. '#' denotes significant difference compared with day 1 of each sample and ‡ indicates a significant difference between films and electrospun mat at the given time point. Data points represent mean ± SD (n=3). Live/dead staining of C2C12 myoblasts grown on (B) TCPS control, (C) SF film, (D) SM film, (E) SF mat and (F) SM mat after 3 days of culture. (Green = FDA (live); red = PI (dead)); scale bar = 100 µm. (G) PicoGreen assay results showing total DNA content of cells on TCP/coverslip, SF film, SM film, SF mat and SM mat samples cultured for a time period of 1, 2 and 3 days respectively. '#' denotes significant difference compared with day 1 of each sample. Data points represent mean ± SD (n=3). A standard curve of known dsDNA (ng/mL) was used to calculate the DNA content from the samples. MTT: 3-(4,5-dimethylthiazol-2-yl)-2,5-diphenyltetrazolium bromide.

A high fraction (>99%) of FDA-stained cells, with only a few nuclei stained with PI, was observed on the scaffolds, indicating excellent biocompatibility of the scaffolds. Homogeneous distribution of cells on the surface of films and infiltration through the pores in the case of electrospun mats was observed for both SF and SM scaffolds. The

evidence for infiltration of cells into the electrospun mats can be seen in Figure 5.5E, F; when the focus is on the surface of the mat, the interior cells are out of focus.[32] In addition to infiltration through pores, the cells grown on electrospun mats showed distinct stretched morphological behavior, unlike the cells cultured on films. Melanin incorporation further assisted in extended morphological stretching and alignment of cells on SM mats as compared to the electrospun mats from SF alone (Figure 5.5E, F).

The proliferation of myoblasts on scaffolds was further evaluated by quantifying the total DNA content of cells cultured on pristine and composite silk scaffolds after 24, 48, and 72 h using PicoGreen assay. As shown in Figure 5.5G, a marked increase in the DNA content of myoblasts grown on each scaffold after 24, 48, and 72 h was observed. There was no significant difference in the DNA content of cells grown on all the scaffolds, indicating the excellent cytocompatibility of scaffolds. The proliferation studies have demonstrated that silk scaffolds are equally compatible with myoblast cells as with the control substrates (TCPS). The topography of scaffolds (films and mats) had the least effect on cell viability and proliferation rate, but rather had a profound effect on the morphological alteration of the myoblasts with an additive effect imparted by melanin incorporation.

5.2.4 Oxidative stress control in myoblasts

Oxidative stress developed in myoblasts during the culture impairs myogenic differentiation and even inhibits myogenesis at higher concentrations.[73,74] Further, the increased oxidative stress plays a detrimental role during muscular pathologies by altering the muscle functionality and even leads to cell death. The protective role of SM scaffolds against the oxidative stress and consequent lethal effect on myoblast culture and

differentiation was therefore evaluated by measuring the intracellular reactive oxygen species (ROS) levels of myoblasts cultured on silk scaffolds using 5-(and-6)-chloromethyl-2′,7′- dichlorodihydrofluorescein diacetate (CM-H2DCFDA) assay. Figure 5.4B shows the DCFDA fluorescence from myoblasts cultured on SF and SM scaffolds for 48 h. A twofold decrease in the DCFDA fluorescence intensity was observed from the myoblasts cultured on SM scaffolds (films and mats) as against the myoblasts cultured on the pristine SF scaffolds. Myoblasts cultured on TCPS acted as a control to observe the oxidative stress of myoblasts on scaffolds, and myoblasts on TCPS with extrinsically added hydrogen peroxide (H_2O_2) served as the positive control for DCFDA fluorescence. The observed decrease in DCFDA fluorescence on SM scaffolds (films and mats) further asserts the protective antioxidant activity of melanin/silk fibroin scaffolds against the basal ROS. Thus, melanin blending with SF has imparted a unique protective function against lethal oxidative stress to the SM scaffolds.

5.2.5 Myogenic differentiation of myoblasts on scaffolds

In the present study, myogenesis was induced by subjecting the myoblasts cultured on SF and SM scaffolds to serum starvation conditions after reaching confluency. Myoblasts started fusing under serum starvation conditions and resulted in the formation of multinucleated myotubes. The high aspect ratio of long myotubes formed on SM scaffolds after 7 days of culture (3 days in differentiation media) was visualized using SEM and the corresponding images are shown in Figure 5.6A-F. Myoblasts cultured on TCPS control showed no myogenic differentiation and remained as individual cells even after 3 d of culture in differentiation medium (Figure 5.6A). SF scaffolds with low or no conductivity resulted in the formation of shorter and less prominent myotubes without any regular alignment (Figure 5.6B, D). The formation of relatively better myotubes on

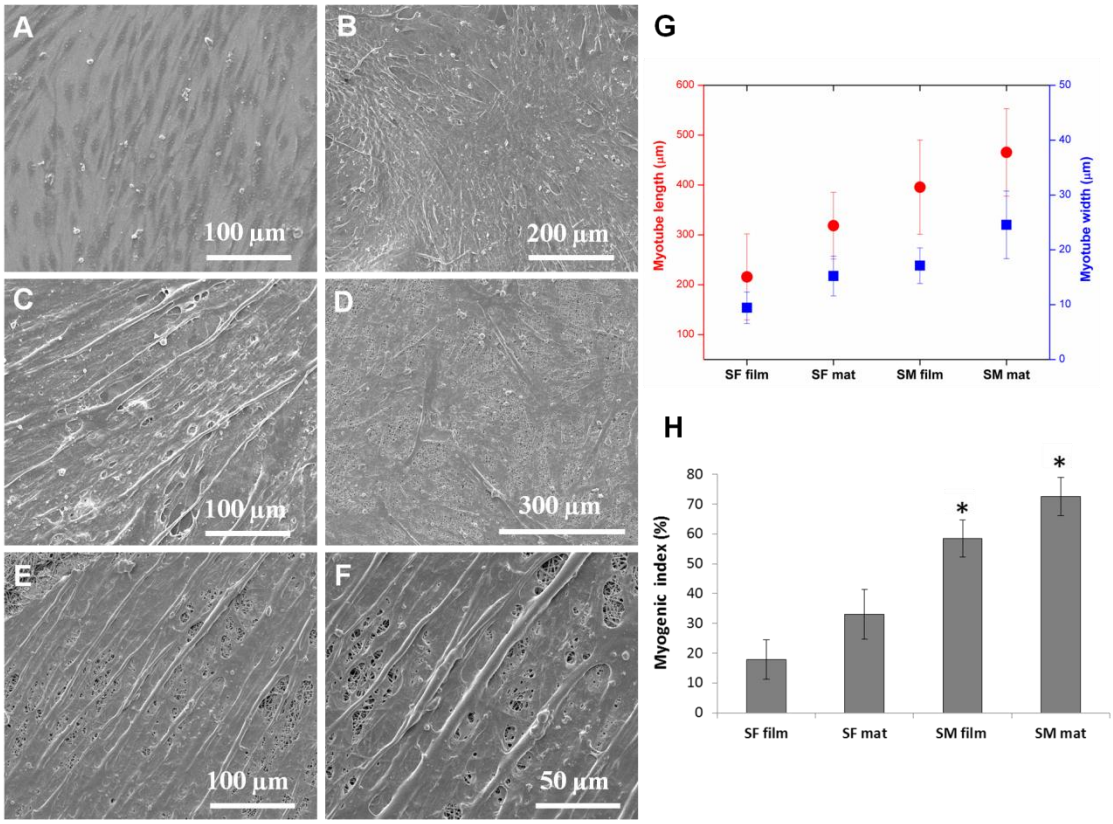

Figure 5.6 Myogenic differentiation of C2C12 myoblasts and quantification of myotube formation on scaffolds. SEM micrographs of myoblasts on (A) TCPS control, (B) SF film, (C) SM film, (D) SF mat, (E) SM mat after 7 days of culture (3 days in serum starvation) and (F) shows the magnified image of myotubes on SM mat. **(**G) and (H) shows quantification of myotube formation and myogenic index of myoblasts cultured on SF film, SM film, SF and SM mats respectively. The average length and width of myotubes on SF and SM scaffolds were calculated after 3 days of differentiation, from the corresponding SEM micrographs. '*' represents significant differences with respect to SF film ($p < 0.05$).

SF electrospun mats, as compared to the SF films, was attributed to the topographical cues of SF mats mimicking ECM and is in agreement with previous reports, highlighting the significance of topography in myoblast differentiation (Figure 5.6D). SM films supported the myogenesis to some extent and formation of short and random myotubes as compared to the SF films and mats, highlighting the instructive role of conducting melanin in myogenesis (Figure 5.6C). The best myogenic differentiation was observed on

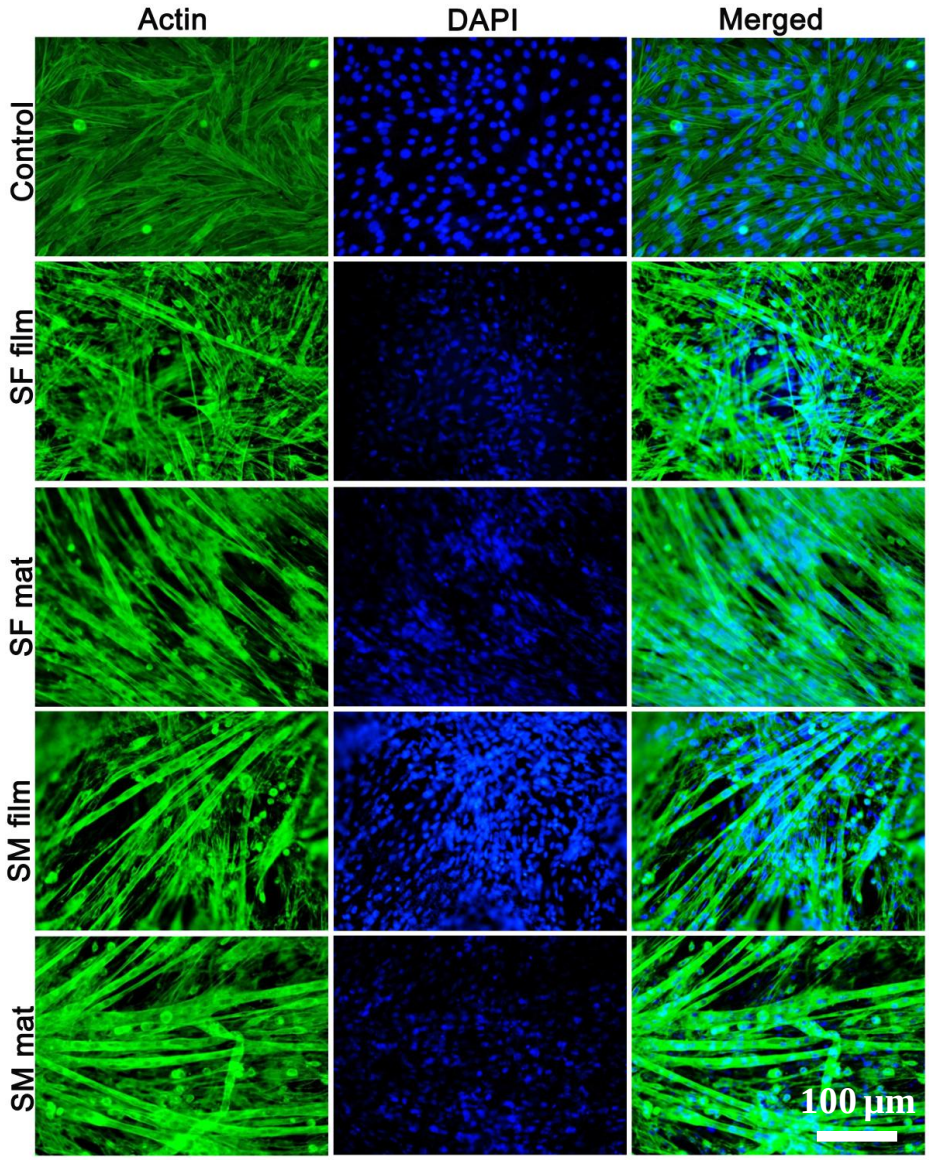

Figure 5.7 Fluorescence staining of myoblasts on control, SF film, SF mat, SM film and SM mat after 3 days in differentiation medium (serum starvation). Actin filaments and nucleus were stained with Alexa Fluor 488-Phalloidin (green) and Hoechst stain (blue) respectively. Scale bar 100 µm, for all the panels.

SM electrospun mats, which combine both the properties of scaffold conductivity and ECM-mimicking topography (Figure 5.6E, F). After 7 days of culture, myoblast cells on SM mats differentiated into well-defined and aligned myotubes with very good myotube aspect ratio (length to width ratio). The extent of myogenesis on different scaffolds was further quantified by measuring the average myotube length and width after 3 days of

culture in differentiation medium. Figure 5.6G shows the calculated average length and width of myotubes on SF and SM scaffolds. A marked increase in myotube length and width on SM electrospun mats from the quantitative calculation further highlighted the potential of SM electrospun mats for skeletal tissue engineering.

The myotube assembly was further analyzed by staining the actin cytoskeleton with Alexa Fluor 488-Phalloidin and by counterstaining the nucleus with Hoechst stain. Figure 5.7 shows the fluorescence images of myoblast cells that had proliferated on SF and SM scaffolds along with the control, visualized after 3 days of culture (in differentiation media). As can be seen in Figure 5.7, after 3 days of culture in serum starvation, a confluent monolayer of individual myoblast cells was observed on the control TCPS. Concurrently on all silk scaffolds, the cells were fused to form multinucleated myotubes (SM mat > SM film > SF mat > SF film > TCPS). Especially, the myotubes formed on SM mats were numerous, with high aspect ratio, and were often branched. There was no appreciable difference in the myotubes number and aspect ratio between SM films and mats, except for the presence of multiple branching in SM mats. Besides, the number of myotubes formed on SM scaffolds was higher than SF scaffolds, suggesting improved myotube organization and differentiation upon incorporation of melanin. The multinucleated myotubes were more aligned on mats than on films, forming long myofibers. In addition, a significant increase in the myogenic index (Figure 5.6H) for both SM film and SM mat indicated the enhanced ability of cells to fuse on melanin-containing matrices, resulting in enriched myoblast differentiation. Moreover, the myogenic index increased from 58% on SM film to 72% on SM mat, suggesting the apparent role of topographical cues in inducing myoblast fusion and differentiation. Overall, the myoblast differentiation studies confirm the crucial role of topography and conductivity of biomaterial scaffolds in determining the myoblast cell fate.

5.3 Conclusion

In conclusion, we have successfully fabricated biocompatible, pristine, and melanin composite silk fibroin biomaterial scaffolds with antioxidant and electroactive properties and further explored their potential use in skeletal muscle tissue engineering. Melanin incorporation showed a distinctly positive effect on the scaffold properties and improved the myogenic differentiation of myoblasts into myotubes in vitro. Silk/melanin composite scaffolds showed strong antioxidant properties, helping in the reduction of the intracellular ROS levels and, hence, the oxidative stress. Silk fibroin/melanin composite electrospun fiber mats supported the proliferation of mouse myoblast C2C12 cells and induced better differentiation into aligned high aspect ratio myotubes compared to the corresponding films, highlighting the significance of both topography and conductivity of scaffolds in muscle tissue engineering. To the best of our knowledge, this study is the first attempt to impart dual functionality of antioxidant property and electrical conductivity to biomaterial scaffolds made exclusively from biopolymers for skeletal muscle tissue engineering. We strongly believe that this study will inspire the development of biomaterial scaffolds with multiple cues in synergy for both *in vitro* and *in vivo* applications.

5.4 Experimental Section

Silk fibroin extraction. Regenerated silk fibroin solution was prepared from the mulberry silkworm *B. mori* cocoons of CB gold variety (Mysuru, India) according to a previously reported protocol.[55] Briefly, water-soluble sericin was removed by boiling the cocoon pieces for 30 min in 0.02 M Na_2CO_3 solution. The resulting native silk fibroin fibers were rinsed with Milli-Q water, and dried and dissolved in 9.3M LiBr (Spectrochem India) at 60 °C for 4 h. The obtained amber-colored solution was dialyzed

against Milli-Q water with a total of six water changes at regular intervals. The aqueous regenerated silk fibroin solution was centrifuged for 20 min at 6000 rpm, 4 °C to remove the insoluble debris, and stored at 4 °C until further use. Lyophilization of aqueous fibroin solution was carried out by initially freezing the solution using liquid N_2, followed by freeze drying at -70 °C for 14 h to yield water-insoluble fibroin sponges (Scheme 5.1).

Preparation of films. Silk fibroin solution (6 wt%) was reconstituted from HFIP at room temperature from silk sponges. Pristine silk fibroin films were prepared by drop-casting the fibroin solution onto the polystyrene substrates. Drop-casted films were air-dried overnight in a fume hood and treated with 90% methanol‑water mixtures for 10 min to promote β-sheet formation. Bioreagent grade synthetic melanin suitable for cell culture experiments was purchased from Sigma (product code: M0418) and used as received for the preparation of scaffolds and all culture experiments. Silk/melanin composite films were prepared from the silk/melanin (wt/wt 90:10) HFIP solution (6 wt%) and subjected to methanol treatment. The treated films were dried under high vacuum to completely remove the solvents from films and stored at room temperature in airtight bags until further use.

Preparation of electrospun mats. SF nonwoven electrospun fiber mats were made by electrospinning from its HFIP solution. SF was reconstituted from HFIP (6 wt%) and electrospinning was carried out at a voltage of 1.5 kV cm^{-1} with a flow rate of 0.8 mL h^{-1} using a 22G blunt-ended needle under ambient conditions. A custom-modified stationary surface consisting of stainless steel mesh fixed onto a stationary collector covered with aluminum foil was used to obtain easily peelable, free-standing electrospun mats (Figure 5.1). Silk/melanin composite mats were prepared similarly by electrospinning silk/melanin HFIP solution (6 wt%; 90/10). The freestanding electrospun fiber mats were

peeled from the collector and treated with 90% methanol–water mixtures for 10 min to increase the aqueous stability of mats through the β-sheet formation in silk. Fiber mats were dried under high vacuum and stored in an air-lock cover until further use at room temperature.

Scanning electron microscopy (SEM). The morphology of drop-casted 2D films and electrospun 3D mat scaffolds was analyzed by field emission scanning electron microscope (Carl Zeiss Ultra 55) at 5 kV. Briefly, the scaffolds were mounted onto SEM stubs using double-sided carbon tape and gold sputtering was carried out on the samples prior to morphological analysis. The average fiber diameter in the case of electrospun mats was determined using ImageJ software. The fiber diameter distributions were measured from 50 different locations on the SEM micrographs and the mean diameter with standard deviation was calculated.

FTIR spectroscopy. The secondary structure of silk in the films and electrospun mat scaffolds was analyzed using FTIR spectroscopy with attenuated total reflection (ATR) sampling technique (GladiATR, PerkinElmer). Briefly, the spectra of as-prepared and aq. methanol treated scaffolds were recorded with 0.2 cm^{-1} data interval and with a resolution of 4 cm^{-1} using the diamond crystal as substrate. All the spectra presented are the average of 64 scans in the wavelength range of 4000-400 cm^{-1} and the data were plotted as % transmittance against wave number (cm^{-1}).

Contact angle measurement. The hydrophilicity of the pristine silk and silk-melanin composite materials was assessed by contact angle measurement (Holmarc). Briefly, pristine silk and silk-melanin composites using HFIP were spin-coated onto glass slides, aq. methanol treatment was carried out, and subsequently, static contact angles were measured using the sessile drop method for both water and DMEM cell culture media in

triplicate. At least three sample sets (n = 3) were used for all the experiments and results were expressed as mean ± standard deviation for all the samples.

Thermal stability. The thermal properties of films and electrospun scaffolds were evaluated using TG (Mettler, TGA/DSC 2) and DSC (TA DSC, Q2000) analysis. TGA measurement was carried out by heating the scaffolds at 5 °C min^{-1} in the temperature range of 40-600 °C under the continuous dry nitrogen flow of 20 mL min^{-1}. DSC was carried out at a heating rate of 5 °C min^{-1} in the temperature range of 40-400 °C under the continuous 20 mL min^{-1} nitrogen gas flow.

Conductivity measurements. Electrical contacts of about 100 nm thickness on the glass slides were made by thermal evaporation of gold using a shadow mask. Samples (films and electrospun mats) for conductivity measurement were prepared on glass slides containing patterned gold electrodes by spin-coating and electrospinning from the corresponding silk fibroin and silk/melanin solutions. The electrical properties of scaffolds were measured for methanol-treated samples under humid conditions to mimic the cell culture environment using Keithley 2420 and a two-point resistivity probe according to previously reported method.[47]

Antioxidant activity. The intrinsic antioxidant activity of silk/melanin solutions and scaffolds was evaluated against the inhibition of lipophilic radical (DPPH) ions using previously reported protocol with slight modifications.[48] The efficiency of silk/melanin solutions and scaffolds to inhibit the DPPH (100×10^{-6} M) radicals in aqueous ethanol was evaluated by incubating 60 μL of solutions (silk and silk/melanin from HFIP) and scaffolds (SF, SM films, and mats) containing equal amount of pure and composite silk material (i.e., the amounts of silk and silk/melanin are same for both solution and scaffolds sample sets used) and measuring the absorbance at 490 nm using a microplate

reader (Eppendorf BioSpectrometer AF2200). Equal weights of silk/melanin used in solution samples and scaffolds form for maintaining the uniformity while comparing the activity of composite among solution and scaffolds (solid). The antioxidant efficacy of solutions and scaffolds was expressed in terms of percentage of free radical inhibition as a function of incubation time.

Cell culture. C2C12 mouse myoblast cell line obtained from National Centre for Biological Science (NCBS) was used in the in vitro cell culture experiments. Cryopreserved cells were revived and expanded in DMEM (Invitrogen) supplemented with 20% fetal bovine serum (FBS; Invitrogen), 1% antibiotic-antimycotic solution (Sigma), and 2×10^{-3} M l-glutamine (Invitrogen). Cell cultures were maintained at 37 °C using a humidified CO_2 incubator (Sanyo, MCO-18AC, USA) and the culture media was changed every alternate day of culture. Cells were detached from the tissue culture flasks after reaching 70%–80% of the confluence using 0.05% trypsin-EDTA (Invitrogen) and sub-cultured for further use. All the cell culture experiments were carried out using cells from passages 3-7.

Cell viability studies. The biocompatibility of scaffolds was evaluated by measuring the viability and proliferation of myoblasts seeded onto the scaffolds. Cell viability test was performed using MTT (3(4,5-dimethylthiazol-2-yl)-2,5-diphenyltetrazolium bromide, Sigma) assay on pristine and silk/melanin composite scaffolds (films and electrospun mats). MTT assay is one of the best quantitative assays to determine the metabolic activity of cells. MTT interacts directly with the mitochondria of live cells and the resulting change in the optical density gives the number of live cells. Approximately 5×10^3 cells mL^{-1} of C2C12 myoblast cells were seeded onto the sterilized samples placed in 24-well plates and incubated for 1, 2, and 3 d in humidified CO_2 incubator at 37 °C. After

the desired incubation period, the medium in the well plate was removed and washed twice with PBS (phosphate buffered saline), followed by addition of 15% MTT reagent (Sigma) prepared in DMEM (without phenol red) for 4 h. The purple-colored formazan crystals formed were solubilized using high purity DMSO (Merck) and the intensity of color was measured by recording the optical density at 595 nm using a microplate reader (iMark, Bio-rad laboratories, India). The measured intensity of formed formazan crystals is the direct measure of the number of viable and metabolically active C2C12 mouse myoblast cells on the scaffolds.

LIVE/DEAD assay. Fluorescence diacetate (FDA) and propidium iodide (PI) dye combination was used for staining the live and dead cells, respectively. Esterases present in the live cells catalyze the de-esterification of nonfluorescent FDA to green fluorescent fluorescein and impart green fluorescent color to the live cells. The red nuclei in the fluorescent images represent the dead cells arising from PI intercalation with nuclear DNA of dead or cell membrane-compromised cells. Myoblasts on scaffolds, after the stipulated period of culture, were washed with 1X PBS and stained with 1 mL of FDA (25 mg mL^{-1}) for 15 min at 37 °C and with 1 mL of PI (10 mg mL^{-1}) for 5 min at room temperature. Samples were washed twice with 1X PBS and myoblast LIVE/DEAD ratio was assessed by fluorescence microscopy imaging within 15-20 min post the staining procedure.

Cell proliferation studies. Picogreen assay was used to measure the proliferation of myoblasts by measuring the total DNA content of the cells cultured on pristine and composite silk scaffolds. Quant-iT Picogreen dsDNA assay kit (Invitrogen) was used to quantify the total DNA content, as per the manufacturer's protocol. After 1, 2, and 3 d of myoblast culture, the samples were washed in 1X PBS and lysed with 250 mL of 0.1%

Triton-X for 10 min. Equal volumes of 1X TE buffer and 100 mL of Picogreen working reagent (1:300 dilution of the stock) were added in a 96-well plate to the cell lysate. The fluorescence intensities were recorded after 5 min incubation using a multimode plate reader (Eppendorf AF2200) with excitation and emission wavelengths of 485 and 535 nm, respectively. A standard curve of known dsDNA (ng/mL) was used to calculate the DNA content from the samples.

Oxidative stress in cells. The reduction of cellular oxidative stress in the myoblasts cultured on SF and SM scaffolds was estimated using 5-(and-6)-chloromethyl-2′,7′-dichlorodihydrofluorescein diacetate (CM-H2DCFDA), a reactive oxygen species (ROS) indicator dye (Invitrogen). CM-H2DCFDA can freely permeate the plasma membrane of intact cells and it is nonfluorescent until the acetate groups are removed by intracellular esterases and oxidation occurs within the cells. When oxidized by various reactive oxygen species, it is irreversibly converted to the fluorescent form DCF which is a measure of the accumulated intracellular ROS. For ROS measurements, myoblasts adhered on scaffolds, after 48 h of culture, were incubated with CM-H2DCFDA (10×10^{-6} M) for 30 min at 37 °C in dark. After 30 min, samples were washed thrice with 1X PBS to remove the extracellular dye and subsequently the intrinsic ROS level of cells on different scaffolds was estimated by measuring the fluorescence intensity. Fluorescence measurements were made using a fluorescence microplate Reader (Eppendorf PlateReader, AF2200) set to 37 °C, using an excitation wavelength of 485 nm and an emission wavelength of 535 nm. For positive control, cells were treated with 1 μL H_2O_2 immediately before fluorescence measurements and the unstained cells were considered as negative control.

Myoblast differentiation studies. Differentiation of myoblasts on scaffolds into multinucleated myotubes was induced by replacing complete media with DMEM containing 1% FBS after the culture attained 90% confluence. Cells were then grown under serum starvation conditions for the complete fusion of myoblasts to give rise to myotubes. The formation of myotubes on the pristine and composite silk scaffolds was analyzed by observing the morphological features under scanning electron microscope and using fluorescence microscope after actin staining. For SEM imaging, the samples were washed with PBS and fixed with 1.5% glutaraldehyde (Loba Chemie, India) in PBS for 30 min at 4 °C. A series of ethanol wash (30%, 50%, 70%, 90%, and 100%) was done subsequently to dehydrate the samples completely. The dried samples were then sputter-coated (Vacuum Tech, Bangalore, India) with gold and observed under scanning electron microscope (FEI Inspect). Actin filaments were visualized under a fluorescence microscope (Nikon Eclipse, model LV100D, Japan) after staining with Alexa Fluor 488-Phalloidin (Invitrogen) for 20 min and the nuclei were counterstained with Hoechst stain 33342 (Invitrogen). Myotube length and width were calculated from SEM images using ImageJ software and all the results presented are the average of five calculations. The myogenic index was quantified as the number of nuclei residing in the cells containing ≥3 nuclei divided by the total number of nuclei from fluorescence micrographs using ImageJ software.

Statistical analysis. Results are reported as mean ± standard deviation and the statistical analysis was carried out using SPSS-16.0 (IBM, USA) software. At least three sample sets (n = 3) were used for all the experiments and were repeated at least thrice. Values of $p < 0.05$ were considered as statistically significant.

5.5 References

1. O'Brien, F. J. Biomaterials & scaffolds for tissue engineering. *Mater. Today* **2006**, *14*, 88-95.

2. Higuchi, A.; Ling, Q. D.; Ko, Y. A.; Chang, Y.; Umezawa, A. Physical cues of biomaterials guide stem cell differentiation fate. *Chem. Rev.* **2013**, *113*, 3297-3328.

3. McCaig, C. D.; Rajnicek, A. M.; Song, B.; Zhao, M. Controlling cell behavior electrically: current views and future potential. *Physiol. Rev.* **2005**, *85*, 943-978.

4. Poltawski, L.; Watson, T. Bioelectricity and microcurrent therapy for tissue healing - a narrative review. *Phys. Ther. Rev.* **2009**, *14*, 104-114.

5. Jain, S.; Sharma, A.; Basu, B. Vertical electric field stimulated neural cell functionality on porous amorphous carbon electrodes. *Biomaterials* **2013**, *34*, 9252-9263.

6. Mitra, J.; Jain, S.; Sharma, A.; Basu, B. Patterned growth and differentiation of neural cells on polymer derived carbon substrates with micro/nano structures *in vitro*. *Carbon* **2013**, *65*, 140-155.

7. Qazi, T. H.; Rai, R.; Boccaccini, A. R. Tissue engineering of electrically responsive tissues using polyaniline based polymers: A review. *Biomaterials* **2014**, *35*, 9068-9086.

8. Matheson, L. A.; Santerre, J. P.; Labow, R. S. Changes in macrophage function and morphology due to biomedical polyurethane surfaces undergoing biodegradation. *J. Cell Physiol.* **2004**, *199*, 8-19.

9. Wattamwar, P. P.; Mo, Y.; Wan, R.; Palli, R.; Zhang, Q.; Dziubla, T. D. Antioxidant activity of degradable polymer poly(troloxester) to suppress oxidative stress injury in the cells. *Adv. Funct. Mater.* **2010**, *20*, 147-154.

10. Liu, W. F.; Ma, M.; Bratlie, K. M.; Dang, T. T.; Langer, R.; Anderson, D. G. Real-time in vivo detection of biomaterial-induced reactive oxygen species. *Biomaterials* **2011**, *32*, 1796-1801.

11. Potter-Baker, K. A.; Capadona, J. R. Reducing the "stress": antioxidative therapeutic and material approaches may prevent intracortical microelectrode failure. *ACS Macro Lett.* **2015**, *4*, 275-279.

12. Pham-Huy, L. A.; He, H.; Pham-Huy, C. Free radicals, antioxidants in disease and health. *Int. J. Biomed. Sci.* **2008**, *4*, 89-96.

13. Essick, E. E.; Sam, F. Oxidative stress and autophagy in cardiac disease, neurological disorders, aging and cancer. *Oxid. Med. Cell. Longevity* **2010**, *3*, 168-177.

14. Reuter, S.; Gupta, S. C.; Chaturvedi, M. M.; Aggarwal, B. B. Oxidative stress, inflammation, and cancer: How are they linked? *Free Radical Biol. Med.* **2010**, *49*, 1603-1616.

15. Fitzmaurice, S. D.; Sivamani, R. K.; Isseroff, R. R. Antioxidant therapies for wound healing: A clinical guide to currently commercially available products. *Skin Pharmacol.*

Physiol. **2011**, *24*, 113-126

16. Cirilo, G.; Iemma, F. *Antioxidant Polymers: Synthesis, Properties, and Applications*, Wiley, LLC, Salem, MA **2012**.

17. Kasoju, N.; Bora, U. Fabrication and characterization of curcumin-releasing silk fibroin scaffold. *J. Biomed. Mater. Res. Part B* **2012**, *100B*, 1854-1866.

18. Chuysinuan, P.; Pavasant, P.; Supaphol, P. Preparation and characterization of caffeic acid-grafted electrospun poly(L-lactic acid) fiber mats for biomedical applications. *ACS Appl. Mater. Interfaces* **2012**, *4*, 3031-3040.

19. Lith, R. V.; Gregory, E. K.; Yang, J.; Kibbe, M. R.; Ameer, G. A. Engineering biodegradable polyester elastomers with antioxidant properties to attenuate oxidative stress in tissues. *Biomaterials* **2014**, *35*, 8113-8122.

20. Wolf, M. T.; Dearth, C. L.; Sonnenberg, S. B.; Loboa, E. G.; Badylak, S. F. Naturally derived and synthetic scaffolds for skeletal muscle reconstruction. *Adv. Drug Delivery Rev.* **2015**, *84*, 208-221.

21. Qazi, T. H.; Mooney, D. J.; Pumberger, M.; Geißler, S.; Duda, G. N. Biomaterials based strategies for skeletal muscle tissue engineering: Existing technologies and future trends *Biomaterials* **2015**, *53*, 502-521.

22. Lawson, M. A.; Purslow, P. P. Differentiation of myoblasts in serum-free media: Effects of modified media are cell line-specific. *Cells Tissues Organs* **2000**, *167*, 130-137.

23. Burattini, S.; Ferri, P.; Battistelli, M.; Curci, R.; Luchetti, F.; Falcieri, E. C2C12 murine myoblasts as a model of skeletal muscle development: Morpho-functional characterization. *Eur. J. Histochem.* **2004**, *48*, 223-233.

24. Ku, S. H.; Lee, S. H.; Park, C. B. Synergic effects of nanofiber alignment and electroactivity on myoblast differentiation. *Biomaterials* **2012**, *33*, 6098-6104.

25. Chen, M. C.; Sun, Y. C.; Chen, Y. H. Electrically conductive nanofibers with highly oriented structures and their potential application in skeletal muscle tissue engineering*Acta Biomater.* **2013**, *9*, 5562-5572.

26. Broda, C. R.; Lee, J. Y.; Sirivisoot, S.; Schmidt, C. E.; Harrison, B. S. A chemically polymerized electrically conducting composite of polypyrrole nanoparticles and polyurethane for tissue engineering. *J. Biomed. Mater. Res. Part A* **2011**, *98*, 509-516.

27. Balint, R.; Cassidy, N. J.; Cartmell, S. H. Conductive polymers: Towards a smart biomaterial for tissue engineering. *Acta Biomater.* **2014**, *10*, 2341-2353.

28. Sirivisoot, S.; Harrison, B. S. Skeletal myotube formation enhanced by electrospun polyurethane carbon nanotube scaffolds. *Int. J. Nanomed.* **2011**, *6*, 2483-2497.

29. Xu, J.; Xie, Y.; Zhang, H.; Ye, Z.; Zhang, W. Fabrication of PLGA/MWNTs composite electrospun fibrous scaffolds for improved myogenic differentiation of C2C12 cells. *Colloids Surf. B* **2014**, *123*, 907-915.

30. Thrivikraman, G.; Mallik, P. K.; Basu, B. Substrate conductivity dependent modulation of cell proliferation and differentiation *in vitro*. *Biomaterials* **2013**, *34*, 7073-7085.

31. Vallejo-Giraldo, C.; Kelly, A.; Biggs, M. J. P. Biofunctionalisation of electrically conducting polymers. *Drug Discovery Today* **2014**, *19*, 88-94.

32. Hardy, J. G.; Villancio-Wolter, M. K.; Sukhavasi, R. C.; Mouser, D. J.; Aguilar, D.; Geissler, S. A.; Kaplan, D. L.; Schmidt, C. E. Electrical stimulation of human mesenchymal stem cells on conductive nanofibers enhances their differentiation toward osteogenic outcomes. *Macromol. Rapid Commun.* **2015**, *36*, 1884-1890.

33. Kundu, S. *Silk biomaterials for tissue engineering and regenerative medicine*, Woodhead Publishing, Cambridge, UK **2014**.

34. Wang, Y. Z.; Kim, H. J.; Vunjak-Novakovic, G.; Kaplan, D. L. Stem cell-based tissue engineering with silk biomaterials. *Biomaterials* **2006**, *27*, 6064-6082.

35. Vepari, C.; Kaplan, D. L. Silk as a biomaterial. *Prog. Polym. Sci.* **2007**, *32*, 991-1007.

36. Seib, F. P.; Kaplan, D. L. Silk for drug delivery applications: Opportunities and challenges. *Isr. J. Chem.* **2013**, *53*, 756-766.

37. Kundu, B.; Kurland, N. E.; Bano, S.; Patra, C.; Engel, F. B.; Yadavalli, V. K.; Kundu, S. C. Silk proteins for biomedical applications: Bioengineering perspectives. *Prog. Polym. Sci.* **2014**, *39*, 251-267.

38. Das, S.; Pati, F.; Choi, Y.-J.; Rijal, G.; Shim, J.-H.; Kim, S. W.; Ray, A. R.; Cho, D.-W.; Ghosh, S. Bioprintable, cell-laden silk fibroin-gelatin hydrogel supporting multilineage differentiation of stem cells for fabrication of three-dimensional tissue constructs. *Acta Biomater.* **2015**, *11*, 233-246.

39. Tansil, N. C.; Koh, L. D.; Han, M.-Y. Functional silk: Colored and luminescent. *Adv. Mater.* **2012**, *24*, 1388-1397.

40. Kim, D. W.; Lee, O. J.; Kim, S.-W.; Ki, C. S.; Chao, J. R.; Yoo, H.; Yoon, S. I.; Lee, J. E.; Park, Y. R.; Kweon, H. Y.; Lee, K. G.; Kaplan, D. L.; Park, C. H. Novel fabrication of fluorescent silk utilized in biotechnological and medical applications. *Biomaterials* **2015**, *70*, 48-56.

41. Parker, S. T.; Domachuk, P.; Amsden, J.; Bressner, J.; Lewis, J. A.; Kaplan, D. L.; Omenetto, F. G. Biocompatible silk printed optical waveguides. *Adv. Mater.* **2009**, *21*, 2411-2415.

42. Omenetto, F. G.; Kaplan, D. L. New opportunities for an ancient material. *Science* **2010**, *329*, 528-531.

43. Kim, D.-H.; Viventi, J.; Amsden, J. J.; Xiao, J.; Vigeland, L.; Kim, Y.-S.; Blanco, J. A.; Panilaitis, B.; Frechette, E. S.; Contreras, D.; Kaplan, D. L.; Omenetto, F. G.; Huang, Y.; Hwang, K.-C.; Zakin, M. R.; Litt, B.; Rogers, J. A. Dissolvable films of silk fibroin for ultrathin conformal bio-integrated electronics. *Nat. Mater.* **2010**, *9*, 511-517.

44. Tao, H.; Kaplan, D. L.; Omenetto, F. G. Silk materials - A road to sustainable high technology. *Adv. Mater.* **2012**, *24*, 2824-2837.

45. McGinnes, J.; Corry, P.; Proctor, P. Amorphous semiconductor switching in melanins. *Science* **1974**, *183*, 853-855.

46. Bothma, J. P.; Boor, J.–de.; Divakar, U.; Schwenn, P. E.; Meredith, P. Device-quality electrically conducting melanin thin films. *Adv. Mater.* **2008**, *20*, 3539-3542.

47. Bettinger, C. J.; Bruggeman, J. P.; Misra, A.; Borenstein, J. T.; Langer, R. Biocompatibility of biodegradable semiconducting melanin films for nerve tissue engineering. *Biomaterials* **2009**, *30*, 3050-3057.

48. Ju, K. Y.; Lee, Y.; Lee, S.; Park, S. B.; Lee, J. K. Bioinspired polymerization of dopamine to generate melanin-like nanoparticles having an excellent free-radical-scavenging property. *Biomacromolecules* **2011**, *12*, 625-632.

49. Mostert, A. B.; Powell, B. J.; Pratt, F. L.; Hanson, G. R.; Sarna, T.; Gentle, I. R.; Meredith, P. Role of semiconductivity and ion transport in the electrical conduction of melanin. *Proc. Natl. Acad. Sci. USA* **2012**, *109*, 8943-8947.

50. Kim, E.; Liu, Y.; Leverage, W. T.; Yin, J. J.; White, I. M.; Bentley, W. E.; Payne, G. F. Context-dependent redox properties of natural phenolic materials. B*iomacromolecules* **2014**, *15*, 1653-1662.

51. d'Ischia, M.; Wakamatsu, K.; Cicoira, F.; Mauro, E. D.; Garcia-Borron, J. C.; Commo, S.; Galván, I.; Ghanem, G.; Kenzo, K.; Meredith, P.; Pezzella, A.; Santato, C.; Sarna, T.; Simon, J. D.; Zecca, L.; Zucca, F. A.; Napolitano, A.; Ito, S. Melanins and melanogenesis: from pigment cells to human health and technological applications. *Pigm. Cell Melanoma Res.* **2015**, *28*, 520-544.

52. d'Ischia, M.; Napolitano, A.; Ball, V.; Chen, C. T.; Buehler, M. J. Polydopamine and eumelanin: from structure-property relationships to a unified tailoring strategy. *Acc. Chem. Res.* **2014**, *47*, 3541-3550.

53. Solano, F. Melanins: Skin pigments and much more-types, structural models, biological functions, and formation routes. *New J. Sci.* **2014**, *2014*, 498276.

54. Kai, D.; Prabhakaran, M. P.; Jin, G.; Ramakrishna, S. Biocompatibility evaluation of electrically conductive nanofibrous scaffolds for cardiac tissue engineering. *J. Mater. Chem. B* **2013**, *1*, 2305-2314.

55. Rockwood, D. N.; Preda, R. C.; Yücel, T.; Wang, X.; Lovett, M. L.; Kaplan, D. L. Materials fabrication from *Bombyx mori* silk fibroin. *Nat. Protoc.* **2011**, *6*, 1612-1631.

56. Kim, H. J.; Kim, U. J.; Vunjak-Novakovic, G.; Min, B. H.; Kaplan, D. L. Influence of macroporous protein scaffolds on bone tissue engineering from bone marrow stem cells. *Biomaterials* **2005**, *26*, 4442-4452.

57. Kim, S. H.; Kim, S. H.; Jung, Y. TGF-β3 encapsulated PLCL scaffold by a supercritical CO_2–HFIP co-solvent system for cartilage tissue engineering. *J. Controlled Release* **2015**, *206*, 101-107.

58. Min, B. M.; Lee, G.; Kim, S. H.; Nam, Y. S.; Lee, T. S.; Park, W. H. Electrospinning of silk fibroin nanofibers and its effect on the adhesion and spreading of normal human keratinocytes and fibroblasts *in vitro*. *Biomaterials* **2004**, *25*, 1289-1297.

59. Sill, T. J.; Recum, H. A. V. Electrospinning: applications in drug delivery and tissue engineering. *Biomaterials* **2008**, *29*, 1989-2006.

60. Bhardwaj, N.; Kundu, S. C. Electrospinning: a fascinating fiber fabrication technique. *Biotechnol. Adv.* **2010**, *28*, 325-347.

61. He, C.; Nie, W.; Feng, W. Engineering of biomimetic nanofibrous matrices for drug delivery and tissue engineering. *J. Mater. Chem. B* **2014**, *2*, 7828-7848.

62. Zhang, F.; Zuo, B.; Fan, Z.; Xie, Z.; Lu, Q.; Zhang, X.; Kaplan, D. L. Mechanisms and control of silk-based electrospinning. *Biomacromolecules* **2012**, *13*, 798-804.

63. Li, Z.; Wang, C. *One-dimensional nanostructures*, Springer, Heidelberg **2013**.

64. Khanum, K. K.; Sandeep, B. S.; Ramamurthy, P. C. Design and morphology control of a thiophene derivative through electrospraying using various solvents. *RSC Adv.* **2015**, *5*, 60419-60425.

65. Meechaisue, C.; Wutticharoenmongkol, P.; Waraput, R.; Huangjing, T.; Ketbumrung, N.; Pavasant, P. Supaphol, P. Preparation of electrospun silk fibroin fiber mats as bone scaffolds: a preliminary study. *Biomed. Mater.* **2007**, *2*, 181-188.

66. Amiraliyan, N.; Nouri, M.; Kish, M. H. Structural characterization and mechanical properties of electrospun silk fibroin nanofiber mats. *Polym. Sci. Ser. A* **2010**, *52*, 407-412.

67. Uyar, T.; Besenbacher, F. Electrospinning of uniform polystyrene fibers: the effect of solvent conductivity. *Polymer* **2008**, *49*, 5336-5343.

68. Kulkarni, A.; Bambole, V. A.; Mahanwar, P. A. Electrospinning of polymers, their modeling and applications. *Polym.-Plast. Technol.* **2010**, *49*, 427-441.

69. Angammana, C. J.; Jayaram, S. H. Analysis of the effects of solution conductivity on electrospinning process and fiber morphology. *IEEE Trans. Ind. Appl.* **2011**, *47*, 1109-1177.

70. Hu, X.; Shmelev, K.; Sun, L.; Gil, E. S.; Park, S. H.; Cebe, P.; Kaplan, D. L. Regulation of silk material structure by temperature-controlled water vapor annealing. *Biomacromolecules* **2011**, *12*, 1686-1696.

71. Kim, Y. J.; Wu, W.; Chun, S.-E.; Whitacre, J. F.; Bettinger, C. J. Biologically derived melanin electrodes in aqueous sodium-ion energy storage devices. *Proc. Natl. Acad. Sci. USA* **2013**, *110*, 20912-20917.

72. Zhou, J.; Zhang, B.; Shi, L.; Zhong, J.; Zhu, J.; Yan, J.; Wang, P.; Cao, C.; He, D. Regenerated silk fibroin films with controllable nanostructure size and secondary structure for drug delivery. *ACS Appl. Mater. Interfaces* **2014**, *6*, 21813-21821.

73. Barbieri, E.; Sestili, P. Reactive oxygen species in skeletal muscle signaling. *J. Signal Transduction* **2012**, *2012*, 982794.

74. Canton, M.; Menazza, S.; Lisa, F. D. Oxidative stress in muscular dystrophy: from generic evidence to specific sources and targets. *J. Muscle Res. Cell Motil.* **2014**, *35*, 23-36.

Chapter 6

Surface Functionalized Silk Fibroin Films for Transdifferentiation of hMSCs into Neuron-like Cells

6.1 Introduction

Stem cells are considered as prospective candidates for tissue engineering (TE), regenerative medicine or therapy and also for developing disease models aimed at drug testing, owing to their unique biological properties, such as the ability to differentiate into various cell types, and hence, organs.[1-4] Stem cell maintenance in the undifferentiated and pluripotent state through self-renewal and modulation of their differentiation into cell lineage of interest lays the foundation for most TE and regenerative medicine applications. Self-renewal and directed *in vitro* differentiation of stem cells are better facilitated on biomaterial scaffolds that mimic the microenvironment of the native biological extracellular matrix (ECM). The scaffolds that promote proliferation and guided (trans)differentiation of stem cells on-demand for clinical needs are considered as ideal biomaterial scaffolds.[5-8] On the other hand, classical approach involves the use of specific biological supplements (cues) along with other soluble growth factors for the modulation of stem cell proliferation and differentiation.[9-12] hMSCs obtained from bone marrow (BMSCs) and adipose tissues (ADSCs) are indispensable for stem cell culture, differentiation studies and stem cell-based therapies, because of their ease of isolation and expansion. These adult stem cells, that are either commercially available or obtained from the patients are ideal for developing stem cell-laden biomaterial scaffolds for therapeutic and diagnostic applications.[11,13-15] In contrast, the use of human embryonic stem cells (hESCs) is limited due to the unavailability, immune response and ethical issues.

Synthetic or natural polymers and inorganic material-based different scaffold formats (films, electrospun mats, sponges and solid surfaces) have been used in conjunction with ECM-mimicking surface functionalization, for maintaining stem cells in culture and for directing their differentiation.[16,17] Strategies including modulation of scaffold properties such as biomaterial stiffness and topography and employment of

external magnetic and electric stimuli among others were used to achieve control over stem cell fate.[18-25] Small molecules of either biological or synthetic origin have also been used to control the differentiation of stem cells under various culture conditions.[26,27] Among all the different biomaterials studied for neuronal tissue engineering, polymeric scaffolds are preferred, owing to their comparable substrate properties with respect to the native biological matrix (ECM). The harsh processing conditions associated with synthesis, limited scaffold format scope and non-free-standing nature of scaffolds made from synthetic polymers limit their exclusive use as biomaterial scaffolds for neural tissue engineering. Furthermore, synthetic polymers lack cell binding motifs and require an additional layer of biopolymer coating to facilitate cellular adhesion and proliferation. In contrast, the biopolymers possess good biocompatibility owing to their biological origin and support cellular adhesion. However, the major shortcomings of biopolymers that need to be addressed are large-scale availability, stability, and processability into various scaffold formats.[11,28-32]

In particular, an ideal biomaterial scaffold for stem cell-based tissue engineering should be biocompatible, biodegradable, and easily malleable into various scaffold formats, preferably under ambient conditions (similar to physiological conditions) and in aqueous solvents. Further, the biomaterial scaffolds must endure sterilization conditions without losing their integrity, be readily available in large amounts for industrial-scale scaffold preparation, remain stable at room temperature to avoid expensive cold storage conditions, and be self-supporting for *in vivo* implantation.[33] Silk fibroin (SF) protein extracted from the cocoons of domesticated silkworm *Bombyx mori* is a high molecular weight protein made of repeating alternating blocks of hydrophobic crystalline β-sheet and hydrophilic amorphous peptide domains.[34,35] SF has been extensively used for various tissue engineering, regenerative medicine, and biomedical applications, because

of its unique biocompatibility, biodegradability with slow degradation rate, moldability into different scaffold formats, and scope for imparting the desired properties by simple physical mixing and covalent modification.[36-42] SF proteins have also been used for coating the poly (*D*, *L*-lactic acid) and polyurethane biomaterial scaffolds to improve their interaction with osteoblasts and fibroblasts, respectively.[43,44] SF biomaterials have been successfully used for various stem cell-based tissue engineering applications and as biomaterial-stem cell interface material for brain electronic-device implants.[45-48] Herein, SF was used as the base biopolymer to fabricate the scaffolds for neural tissue engineering, because of its proven unique physical, chemical and biomaterial properties.

In this study, the fabrication of free-standing SF films (SFFs) surface functionalized with integrin-binding short peptides (YIGSR: Tyr-Ile-Gly-Ser-Arg and GYIGSR: Gly-Tyr-Ile-Gly-Ser-Arg) derived from the ECM protein laminin, and their potential application for directed *in vitro* differentiation of hMSCs into neuron-like cells is demonstrated. Bone marrow-derived adult hMSCs were chosen to study the anticipated biomaterial properties of surface-functionalized SFFs for stem cell-based tissue engineering applications. YIGSR, a pentapeptide occurring at 929-933 amino acid positions in high molecular weight ECM glycoprotein laminin (~ 900 kDa) is the major integrin-binding motif that facilitates cellular adhesion.[49] YIGSR and its analogs from laminin protein were used previously to functionalize the biomaterial scaffolds made from synthetic polymers and inorganic materials, and such scaffolds are demonstrated to promote embryonic stem cell adhesion, proliferation and in some cases for the neurite outgrowth.[50-54] YIGSR (L1) and its derivative GYIGSR (L2) with an additional flexible glycine amino acid were custom-prepared using solid phase peptide synthesis (SPPS) and tethered onto the surface of SFFs, post-film fabrication. SFFs were functionalized by both

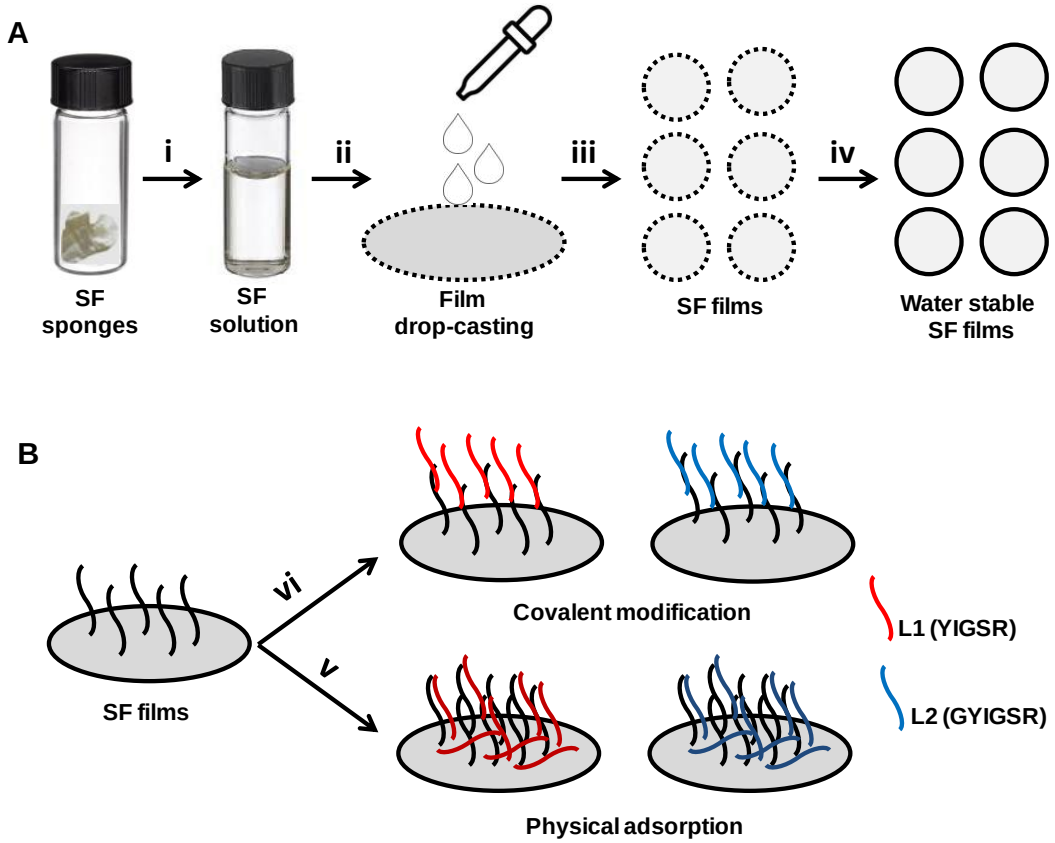

Scheme 6.1 Fabrication of functionalized SFFs. (A) Schematic showing the preparation of free-standing SFFs by drop-casting from SF HFIP solution. (i) Preparation of SF HFIP solution (4 wt%) from SF sponges; (ii) SFF drop-casting from HFIP solution under ambient conditions; (iii) Air drying of drop-casted SFFs; (iv) Aqueous methanol treatment of SFFs to improve the water stability. (B) Schematic showing the surface functionalization of SFFs through physical adsorption, (v) SFF incubation with peptides L1 (YIGSR), L2 (GYIGSR) and laminin in PBS for 4h; and through covalent grafting, (vi) EDC/NHS activation of SFFs, covalent amide bond formation with peptides L1 and L2 in PBS. HFIP: hexafluoro-2-propanol; PBS: phosphate buffered saline; EDC: 1-ethyl-3-(3-dimethylaminopropyl)carbodiimide; NHS: *N*-hydroxysuccinimide.

physical adsorption and by covalent amide bond formation to study the effect of nature of functionalization and presence of additional glycine linker as in L2 in inducing the hMSC proliferation and differentiation. The results obtained were also compared with that of laminin protein-coated SFFs. The results of hMSC adhesion, proliferation, and differentiation into neuron-like cells in the presence of retinoic acid exemplified the

significance of covalent surface functionalization of SFFs with GYIGSR. Maintaining and directing the transdifferentiation of hMSCs showed the potential of SFFs covalently functionalized with simple laminin peptide (GYIGSR) for stem cell-based TE and regenerative medicine applications.

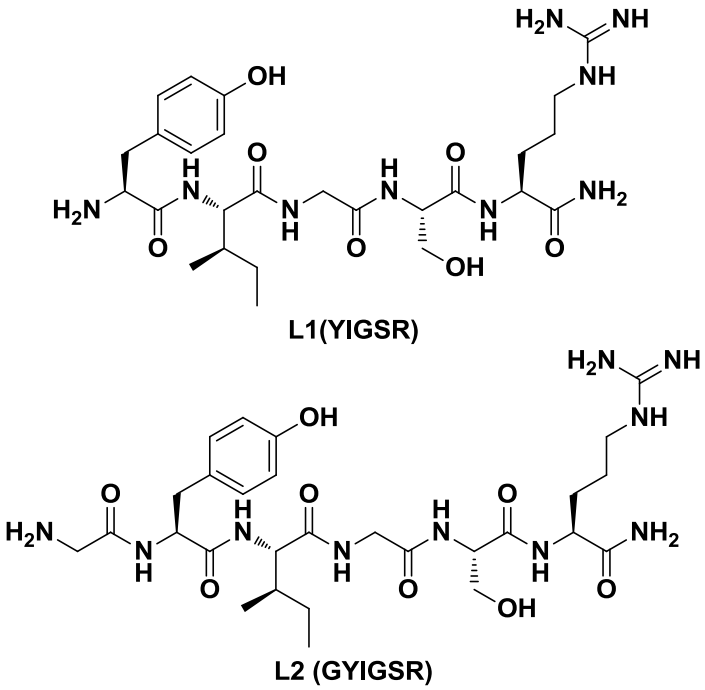

Scheme 6.2 Chemical structures of integrin binding laminin-derived peptide motifs. L1: YIGSR; L2: GYIGSR.

6.2 Results and Discussion

6.2.1 Synthesis of surface-functionalized SFFs

SF protein was extracted from the cocoons of domesticated mulberry silkworm *Bombyx mori* and lyophilized to obtain silk sponges according to the protocols, reported elsewhere.[42,55] Solution parameters such as protein (SF) concentration, the chemistry of solvent, and process parameters such as drop-casting conditions, and drying conditions were optimized to obtain free-standing, flexible and crack-free SFFs under ambient conditions. SFFs were prepared from 4 wt% solutions of SF in hexafluoro-2-propanol

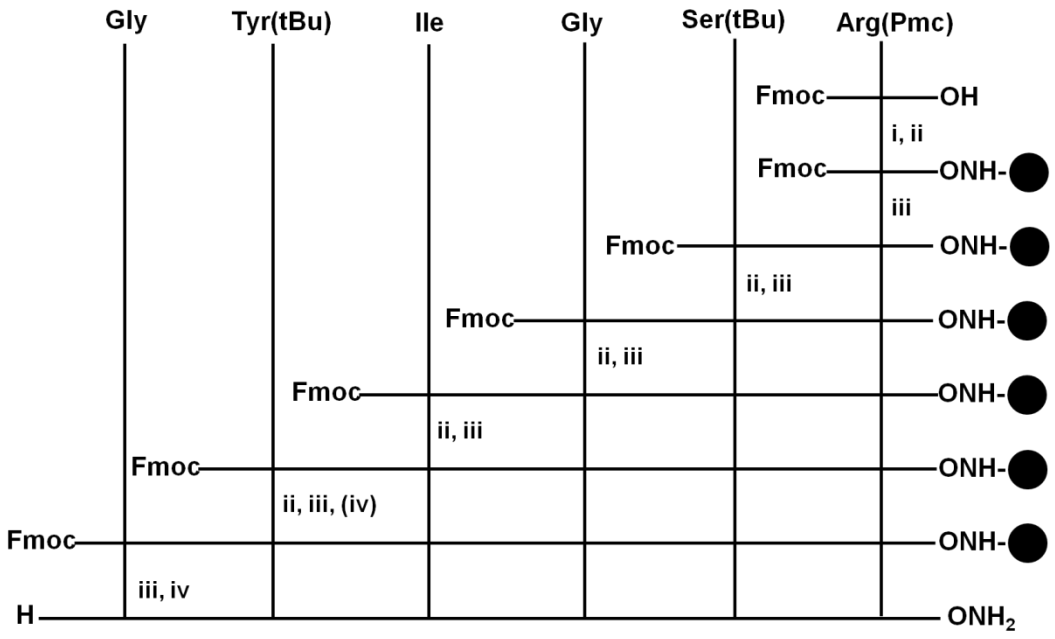

Scheme 6.3 Schematic showing the solid phase peptide synthesis (SPPS) of peptides L1 (YIGSR) and L2 (GYIGSR) on rink amide resin. (i) Fmoc-deprotected rink amide resin; (ii) HBTU in DMF, DIPEA in NMP; (iii) 40% piperidine in DMF; (iv) TFA:H_2O:TIPS (90:05:05) and the synthesis was carried out under ambient conditions. HBTU: O-(benzotriazol-1-yl)-*N,N,N',N'*-tetramethyluronium hexafluorophosphate; DIPEA: *N*,*N*-diisopropylethylamine ; DMF: *N*,*N*-dimethylformamide; NMP: *N*-methyl-2-pyrrolidone; TFA: trifluoroacetic acid; TIPS: triisopropyl silane.

(HFIP) by the drop-casting method, and the obtained films were treated with aqueous methanol to impart water stability through induced β-sheet formation (Scheme 6.1A). The desired laminin peptides L1 and L2 (Scheme 6.2) were prepared on rink amide resin using solid phase peptide synthesis (Scheme 6.3), and purified using semi-preparative high performance liquid chromatography (HPLC), while the integrity of prepared peptides was established by high-resolution mass spectrometry (HRMS) (Figures 6.7 and 6.8).

SFFs were surface-functionalized with laminin peptides (L1 and L2) through physical adsorption and covalent amide bond formation using suitably modified protocols, reported in the literature. (Schemes 6.1B).[56-58] Briefly, surface covalent

functionalization of SFFs was achieved by the amide bond formation by surface functional group activation, followed by 1-ethyl-3-(dimethylaminopropyl) carbodiimide hydrochloride (EDC.HCl)/*N*-hydroxysuccinimide (NHS) peptide coupling. Peptides (L1 and L2) and laminin protein were physically adsorbed on the SFF surface by incubating with the corresponding solutions in phosphate buffered saline (PBS). All the functionalized SFFs were then rinsed thoroughly with excess PBS and milli-Q water, dried under vacuum at room temperature and stored in air-tight bags until further use. TCPS, unmodified SFFs (UM-SFF) and laminin protein-coated SFFs (Lam-SFF) were used as control substrates to study the effect of SF and efficiency of short peptide-tethered SFFs for stem cell proliferation and differentiation applications. The pristine un-modified (UM-SFF) SFFs, the physically modified ones with peptide L1 (PL1-SFF), L2 (PL2-SFF) and laminin protein (Lam-SFF), and the covalently functionalized SFFs with L1 (CL1-SFF) and L2 (CL2-SFF) were characterized thoroughly using various biophysical techniques, and their potential use as biomaterial scaffolds in cell culture and tissue engineering applications was studied.

6.2.2 Characterization of SFFs

The surface morphology of pristine aqueous methanol-treated SFFs and the effect of functionalization on the integrity of films were analyzed using scanning electron microscopy (SEM). Pristine UM-SFF showed a homogenous smooth surface, free from both microscopic and macroscopic cracks, making them suitable scaffolds for cell culture applications. SEM micrographs of surface-functionalized SFFs showed smooth surface morphology, and hence, surface functionalization did not affect the integrity of the films data not shown). The surface morphology of SFFs was studied using atomic force microscopy (AFM) to further understand the effect of functionalization (physical

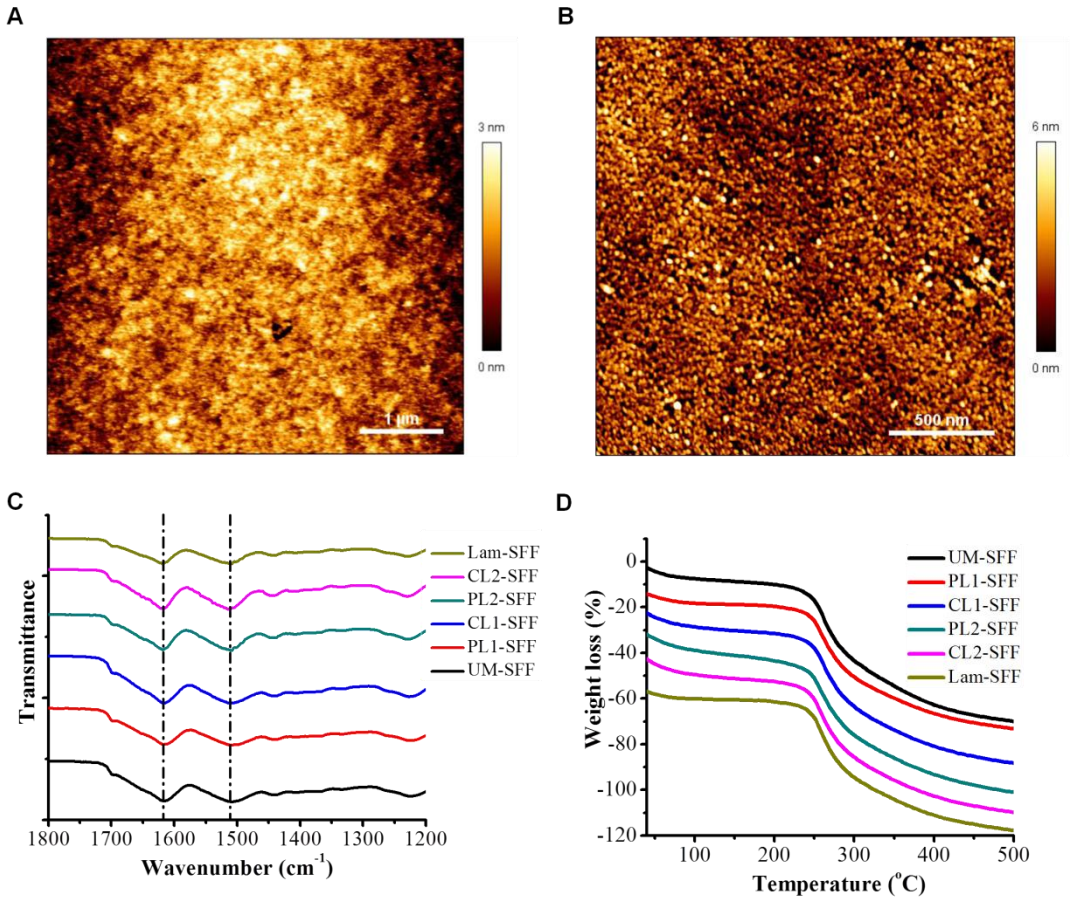

Figure 6.1 Characterization of pristine and surface functionalized SFFs. AFM micrographs of (A) UM-SFF (Roughness values Ra = 512 nm, RMS = 637 nm) and (B) CL1-SFF (Roughness values Ra = 940 nm, RMS = 1250 nm). (C) FTIR analysis of aqueous methanol treated pristine and surface functionalized SFFs. Vertical dotted lines are inserted to visualize and compare the SF amide absorption in SFFs. (D) Thermogravimetric (TG) graphs of SFFs showing high decomposition temperatures (>250 ºC).

adsorption and covalent modification). AFM images (roughness profile) of pristine (UM-SFF) and covalently modified SFF with L1 (CL1-SFF) are shown in Figures 6.1.AFM analysis indicated an increase in the surface roughness upon functionalization (from 637 pm for UM-SFF to 1.25 nm for CL1-SFF) in the nanoscale regime. The observed overall marginal increase in the RMS (root mean square) roughness can be attributed to the exposure of the SFFs to the phosphate buffered saline (PBS) and to other reagents used

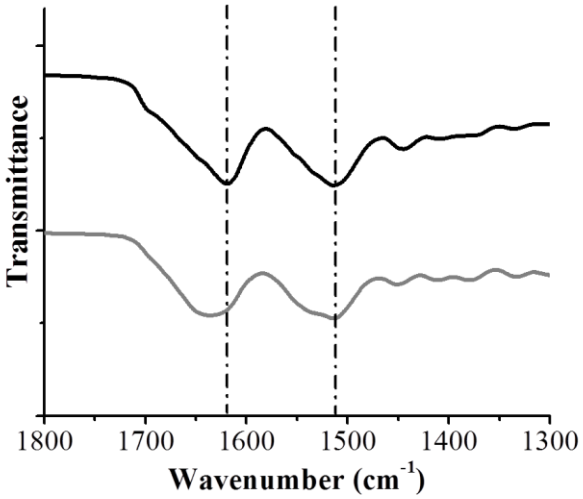

Figure 6.2 FT-IR analysis of as prepared and aqueous methanol treated SFFs. Gray line represents as prepared and the black line represents aqueous methanol treated SFFs. Vertically dotted lines are inserted to visualize, shift in the silk fibroin amide absorption before and after aqueous methanol treatment.

for the functionalization process and peptide tethering. The overall surface morphology (SEM) and roughness (AFM) analysis indicated crack-free, uniform films and the compatibility of protocols used for the surface modification in retaining the integrity of films.

The secondary structure of silk (β-sheet structure of crystalline domain) in SFFs was analyzed using Fourier transform infrared spectroscopy (FTIR) analysis in the amide-I (C=O stretching) and amide-II (N-H stretching) regions. As-prepared SFFs showed amide peaks, which are characteristic of the co-existence of random helical and β-sheet conformations, *i.e.* silk-I structure (1650, 1621, 1514 cm^{-1}). The shifting of IR absorption peaks upon aqueous methanol treatment for UM-SFF indicated improved β-sheet content (silk-II structure; 1699, 1619, and 1512 cm^{-1}) (Figure 6.2). Similar to aqueous methanol-treated UM-SFF, vibration frequencies, characteristic of β-sheet rich silk-II structure, were observed for all the functionalized SFFs (PL1-SFF: 1699, 1618, and 1508 cm^{-1};

CL1-SFF: 1699,1618, and 1511 cm^{-1}; PL2-SFF: 1697,1618, and 1512 cm^{-1}; CL2-SFF: 1699,1618, and 1515 cm^{-1}; Lam-SFF: 1699,1620, and 1510 cm^{-1}). Such observations indicate the retention of the β-sheet secondary structure, and hence, stability under culture conditions (Figure 6.1C). FTIR analysis further emphasized that the functionalization has a trifling effect on the stability and integrity of SFFs. Thermogravimetric (TG) analysis was carried out to evaluate the thermal stability and decomposition behavior of SFFs with increasing temperature. Pristine and functionalized SFFs showed very good thermal stability with decomposition temperatures above 250 ºC. In particular, a weight loss of less than 50% was observed even at temperatures as high as 500 ºC (Figure 6.1D). Therefore, high decomposition temperatures (>250 ºC) of SFFs indicate the potential of SFFs for room temperature storage, avoiding expensive cold storage conditions.

Hydrophilic property of biomaterial scaffolds is vital in modulating the cellular adhesion, proliferation, and differentiation of various cell types. To assess the hydrophilic nature of SFFs, contact angle (CA) measurements were performed using the sessile drop technique with Milli-Q water and alpha minimum essential medium (αMEM) cell culture medium under ambient conditions. Pristine UM-SFF films showed a contact angle of 64.6 ± 0.1 for water and 55.9 ± 0.9 for αMEM culture medium. On the other hand, surface functionalization marginally altered the hydrophilicity of scaffolds, which is reflected in the contact angle values for surface-functionalized SFFs (PL1-SFF: 64.5 ± 0.8 (H_2O), 53.1 ± 0.9 (αMEM); CL1-SFF: 61.2 ± 0.6 (H_2O), 55.9 ± 0.9 (αMEM); PL2-SFF: 61.9 ± 0.6 (H_2O), 50.7 ± 0.2 (αMEM); CL2-SFF: 60.6 ± 0.6 (H_2O), 54.9 ± 0.7 (αMEM); Lam-SFF: 65.4 ± 0.2 (H_2O), 59.9 ± 0.8 (αMEM)) (Table 6.1). Overall, contact angle measurements of SFFs using water and cell culture medium established the hydrophilic nature of functionalized SFFs.

Table S1. Hydrophilicity of pristine and surface functionalized SFFs. Contact angle values for water and αMEM droplets on the surface of SFFs measured under ambient conditions.

Sample	H_2O Contact angle	αMEM Contact angle
UM-SFF	64.6 ± 0.1	55.9 ± 0.9
PL1-SFF	64.5 ± 0.8	53.1 ± 0.9
CL1-SFF	61.2 ± 0.6	55.9 ± 0.9
PL2-SFF	61.9 ± 0.6	50.7 ± 0.2
CL2-SFF	60.6 ± 0.6	54.9 ± 0.7
Lam-SFF	65.4 ± 0.2	59.9 ± 0.8

6.2.3 Cell culture

hMSCs of bone marrow origin were chosen for the cell culture and intended transdifferentiation studies. The viability of hMSCs on SFFs was evaluated using 3-(4,5-dimethylthiazol-2-yl)-2,5-diphenyltetrazolium bromide (MTT) assay. MTT, chemically a tetrazolium derivative, is reduced by cellular oxidoreductases to purple-colored formazan crystals inside the cells. Thus, the amount of purple-colored formazan produced is measured by a change in the optical density at 595 nm, which gives information about cell viability on SFFs. TCPS served as a control to compare the suitability of SFFs for cell culture applications. Similarly, pristine silk films (UM-SFF) served as the control substrates to study the effect of surface functionalization on cell viability and proliferation. As shown in Figure 6.3A, no significant change in the hMSC cell number on TCPS and SFFs after 1-day culture could be recorded and such observations indicate the suitability of SFFs for hMSCs adhesion and viability, comparable to commercial cell

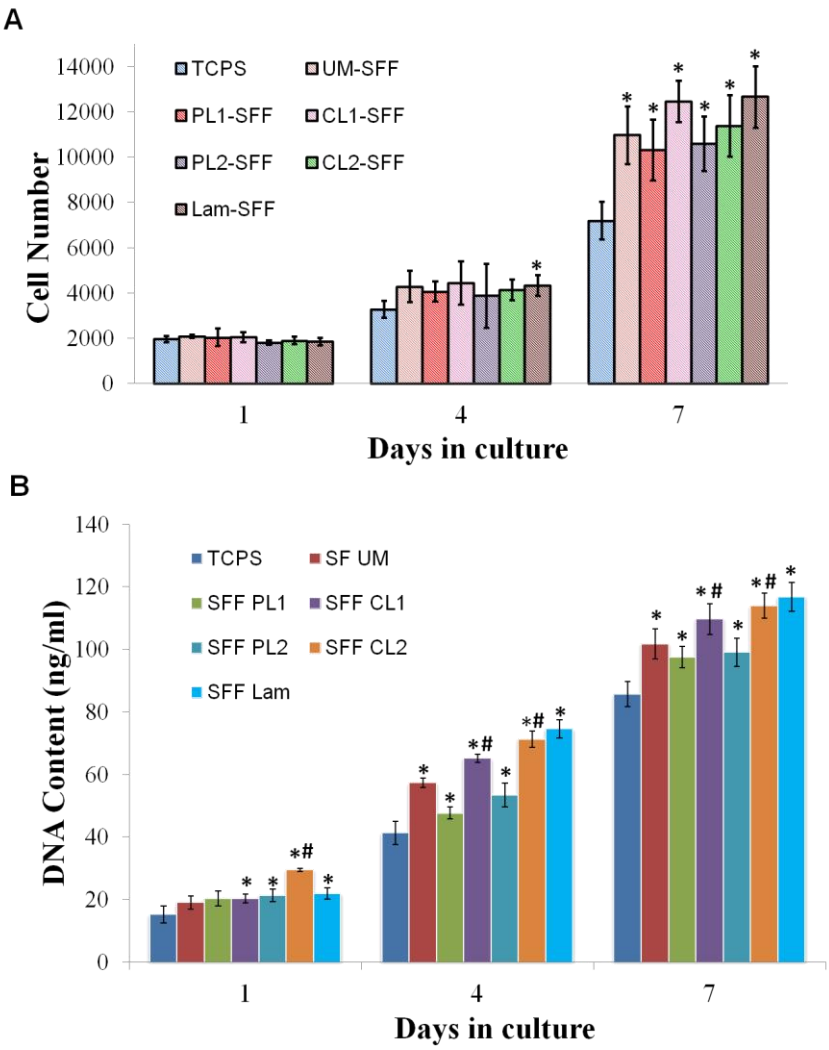

Figure 6.3 Cell viability and proliferation of hMSCs cultured on pristine and surface functionalized SFFs. (A) MTT assay results showing number of viable cells on TCPS control, pristine and functionalized SFF scaffolds for the culture period of 1, 4 and 7 days. '*' represents statistically significant difference ($p < 0.05$) in cell number with respect to the hMSCs cultured on TCPS control substrate. (B) PicoGreen assay results show the total DNA content of hMSCs cultured on TCPS/coverslip, pristine and functionalized SFFs after 1, 4 and 7 days of culture. '*' represents statistically significant difference ($p<0.05$) in the DNA content with respect to DNA content of hMSCS cultured on tissue culture treated control substrate (TCPS/coverslip). '#' represents statistically significant difference ($p<0.05$) of DNA content with respect to physically modified counterparts within the group. A standard curve of known dsDNA (ng/mL) concentration was used to calculate the DNA content from the samples. All data points represent mean ± SD (n=3). MTT: 3-(4,5-dimethylthiazol-2-yl)-2,5-diphenyltetrazolium bromide.

culture standard TCPS. On the contrary, a significant increase in the number of hMSCs on day 7 of culture was observed for all SFFs in comparison to TCPS, demonstrating the beneficial effect of SFFs for stemness in terms of sustained maintenance and proliferation in culture *in vitro* (Figure 6.3A).

The proliferation profile of hMSCs over a period of seven days in culture was evaluated by quantifying the total DNA content of cells cultured on TCPS, pristine and surface-functionalized SFF scaffolds after 1, 3, and 7-day intervals using PicoGreen assay (Figure 6.3B). A marked increase in the total DNA content of hMSCs grown on each SFF scaffold compared to cells grown on TCPS after 3 and 7-days in culture ($p<0.05$) indicated the synergistic benefits of SFFs in promoting the hMSCs viability and proliferation for extended periods of *in vitro* (7 days) cultures. A thorough analysis of hMSC proliferation data indicated a statistically significant increase in the DNA content of cells grown on covalently modified SFFs (CL1-SFF and CL2-SFF) as compared to their physically modified counterparts (PL1-SFF and PL2-SFF; $p<0.05$). This important observation highlights the significance of covalent modification over physical adsorption. As expected, laminin-functionalized SFFs (Lam-SFF) showed better hMSC proliferation compared to TCPS.

The cytocompatibility and suitability of SFFs for the proposed hMSC culture studies was further assessed by LIVE/DEAD staining assay. hMSCs grown on TCPS and SFFs were stained with fluorescein diacetate (FDA) and propidium iodide (PI) to stain the cell cytoplasm (green) and nuclei (red) in the case of live and dead cells, respectively. FDA is cell permeable and gets de-esterified by cellular enzymes to give a green color to the live cell cytoplasm upon excitation, whereas PI is impermeable to viable cell membranes and stains dead and cell membrane-compromised cells through DNA

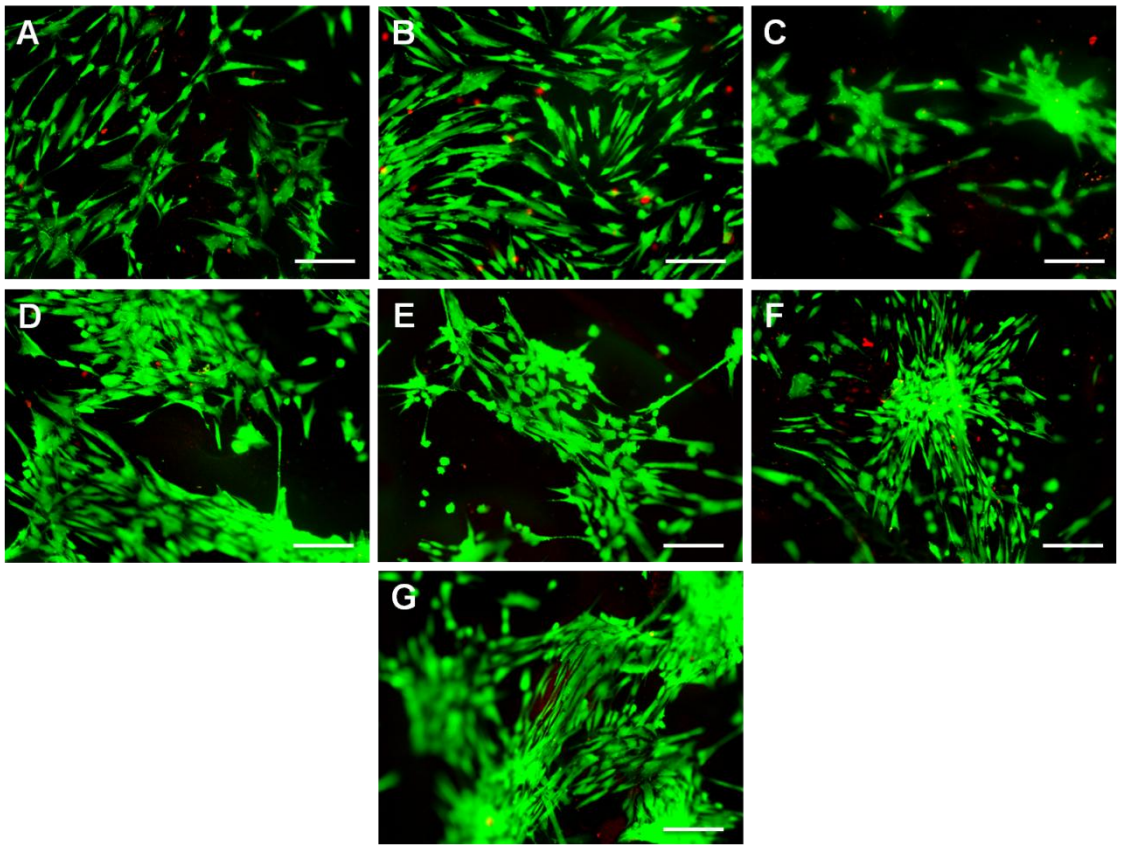

Figure 6.4 Live/dead staining of hMSCs on (A) TCPS control, (B) UM-SFF, (C) PL1-SFF, (D) CL1-SFF, (E) PL2-SFF, (F) CL2-SFF and (G) Lam-SFF after 3 days of culture. Green = FDA (live); red = PI (dead); scale bar = 100 μm. FDA: fluorescein diacetate; PI: propidium iodide.

intercalation. Figure 6.4 shows the representative images of FDA-PI stained fluorescence images of hMSCs on TCPS and SFFs after 3 days of culture. A significant number of hMSCs stained with FDA were observed for TCPS and all SFFs with only a few nuclei stained red with PI. This corroborates with the MTT and PicoGreen analysis, highlighting the cytocompatibility of SFFs for hMSCs culture experiments, *in vitro*. Moreover, hMSCs adhered to CL2-SFF and Lam-SFF tend to form cellular aggregates, partly resembling the neurosphere-like structures generated from neural stem cells (NSCs).[59]

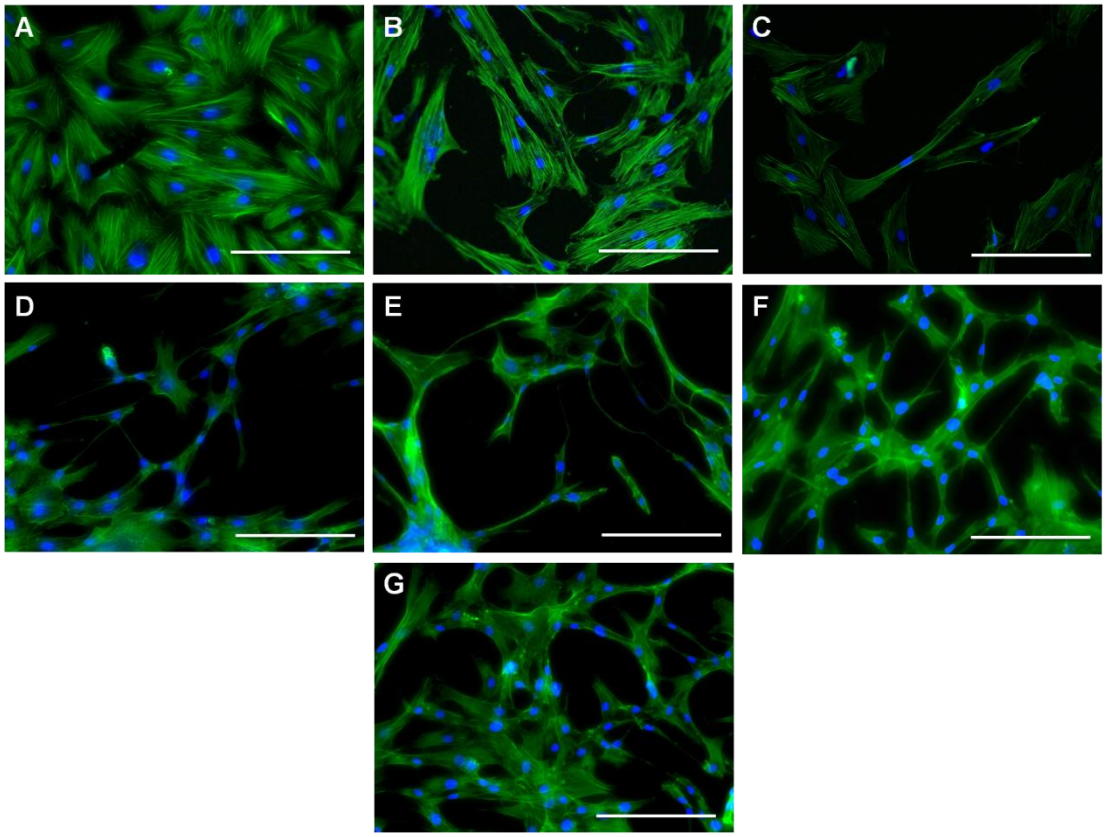

Figure 6.5 Influence of surface functionalization on neuron-like morphological transitions of hMSCs. Fluorescence images of hMSCs cultured on (A) TCPS control, (B) UM-SFF, (C) PL1-SFF, (D) CL1-SFF, (E) PL2-SFF, (F) CL2-SFF and (G) Lam-SFF in neuronal differential media for 7 days. hMSC cytoskeleton stained green with Alexa Fluor 488-Phalloidin and nuclei counterstained blue with DAPI. Scale bar = 100 μm.

6.2.4 Differentiation of hMSCs into neuron-like cells

Transdifferentiation of hMSC into neuronal lineage was achieved by culturing cells on the surface-functionalized SFF scaffolds in the presence of biochemical cue, retinoic acid [RA: (2E,4E,6E,8E)-3,7-dimethyl-9-(2,6,6-trimethylcyclohexen-1-yl)nona-2,4,6,8-tetraenoic acid]. hMSCs cultured on SFFs in regular αMEM culture media did not show any significant morphological transformation, indicating the absence of any differentiation (data not shown). High proliferation of hMSCs cultured on functionalized SFFs as compared to TCPS control in the absence of biochemical cue for differentiation highlights the potential use of SFFs as scaffolds for maintaining hMSCs in the

undifferentiated pluripotent state for TE applications. RA, a metabolite of Vitamin A, is known to induce the (trans)differentiation of embryonic and adult stem cells to neuron-like cells when used in combination with appropriate biomaterial scaffolds.[60,61] The morphological changes of hMSCs, were monitored using fluorescence microscopy analysis after cell staining and the representative merged fluorescence images are shown in Figure 6.5. The cytoskeleton was stained with Alexa Fluor 488-Phalloidin, and DAPI was used to counterstain the nuclei of fixed cells on TCPS and SFFs after 7 days of hMSCs culture in neuronal induction media. Cells cultured on control substrate (TCPS or glass coverslip) showed well spread spindle-like morphology, typical of the undifferentiated hMSCs (Figure 6.5A). In contrast, hMSCs cultured on laminin-coated SFFs (Lam-SFF) exhibited elongated and interconnected cellular networks similar to NSC culture *in vitro* (Figure 6.5G). hMSCs cultured on pristine (UM-SFF) films exhibited slightly stretched morphology as compared to the cells on control TCPS substrate (Figure 6.5B). hMSCs cultured on physically modified SFFs with YIGSR peptide (PL1-SFF) showed slightly stretched morphology similar to UM-SFF, and few cells showed elongated cell morphology (Figure 6.5C). Likewise, cells cultured on covalently modified SFFs (CL1-SFF) showed stretched morphology similar to PL1-SFF while some of the cell population showed elongated and interconnected cellular networks (Figure 6.5D). hMSCs cultured on SFFs physically modified with L2 (PL2-SFF) largely showed laterally extended morphology comparable to hMSCs on PL1-SFF and cellular connectivity resembling cells on CL1-SFF (Figure 6.5E). In contrast, hMSCs cultured on SFFs covalently modified with L2 (CL2-SFF) showed a uniform population of cells that were laterally elongated and well-interconnected as well (Figure 6.5F). The observed morphological changes of hMSCs from well-spread spindle-like individual cells to laterally elongated and interconnected cellular network on CL2-SFF scaffolds was similar

to the cell growth and differentiation on laminin-functionalized SFFs (Lam-SFF). Such cellular morphological changes certainly indicate the transdifferentiation of hMSCs to become NSC-like cells. The observed morphological changes of hMSCs were more prominent on CL2-SFF and were comparable to Lam-SFF, indicating the advantage of flexible glycine linker in integrin binding and modulating the differentiation of stem cells. Further, directed differentiation of hMSCs into NSC-like cells only in the presence of RA exemplifies the potential biomaterial platforms for on-demand control of stem cell differentiation fate. NSC-like morphological features were observed only for hMSCs grown on CL1-SFF, CL2-SFF, and Lam-SFF. Hence, PL1-SFF and PL2-SFF scaffolds were excluded from further gene expression studies.

6.2.5 Gene expression analysis

The observed phenotypic or morphological changes of hMSCs were further corroborated with gene expression and densitometric analysis of neuron-specific markers using semiquantitative reverse transcription-polymerase chain reaction (RT-PCR). mRNA levels of neuron-specific markers, such as nestin (NES), β-tubulin III (TUBB3 or TUJ1), neurofilament light polypeptide (NEFL), and microtubule-associated protein 2 (MAP2) were monitored, while glyceraldehyde-3-phosphate dehydrogenase (GADPH) served as the internal control. The PCR products were then separated using gel electrophoresis and quantified by scanning in a gel documentation system. RT-PCR analysis demonstrated changes in the gene expression of neuronal specific markers for hMSCs grown on CL1-SFF and CL2-SFF, in comparison to the control TCPS and UM-SFF on day 7 (Figure 6.6). The gene expression of markers specific to neuronal progenitor cells (NES), immature neurons (TUBB3) was up-regulated for the hMSCs cultured on CL1-SFF as compared to control TCPS and UM-SFF scaffolds. Conversely, both MAP2 and NEFL,

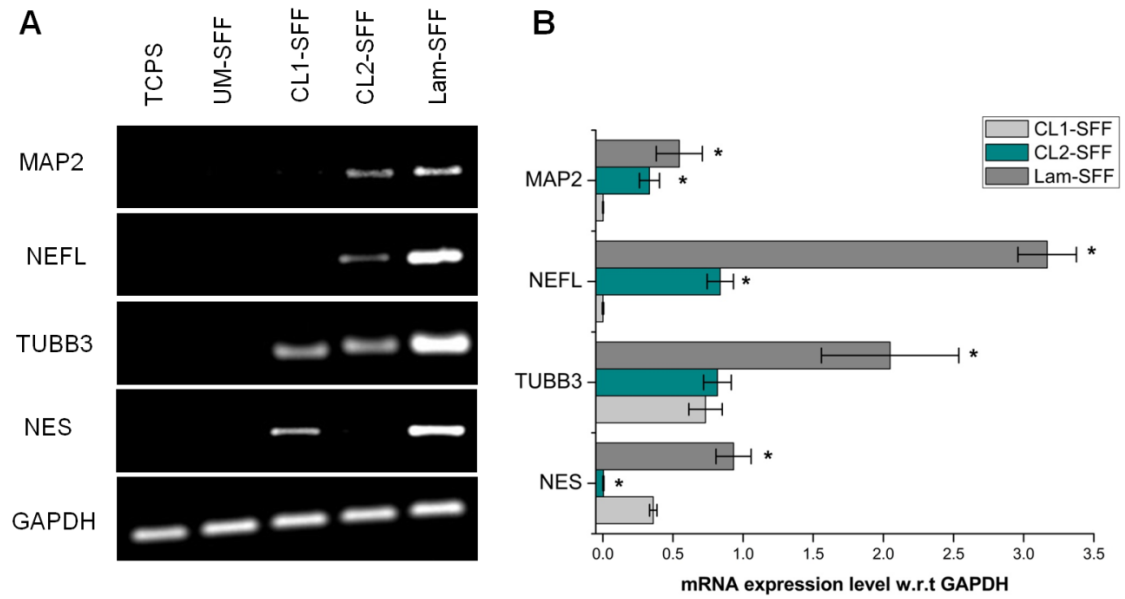

Figure 6.6 Influence of SFF surface functionalization on inducing transdifferentiation of hMSC into neuron-like cells. (A) Neuronal gene marker analysis of hMSCs cultured on TCPS, UM-SFF, CL1-SFF, CL2-SFF and Lam-SFF for 7 days in neuronal differentiation medium containing retinoic acid (RA, 1 µM). (B) Quantitative analysis of neuronal progenitor (NES) premature (TUBB3, NEFL) and mature neuronal expression (MAP2) in hMSCs cultured on TCPS, UM-SFF, CL1-SFF, CL2-SFF and Lam-SFF after 7 days. '*' represents statistically significant difference ($p<0.05$) with respect to internal GAPDH control. NES: nestin; TUBB3: class III β-tubulin; NEFL: neurofilament light polypeptide; MAP2: microtubule-associated protein 2; GAPDH: glyceraldehyde-3-phosphate dehydrogenase.

which are the markers for mature neurons, were faintly expressed in cells cultured on CL1-SFF. Interestingly, hMSCs cultured on CL2-SFF showed up-regulation of gene expression for progenitor, mature neuron-specific markers (TUBB3, NEFL, MAP2) (Figure 6.6). Relatively low levels of NES expression can be attributed to the fact that hMSCs on CL2-SFF were likely to have a mixed population of progenitor and mature cells, with a majority of mature cells leading to the lesser amount of NES expression. Overall, gene expression analysis exemplified the significance of covalent modification of SFFs for neural tissue engineering and further portrayed the importance of additional

Table 6.2 List of primers used for the semi-quantitative RT-PCR neuronal specific gene expression analysis. NES: nestin; TUBB3: class-III beta tubulin; NEFL: neurofilament light polypeptide; MAP2: microtubule-associated protein 2.

Genes	Primer Sequence		Amplicon Size (bp)
	Forward	Reverse	
GAPDH	AGGTCGGTGTGAACGGATTTG	TGTAGACCATGTAGTTGAGGTCA	123
NES	AACAGCGACGGAGGTCTCTA	TTCTCTTGTCCCGCAGACTT	220
TUBB3	ATGTGGTGCGGAAGGAGTGTGAAA	TGTTCATGATGCGGTCGGGATACT	144
NEFL	ACCTCCTCAACGTGAAGATGGCTT	ACTCTTCCTTGGCAGCTTCTTCCT	384
MAP2	TAACCAACCACTGCCAGACCTGAA	GCCACATTTGGATGTCACATGGCT	232

glycine amino acid linker in between the SFF surface and laminin peptide (YIGSR), in aiding hMSCs differentiation into neuron-like cells.

6.3 Conclusion

In conclusion, we have successfully fabricated ECM-mimicking, laminin-peptide (YIGSR) functionalized, free-standing silk fibroin films and showcased their potential application for stem cell proliferation and differentiation into neuronal cells. Surface functionalization of SFFs was evaluated through physical adsorption and covalent bond formation for guiding such differentiation. Surface-functionalized SFFs showed good compatibility with hMSCs and promoted their stemness (sustained proliferation without detectable differentiation). In contrast, SFFs modified by covalent bond formation with integrin-binding laminin-derived peptides (YIGSR in CL1-SFF and GYIGSR in CL2-SFF) successfully induced the differentiation of hMSC into neuron-like cells, comparable

to laminin protein-coated SFFs (Lam-SFF). Such important observation demonstrates the potential of such short peptides in replacing the laminin protein on suitably fabricated silk fibroin scaffold for neuronal tissue engineering applications. CL1-SFF having YIGSR on its surface supported the differentiation into neuronal progenitor cells but failed to promote matured neurons. Interestingly, CL2-SFF with additional glycine linker between SFF surface and YIGSR was the best scaffold in promoting differentiation of hMSCs into matured neuron-like cells. Overall, CL2-SFF substrates showed better differentiation efficiency compared to other functionalized SFFs including the physically coated counterpart (PL2-SFF). This highlighted the significance of permanent surface modification, i.e., covalent amide bond formation for intended long-term use of SFF biomaterial scaffolds. Altogether, laminin peptide functionalized SFF offers several benefits including ease of short peptide synthesis, aqueous functionalization route, and long-term stability. Moreover, the flexibility to maintain hMSCs in an undifferentiated state as well as to induce neuronal lineage commitment on-demand in the presence of retinoic acid make SFFs, ideal biomaterial scaffolds tissue engineering and regenerative therapy applications.

6.4 Experimental Section

6.4.1 Materials and methods

All the chemicals and solvents were purchased either from Sigma-Aldrich or Spectrochem India and used for peptide synthesis without further purification unless otherwise specifically mentioned. Fmoc amino acids with appropriate side chain protection group were obtained from Novabiochem and used as received. Preparative high performance liquid chromatography (HPLC, Shimadzu LC-8A) was used to purify peptides and their purity was monitored at 215 nm for peptide content. High resolution

mass spectrometry (HRMS, Agilent UHD Accurate-Mass Q-TOF LC/MS system) was used to further confirm the integrity of peptides. Mulberry silkworm *Bombyx mori* cocoons of CB gold variety for scaffold preparation were procured from Ramnagara silk cocoon market, Karnataka, India.

6.4.2 Solid phase synthesis of peptides

Peptides YIGSR (L1) and GYIGSR (L1) were synthesized using standard solid phase peptide synthesis (SPPS) through Fmoc-chemistry on Multisyntech Syro II automated peptide synthesizer. Fmoc-Rink amide resin (Novabiochem) was used as solid support for the synthesis. O-(benzotriazol-1-yl)-*N*,*N*,*N'*,*N'*-tetramethyluronium hexafluorophosphate (HBTU, Novabiochem) along with N, N-diisopropylethylamine (DIPEA, Spectrochem, India) was used as activation mixture and 4 equivalents of Fmoc protected amino acids (0.5 mmol) in *N*,*N*-dimethylformamide (DMF, Spectrochem, India) were used for peptide couplings at room temperature. 40% Piperidine in DMF was used for the deprotection of Fmoc- group from N-terminus of amino acids. Peptide cleavage from the resin and side chain deprotection was achieved by reacting the resin with cleavage cocktail (TFA:DCM:TIPS, 90:05:05) for 15 min at room temperature. The peptide was cleaved from the resin on cleavage transfer workstation of the peptide synthesizer using inert gas (dry N_2) positive pressure. Peptides were precipitated from the cleavage cocktail and purified by reverse phase preparative HPLC. The integrity of synthesized peptides was confirmed by HRMS analysis.

6.4.3 Preparation of surface functionalized SFFs

Silk fibroin extraction. Silk fibroin solution was prepared from the cocoons of mulberry silkworm *Bombyx mori* according to the protocols reported by us and others.[42,55] The cocoons were cut into approximately 4 cm x 4 cm size pieces, washed thoroughly with deionised water and boiled for 30 min in 20 mM Na_2CO_3 solution. The silk fibroin was washed thoroughly with plenty of milli-Q water to remove the water-soluble sericin outer layer. The obtained native silk fibroin was dissolved in 9.3M LiBr at 60 ºC and the resulting amber-colored solution was dialyzed using an activated 14 kDa MWCO cellulose membrane (Sigma) against milli-Q water with a total of six water changes at regular intervals. Lyophilization of aqueous regenerated silk fibroin solution was carried out by initially freezing the solution using liquid N_2 followed by freeze drying at -70 ºC for 24 h to yield fibroin sponges.

Preparation of SFFs. Silk fibroin sponges were dissolved in HFIP (4 wt %) at room temperature and silk fibroin films (SFFs) were prepared by the drop-casting method according to the protocols reported by us earlier.[42] Drop-casted films were air dried overnight at 25 ºC and treated with 90% methanol-water mixture (v/v) to promote the β-sheet formation that increases the stability of films when they are used in water and in culture media. The films were further air dried overnight at room temperature and stored in air-tight bags. Physical and chemical modifications were carried out using water stable SFFs obtained after methanol treatment.

Physical adsorption of peptides on SFFs. Physical surface adsorption of laminin-derived integrin binding peptides (L1 and L2) and laminin protein from Engelbreth-Holm-Swarm murine sarcoma basement membrane (Sigma, L 2020) on SFFs was achieved by incubating the films with L1, L2 (0.2 mg peptide/mL of PBS, pH 7.4) and

laminin (20 µg/mL) solutions for 4 h at 37 ºC. The films were then rinsed twice each with PBS and milli-Q water, dried under vacuum at room temperature.

Covalent functionalization of SFFs. The surface covalent functionalization of SFFs with peptides (L1 and L2) was carried out using reported methods with slight modifications.[56-58] SFFs were soaked in PBS (10 mM, pH 6.5) for 30 min to achieve the surface realignment of hydrophilic groups and to promote the covalent functionalization. The activation of -COOH groups of Asp and Glu amino acids of PBS soaked SFFs was achieved by treating with activation buffer containing 1-ethyl-3-(dimethylaminopropyl) carbodiimide hydrochloride (EDC.HCl)/N-hydroxysuccinimide (NHS) solution (0.5 mg/mL of EDC and 0.7 mg/mL of NHS in PBS buffer) for 15 min at ambient conditions. The activated NHS esters of SFFs were reacted with laminin-derived integrin binding peptide motifs YIGSR (L1) and GYIGSR (L2) (0.2 mg/mL) in PBS (pH 7.4) at ambient temperature for 2 h. After the reaction, SFFs were washed with PBS (pH 7.4) for 5 min, rinsed twice with PBS and once with milli-Q water to remove the buffer salts from the film surface and dried in vacuum at room temperature.

6.4.4 Characterization of surface functionalized SFFs

Scanning electron microscopy (SEM). The surface morphology of as-prepared, aqueous methanol treated, and surface modified (both physical and chemical) SFFs was analyzed by field emission scanning electron microscope (FESEM, Carl Zeiss Ultra 55) at 5-10 kV. SFF samples were mounted onto SEM stubs using double-sided carbon tape and gold sputtering was carried out on the samples, prior to morphological analysis.

Fourier-transform infrared (FTIR) spectroscopy. The secondary structure of silk in the pristine and functionalized films was analyzed using FTIR spectroscopy with

attenuated total reflection (ATR) sampling technique (GladiATR, PerkinElmer). Briefly, the spectra of as- prepared, aqueous methanol treated and surface functionalized SFFs were recorded with 0.2 cm^{-1} data interval and with a resolution of 4 cm^{-1} using the diamond crystal as substrate. All the spectra presented are an average of 64 scans in the wavelength range of 4000-400 cm^{-1} and the data was plotted as % transmittance (% T) against wavenumber (cm^{-1}).

Atomic force microscopy (AFM). The surface morphology and roughness of the samples were measured using atomic force microscope (JPK, NanoWizard® 3-AFM). Samples were adhered onto microscope glass slide using 2 component epoxy glue and the analysis was carried out in intermittent contact (AC) mode under ambient conditions.

Surface wettability of SFFs. The wettability of the pristine and surface functionalized SFFs was assessed by contact angle measurements (Holmarc). Briefly, pristine and surface functionalized silk films were prepared on glass coverslips and subsequently contact angles were measured using sessile drop method for both milli-Q water and αMEM cell culture media under ambient conditions. The results were presented as mean ± standard deviation (n=3).

Thermal stability of SFFs. Thermal stability and decomposition properties of pristine and surface functionalized SFFs were evaluated using thermogravimetric analysis (TGA; Mettler, TGA/DSC 2). TGA measurement was carried out by heating the SFFs (pristine and functionalized) at 5 ºC/min in the temperature range of 40 ºC to 800 ºC under a continuous flow of dry nitrogen (20 mL/min).

6.4.5 In vitro cell culture experiments

Cell culture. Human mesenchymal stem cells (hMSCs) were procured from Institute for Regenerative Medicine, Texas A&M HSC COM, USA and all the experiments involving hMSCs were carried out with the prior approval from the Institutional Committee for Stem Cell Research and Therapy (IC-SCRT), Indian Institute of Science, Bengaluru. The cells from cryopreserved stock were revived and grown in complete growth medium containing alpha modified Eagle's medium (αMEM; Invitrogen) supplemented with 20% fetal bovine serum (MSC FBS; Invitrogen), 1% antibiotic-antimycotic solution (Sigma) and 2 mM L-glutamine (Invitrogen).

Cell cultures were maintained at 37 ºC, 95% humidity and 5% CO_2 using a humidified CO_2 incubator (Sanyo, MCO-18AC, USA) and the culture media was changed every alternate day of culture. Cells were detached from the tissue culture flasks upon reaching 70-80% of confluency using 0.05% trypsin-EDTA (Invitrogen) and harvested by neutralizing with complete media and centrifugation at 1500 rpm for 5 min. The cells were then subcultured for further use as required.

Cell viability studies. The cytocompatibility of functionalized SFFs was evaluated by measuring the viability and proliferation of hMSCs seeded onto 16 mm diameter circular SFFs with an average thickness of 15 µm. Cell viability test was performed using MTT (3-(4,5-dimethylthiazol-2-yl)-2,5-diphenyltetrazolium bromide, Sigma) assay on pristine and functionalized SFFs. MTT interacts with mitochondrial reductases of live cells and the resulting change in the optical density give the number of live cells. Approximately $l0^4$ cells/mL of hMSCs were seeded on the sterilized films placed in 24 well plates and incubated for 1, 4 and 7 days in humidified CO_2 incubator. Cell culture media in the wells was removed and washed twice with PBS after a stipulated period of culture, 15% MTT

reagent (Sigma) prepared in DMEM (without phenol red) was added and incubated for 4 h at 37 ºC. The purple colored formazan crystals formed was solubilized using high purity DMSO (Merck) and the intensity of color was measured by recording the optical density at 595 nm using a microplate reader (iMark, Bio-rad Laboratories, India). The measured intensity of formed formazan crystals is the direct measure of number of viable and metabolically active hMSCs on the SFFs.

LIVE/DEAD assay. Live and dead hMSCs on the SFFs were stained using fluorescein diacetate (FDA; green) and propidium iodide (PI; red) dye, respectively. Green fluorescence color is imparted to the live cells by de-esterification action of esterases which convert non-fluorescent FDA to green fluorescent fluorescein. Cell-impermeable PI intercalates with nuclei of dead or cell membrane compromised cells and imparts red fluorescence. hMSCs cultured on SFFs for the stipulated period were washed with 1X PBS, stained with 1 mL of FDA (25 mg/mL) for 15 min at 37 °C and with 1 mL of PI (10 mg/mL) for 5 min at room temperature. Samples were washed twice with 1X PBS and hMSC LIVE/DEAD ratio was assessed by fluorescence microscopy imaging within the 15–20 min of post staining procedure.

Cell proliferation studies. The proliferation of hMSCs on pristine and functionalized SFFs was evaluated using PicoGreen assay by measuring the total DNA content of the cells on the scaffolds. Quanti-iT Picogreen dsDNA assay kit (Invitrogen) was used to quantify the total DNA content. DNA quantification was carried out as per manufacturer's protocol. After 1, 4 and 7 days of culture, the samples were washed in 1X PBS and lysed with 250 mL of 0.1% Triton-X for 10 min. Equal volumes of 1X TE buffer and 100 mL of Picogreen working reagent (1: 300 dilution of the stock) were added in a 96 well plate to the cell lysate. The fluorescence intensity was recorded after 5

min incubation using a multi-mode plate reader (Eppendorf AF2200) with excitation and emission wavelengths of 485 and 535 nm, respectively. The total amount of DNA of cells cultured on different scaffolds was quantified using a standard curve of known dsDNA (ng/mL) concentration and fluorescence intensity.

6.4.5 hMSC neuronal differentiation and RT-PCR

hMSC differentiation studies. Differentiation of hMSCs into neuron-like cells was induced by the addition of 1 μM retinoic acid (RA) to αMEM culture media. The formation of neuron-like cells on the pristine and surface functionalized SFFs was analyzed by observing the morphological features using fluorescence microscopy analysis after 7 days in culture. After 7 days of culture, the TCPS and SFF-cell constructs were rinsed twice with PBS and fixed in 4% paraformaldehyde (Merck, India) for 20 min. The cell-scaffold constructs were further rinsed in PBS, permeabilized with 0.1% Triton-X-100 (Sigma, USA) for 10 min, followed by washing in PBS and blocking with 1% BSA for 30 min. The fixed and permeabilized cells were then stained with Alexa Fluor 488-Phalloidin (1:200 dilution, Invitrogen) for 20 min to visualize the cytoskeleton F-actin filaments, and counterstained with 1 mg/mL of DAPI stain (Invitrogen) to observe the cell nuclei. Fluorescence images were obtained using an inverted fluorescence microscope (Nikon Eclipse, model LV100D, Japan).

Semi-quantitative RT-PCR analysis. Approximately, 10^4 hMSCs/mL were seeded on sterile TCPS, peptide and laminin functionalized SFFs in 24 well plates and maintained for 7 days in humidified CO_2 incubator with the addition of biochemical cue retinoic acid (1 μM) in αMEM media. For mRNA analysis, total RNA was extracted using TRIzol (Invitrogen, USA) reagent, according to the manufacturer's protocol. The quality and

quantity of total extracted RNA samples were then examined using spectrophotometric OD260 (RNA) and OD280 (protein) measurements. RNA samples with an optical density ratio (OD260/OD280) greater than 1.9 were used for cDNA synthesis. The total RNA (0.5 µg) was reverse transcribed using the First-Strand cDNA Synthesis Kit (Fermentas, USA). PCR procedure was carried as follows: 5 min at 94 °C (1 cycle); 30 s at 94 °C (denaturation step), 30 s at the appropriate annealing temperature for the primer set under study (55-60 °C), 1 min at 72 °C (extension step) for the 25-30 cycles and a final annealing step for 7 min at 72 °C . The PCR products were separated by electrophoresis and quantified using gel documentation system. GAPDH mRNA level was used as internal normalization control. The primer sequences for the genes of interest are listed in Table 6.2.

Statistical analysis. All the results are reported as mean ± standard deviation and the statistical analysis was carried out using SPSS-16.0 (IBM, USA) software. At least three sample sets (n=3) were used for all the experiments and was repeated at least thrice. Values are considered statistically significant only when $p < 0.05$.

6.5 Appendix

- HPLC chromatogram and HMRS spectrum of L1
- HPLC chromatogram and HMRS spectrum of L2

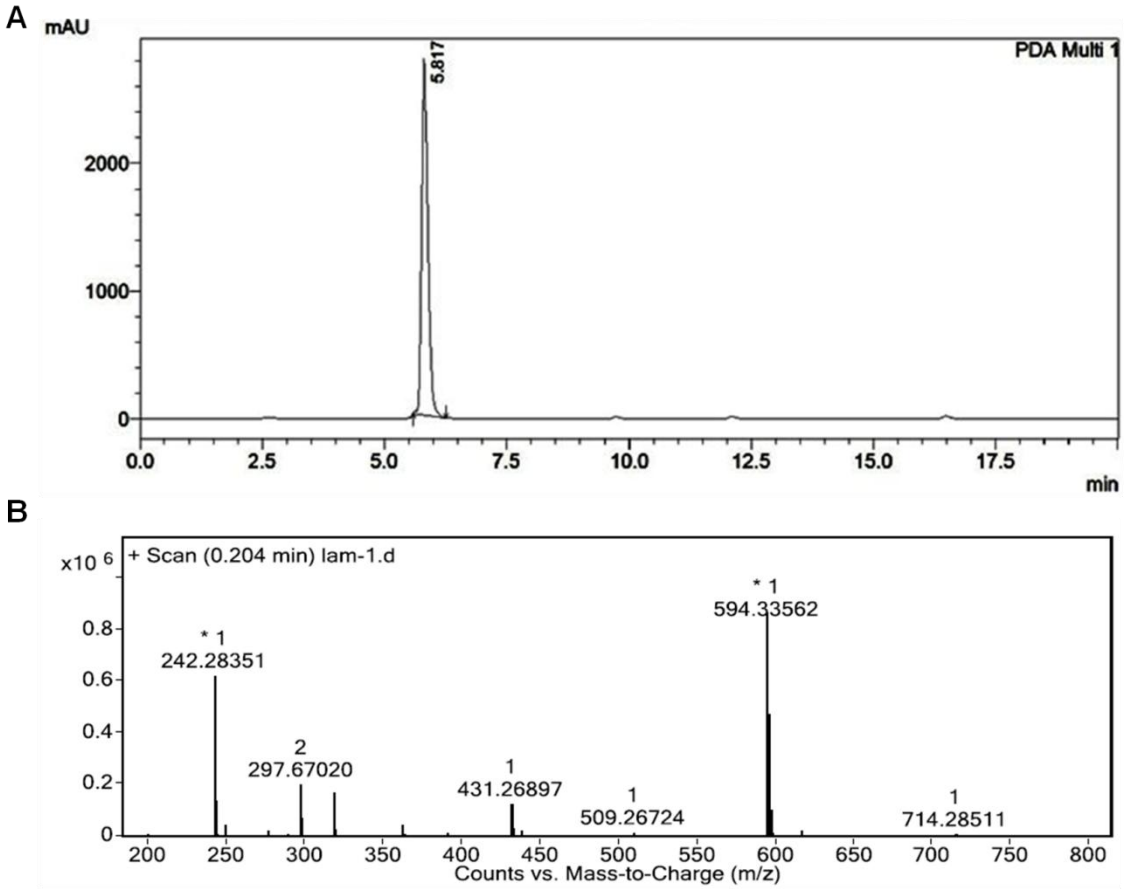

Figure 6.7 Characterization of L1 (YIGSR). (A) HPLC chromatogram showing the purity of L1. The chromatogram absorption was monitored at 215 nm using PDA detector. (B) HRMS spectrum of L1. HRMS (ESI): m/z calcd for $C_{26}H_{44}N_9O_7$: 594.3364 $[M+H]^+$; found: 594. 3356.

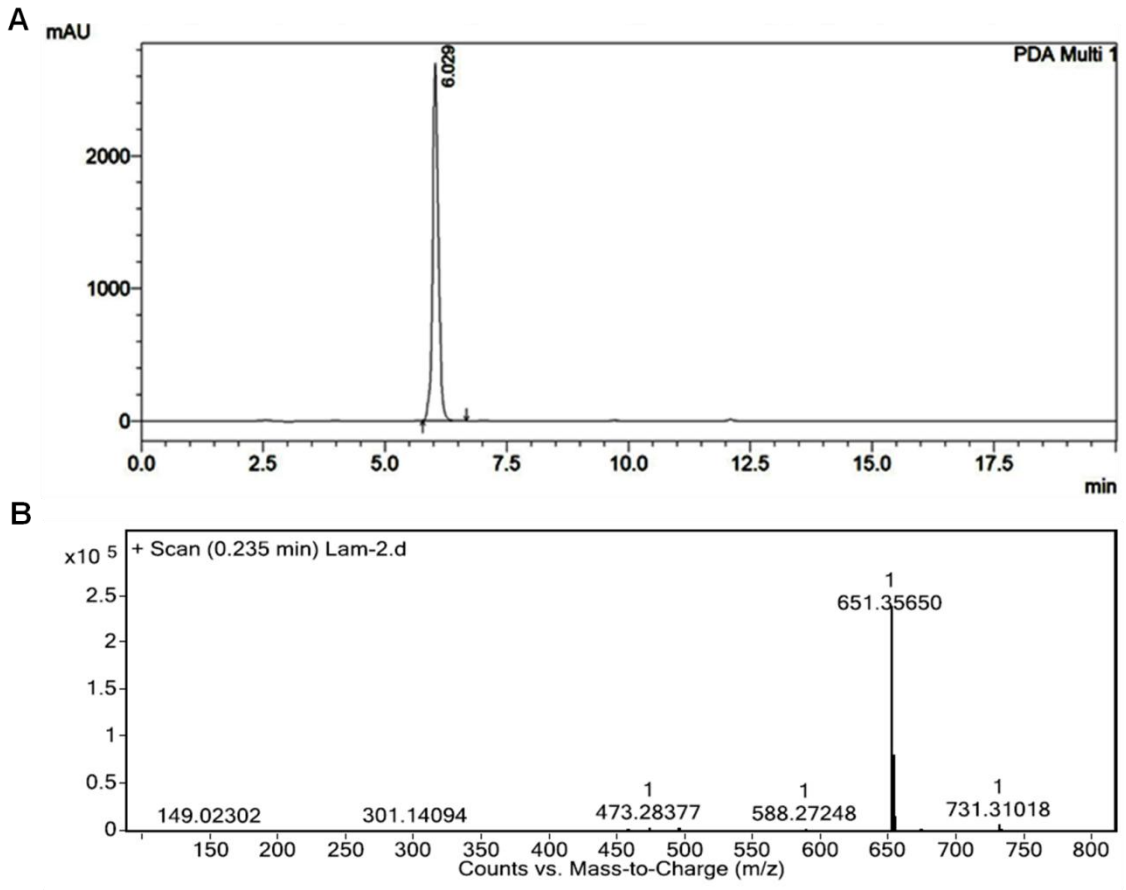

Figure 6.8 Characterization of L2 (GYIGSR). (A) HPLC chromatogram showing the purity of L2. The chromatogram absorption was monitored at 215 nm using PDA detector. (B) HRMS spectrum of L2. HRMS (ESI): m/z calcd for $C_{26}H_{47}N_{10}O_8$: 651.3578 $[M+H]^+$; found: 651.3565.

6.6 References

1. Bianco, P.; Robey, P. G. Stem cells in tissue engineering. *Nature* **2001**, *414*, 118-121.

2. Rosenthal, N. Prometheus's vulture and the stem-cell promise. *N. Engl. J. Med.* **2003**, *349*, 267-274.

3. Nelson, T. J.; Behfar, A.; Yamada, S.; Martinez-Fernandez, A.; Terzic, A. Stem cell platforms for regenerative medicine. *Clin. Transl. Sci.* **2009**, *2*, 222-227.

4. Marshak, D. R.; Gardner, R. L.; Gottlieb, D. *Stem cell biology*, Cold Spring Harbor Laboratory Press, Cold Spring Harbor, New York **2001**.

5. Lutolf, M. P.; Gilbert, P. M.; Blau, H. M. Designing materials to direct stem-cell fate. *Nature* **2009**, *462*, 433-441.

6. Gattazzo, F.; Urciuolo, A.; Bonaldo, P. Extracellular matrix: a dynamic microenvironment for stem cell niche. *Biochim. Biophys. Acta*. **2014**, *1840*, 2506-2519.

7. O'Brien, F. J. Biomaterials & scaffolds for tissue engineering. *Mater. Today* **2006**, *14*, 88-95.

8. Watt, F. M.; Huck, W. T. S. Role of the extracellular matrix in regulating stem cell fate. *Nat. Rev. Mol. Cell Biol.* **2013**, *14*, 467-473.

9. Guilak, F.; Cohen, D. M.; Estes, B. T.; Gimble, J. M.; Liedtke, W.; Chen, C. S. Control of stem cell fate by physical interactions with the extracellular matrix. *Cell Stem Cell* **2009**, *5*, 17-26.

10. Discher, D. E.; Mooney, D. J.; Zandstra, P. W. Growth factors, matrices, and forces combine and control stem cells. *Science* **2009**, *324*, 1673-1677.

11. Higuchi, A.; Ling, Q. D.; Ko, Y. A.; Chang, Y.; Umezawa, A. Biomimetic cell culture proteins as extracellular matrices for stem cell differentiation. *Chem. Rev.* **2012**, *112*, 4507-4540.

12. Brizzi, M. F.; Tarone, G.; Defilippi, P. Extracellular matrix, integrins, and growth factors as tailors of the stem cell niche. *Curr. Opin. Cell Biol.* **2012**, *24*, 645-651.

13. Tuan, R. S.; Boland, G.; Tuli, R. Adult mesenchymal stem cells and cell-based tissue engineering. *Arthritis Res. Ther.* **2003**, *5*, 32-45.

14. Caplan, A. I. Adult mesenchymal stem cells for tissue engineering versus regenerative medicine. *J. Cell. Physiol.* **2007**, *213*, 341-347.

15. Higuchi, A.; Chuang, C. W.; Ling, Q. D.; Huang, S. C.; Wang, L. M.; Chen, H.; Chang, Y.; Wang, H. C.; Bing, J. T.; Chang, Y.; Hsu, S. T. Differentiation ability of adipose-derived stem cells separated from adipose tissue by a membrane filtration method. *J. Membr. Sci.* **2011**, *366*, 286-294.

16. Toh, Y. C.; Blagovic, K.; Voldman, J. Advancing stem cell research with microtechnologies: opportunities and challenges. *Integr. Biol.* **2010**, *2*, 305-325.

17. Higuchi, A.; Ling, Q. D.; Chang, Y.; Hsu, S. T.; Umezawa, A. Physical cues of biomaterials guide stem cell differentiation fate. *Chem. Rev.* **2013**, *113*, 3297-3328.

18. Wen, J. H.; Vincent, L. G.; Fuhrmann, A.; Choi, Y. S.; Hribar, K. C.; Taylor-Weiner, H.; Chen, S.; Engler, A. J. Interplay of matrix stiffness and protein tethering in stem cell differentiation. *Nat. Mater.* **2014**, *13*, 979-987.

19. Ye, K.; Wang, X.; Cao, L.; Li, S.; Li, Z.; Yu, L.; Ding, J. Matrix stiffness and nanoscale spatial organization of cell-adhesive ligands direct stem cell fate. *Nano Lett.* **2015**, *15*, 4720-4729.

20. Yim, E. K. F.; Pang, S. W.; Leong, K. W. Synthetic nanostructures inducing differentiation of human mesenchymal stem cells into neuronal lineage. *Exp. Cell Res.* **2007**, *313*, 1820-1829.

21. McNamara, L. E.; McMurray, R. J.; Biggs, M. J. P.; Kantawong, F.; Oreffo, R. O. C.; Dalby, M. J. Nanotopographical control of stem cell differentiation. *J. Tissue Eng.* **2010**, *2010*, 120623.

22. Kim, H.; Kim, I.; Choi, H. J.; Kim, S. Y.; Yang, E. G. Neuron-like differentiation of mesenchymal stem cells on silicon nanowires. *Nanoscale* **2015**, *7*, 17131-17138.

23. Boda, S. K.; Thrivikraman, G.; Basu, B. Magnetic field assisted stem cell differentiation-role of substrate magnetization in osteogenesis. *J. Mater. Chem. B*, **2015**, *3*, 3150-3168.

24. Thrivikraman, G.; Madras, G.; Basu, B. Intermittent electrical stimuli for guidance of human mesenchymal stem cell lineage commitment towards neural-like cells on electroconductive substrates. *Biomaterials* **2014**, *35*, 6219-6235.

25. Thrivikraman, G.; Madras, G.; Basu, B. *Biomaterials*, Electrically driven intracellular and extracellular nanomanipulators evoke neurogenic/cardiomyogenic differentiation in human mesenchymal stem cells. *Biomaterials* **2016**, *77*, 26-43.

26. Lairson, L. L.; Lyssiotis, C. A.; Zhu, S.; Schultz, P. G. Small molecule-based approaches to adult stem cell therapies. *Annu. Rev. Pharmacol. Toxicol.* **2013**, *53*, 107-125.

27. Davies, S. G.; Kennewell, P. D.; Russell, A. J.; Seden, P. T.; Westwood, R.; Wynne, G. M. Stemistry: the control of stem cells in situ using chemistry. *J. Med. Chem.* **2015**, *58*, 2863-2894.

28. Kumbar, S.; Laurencin, C.; Deng, M. *Natural and Synthetic Biomedical Polymers*, Elsevier, Burlington, MA, USA **2014**.

29. Lutolf, M. P.; Hubbell, J. A. Synthetic biomaterials as instructive extracellular microenvironments for morphogenesis in tissue engineering. *Nat. Biotechnol.* **2005**, *23*, 47-55.

30. Kohane, D. S.; Langer, R. Polymeric biomaterials in tissue engineering. *Pediatr. Res.* **2008**, *63*, 487-491.

31. Dhandayuthapani, B.; Yoshida, Y.; Maekawa, T.; Kumar, D. S. Polymeric scaffolds in tissue engineering application: a review. *Int. J. Pol. Sci.* **2011**, *2011*, 290602.

32. Li, H.; Cooper-White, J. J. Changing ligand number and type within nanocylindrical domains through kinetically constrained self-assembly-impacts of ligand 'redundancy' on human mesenchymal stem cell adhesion and morphology. *Biomater. Sci.* **2014**, *2*, 1693-1705.

33. Abbott, R. D.; Kaplan, D. L. Engineering biomaterials for enhanced tissue regeneration. *Curr. Stem Cell Rep.* **2016**, *2*, 140-146.

34. Zhou, C. Z.; Confalonieri, F.; Medina, N.; Zivanovic, Y.; Esnault, C.; Yang, T.; Jacquet, M.; Janin, J.; Duguet, M.; Perasso, R.; Li, Z. G. Fine organization of *Bombyx mori* fibroin heavy chain gene. *Nucleic Acids Res.* **2000**, *28*, 2413-2419.

35. Matsumoto, A.; Lindsay, A.; Abedian, B.; Kaplan, D. L. Silk fibroin solution properties related to assembly and structure. *Macromol. Biosci.* **2008**, *8*, 1006-1018.

36. Kundu, S. C. *Silk Biomaterials for Tissue Engineering and Regenerative Medicine*, Woodhead Publishing, Cambridge, UK **2014**.

37. Mandal, B.; Kaplan, D. L. Biologic Biomaterials: Silk. In *Biomaterials: Principles and Practices*; Wong, J. Y.; Bronzino, J. D.; Peterson, D. R., Ed.;, CRC Press, Boca Raton, FL, USA, **2013**; pp 7.1-7.24.

38. Vepari, C.; Kaplan, D. L. Silk as a biomaterial. *Prog. Polym. Sci.* **2007**, *32*, 991-1007.

39. Seib, F. P.; Kaplan, D. L. Silk for drug delivery applications: opportunities and challenges. *Isr. J. Chem.* **2013**, *53*, 756-766.

40. Kundu, B.; Kurland, N. E.; Bano, S.; Patra, C.; Engel, F. B.; Yadavalli, V. K.; Kundu, S. C. Silk proteins for biomedical applications: bioengineering perspectives. *Prog. Polym. Sci.* **2014**, *39*, 251-267.

41. Omenetto, F. G.; Kaplan, D. L. New opportunities for an ancient material. *Science* **2010**, *329*, 528-531.

42. Manchineella, S.; Thrivikraman, G.; Khanum, K. K.; Ramamurthy, P. C.; Basu, B.; Govindaraju, T. Pigmented silk nanofibrous composite for skeletal muscle tissue engineering. *Adv. Healthcare Mater.* **2016**, *5*, 1222-1232.

43. Cai, K.; Yao, K.; Cui, Y.; Yang, Z.; Li, X.; Xie, H.; Qing, T.; Gao, L. Influence of different surface modification treatments on poly(D, L-lactic acid) with silk fibroin and their effects on the culture of osteoblast in vitro. *Biomaterials* **2002**, *23*, 1603-1611.

44. Chiarini, A.; Petrini, P.; Bozzini, S.; Pra, I. D.; Armato, U. Silk fibroin/poly(carbonate)-urethane as a substrate for cell growth: in vitro interactions with human cells. *Biomaterials* **2003**, *24*, 789-799.

45. Wang, Y. Z.; Kim, H. J.; Vunjak-Novakovic, G.; Kaplan, D. L. Stem cell-based tissue engineering with silk biomaterials. *Biomaterials* **2006**, *27*, 6064-6082.

46. Benfenati, V.; Stahl, K.; Gomis-Perez, C.; Toffanin, S.; Sagnella, A.; Torp, R.; Kaplan, D. L.; Ruani, G.; Omenetto, F. G.; Zamboni, R.; Muccini, M. Biofunctional silk/neuron interfaces. *Adv. Funct. Mater.* **2012**, *22*, 1871-1884.

47. Tien, L. W.; Wu, F.; Tang-Schomer, M. D.; Yoon, E.; Omenetto, F. G.; Kaplan, D. L. Silk as a multifunctional biomaterial substrate for reduced glial scarring around brain-penetrating electrodes. *Adv. Funct. Mater.* **2013**, *23*, 3185-3193.

48. Tang-Schomer, M. D.; Hu, X.; Hronik-Tupaj, M.; Tien, L. W.; Whalen, M. J.; Omenetto, F. G.; Kaplan, D. L. Film-based implants for supporting neuron-electrode integrated interfaces for the brain. *Adv. Funct. Mater.* **2014**, *24*, 1938-1948.

49. Graf, J.; Iwamoto, Y.; Sasaki, M.; Martin, G. R.; Kleinman, H. K.; Robey, F. A.; Yamada, Y. Identification of an amino acid sequence in laminin mediating cell attachment, chemotaxis, and receptor binding. *Cell* **1987**, *48*, 989-996.

50. Silva, G. A.; Czeisler, C.; Niece, K. L.; Beniash, E.; Harrington, D. A.; Kessler, J. A.; Stupp, S. I. Selective differentiation of neural progenitor cells by high-epitope density nanofibers. *Science* **2004**, *303*, 1352-1355.

51. Li, Y. C.; Liao, Y. T.; Chang, H. H.; Young, T. H. Covalent bonding of GYIGSR to EVAL membrane surface to improve migration and adhesion of cultured neural stem/precursor cells. *Colloids Surf. B*, **2013**, *102*, 53-62.

52. Callahan, L. A. S.; Xie, S.; Barker, I. A.; Zheng, J.; Reneker, D. H.; Dove, A. P.; Becker, M. L. Directed differentiation and neurite extension of mouse embryonic stem cell on aligned poly(lactide) nanofibers functionalized with YIGSR peptide. *Biomaterials* **2013**, *34*, 9089-9095.

53. Zheng, J.; Kontoveros, D.; Lin, F.; Hua, G.; Reneker, D. H.; Becker, M. L.; Willits, R. K. Enhanced schwann cell attachment and alignment using one-pot "dual click" GRGDS and YIGSR derivatized nanofibers. *Biomacromolecules* **2015**, *16*, 357-363.

54. Wang, K.; Tang, R. Y.; Zhao, X. B.; Li, J. J.; Lang, Y. R.; Jiang, X. X.; Sun, H. J.; Lin, Q. X.; Wang, C. Y. Covalent bonding of YIGSR and RGD to PEDOT/PSS/MWCNT-COOH composite material to improve the neural interface. *Nanoscale* **2015**, *7*, 18677-18685.

55. Rockwood, D. N.; Preda, R. C.; Yücel, T.; Wang, X.; Lovett, M. L.; Kaplan, D. L. Materials fabrication from *Bombyx mori* silk fibroin. *Nat. Protoc.* **2011**, *6*, 1612-1631.

56. Sofia, S.; McCarthy, M. B.; Gronowicz, G.; Kaplan, D. L. Functionalized silk-based biomaterials for bone formation. *J. Biomed. Mater. Res. Part B* **2000**, *54*, 139-148.

57. Bai, L.; Zhu, L.; Min, S.; Liu, L.; Cai, Y.; Yao, J. Surface modification and properties of *Bombyx mori* silk fibroin films by antimicrobial peptide. *Appl. Surf. Sci.* **2008**, *254*, 2988-2995.

58. Murphy, A. R.; Kaplan, D. L. Biomedical applications of chemically-modified silk fibroin. *J. Mater. Chem.* **2009**, *19*, 6443-6450.

59. Ma, K.; Fox, L.; Shi, G.; Shen, J.; Liu, Q.; Pappas, J. D.; Cheng, J.; Qu, T. Generation of neural stem cell-like cells from bone marrow-derived human mesenchymal stem cells. *Neurol. Res.* **2011**, *33*, 1083-1093.

60. Okada, Y.; Shimazaki, T.; Sobue, G.; Okano, H. Retinoic-acid-concentration-dependent acquisition of neural cell identity during in vitro differentiation of mouse embryonic stem cells. *Dev. Biol.* **2004**, *275*, 124-142.

61. Maden, M. Retinoic acid in the development, regeneration and maintenance of the nervous system. *Nat. Rev. Neurol.* **2007**, *8*, 755-765.

List of Publications

PhD Thesis

- **Manchineella, S.**; Govindaraju, T. Hydrogen Bond Directed Self-Assembly of Cyclic Dipeptide Derivatives: Gelation and Ordered Hierarchical Architectures. *RSC Adv.* **2012**, *2*, 5539-5542.

- **Manchineella, S.**; Prathyusha, V.; Priyakumar, U. D.; Govindaraju, T. Solvent-Induced Helical Assembly and Reversible Chiroptical Switching of Chiral Cyclic-Dipeptide-Functionalized Naphthalenediimides. *Chem. Eur. J.* **2013**, *19*, 16615-16624.

- **Manchineella, S.**; Greeshma, T.; Khanum, K. K.; Ramamurthy, P. C.; Basu, B.; Govindaraju, T. Pigmented Silk Nanofibrous Composite for Skeletal Muscle Tissue Engineering. *Adv. Healthcare Mater.* **2016**, *5*, 1222-1232.

- **Manchineella, S.**; Greeshma, T.; Basu, B.; Govindaraju, T. Surface-Functionalized Silk Fibroin Films as a Platform To Guide Neuron-like Differentiation of Human Mesenchymal Stem Cells. *ACS Appl. Mater. Interfaces* **2016**, *8,* 22849-22859.

- **Manchineella, S.**; Govindaraju, T. Cyclic Dipeptide Ambidextrous Supergelators: Structure-Gelation Studies and *In Situ* Hydrogelation at Physiological pH. **2016** (*manuscript under preparation*).

- **Manchineella, S.**; Chandrashekar, V.; Govindaraju. T. Phenolic Amino Acid Containing Antioxidant Cyclic Dipeptides for Therapeutic Applications. **2016** (*manuscript under preparation*).

- **Manchineella, S.**; Govindaraju, T. Molecular Self-Assembly of Cyclic Dipeptide Derivatives and Their Applications. *ChemPlusChem* **2016** (**DOI**: 10.1002/cplu.201600450).

Miscellaneous

- **Shivaprasad, M.**; Govindaraju, T. Rhodamine Based Bright Red Colourimetric and Turn-On Fluorescence Chemosensor for Selective Detection of Cu^{2+}. *Mater. Technol.* **2011**, *26*, 168-172.

Patent

- **Shivaprasad, M.**; Govindaraju, T. Modified Silk with Conducting Biopolymer and Peptide Epitopes and Their Biomaterial Applications Thereof. **2016** (India Provisional Patent Filed).

Miscellaneous Highlights of Ph.D Work

- ✓ Received **Graduate Student Travel Grant** to deliver an oral presentation at **8th Annual International Workshop on Advanced Materials** organized by Ras Al Khaimah Center for Advanced Materials (RAKCAM), Ras Al Khaimah, United Arab Emirates in 2016.

- ✓ Received **Best Poster Award** at **Winter School** on **Frontiers in Material Science-2013**, organized by University of Cambridge and ICMS at Bangalore, India in 2013.

- ✓ Received **Best Poster Award** at **Chennai Chemistry Conference-2013**, Central Leather Research Institute (CLRI), Chennai, India in 2013.

- ✓ Part of research work is highlighted in **ChemistryViews** as "Pigments in Tissue Engineering" in 2016.

Brief Curriculum Vitae

Shivaprasad Manchineella was born on 25th July 1988 in Rangapuram, Telangana (India). He obtained his B.Sc. from Kakatiya University (India) in 2008 and his M.Sc. (Organic Chemistry) from Osmania University (India) in 2010. He was selected for the Summer Research Fellowship Program (SRFP, 2009) of Jawaharlal Nehru Centre for Advanced Scientific Research (JNCASR) and awarded Rajiv Gandhi Science Talent Research Fellow for the year 2009 in chemical sciences. He subsequently joined the research group of Professor T. Govindaraju at JNCASR for his Ph.D. in 2011. His research interest focuses on understanding the principles of biomolecular hierarchical assemblies, the development of affordable short-peptide- and protein-based smart (bio)materials for tissue engineering, regenerative medicine, diagnostic and healthcare applications.